MIGRATION AND ELECTROPOLYMERIZATION OF METHYL METHACRYLATE IN HARDENED CEMENT PASTE VIA ELECTROKINETIC TREATMENT

by

Xi Xie, M.S.

A Dissertation Presented in Partial Fulfillment
of the Requirements of the Degree
Doctor of Philosophy

COLLEGE OF ENGINEERING AND SCIENCE
LOUISIANA TECH UNIVERSITY

August 2019

LOUISIANA TECH UNIVERSITY

GRADUATE SCHOOL

June 10, 2019
Date of dissertation defense

We hereby recommend that the dissertation prepared by

Xi Xie, M.S.

entitled **MIGRATION AND ELECTROPOLYMERIZATION OF METHYL METHACRYLATE IN HARDENED CEMENT PASTE VIA ELECTROKINETIC TREATMENT**

be accepted in partial fulfillment of the requirements for the degree of

Doctor of Philosophy in Engineering, Materials & Infrastructure Systems Conc.

Henry E. Cardenas, Supervisor of Dissertation Research

Xingran Wang,
Head of Engineering

Members of the Doctoral Committee:
Dr. Henry Cardenas
Dr. David Hall
Dr. Arun Jaganathan
Dr. Xingran Wang
Dr. Sven Eklund

Approved:

Hisham Hegab
Dean of Engineering & Science

Approved:

Ramu Ramachandran
Dean of the Graduate School

GS Form 13a
(10/18)

ABSTRACT

Porous concrete structures are susceptible to the intrusion of chemical species, such as sulfates, chlorides, and carbon dioxide. Many technologies have been developed to repair or rehabilitate damaged concrete. These include cathodic protection, corrosion inhibitor addition, or the use of coatings and sealers. In recent years, a developing technology, electrokinetic nanoparticle treatment, has been shown to reduce concrete porosity, increase strength, promote corrosion resistance, and extend durability. This dissertation was conducted to explore a novel treatment to reduce the porosity of concrete via the application of electrokinetic transportation and electro-initiated polymerization of methyl methacrylate (MMA).

Potassium persulfate (PSP) was used to help initiate polymerization of MMA electrochemically at the cathode. This was first attempted in beaker tests (involving just MMA and deionized water). FTIR-ATR analysis indicated that solid deposits obtained from the beaker tests were PMMA. Without the PSP in the beaker tests, no deposit was obtained.

With the addition of PSP, the electrochemical treatment conducted on hardened cement paste (HCP) specimens yielded a yellowish, odorless, oil-like liquid. This liquid was extracted by acetone solvent exchange. FTIR-ATR analysis indicated that the liquid was likely to be the copolymer of MMA and methacrylic acid (MAA). An O-H bond was detected during the FTIR-ATR analysis indicating that the polymerization of MMA or MAA was initiated predominantly by OH radicals instead of sulfate radicals. Hydroxide ions are common in the caustic environment within HCP. The sulfate radicals could have reacted with hydroxide ions to produce sulfate ions and OH radicals.

Without the addition of PSP, a similar organic liquid was also extracted from the MMA-treated HCP samples. FTIR-ATR analysis of the liquid indicated that it was likely to be an MMA/MAA copolymer. A strong O-H stretch was observed on the ATR spectrum of the liquid. This indicate that OH radicals may have initiated the polymerization of MMA/MAA.

The corrosion potentials and current densities used in these treatments appeared to significantly influence the polymerization of MMA/MAA. A very limited amount of the liquid was extractable from the MMA-treated HCP in the low-voltage trials (+0.49 V vs. the $Cu/CuSO_4$ reference electrode (CSE)). This was because the low voltages caused the reduction of hydroxide ions at the anode to decrease and the formation of OH radicals to drop as well.

Apparently, a solid phase of PMMA did not form in the pores of HCP regardless of whether or not PSP was used. This may be attributed to the high-pH environment in HCP which could have caused the MMA or PMMA to hydrolyze and produce either MAA or a MAA/MMA copolymer. The lack of solids in the pores of MMA-treated HCP specimens resulted in no significant increase in strength or reduction in porosity. Future work is needed to investigate the impact of stabilizing inhibitors that are typically packed into industrial shipments of MMA monomer. Additionally, future work needs to examine the impact of lowering the pH of the treatment solution in order to facilitate a hydrolysis-free environment for reducing hydrolysis of MMA and PMMA. This could encourage the production of solid phase reactants that may enhance strength and durability.

APPROVAL FOR SCHOLARLY DISSEMINATION

The author grants to the Prescott Memorial Library of Louisiana Tech University the right to reproduce, by appropriate methods, upon request, any or all portions of this Dissertation. It is understood that "proper request" consists of the agreement, on the part of the requesting party, that said reproduction is for his personal use and that subsequent reproduction will not occur without written approval of the author of this Dissertation. Further, any portions of the Dissertation used in books, papers, and other works must be appropriately referenced to this Dissertation.

Finally, the author of this Dissertation reserves the right to publish freely, in the literature, at any time, any or all portions of this Dissertation.

Author _____

Date _____

DEDICATION

To my parents and wife

Lvyuan Zhan, Zhanbiao Xie, Shiqing Luo, Ying Li, and Jia Luo

To my advisor

Dr. Henry E. Cardenas

TABLE OF CONTENTS

LIST OF TABLES

LIST OF FIGURES

ACKNOWLEDGMENTS

I have to start by thanking my adviser, Dr. Henry E. Cardenas, for leading me to design research, conduct experiment, and analyze data. Also, with his constant guidance, support, and patience, we are developing the technology of electropolymerization in concrete. I also want to thank my mother and father, Lvyuan Zhan and Zhanbiao Xie, for their financial and mental support. I would like to express my gratitude to my parents in law, Ying Li and Shiqing Luo, for their understanding and support on my research. I would like to thank my wife, Jia Luo, for her accompanying and taking care of my life in Ruston during my study. I want to thank Dr. Sven Eklund for his patient guidance on organic chemistry and the instrumentation. I would like to express my sincere gratitude to my advisory committee members, Dr. David Hall, Dr. Arun Jaganathan, and Dr. Xingran Wang, for their teaching in engineering classes and assistance on my research. I also want to thank Dr. Tom Iseley and Dr. John Matthews for teaching me trenchless technology and providing the opportunities to participate in many meetings. I would like to express my gratitude to my research team members, Huayuan Zhong, Jiaming Huang, Frank Edokpayi, Aawaz, and Konstantin, for their help on conducting experiments. I would like to thank my roommate, Yue Gu, for his help to settle in an apartment. I would like to thank my friends, Yibo Chen, Sui Zhang, Haibo Zhang, and Zibo Wang, for their help to get familiar with American life. At last, I want to express my gratitude to Louisiana Tech

University and staff for constantly supporting my assistantship and providing a perfectly academic research environment.

CHAPTER 1

INTRODUCTION

This study was conducted to explore the possibility of reducing the porosity of hardened cement paste (HCP) via electro-initiated polymerization of methyl methacrylate (MMA). The MMA monomers were transported into the pores of HCP by application of electrophoretic migration. The migrated MMA monomers electropolymerized at the electrode embedded in the HCP specimens. The polymerized MMA formed a macromolecule (polymer) which was expected to reduce the porosity of HCP and promote strength. The intended product was a macromolecule of poly(methyl methacrylate) (PMMA), which is known for its excellent chemical resistance and mechanical strength [1]. The reduced porosity can yield higher strength, better corrosion resistance, and extended service life.

In order to achieve the goal of reducing HCP porosity, a series of experiments were designed to obtain polymers in HCP. Electro polymerization proof of concept tests were designed to confirm the PMMA formation in an aqueous system. In order to prevent the corrosion of the rebar during the MMA treatments, an electrodeposit was developed to act as a high-resistance barrier and a sacrificial coating. Process parameters such as applied potentials and initiator chemical concentrations were studied in order to enhance the MMA treatment outcomes.

1.1 Problem

Reinforced concrete is a widely used material in construction such as bridges, roadways, and other large structures. However, concrete structures can suffer damage from harsh environments, causing the embedded steel to corrode. The National Association of Corrosion Engineers estimated that the annual direct cost of replacement and maintenance of concrete highway bridges in the U.S. was $13.6 billion in [2]. The indirect cost of this degradation (such as traffic delays and lost productivity) was estimated to be as high as ten times this direct cost.

The failure of reinforced concrete occurs in two modes. One type is a concrete material failure. Concrete structures can be attacked by various species from the adjacent environment such as sulfate ions and carbon dioxide [3, p. 485]. Sulfate can decalcify the C-S-H gel in the concrete and soften the matrix. Moreover, excessive sulfate ions in the concrete can react with aluminate to form ettringite, which causes profound microcracking in the concrete structure. When carbon dioxide enters the pores of the concrete, it dissolves into the pore fluid and becomes carbonic acid, which can also soften the C-S-H gel. Another major mode of failure is the rebar failure [4, p. 46]. Chloride intrusion is a major factor that causes the corrosion of the rebar. Corroded rebar expands and exerts tensile forces on the surrounding concrete. This tension causes the concrete to crack, and the cracks later propagate to the surface of the structure. Cracked concrete loses its functionality and can cause leakage problems.

1.2 Objective

The objective of this study was to develop a scheme to polymerize MMA in the pores of HCP via electrical conduction and electro-initiation. After treatment, it was

expected to reduce the porosity of the HCP specimens and enhance their strength. At the beginning of this study, the proof tests of poly(methyl methacrylate) (PMMA) were conducted to check the possibility of the formation of macromolecules. Moreover, in order to prevent corrosion of the steel bars subjected to the anodic polarization, low voltages were applied to avoid the steel bars from entering the trans passive region of the Roubaix Diagram. It was anticipated that this coating would exhibit a sacrificial coating behavior on the surfaces of the steel bars. The electrical properties and corrosion resistance of the coatings was tested. Also, an initiator was applied to test for enhanced production of polymers under various concentrations and treatment times.

1.3 Approach

After demonstrating the possibility of electro-initiated polymerization of MMA in the beaker proof tests, MMA monomers were applied in MMA treatments on HCP specimens. The experimental plan of each MMA treatment is shown in Figure 1-1(a). One experiment (Section 3.11) subjected reinforced HCP specimens to electrodeposition treatment prior to MMA treatment, and others were subjected to MMA treatments only. After the MMA treatments, the treated HCP specimens were subjected to the indirect tensile strength testing and porosity testing. Moreover, the treated HCP samples were subjected to organic fluid extraction. The extracted samples were characterized by Attenuated Total Reflectance - Fourier-Transformed Infrared Spectroscopy (ATR). One experiment (Section 3.14) had HCP samples analyzed by the Energy Dispersive X-ray Fluorescence (EDXRF). Figure 1-1(b) shows the experimental plan of the electro-deposition (ED) treatment and the anodic polarization of 1018 steel bars. After the ED treatment, each trial had some samples obtained from the bars. These samples were

examined via Field Emission Scanning Electron Microscopy and analyzed by Energy Dispersive Spectroscopy.

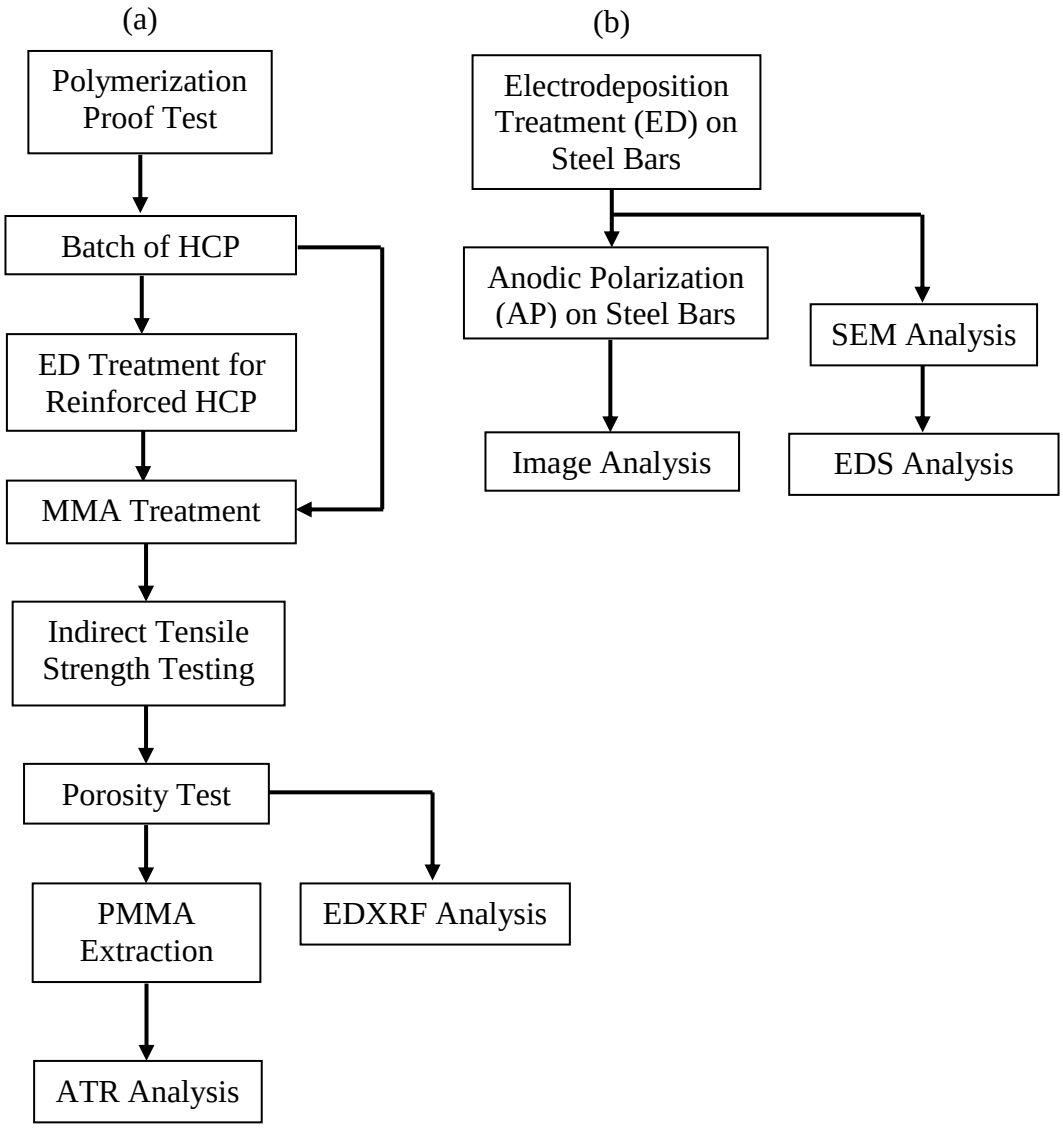

Figure 1-1: Experimental plan of MMA treatment on HCP specimens (a) and electrodeposition/anodic polarization treatment on 1018 steel bars (b).

1.4 Overview

This dissertation provides a brief background about the Portland cement paste history, hydration of cement paste, relationship between porosity and mechanical

properties, sulfate attack, and some common techniques to rehab concrete structures (See Section 2.1). Moreover, the mechanism of radical polymerization of MMA is introduced in Section 2.2. Section 2.3 focuses on the factors influencing the electro-initiated polymerization of MMA. Also, the basic model of electrical conduction in the solution is provided in Section 2.5. Section 2.6 introduces the corrosion theory related to steel.

In Chapter 3, Section 3.1 provides information about the chemicals and instruments applied in this study. The measurement of corrosion potential (EMF) and maintenance of the $Cu/CuSO_4$ reference electrode are described in Section 3.2. Sections 3.7-3.10 describe the preparation of HCP specimen, and how to measure the strength and porosity of HCP. Sections 4-5 are the experiments conducted on the steel bars (ED treatment and polarization). Section 3.3 is the experiment conducted to prove the electro polymerization of MMA, and Sections 3.11-3.14 are the MMA treatments on HCP specimens.

Chapter 4 presents and discusses the data collected during the ED or MMA treatments. Section 4.1 discusses the results of the electro-polymerization proof of concept test in the aqueous system. Section 4.2 discusses the results of electro-deposition and anodic polarization applied to the 1018 steel bars. Section 4.4 discusses the results of potentiodynamic polarization of 1018 steel. Sections 4.5-4.7 discuss the results of MMA treatments applied to the titanium wires (Ti-wire) embedded HCP specimens or 1018 steel bars reinforced HCP specimens. All the collected and calculated data are presented in Appendix A-H. Section 4.8 discusses the possible mechanism of electro-initiated polymerization of MMA in the HCP specimens. Section 4.9 describes the future works.

CHAPTER 2

BACKGROUND

In this chapter, Section 2.1 introduces the history of concrete, hydration, porosity (and its influence on strength), polymer-impregnated concrete, and common techniques applied to the repair or rehabilitation concrete structures. Sections 2.2 and 2.3 introduce the electro-initiated polymerization of methyl methacrylate. These sections include the polymerization processes, factors influencing polymerization, and its initiation. Section 2.4 introduces the evaluation techniques and instruments applied in this study. Section 2.5 introduces the theory of electrokinetics, which includes ionic conduction and electrophoresis. Section 2.6 introduces the corrosion process. This section includes corrosion theory, polarization and the passivation of steel, and the corrosion rate calculation according to a function of current density.

2.1 Concrete and Portland Cement

This section introduces the concrete history, the hydration of cement paste, the significance of porosity on concrete properties, literature reviews about polymer impregnated concrete, and corrosion in concrete structures.

2.1.1 Concrete Materials

Concrete is a common material universally applied for municipal infrastructure, including pipelines, roads, bridges, and buildings. Generally speaking, concrete is a mixture of filler materials and binder [1]. Filler materials can be either coarse or fine

aggregates. The cement binder acts as a glue to fill the space between the aggregate particles and hold them together. To reduce the expense of construction when applying concrete materials, inert rocks (coarse or fine) and the cement paste are used as the filler and the binder, respectively. If the cement and water are treated as the filler and binder, the mixture is referred to as the cement paste. When cement paste is used in the construction, it acts as the binder. The specimen made of hardened cement paste (HCP) is used in this study. This is because a lot of things are easier to try out on HCP first before seeing if it works in concrete. Moreover, the HCP specimens do not contain the aggregates which may increase the difficulty to analyze the chemical compositions of the specimens after some electrochemical treatments.

Portland cement concrete, calcium aluminate cement concrete, and polymer concrete are three types of common concrete used by civil engineers for constructions of the infrastructure [1]. The Portland cement is the most frequently used binder in 95% of conditions. In 1817, Joseph Aspdin first manufactured Portland cement powder in his kitchen by heating limestone and clay which were collected from the Isle of Portland. At the time, he applied for the patent and he named it Portland cement [5]. Until now, it is still unclear how Aspdin made this cement since his methods did not produce enough high temperature to calcine limestone. Twenty years later in 1837, Isaac Johnson manufactured modern cement powder by applying a temperature of approximately 1400-1500°C which was very similar to the temperature used today [6]. Based on the intended use, Portland cement types (I-V) are described in ASTM C150 – Standard Specification for Portland cement [7]. These types are shown in Table 2-1.

Table 2-1: General features and applications of Portland cement [3] [8]

Type	Classification	Applications
I	General Purpose	General constructions (buildings, pavements or bridges)
II	Moderate Sulfate Resistance	Structures exposed to Moderate sulfate-attacking environment
III	High Early Strength	Rapid construction, Cold Weather Concreting
IV	Low Heat of Hydration	Massive structures, such as dam
V	High Sulfate Resistance	Structures exposed to severe sulfate-attacking environment

In the current study, Portland cement type I and II blend was used to batch HCP specimens which were subjected to various electrochemical treatments. The mill test report of the Portland cement used in this study is presented in Appendix A, and the oxide compositions of the cement are listed in Table 3-5. In the cement industry, the oxide notations are abbreviated to shorthand notations listed in Table 2-2. Each oxide is represented by a single capital letter. The chemical compositions in an HCP specimen are replaced by the shorthand notations. For instance, tricalcium silicate ($3CaO{\cdot}SiO_2$) is written as C_3S. Gypsum ($CaSO_4{\cdot}2H_2O$) is written as $C\bar{S}H_2$. Calcium carbonate ($CaCO_3$) is written as $C\bar{C}$.

Table 2-2: Shorthand notations of oxides in Portland cement type I

Oxide	CaO	SiO_2	Al_2O_3	Fe_2O_3	MgO	K_2O	Na_2O	SO_3	CO_2	H_2O
Letter	C	S	A	F	M	K	N	$\bar{S}$	$\bar{C}$	H

2.1.2 Hydration of Portland Cement Paste

The hardening process of cement paste is referred to as hydration [1]. The typical compositions in Portland cement are listed in Table 2-3. The hydration of the cement paste represents a series of reactions of the listed chemicals and water. When the hydration reactions are complete, the resultant solids are referred to as the hydration products (HCP).

Table 2-3: Typical compositions of Portland cement type I [9] [10, p. 209]

Chemical Name	Shorthand Notation	Weight Percent
Tricalcium Silicate	C_3S	53
Dicalcium Silicate	C_2S	21
Tricalcium Aluminate	C_3A	11
Tetracalcium Aluminoferrite	C_4AF	8
Calcium Sulfate Dihydrate (Gypsum)	$C\bar{S}H_2$	2

The most important hydration reactions are the hydrating tricalcium/dicalcium silicate. The reaction equations are shown in Eq. 2-1 and Eq. 2-2:

$$2C_3S + 11H \rightarrow C_3S_2H_8 + 3CH\ , \qquad \textbf{Eq. 2-1}$$

$$2C_2S + 9H \rightarrow C_3S_2H_8 + CH\ , \qquad \textbf{Eq. 2-2}$$

where H is water, CH is calcium hydroxide, and $C_3S_2H_8$ is calcium silicate hydrated (C-S-H gel). Tricalcium aluminate reacts with water and gypsum to produce ettringite as shown in Eq. 2-3 [11] [12]:

$$C_3A + 3C\bar{S}H_2 + 26H \rightarrow C_6A\bar{S}_3H_{32}\ , \qquad \textbf{Eq. 2-3}$$

where $C_6A\bar{S}_3H_{32}$ is ettringite. It exhibits a needle-like crystal structure when it is observed under a microscope [13]. If the gypsum is all consumed before C_3A, the ettringite will continue reacting with C_3A to produce monosulfoaluminate (MA) shown in Eq. 2-4 [14]:

$$2C_3A + C_6A\bar{S}_3H_{32} + 4H \rightarrow 3C_4A\bar{S}H_{12}\,, \qquad \textbf{Eq. 2-4}$$

where $C_4A\bar{S}_3H_{12}$ is MA. Since the reaction of Eq. 2-3 is faster than the diffusion of gypsum, before forming the needle-like crystal, the ettringite may rapidly react with C_3A and water to produce MA. After production of MA, however, if a sufficient amount of sulfate ions are provided from the environment, ettringite will be produced again as shown in Eq. 2-5 [1]. This is the mechanism of sulfate attack in concrete:

$$C_4A\bar{S}_3H_{12} + 2C\bar{S}H_2 + 16H \rightarrow C_6A\bar{S}_3H_{32}\,, \qquad \textbf{Eq. 2-5}$$

The hydration of tetracalcium aluminoferrite (C_4AF) is very similar to that of C_3A. After reacting with gypsum and water, the products are iron-substituted monosulfoaluminate shown in Eq. 2-6 [15]:

$$C_4AF + 3C\bar{S}H_2 + 21H \rightarrow C_6(A,F)\bar{S}_3H_{32} + (F,A)H_3\,, \qquad \textbf{Eq. 2-6}$$

where $C_6(A,F)\bar{S}_3H_{32}$ is the monosulfoaluminate that may contain alumina or iron oxide. It can be found that gypsum is one of the reactants in both Eq. 2-3 and Eq. 2-6. Since in Eq. 2-3 C_3A can react with gypsum more rapidly than C_4AF in Eq. 2-6, Eq. 2-3 can consume more gypsum than Eq. 2-6.

Figure 2-1 shows the degree of hydration of Type I Portland cement with time [1]. It can be found that C_3A and C_3S hydrate more rapidly than the C_2S and C_4AF. In a hardened cement paste specimen, C_3S and C_2S tend to have more impact than C_3A and C_4AF on strength. At the early batch ages (3-4 weeks), the rapid reactivity of C_3S tends to

contribute more than C_2S on strength. However, at later hydration times (> 100 days), C_3S and C_2S tend to exhibit similar contributions to strength. The strength of hardened cement paste (HCP) is proportional to the hydration time [16]. If the HCP specimens have more time to hydrate, the ultimate strength is increased.

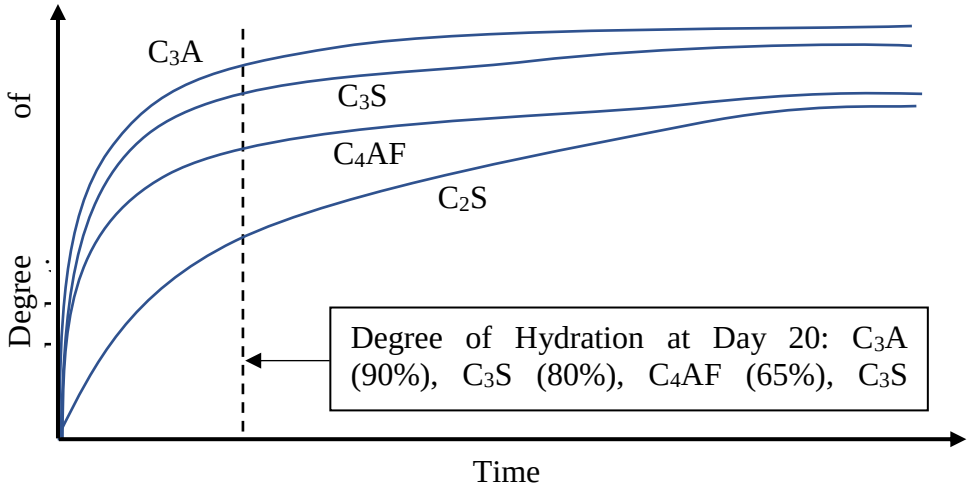

Figure 2-1: Rate of hydration of type I Portland cement [3, p. 24]. Reprinted from [3] by permission of Pearson Education, Inc., New York, New York.

The schematic processes of cement hydration are shown in Figure 2-2 [17]. At Day 0, the hydration starts. No C-S-H or calcium hydroxide (CH) has formed (See Figure 2-2(a)). After a few weeks, the C-S-H can be observed growing at the cement grain surfaces, which start to shrink (See Figure 2-2(b) and (c)). Meanwhile, as a product of hydration, CH nucleates and grows freely within the capillary pores that are saturated with water. With further hydration, capillary pores start to become somewhat disconnected. It was observed in the literature that when the total capillary porosity falls below 20%, the capillary pores tend to become disconnected and more tortuous [18]. Reducing porosity and increasing tortuosity makes the diffusivity of hydrating cement

decrease and the rate of hardening decrease. After hydration, about 60% of the hardened cement paste's solid volume is C-S-H. Calcium hydroxide crystals occupy 20-25% of this solid volume. The calcium sulfoaluminates make up 10-15%.

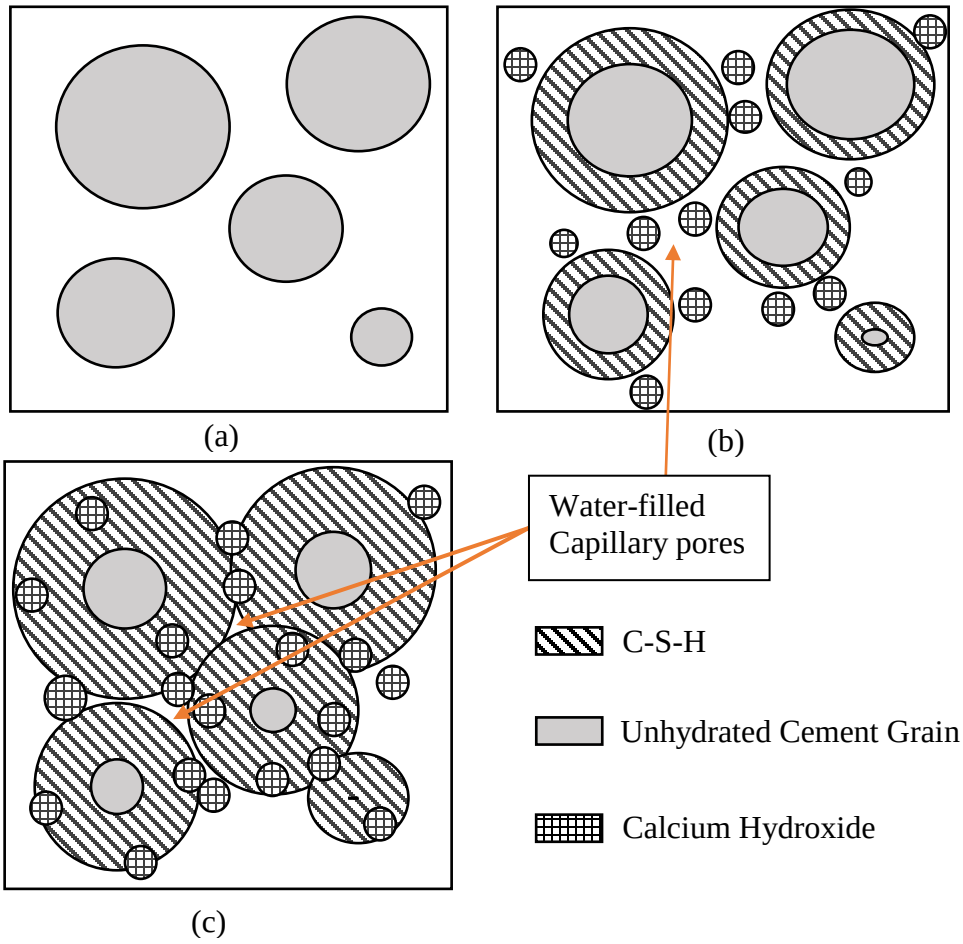

Figure 2-2: Schematic processes of hydration in Portland cement paste [17]. (a) Initial mix of cement paste. (b) Cement paste at 7 days. (c) Cement paste at 28 days.

2.1.3 The Porosity of Hardened Cement Paste

Figure 2-2 shows that the hydration process of cement particles causes the capillary pores to decrease in volume. During hydration, these capillary pores are filled with water and a relatively low concentration (~0.2 mol/L) of alkali hydroxide [19]. The

capillary pore sizes can range from 10 to 10,000 nm, which are easily observed by scanning electron microscopy. The ratio of the capillary volume and total volume of hydrated products is a measure of the porosity of hardened cement paste. It is difficult to derive the accurate porosity and the pore size distribution of an HCP sample by using current experimental instruments. This is because the HCP samples are required to be dried prior to the porosity measurements or pore size characterization, but the drying process inevitably changes the pore structures [20]. Moreover, in the measurement of pore size distribution, the shape of the pore is assumed to be a definite geometrical shape (round), but SEM image shows that the actual shape of the pore is irregular [1]. Based on the pore size, the classification of the pores is presented in Table 2-4.

Table 2-4: Classification of pore sizes in hardened cement paste [3, p. 75]

Designation	Diameter	Description
Capillary Pores	10,000-50 nm	Macropores (Large)
	50-10 nm	Large Mesopores (Medium)
Gel Pores	10-2.5 nm	Small Mesopores
	2.5-0.5 nm	Micropores
	< 0.5 nm	Interlayer spaces

Mercury intrusion porosimetry (MIP) is a method to measure the pore size distribution. MIP can be used to evaluate the pore size distribution, porosity, and the pore's volume [21]. In this approach, dried HCP particles are placed in a chamber that is full of mercury when the test starts. The liquid mercury is pressurized to move into the pores of the HCP sample. Pressure increases at a designated rate, while the mercury fills

the large capillary pores of the sample. As the pressure increases, mercury fills progressively smaller pores. This means that, under a specific pressure, only one size of the pore (or larger pores) can be filled with mercury. After testing, a curve of the pore's volume vs. equivalent diameter can be obtained (as shown in Figure 2-3). The pore's volume can be calculated by integrating this curve.

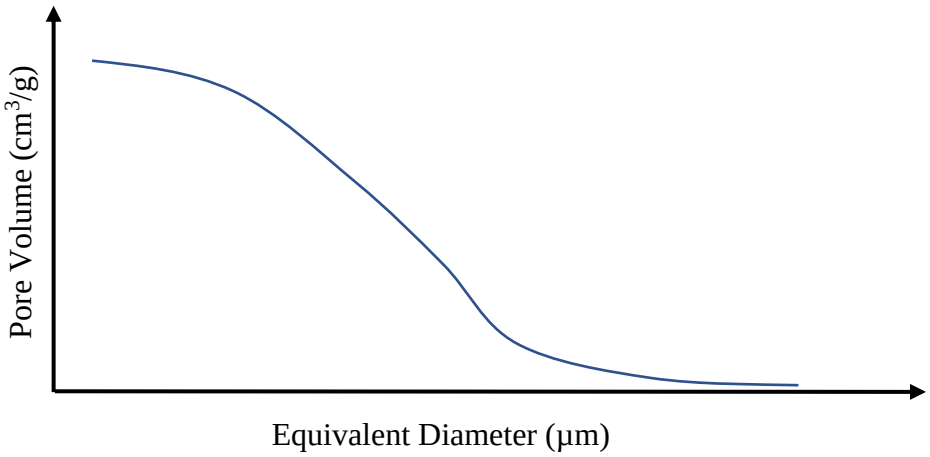

Figure 2-3: Mercury intrusion porosimetry curve shape representative of hardened Portland cement.

Drying the HCP specimens in the 105°C oven and monitoring the mass change is an easier method to obtain the porosity compared with MIP. T. C. Powers proposed a series of empirical equations to estimate the capillary and the gel pore volumes of the hydrated cement at the different degrees of hydration [22] [23]. Based on his study, the water that exists in the capillary pores (> 10 nm) and the gel (< 10 nm) pores is evaporable at 105°C. The total porosity (capillary and gel pores) of the HCP sample is calculated from the empirical Eq. 2-7:

$$P_T = \frac{(w/c) - 0.19\alpha}{(w/c) + 0.32} \times 100\%\,, \qquad \textbf{Eq. 2-7}$$

where P_T is the total porosity of the HCP sample, α is the degree of hydration (0~1), (w/c) is the water-cement ratio. The capillary porosity of an HCP sample is calculated through Eq. 2-8:

$$P_c = \frac{(w/c) - 0.36\alpha}{(w/c) + 0.32} \times 100\%\,, \qquad \textbf{Eq. 2-8}$$

where P_c is the capillary porosity of the HCP sample. Assuming the water-cement ratio is 0.48, and the hydration is complete ($\alpha = 1$), it can be calculated that the total porosity P_T in this case is 36.3% and the capillary porosity is 15.0%. Figure 2-4 shows the porous water volume relationships with respect to the degrees of hydration and the water-cement ratio.

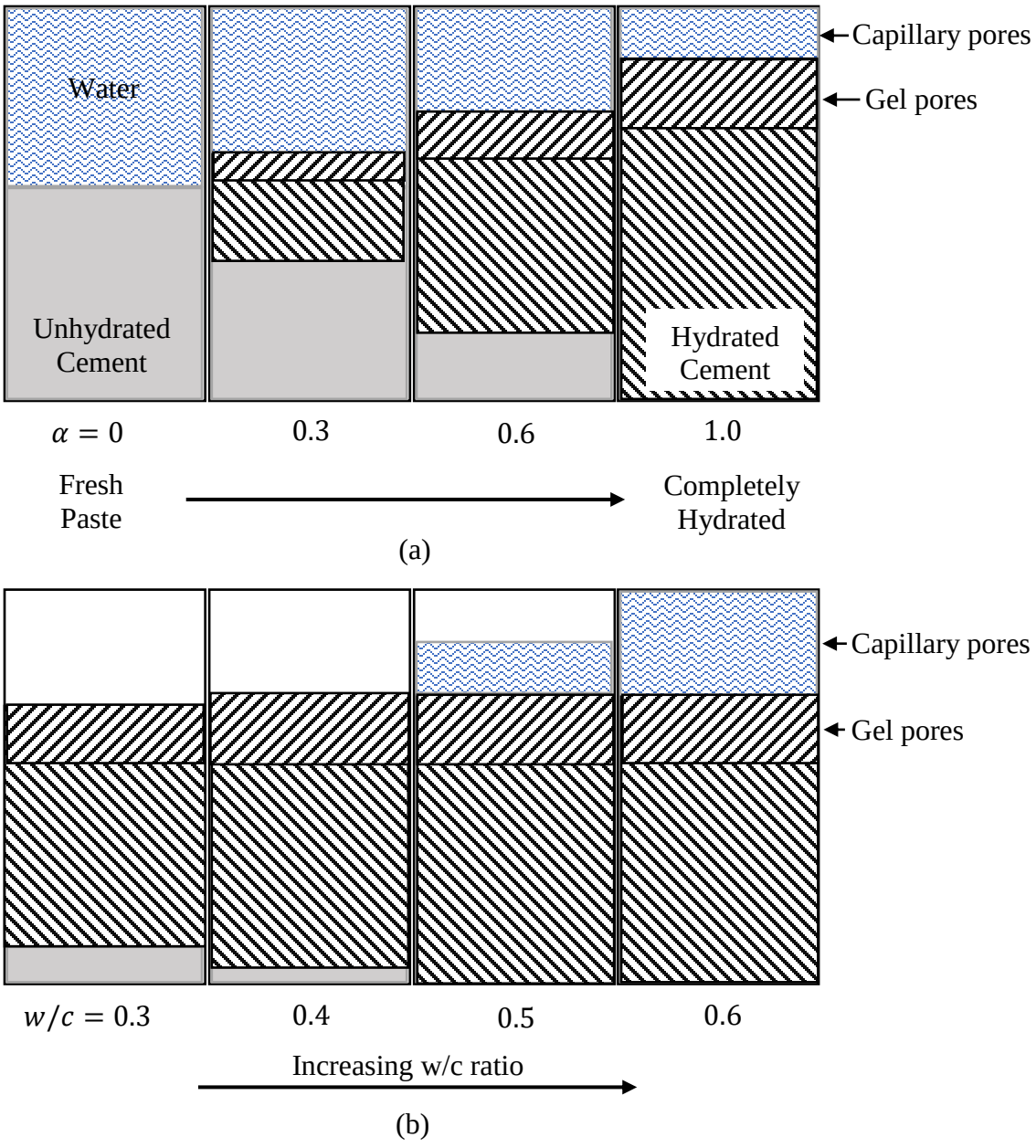

Figure 2-4: Porous water volume (gel and capillary) relationships with degrees of hydration (a) and water-cement Ratio (b) [22]. Reprinted from [3] by permission of Pearson Education, Inc., New York, New York.

2.1.4 Polymer Impregnated Concrete

It is discussed in the previous section that the strength of HCP is proportional to its porosity. If the porosity of HCP is reduced significantly, the strength will increase.

One method to reduce the porosity of HCP is to reduce the water-cement ratio. However, the percentage of unhydrated cement may increase in HCP as a result of decreasing the water-cement ratio. One of the techniques to reduce the porosity of concrete is to impregnate polymer into the pores [1]. There are many organic monomers suitable for being impregnated into concrete. The best monomer has the following features; low viscosity, relatively high boiling point, low toxicity, ease of polymerization, low cost, and availability. One of the candidates is the methyl methacrylate (MMA). The low viscosity of MMA makes impregnation easier than other monomers. The low-temperature requirement of polymerization makes it possible to be applied to the large concrete structures. The MMA-impregnated concrete exhibits a remarkable increase in compressive strength, durability, and a decrease in water absorption [24].

The process of manufacturing polymer impregnated concrete involves three major steps: drying, impregnation, and polymerization. The first step is to evaporate the water from the pores. Concrete samples are placed in an oven for 24 hours or more at temperatures ranging from 110-150°C (depending on the water-cement ratio and the size of the sample) [25]. After drying, micro cracks may occur in the concrete. This negative impact will be compensated by the impregnated monomer since the cracked zones provide extra volume for impregnation. After drying, the concrete samples are subjected to a vacuum at 8.0 kPa for one hour to remove additional water content from within the pores. The next step is to apply pressure to drive the monomer liquid into the pores. The concrete samples are immersed in the monomer liquid for one hour, and the monomer is pushed at a pressure of 70-200 kPa into the pores for approximately 40 minutes or until the volume of the monomer liquid stops decreasing. For a real concrete structure, it

would be difficult to implement such a large pressurization instrument. Under this circumstance, the structure can barely be soaked in the monomer liquid for 8-12 hours to achieve a 70-80% impregnation. The depth of the monomer intrusion is dependent on the viscosity of the monomer, temperature, and soaking time [3]. It was tested on a highway bridge deck that the approximate depth of the polymer's intrusion was 0.75-1 inch [24]. The final step is to polymerize the monomer liquid in the pores in order to convert the liquid monomer to the solid polymer. Polymerization of monomer requires the initiators (Polymerization starter) to trigger the reactions. This polymerization triggering reaction is referred to as the initiation step. (This will be described further in Sections 2.2 and 2.3). There are many methods to initiate the polymerization of MMA, but the most popular way is to heat the concrete at temperatures of 65-100°C for 30 minutes to 1 hour. If the concrete structure is too large to put in an oven, then steam can be sprayed on the surface of the concrete structure. Heating time determines the yields of PMMA in the concrete.

Many types of polymers or copolymers have been applied to strengthen the concrete [26]. As mentioned before, MMA is a popular monomer with many satisfying features. The MMA impregnated concrete was tested by Yimprasert *et al.* with regard to strength and durability [24]. Table 2-5 shows the strength and durability of polymer impregnated concrete as compared to untreated control specimens. It was observed that the overall performance of the MMA impregnated concrete exceeded the conventional concrete. During chloride intrusion testing, 3-wt% NaCl (simulated seawater) was sprayed on the concrete samples twice a day, for 5 days each week, for 20 months. At the end of the test, the un-impregnated concrete samples exhibited cracks along the rebars,

which were found to have 28% of the surface area corroded. The PIC samples were still in good condition and exhibited only a 1% corroded area on the rebar.

Table 2-5: Strength and durability of PMMA polymer impregnated concrete [3] [24].

Properties	**Control Concrete**	**PMMA Impregnated Concrete**
Compressive Strength (psi) (1)	5330	15250
Tensile Strength (psi) (1)	477	1038
Modulus of Elasticity (psi x10^6) (1)	3.1	6.0
Freeze-thaw Cycles(1)	40	> 120(3)
Chloride Ion Content (ppm) (1)	2500	< 400
Sulfate Attack (Expansion %) (2)	0.466	0.006
Acid Resistance (weight loss %) (2)	27	9
Abrasion Resistance (Abrasion Depth, mm) (2)	1.25	0.38

(1) Data derived from [24].
(2) Data derived from [3].
(3) Freeze-thaw test terminated at the 120 cycles.

Although the results of the performance of PIC in Table 2-5 seemed to be remarkable, some of the results from the durability testing were predictable [3]. For example, since the PIC samples lost all of the capillary porous water after drying, it is not surprising that the PIC exhibited a higher resistance against the freeze-thaw attack. Reduction of porosity provided limited access for sulfate ions to intrude the PIC samples, so the expansion was also reduced. Moreover, another limitation of the PIC samples is the loss of strength when the PIC structure is subjected to fire. Although fire will not

ignite the polymer in the concrete, the low glass transition (105 ℃ for PMMA [27]) makes the dissolution of polymer possible. Also, dissolved polymer flows can flow out of concrete and get ignited to produce harmful fumes. This may require the application of flame-retardants to the PIC concrete structure [1].

PIC has remarkable strength and durability even though it is limited by its flame and heat resistance. In the current study, a new way is explored to transport MMA monomer electro kinetically into the pores of hardened cement paste and to initiate the polymerization electrically in order to reduce porosity for the benefit of strength and durability.

2.1.5 Sulfate Attack in HCP

Sulfate-exposed hardened cement paste and concrete can suffer cracking, softening and spalling [13]. Since concrete is often used as a foundation material which is exposed to the soils or seawater, sulfate salts in those environments are often the source difficulty for these structures. It was discussed in Eq. 2-3 that gypsum in HCP reacts with calcium aluminate (C_3A) to produce ettringite. Growing ettringite crystals cause the surrounding matrix to crack. When the gypsum concentration is limited (< 3 wt%), the ettringite can react with C_3A further to produce monosulfoaluminate (MA). If the concentration of sulfate ions in the HCP increases over time, the gypsum can be produced as shown here in Eq. 2-9:

$$CH + SO_4^{2-} \leftrightarrow C\bar{S}H_2 + 2OH^- , \qquad \textbf{Eq. 2-9}$$

where CH is calcium hydroxide, SO_4^{2-} is sulfate ions, $C\bar{S}H_2$ is gypsum, OH^- is hydroxide ions. At low temperature (< 8 ℃), the occurrence of carbonation (CO_2

intrusion) and the presence of sulfate ions can induce the formation of thaumasite ($C_3S\bar{C}\bar{S}H_{15}$), which also causes damage to concrete structures [28] [29] [30].

Ettringite, gypsum, and thaumasite are three major sulfate-related products that can be damaging to concrete structures [31] [32] [33]. There has been controversy as to which sulfate-reacted product tends to cause the most expansion and damage in the concrete. For instance, we observed the needle-like ettringite in the micro cracks of the concrete [1] [13]. Several studies indicated that relatively high content (8.7% in cement) of C_3A in cement paste has caused the early failure of concrete (C_3A is a major component of the reaction that produces ettringite) [34]. It was also possible that a high content of C_3S may cause premature failure because of the formation of gypsum [35] [36]. The forming of gypsum converts calcium hydroxide (CH) which is referred to as the process of decalcification. The loss of CH can cause the strength of the concrete to decrease significantly. Moreover, it is mentioned in the literature that the formation of gypsum has caused the solid volume to increase in the vicinity of 20%. These findings indicated the gypsum was the source of the expansion [1].

The expansion of the concrete under the sulfate attack can possibly be due to the interaction of both ettringite and gypsum. During the early stage of sulfate exposure (< 90 days), the sulfate ions tend to first react with calcium hydroxide to form gypsum. Later, the gypsum reacts with tricalcium aluminate and water to form ettringite (Eq. 2-3) [13]. The forming ettringite does not affect the strength of concrete. When the concentration of calcium ions in the pore fluid is consumed by ettringite formation, calcium hydroxide dissolution will ensue. The depletion of calcium hydroxide will increase the capillary porosity of the cement paste matrix. This change can accelerate the intrusion of sulfate

into the microstructure, which supports an even greater rate of decalcification. The comprehensive interaction of both HCP expansion and decalcification tends to reduce the strength of concrete significantly.

Some practical ways can be adopted to mitigate the damage of sulfate ions. The first one is to use Type V Portland cement which has a low content of tricalcium aluminate compared with Type I [37]. This reduces one of the reactants required for ettringite formation. The second way is to utilize fly ash and silica fume as admixtures to increase the resistance to sulfate attack [38]. Steam curing may be another way to prevent sulfate attack because a hydrotalcite-type phase (absorbing sulfate ions) hinders the formation of ettringite [39] [40]. Also, a novel attack recovery method was developed by Kupwade-Patil and Cardenas that applies electro kinetic nanoparticle treatment in concrete to extract sulfates while reducing the porosity simultaneously, which mitigates the reduction of strength [41] [42].

2.1.6 Repair and Rehabilitation Techniques

When the cracking of concrete structure is visible, this means the concrete structures are susceptible to the environmental attacks such as chloride and sulfate ions, bacteria growth, and erosions. If no proper attention or action is taken to mitigate the problem, failures of the concrete structures may result in catastrophic economic loss and personal injury. Until now, the popular concrete repair and rehabilitation techniques include cathodic protection, electrochemical chloride extraction, corrosion inhibitors, crack sealer, overlay, polymer coating, and plastic wrapping. Also, the currently developing electro kinetic nanoparticle treatment has good potential for concrete crack repair and strengthening.

Although technically there are many techniques available for repairing concrete cracks quickly, the most economical and effective way is to apply an asset management plan for any utility [43]. This is because asset management transforms the working schedule from reactive to proactive (proper routine inspections and maintenance). In the short term, it may be costlier than the old management plan, but in the long term, it saves more funding.

Cathodic protection (CP) is used to establish an electrochemical cell between the cathode (reinforcement in concrete) and an installed anode. This cell significantly mitigates the corrosion of reinforcement. CP can be applied via two types of systems: sacrificial anode CP and impressed current CP [44]. The sacrificial anode CP system uses an electric circuit built between the rebar (steel) and another more active metal (zinc) in the corrosive environment [4]. The sacrificial metal is located outside of the concrete structure (such as the surrounding soil or water). When the sacrificial anode CP system is unable to produce enough current to protect the rebar, a power supply is applied in the circuit to increase the current. This is an impressed current CP system. In the impressed current CP system, the anode is made of highly inert materials, such as high silicon cast iron, graphite, platinized titanium, and lead. Table 2-6 introduces the advantages and disadvantages of these two systems.

Table 2-6: Advantages and disadvantages of sacrificial anode CP and impressed current CP [4] [45].

Sacrificial Anode CP		**Impressed Current CP**	
Advantage	**Disadvantage**	**Advantage**	**Disadvantage**
No External Power	Fixed Driving Voltage	Suitable for Large Structures	External Power
Low Sensitivity to Soil Resistivity	Only Suitable for Small Repairs	25 Years Life Expectancy	Soil Resistivity lower than 3000 ohm-cm
Easily Installed	10 Years Life Expectancy	Changeable Current	More Complicated System
Easily Maintained	Hard to Trace	More Economical	Costly Traffic Management
Evenly Distributed Current Density			

Electrochemical chloride extraction (ECE) is used to apply electro kinetic treatment to extract chloride ions from the concrete structures. The installation of ECE is similar to the impressed current CP. The anode is located outside of the concrete, and the cathodic charging is applied to the rebar of the concrete. During treatment, the structure is kept wet with an aqueous system which may contain alkali species. The suggested current density (at the rebar surface) is 2 A/m^2 [46]. It was mentioned that the ECE treatment increased the contents of Ca^{2+}, K^+, Na^+, and OH^- around the rebar so that a lamellar hydration product with a high Ca/Si ratio is formed. However, the ECE treatment can also cause the cracking and decomposition of C-S-H at the rebar-concrete interface. The cracking may be a reason why the porosity of the concrete was observed to increase after some ECE treatments [47]. One study indicated that elevated temperature increased the efficiency of the extraction [48]. Garces *et al.* applied conductive shotcrete (mixed with

graphite) layer on the concrete surface as the anode used to extract the chloride ions [49]. It was recommended that the ECE should not be applied to the pre-stressed concrete because the reduction of the hydrogen ions caused the embrittlement of the pre-stressed rebar [50].

Corrosion inhibitors are species that can be provided to the concrete to reduce, slow down or prohibit the intruded particles (chloride or carbon dioxide) from corroding the rebar [51]. An alkaline porous fluid in all concrete structures around the rebar acts as a passive layer of corrosion inhibitors [4]. The fluid is saturated with calcium hydroxide which can react with carbon dioxide to produce calcium carbonate. As an admixture, the developed inhibitors are chromates, phosphates, sodium benzoate, sodium nitrate, calcium nitrate, sodium tetraborate, and zinc borate [52]. Currently, the most widely used inhibitor is calcium nitrate, which is an anodic inhibitor used to enhance the passivity of the rebar through the following equation against the intrusion of chloride ions [53] [54]:

$$4Fe^{2+} + 4OH^{-} + 2NO_2^{-} \leftrightarrow 2NOFe_2O_3 + 2H_2\,, \qquad \textbf{Eq. 2-10}$$

where $Fe^{2+}$is the corroded iron, NO_2^{-} is the nitrate ions, and $NOFe_2O_3$ is the iron oxide inhibitor that forms on the surface of the rebar and limits the chloride damage. The recommended weight ratio of chloride and nitrate was lower than 1.5 for obtaining full passivity [55].

There are many concrete crack sealing products in the market available that are chosen based on the level of the concrete cracking condition [1]. Organic compounds, such as epoxy resins, are widely applied to fix fine cracks (> 0.05 mm) by the injection of the uncured epoxy for the structural purpose. Epoxy has excellent mechanical strength (> 12000 psi), but it needs hours to harden [56]. This slow hardening time may facilitate the

flow into the finer cracks. If structural purposes are not a consideration, polyurethanes can be used as good leak stop remedies instead of epoxy. Polyurethanes can harden in minutes after injection. This elastomeric material exhibits a useful tolerance for the continued movement of concrete adjacent to the crack. Inorganic compounds, such as silicone caulks, mortars, grouts or cement, are used to seal large concrete cracks or joints. Before applying sealers, it is recommended to clean the surface of the cracked area in order to obtain a firm bonding between concrete and sealer.

When concrete structures have severe weight loss due to sulfate attack, erosion, or long-time use, overlay of the concrete surfaces, as a rehabilitation method, is commonly applied to extend the life expectancy of concrete structures. Seven types of overlay are widely used: epoxy, latex modified concrete, silica fume modified concrete, a polyester polymer, asphalt with a liquid membrane, asphalt with a sheet membrane, and asphalt without a membrane [57]. On the vertical surface, shotcrete is frequently used [1]. When applying shotcrete, reinforcements (steel meshes) are applied to the damaged concrete structure. This mesh is designed to slow down the shotcrete flowing vertically so that cement paste has enough time to harden at the point of application.

Recently, significant attention has been paid to trenchless technologies and their applications to underground concrete structures, such as manholes and pipelines. Many trenchless technologies are developed to repair, rehabilitate or replace these underground structures. These technologies include the cured-in-place pipe (CIPP), wrapping, and coating.

Concrete wrapping is used to apply a sealing band for concrete pipe, manholes, and precast box sections as per ASTM C877-16 [58]. Usually, only the joints are

wrapped in order to prevent intrusion of corrosive ions. If the working environment is very corrosive, full wrapping will be applied on all the exposed surfaces of the concrete. Wrapping materials include polypropylene and carbon fiber. A common alternative to provide coatings that are used to spray a thin polymer on the surface of the concrete pipeline when it is subjected to corrosive wastewater or storm water.

CIPP is a widely used rehabilitation method in the U.S. to repair the existing pipelines (structural or non-structural) [59]. CIPP uses hot steam to inflate and cure a soft cloth pipeline (soaked with resin) in the existing pipeline. Since the cloth is very soft, it will reshape automatically to fit the old pipeline. The polymerization of the resin in the cloth is facilitated by the hot steam over the course for several hours. After completion of polymerization, the cloth-hardened pipeline has higher strength and sometimes an increased capacity.

The mechanism of electro kinetic nanoparticle (EN) treatment is a process under development that is similar to electrochemical chloride extraction. The EN treatment is provided by applying an electric field to transport positively charged nanoparticles (colloidal alumina or silica) into the concrete's pores [42]. The reinforcement is used as the cathode, and the anode (titanium mesh) is located outside of the concrete. After the EN treatment, the strength of concrete increases and the porosity reduces significantly. Moreover, EN treatment has been used to treat concretes' cracks to stop the leakage of storm water into the structures.

2.2 Chain Radical Polymerization Mechanism

In this section, the mechanism of the initiation of polymerization will be discussed as it pertains to a focus area of the current study. Generally speaking, the

polymerization of alkenes, such as MMA, includes three steps – initiation, propagation, and termination [60]. Polymerization of MMA is the chain polymerization. Many chemical or physical methods have been developed to initiate the polymerization of MMA successfully.

2.2.1 Methyl Methacrylate Monomer

The monomer, methyl methacrylate (MMA), is a vinyl monomer attached to an ester group (-$COOCH_3$) and an alkyl group (-CH_3). The molecular structure is shown in Figure 2-5. The chemical and physical properties are listed in Table 2-7.

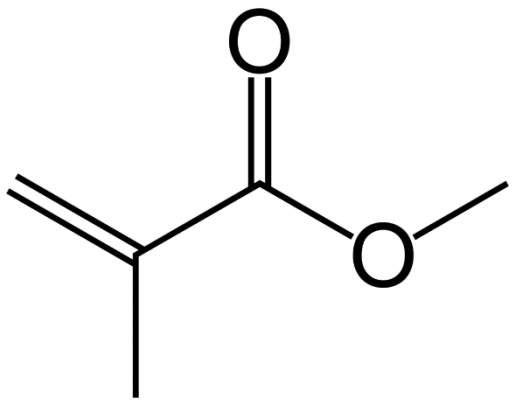

Figure 2-5: Molecular structure of methyl methacrylate.

Table 2-7: Chemical and physical properties of MMA [60] [61].

Physical State	Clear liquid
Chemical Formula	CH2=C(CH3)COOCH3
Molecular Mass	100.12 g/mol
Density	0.95 g/cm^3
Solubility	1.5g/100g at 30 ℃
Melting Point	-48 ℃
Boiling Point	101 ℃
Viscosity	0.6 cps at 25 ℃
Auto Ignition	435 ℃
Flash Point	10 ℃
National Fire Protection Association (NFPA) Ratings	Health 2; Flammability 3; Reactivity 2

2.2.2 Polymerization Process

Two common types of polymerization include step polymerization and chain polymerization. Step polymerization is also referred to as condensation polymerization. This polymerization includes a condensation reaction, which usually eliminates a water molecule as shown in Eq. 2-11 [60]:

$$n(HO-R-OH)+n(HO_2C-R'-CO_2H) \rightarrow H(OR-OCO-R'-CO)_nOH+(2n-1)H_2O\ , \quad \textbf{Eq. 2-11}$$

where $(HO-R-OH)$ is the diol, $(HO_2C-R'-CO_2H)$ is the diacid, $H(OR-OCO-R'-CO)_nOH$ is the polyesters. During polymerization (2n-1), molecules of water are eliminated. The mass of the final polymer (polyester) is less than the sum of masses of the reactants. This is the reason why it is referred to as condensation polymerization.

Chain polymerization is referred to as addition polymerization [62]. Unlike condensation polymerization, the monomers used in chain polymerization always have carbon-carbon double/triple bonds. During polymerization, these bonds convert into saturated (single bond) linkages shown in Eq. 2-12:

$$nCH_2 = CHY \rightarrow -(CH_2 - CHY)_n - , \qquad \textbf{Eq. 2-12}$$

where Y is a substituent attached to the vinyl monomer; Y can be a hydrogen, alkyl, aryl, nitrile, ester, acid, ketone, ether, or a halogen. This type of polymerization looks like the individual monomers are being added to a lengthening chain.

Chain polymerization of monomers includes three steps: initiation, propagation, and termination [60]. Initiation is the start of polymerization. The reactive species that initiate polymerization is referred to as active radicals. These radicals are produced from the decompositions of some compounds which are termed as the initiators. Under normal conditions, the addition of initiators may not initiate polymerization. This is because the initiators are not reactive until they are activated. When the temperature is elevated, or electric potential is provided, the initiators may convert into the active state (become radicals) which are now equipped to break carbon-carbon double bonds. This process is the initiation shown in Eq. 2-13 and Eq. 2-14.

$$I \xrightarrow{\uparrow T \; or \; e^-} R^* , \qquad \textbf{Eq. 2-13}$$

$$R^* + MMA \rightarrow R(MMA)^* , \qquad \textbf{Eq. 2-14}$$

where I is the initiator, R^* is the radical, T is the temperature, e^- is an electron, R(MMA) is the initiated PMMA (only containing one monomer). It should be noted that the newly formed $R(MMA)^*$ has the ability to react to another MMA monomer to form a new radical $R(MMA)_2^*$ as shown in Eq. 2-15:

$$R(MMA)^{*} + MMA \rightarrow R(MMA)_2^{*}\,, \qquad \textbf{Eq. 2-15}$$

$$R(MMA)_2^{*} + (n-2)MMA \rightarrow R(MMA)_n^{*}\,, \qquad \textbf{Eq. 2-16}$$

If the $R(MMA)_2^{*}$ continuously reacts with additional monomers, it will grow into a large radical ($R(MMA)_n^{*}$) which contains (n) molecules of MMA as shown in Eq. 2-16. This process is referred to as propagation.

Propagating radicals tend to exhibit two types of arrangements for connecting monomers as shown in Figure 2-6 [63]. One is the head-to-tail (H-T) placement. The other one is the head-to-head (H-H) placement. The H-T placement is predominant because successive propagation as shown in Figure 2-6(a) is favored on both steric and resonance grounds. The propagating radical (a) is the more stable radical because it can be stabilized by the resonance effects of the substituents of the ester group ($-COOCH_3$) and the alkyl group ($-CH_3$). The substituents cannot stabilize the radical (b) since they are not attached to the carbon that holds the unpaired electron. Moreover, the attachment of a new monomer on the propagating radical as shown in Figure 2-6(a) is

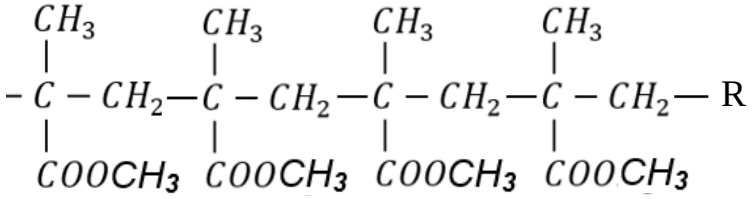

(a)

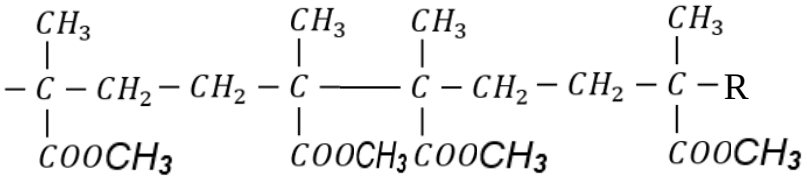

(b)

Figure 2-6: Arrangements of propagating MMA radicals. (a) Head-to-tail (H-T) placement. (b) Head-to-head (H-H) placement.

sterically easier than that on the propagating radical as shown in Figure 2-6(b).

Theoretically, the predicted H-T placement is the predominant arrangement of propagating radicals [60]. Also, H-T placement has been experimentally verified for a number of polymers via high-resolution nuclear magnetic resonance spectroscopy. It was found that poly(vinyl acetate), poly(vinyl chloride), and poly(vinyl alcohols) only 1-2% of H-H placements after the polymerizations [64]. After the polymerization of polystyrene, no H-H placement was detected [65]. The extent of H-H placement in poly(vinyl fluoride) and poly(trifluoroethylene) were 10% and 12 %, respectively [66] [67]. Poly(vinylidene fluoride) initiated by tert-butyl peroxypivalate had 5% of H-H placement [68]. The temperature of polymerization can influence the content of H-H placement in polymers [69]. It was observed in the literature that the H-H placement in poly(vinyl acetate) increased from 1% to 2% when the polymerization temperature was increased from 40 to 100 ℃ [60]. The extent of H-H placement in poly(trifluoroethylene) increased from 10 to 14% when the temperature was increased from -80 to 80℃. Pure H-H polymers, such as polyolefins, acrylates, and poly(vinyl halides), can be obtained using unconventional polymerization techniques [70]. For example, the H-H poly(acrylates) were synthesized by copolymerization, by polymerization with poly(vinyl halides), and by halogenation of poly(1, 4-butadiene).

Termination of polymerization means that the propagating radicals stop growing and become relatively stable polymers [60]. During the propagation of radicals, the concentration of monomers decreases, and the radicals have diminishing chances to collide with the monomers. When two radicals collide and react with each other, they are said to form a dead polymer shown in Eq. 2-17:

$$R(MMA)_n^* + (MMA)_m^* R \rightarrow R(MMA)_{m+n} R\,, \qquad \textbf{Eq. 2-17}$$

where $R(MMA)_n^*$ and $(MMA)_m^* R$ are the propagating radicals containing (n) and (m) molecules of MMA, respectively, $R(MMA)_{m+n} R$ is the dead polymer. This type of termination of polymerization is referred to as the combination of two propagating radicals. Another type of termination is referred to as disproportionation. This type is shown in Figure 2-7. In this case, it can be observed that one hydrogen radical is transferred from an MMA radical center to another MMA radical center. This produces one saturated polymer and one unsaturated polymer as shown in Figure 2-7. At a temperature of 25 ℃, one study showed that the ratio of disproportionation and combination polymers was 73:27 for the poly(methyl methacrylate) [71]. When the temperature increased to 100 ℃, the ratio was 67:33. Unsaturated polymer is similar to an MMA monomer, which can continue to participate the polymerization.

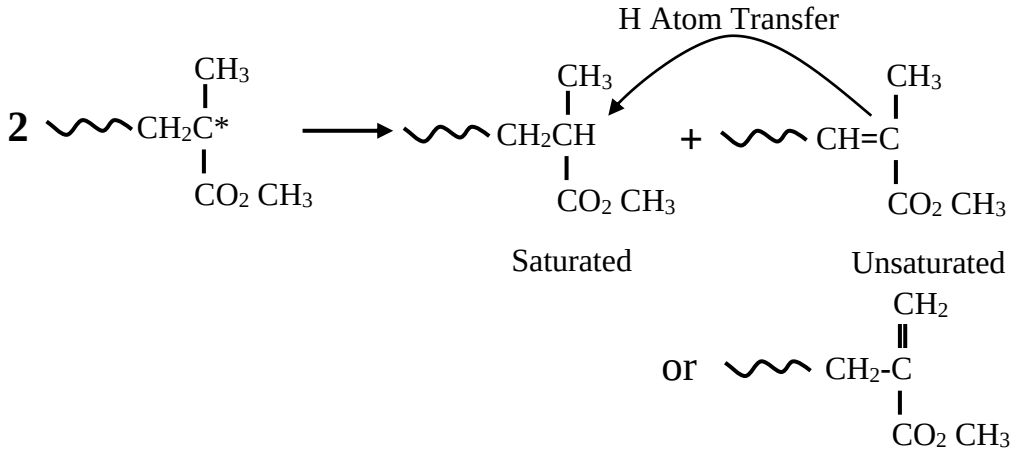

Figure 2-7: Disproportionation of propagating MMA radicals.

2.2.3 Initiation of Chain Radical Polymerization

Initiators can be turned into the reactive species (radicals) under specific conditions (temperature, light, or electricity) as shown in Eq. 2-13. Many types of initiation processes have been developed to start the polymerization, such as thermal decomposition, oxidation-reduction (redox) initiation, photochemical initiation, ionizing radiation, plasma initiation, sonication decomposition, and electrochemical initiation. Each initiation method may result in a different polymerization rate, molecular weight, and conversion rates.

Thermal decomposition initiation involves the decomposition of an initiator at a specific temperature (> 323 K). This process is shown in Eq. 2-13. The peroxyl compounds which contain O-O, N-O, or S-S bonds can be used as initiators, such as acyl peroxides, alkyl peroxides, hydroperoxides, ketone peroxides, and peresters [60]. These compounds have bonds (O-O, etc.) with dissociation energies in the range of 100-170 kJ/mol. Moreover, azo compounds, such as 2,2'-Azobis(isobutyronitrile), dilauroyl peroxide, or 4,4'-azobis(4-cyanovaleric acid), can be used as thermal initiators, but their decompositions may produce nitrogen gas [72]. The C-N bond dissociation energy (~290 kJ/mol) is higher than that of the O-O bond. Compounds with higher or lower dissociation energy may dissociate too slowly or too quickly at a specific temperature.

The half-life of an initiator is the time required to decompose the initiator when its concentration is one half its original value. Half-life is an import index to measure the functional capacity of an initiator. The half-life is dependent on temperature. Increasing the temperature shortens the time of decomposition. Table 2-8 lists the half-life of

potassium persulfate in various solution pH values at 50℃. It is also provided that its half-life is 10 hours at the temperature of 70℃ in 0.1 mol/L NaOH solution [73].

Table 2-8: The rates of decomposition of potassium persulfate as a function of pH [74].

pH (50 ℃)	1.0	1.6	3.0	7.0	10.0
Half-life (Hours)	20	65	125	130	210

Redox initiation involves reactions between reducing agents and oxidants that produce free radicals which initiate the polymerization of MMA. An important advantage of the redox system is that the initiation can occur at a rather low temperature (0-50 ℃). The activation energy required to generate radicals is approximately 40 kJ/mol. This is significantly lower than the dissociation energy (> 100 kJ/mol) required to produce radicals from thermal decomposition [75]. This low-temperature requirement makes the equipment and execution of polymerization much easier.

There several types of redox initiation systems that have been developed. One approach involves the application of ferrous ions to promote the decomposition of organic peroxides such as shown in Eq. 2-18:

$$ROOR \xrightarrow{Fe^{2+}} RO^{-} + RO^{*}, \qquad \textbf{Eq. 2-18}$$

where ROOR is the organic peroxide, RO^{-} is the produced anion, RO^{*} is the radical. The ferrous ion can be replaced to other reductants, such as Cr^{2+}, V^{2+}, Ti^{3+}, Cu^{+}, and Co^{2+} [60].

Another approach of the redox initiation is to combine inorganic reductants and oxidants to initiate radical polymerization. For instance, potassium persulfate (reductant:

$K_2S_2O_8$) and sodium thiosulfate (Oxidant: $Na_2S_2O_3$) are used as redox initiators to initiate polymerization of MMA [76]. The reaction equation is presented in Eq. 2-19:

$$^{-}O_3SOOSO_3^{-} + S_2O_3^{2-} \rightarrow SO_4^{2-} + S_2O_3^{-*} + SO_4^{-*}, \qquad \textbf{Eq. 2-19}$$

where $^{-}O_3SOOSO_3^{-}$ is the persulfate ion, $S_2O_3^{2-}$ is the thiosulfate ion, SO_4^{2-} is the sulfate ion, and both $S_2O_3^{-*}$and SO_4^{-*} are radicals. Furthermore, the persulfate ions can react with ferrous ions to produce sulfate radicals shown in Eq. 2-20 [77] [78]:

$$^{-}O_3SOOSO_3^{-} + Fe^{2+} \rightarrow Fe^{3+} + SO_4^{2-} + SO_4^{-*}, \qquad \textbf{Eq. 2-20}$$

where Fe^{2+} and Fe^{3+} are the ferrous and ferric ions. Also, an important study showed that in alkaline solutions, the sulfate radicals react with hydroxide ions to produce hydroxyl radicals as shown in Eq. 2-21 [79]:

$$SO_4^{-*} + OH^{-} \rightarrow SO_4^{2-} + OH^{*}, \qquad \textbf{Eq. 2-21}$$

where OH^{-} is the hydroxide ion, OH^{-*} is the hydroxide radical. When the pH value of the solution is 12, one study found that the hydroxide radicals are the predominant radicals that are being activated during polymerization [80].

An additional means of redox initiation is conducted by applying alcohols and metallic ions [62]. For instance, Ce^{3+}, V^{5+}, Cr^{6+}, and Mn^{3+} can react with an alcohol to produce radicals that initiate polymerization of methyl methacrylate [81]. The redox reaction is shown in Eq. 2-22:

$$RCH_2OH + Ce^{4+} \rightarrow Ce^{3+} + H^{+} + RCHOH^{*}, \qquad \textbf{Eq. 2-22}$$

where RCH_2OH is the alcohol, Ce^{4+} and Ce^{3+} are cerium ions, H^{+} is the hydrogen ion, $RCHOH^{*}$ is the produced radical.

Polymerization can be initiated photochemically by ultraviolet or visible light when the initiators are light-sensitive species, such as thioxanthone and titanium dioxide

[82] [83]. Photochemical initiation has two types. One type involves decomposing the photochemical initiator into a radical by applying a specific frequency of light. The other type works by photoexcitation of a compound. This compound is thus activated to react with another species to form radicals. Photochemical initiation has many advantages and limitations. This type of initiation is easily controlled by adjusting the intensity of light and temperature. Moreover, there is no need for solvents; it avoids environmental contamination and has considerable economic benefits. However, light energy cannot activate polymerization thoroughly because the penetration of light is not deep. This technique is highly suitable for fabricating coatings on the surface of a structure such as pipelines [84]. Only the monomers whose double bonds are conjugated with other groups can absorb ultraviolet or other light frequencies to form radicals, such as MMA, styrene [60]. It is necessary to select a proper glass container for polymerization because the common glassware cannot transmit the light whose wavelength is below 300 nm. Usually, the aromatic ketones and their derivatives, such as benzoin, benzyl ketals, and aroylphosphine oxides, are applied as the commercial initiators in photochemical polymerization since they can absorb longer wavelength light [85].

Ionizing radiation such as electrons, neutrons, γ-radiation, and α-particles can also be used for initiation [86] [60]. Ionizing radiation tends to provide higher energy and shorter wavelengths than ultraviolet. When a compound C is ionized, it will eject an electron and become a cation C^+. This high energy cation C^+ tends to be unstable and can soon dissociate to produce a new radical A* and another cation species B^+. The released electron can be attracted by $B^{+,}$ and their combination can form a B* radical. Alternatively, compound C can absorb the released electron and form anion C^-. This

anion can also dissociate to form radical B* and a new anion A^-. This anion (A^-) can release the electron and form the radical A*. These radicals A* and B* are now directly involved with initiating polymerization.

High-intensity ultrasound (> 16 kHz) can be applied as an initiator for polymerization of MMA [87]. Ultrasound causes the liquid to vibrate intensely so that the gas cavities produce and collapse very quickly. This causes the local areas of high temperature and pressure that can excite chemical species to break bonds and form radicals. The use of azo compounds in the system can significantly increase the efficiency of polymerization. However, this method is limited by the viscosity of the liquid because highly viscous liquids can tend to hinder the transmission of ultrasound waves. Currently, the ultrasound-initiated polymerization is applied in rapid welding of plastics [88].

Air plasma can also be applied to initiate the polymerization of MMA for producing the microscale polymer beads [89]. The gaseous monomer is placed in a region where the plasma is produced at low pressure and temperature. Plasma polymerization can produce thin polymer films or coatings on the structures' surfaces.

2.3 Electro-initiated Polymerization of MMA

In a liquid system containing MMA monomer, the polymerization of MMA can be initiated by applying cathodic or anodic potential at the electrode. This method is termed as electrochemical polymerization or electro-initiated polymerization. During the polymerization of MMA, many factors influence the conversion or molecular weight of the poly(methyl methacrylate) (PMMA) such as materials of the electrode, solution components, initiators, temperature, voltage and current, and the oxygen content of the environment. In this section, the effects of the factors will be discussed. Depending on

the electrode where the initiation occurs, the polymerization is referred to as cathodic or anodic radical polymerization.

2.3.1 Materials of Electrode

The electro-initiated polymerization of MMA is greatly influenced by the material of the cathode when the radical is produced at this electrode (cathodic potential) [90]. In one study, sulfuric acid was applied as the initiator under a current of 100 mA for one hour. The electrodes were ranked by the researchers based on the conversion efficiency of MMA from high to low (Pb, Hg, Sn, Zn, Cu, Cd, Ni, Pt, Al, Ag, and Fe). The surface area of the electrodes in the solution was 1.0 cm^2. The results showed that the lead cathode induced the highest conversion rate of 43.3 % of the MMA, and the iron cathode induced the lowest conversion rate of 0 %. The highest molecular weight of PMMA was obtained when the platinum cathode was applied. It was concluded that the different electrodes had different corrosion potentials and the reduction rate of hydrogen ions was different in each case. Increasing the reduction rate made more hydrogen radicals available to initiate the polymerization. Moreover, the adsorption of PMMA on the cathode was problematic, so it required the highest potential of the system to increase over time in order to maintain a constant current (and conversion rate). This was because of the adsorption of PMMA created a thin film that increased the resistance of the electrode.

In other cases, the anode can be configured to produce radicals. In one such study conducted by Pistoia *et al*., it was found that the adsorption of initiators on the anode was significantly influencing the conversion of MMA [91]. Anode was expected to be the place where the polymerization occurred. The electrolyte was a mixture of MMA and

nitric acid. The polymerization of MMA was electro-initiated under a current of 5 mA for 80 minutes. Five types of materials were tested, such as graphite, platinized Pt, Au, Pt, and Al. The anode made of carbon induced the highest yield (81.8% MMA conversion) for PMMA production, and the aluminum anode induced the lowest yield (0.86%). The anode made of platinum exhibited the highest molecular weight of PMMA. It was expected that the graphitic anode would have the most effective surface area for supporting initiation. Furthermore, the platinized Pt anode with its more highly effective surface area had more conversion than the normal Pt anode. This indicated that the effective area was an important factor in the initiation.

2.3.2 Electric Current

Electric current is applied to oxidize/reduce the species around the anode/cathode. The electrochemical reactions can produce radicals to initiate polymerization. Since the current is directly related to the production of radicals, the increasing current causes the conversion rate of MMA to increase [90] [92]. However, the conversion rate of MMA is limited to a threshold value that stops increasing even as the current continues to increase. On the contrary, in some cases, the conversion of MMA decreases when the current is higher than the specific value [93] [94]. This may be because the rapidly produced radicals terminate the chain polymerization at an early time of the polymerization process. Under these circumstances, it would be expected that more short-chain polymers (oligomers: the molecular weight < 1000 g/mol) would tend to be produced in the system. However, another study showed that the oligomer yield decreased when the current increased [91]. This indicated that the rapidly initiated monomer might increase the

viscosity of the liquid around the electrode. The increased viscosity may have caused the diffusion of MMA to become more difficult, and the oligomers' yield decrease.

The specific value of the electric current which causes the highest conversion of MMA is dependent on the components of the solution system. Yashoda *et al*. found that the value was 300 mA (6.25 x 103 A/m2) when the solution consisted of 0.75 mol/L MMA, 0.01 mol/L NH_2OH, 0.5 mol/L H2SO4, 0.05 mol/L Ti^{4+}, and 40% of methanol by volume [93]. Aurizi *et al.* found that the value was 50 mA (5 x 104 A/m2) when the solution consisted of 3.5 ml of methanol, 3.5 ml of H_2SO_4, and 3.0 ml of MMA [94].

2.3.3 Temperature and Oxygen Gas Effects

There is a specific temperature which induces the highest conversion of MMA. It was found that when the temperature of the solution was 25 ℃, the highest conversion of PMMA was obtained using a simple solution (0.9 mol/L MMA, 0.005 mol/L Ce^{4+}, 0.3 mol/L H_2SO_4) and a voltage of 2.5 V [95]. Moreover, it was found that when the temperature was higher than 65 ℃, the conversion of the PMMA would be constant [96]. Yashoda *et al*. found that when the temperature was 32 ℃, the highest conversion of MMA was obtained (This was the same solution presented in Section 2.3.2) [93]. Temperature is related to the molecular Brownian motion of the molecules of a fluid system [97]. The higher temperature of a liquid system causes particles to have a higher diffusion rate. Higher diffusion rate causes the active radicals to react with monomers more rapidly. When the temperature of the polymerization system is increased, the initiation, propagation and termination rates also tend to increase. At the early stage of polymerization, the concentration of the monomers is much higher than that of the active radicals, so the propagation rate is much higher than the initiation and termination rate

(initiation rate = termination rate) [60]. As the temperature increases before the specific temperature, the increase of propagation rate is more than that of the initiation/termination rate. This causes the conversion of MMA to increase. As the temperature keeps increasing after the specific temperature, the termination/initiation rate is possibly more predominant so that the polymerization terminates quickly. The over-high temperature may cause newly formed radicals to react rapidly with other chemicals to form byproducts which do not contribute to polymerization. For instance, the reduction of hydrogen ions to form H_2 gas cannot initiate polymerization.

Several studies demonstrated that oxygen gas in the environment had a negative effect on the conversion of MMA during electro-initiated polymerization [98] [94] [90] [95]. The extent of the decrease on conversion due to the oxygen gas was influenced by the polymerization systems (different initiators, solvents or applied voltages). It was possible that the presence of oxygen in the liquid system consumed some of the active radicals and formed hydroxyl radicals, which resulted in low molecular weight and conversion [99].

2.3.4 Components of Solution

An electro-initiated polymerization system for MMA conversion usually includes electrodes, a solvent, a monomer, and an initiator. Sometimes other additives are added in the system to obtain good dispersion or increased the solubility of MMA. This stabilizer is poly(vinyl pyrrolidone) [96]. A preferred solvent is usually some combination of water and methanol. The initiators used in these processes have been classified into two types – inorganic and organic. Initiator selection has been based on the electrode where the initiation will occur (anode versus cathode).

Many studies demonstrated the existence of optimized ratios among the components of the electro polymerization systems. Each study showed that there were specific concentration percentages which induced the highest conversion rates of MMA. In one example involving cathodic radical polymerization, the water concentration was 2 mol/L (in MMA-H_2O-H_2SO_4 system) for obtaining the best yield of PMMA [90]. However, in an anodic radical polymerization example, the water acted as an inhibitor which caused zero conversion of MMA [94]. Other studies indicated that when the concentration of MMA was 0.05 or 0.9 mol/L (for different specific polymerization systems), the conversion of MMA was the highest in those respective cases [95] [96].

Theoretically, if all newly produced, reactive radicals obtained from initiators are used to initiate polymerization, the production rate of the radicals will be equal to the initiation rate. In contrast, the radicals are also terminating the polymerization process of a given molecule, so the termination rate is theoretically equal to the initiation rate [60]. Therefore, the concentration of the initiator has to have a specific value in order to obtain the highest conversion rate of MMA. Sarac *et al*. obtained the highest conversion rate of MMA when the concentration of ceric sulfate was 0.005 mol/L (0.9 mol/L MMA and 0.3 mol/L H_2SO_4) [95]. Yashoda *et al*. applied 0.006 mol/L of titanium sulfate or 0.008 mol/L of hydroxylamine sulfate in different MMA polymerization systems to obtain the highest conversion [93]. Moreover, other initiators, such as potassium persulfate [100], tetra-n-butylammonium perchlorate [101], nitric acid [91], lithium acetate [98], and sulfuric acid [92], have also been applied to initiate polymerization of MMA. The scheme for initiation using potassium persulfate is shown in Eq. 2-23 as follows:

$$S_2O_8^{2-} + e^- \rightarrow SO_4^{2-} + SO_4^{-\,*}, \qquad \textbf{Eq. 2-23}$$

where $S_2O_8^{2-}$ is the persulfate ion, e^- is an electron, SO_4^{2-} is the sulfate ion and SO_4^{-*} is the sulfate radical.

For shipping and stability purposes, MMA liquid monomer often contains a very small proportion of mequinol (< 1%) working as an inhibitor to prevent the spontaneous polymerization of MMA. This is because the pure MMA can spontaneously polymerize without the addition of initiator. It can also be initiated by ultraviolet light. An excessive concentration of initiator can overwhelm the effect of an inhibitor. Also, the mequinol can be removed by washing the MMA liquid with 5% sodium hydroxide solution until a relatively inhibitor-free MMA liquid is obtained [102]. An alumina powder column can also be applied to remove the inhibitor [103].

2.3.5 Post-polymerization and Long-living Radicals

After turning off the power supply in an electro-initiated polymerization, the initiation and polymerization are generally expected to cease because no radicals are being produced. However, several studies indicated that after stopping the voltage-induced production of initiators, the polymerization can still occur since, after a period of time, the conversion of MMA was observed to continue [92] [100]. This phenomenon has been referred to as post-polymerization. Post-polymerization indicates that long-lived radicals may continue to exist in the systems even after the electric field has been removed.

Two possible reasons were reported for these long-living radicals [100]. The first one is the occlusion of the radicals within the polymeric phase of a heterogeneous medium (MMA-water-initiator system) [100] [104]. These polymeric phases can form as a result of the polymerization process. It appears that these phases can temporarily trap

radicals within these phases and so delay the time at which the initiator can resume polymerization. When these radicals collide with each other, the combination reaction (Eq. 2-17) occurs and a terminated polymer chain is produced. If the radicals collide with other activation-receptive elements of the system, the polymerization can continue to occur.

2.4 Evaluation Techniques

In this section, the evaluation techniques applied to analyze data and chemical species are introduced. The techniques include the statistical analysis tools (F test and Student's T test), Fourier-Transform Infrared Spectroscopy (FTIR), and Energy Dispersive X-ray Fluorescence. Their basic theories and mechanisms will be introduced in the following sections.

2.4.1 Statistical Analysis Tools

When two average values from two series of numbers are very close (or not close), it is difficult to state that these two average values are 100% different. Hence, two statistical steps are commonly applied to confirm whether two average values are significantly different with respect to a specific confidence level: F test and the Student's T test [105]. F test is the first step to determine whether two series of numbers have significantly different variances (where the variance is the square of the standard deviation) at a specific confidence level. The Student's T test (T test) is the second step to determine whether two series of numbers have significantly different average values at a specific confidence level. The F test is conducted before the T test because the similarity of variances is used to calculate the Student's T test result.

Supposing the first series has n_1 numbers and the second series has n_2 numbers. The first step in the F test is to calculate the variances of two series as shown in Eq. 2-24 [105]:

$$S_n^2 = \frac{1}{n}\sum_{i=1}^{n}(x_i - \bar{x})^2, \qquad \textbf{Eq. 2-24}$$

where S_n^2 is the variance, n is the number of the series, x_i is the designated number, $\bar{x}$ is the mean value of the series. After calculating two variances S_1^2 and S_2^2 for two series, the F test value is calculated via Eq. 2-25:

$$F_{cal} = \frac{S_1^2}{S_2^2}\ , \qquad \textbf{Eq. 2-25}$$

where F_{cal} is the F test value. It should be noted that the bigger variance is the numerator in Eq. 2-25. This guarantees that $F_{cal} \geq 1$. Subsequently, the degrees of freedom are calculated through Eq. 2-26:

$$f_1 = n_1 - 1\ , f_2 = n_2 - 1\ , \qquad \textbf{Eq. 2-26}$$

where f_1 and f_2 are the degrees of freedom of the two series. From Table 2-9, the critical value of the F Test, F_{crt}, can be obtained according to degrees of freedom. If $F_{cal} \geq F_{crt}$, it can be stated that these two variances from the n_1 and n_2 series are significantly different at the 95% confidence level. In contrast, if $F_{cal} < F_{crt}$, then the two variances cannot be considered significantly different.

Table 2-9: Critical value of F test at the 95% confidence level [105]**.**

	Degrees of freedom for n_1								
Degrees of freedom for n_2		2	3	4	5	6	7	8	9	10
	2	19.00	19.16	19.25	19.30	19.33	19.35	19.37	19.39	19.40
	3	9.55	9.28	9.12	9.01	8.94	8.89	8.84	8.81	8.79
	4	6.94	6.59	6.39	6.26	6.16	6.09	6.04	6.00	5.96
	5	5.79	5.41	5.19	5.05	4.95	4.88	4.82	4.77	4.74
	6	5.14	4.76	4.53	4.39	4.28	4.21	4.15	4.10	4.06
	7	4.74	4.35	4.12	3.97	3.87	3.79	3.73	3.68	3.64
	8	4.46	4.07	3.84	3.69	3.58	3.50	3.44	3.39	3.35
	9	4.26	3.86	3.63	3.48	3.37	3.29	3.23	3.18	3.14
	10	4.10	3.71	3.48	3.33	3.22	3.14	3.07	3.02	2.98

After judging the similarity of the two variances, the second step is to judge the similarity of the average values of the two series as per the calculation of the Student's T test [105]. After the F Test, if the two variances of these two series are not significantly different ($F_{cal} < F_{crt}$), the value of the T test can be calculated via Eq. 2-27 and Eq. 2-28 (substitute 2-27 into 2-28).

$$s_{pooled} = \sqrt{\frac{S_1^2(n_1 - 1) + S_2^2(n_2 - 1)}{n_1 + n_2 - 2}}, \qquad \textbf{Eq. 2-27}$$

$$t_{cal} = \frac{|\bar{x}_1 - \bar{x}_2|}{s_{pooled}} \sqrt{\frac{n_1 n_2}{n_1 + n_2}}, \qquad \textbf{Eq. 2-28}$$

where $\bar{x}_1, \bar{x}_2$ are the average values of the two series, n_1, n_2 are the numbers of the two series, S_1^2, S_2^2 are the variances, s_{pooled} is a middle value, and $n_1 + n_2 - 2$ is the total

degree of freedom. From Table 2-10 the critical value of the T test, t_{crt}, can be obtained according to the degree of freedom. If $t_{cal} \geq t_{crt}$, it can be stated that two mean values from the n_1 and n_2 series are significantly different at various confidence levels. If $t_{cal} < t_{crt}$, the two mean values are then said to be "not significantly different."

Table 2-10: Critical value of T test at various confidence levels

	Confidence Level (%)						
Degree of freedom ($n_1 + n_2 - 2$)		90	95	98	99	99.5	99.9
	2	2.920	4.303	6.965	9.925	14.089	31.598
	3	2.353	3.182	4.541	5.841	7.453	12.924
	4	2.132	2.776	3.747	4.604	5.598	8.610
	5	2.015	2.571	3.365	4.032	4.773	6.869
	6	1.943	2.447	3.143	3.707	4.317	5.959
	7	1.895	2.365	2.998	3.500	4.029	5.408
	8	1.860	2.306	2.896	3.355	3.832	5.041
	9	1.833	2.262	2.821	3.250	3.690	4.781
	10	1.812	2.228	2.764	3.169	3.581	4.587

After the F Test, if two variances of these two series are significantly different ($F_{cal} > F_{crt}$), the value of the T test and the degree of freedom can be calculated via Eq. 2-29 and Eq. 2-30, respectively:

$$t_{cal} = \frac{|\bar{x}_1 - \bar{x}_2|}{\sqrt{(S_1^2/n_1) + (S_2^2/n_2)}}, \qquad \textbf{Eq. 2-29}$$

$$degree\ of\ freedom = \frac{[(S_1^2/n_1) + (S_2^2/n_2)]^2}{\frac{(S_1^2/n_1)^2}{n_1 - 1} + \frac{(S_2^2/n_2)^2}{n_2 - 1}}. \qquad \textbf{Eq. 2-30}$$

Following these calculations and according to the degrees of freedom, the critical value of the T test can be obtained from Table 2-10. Subsequently, the t_{cal} and t_{crt} are compared to judge the similarity of the two mean values.

Error bars are frequently used in diagrams in this study to describe the uncertainty of an average value. The scale of error bars in every diagram is defined as follows [106]:

$$Error\ bar = \pm \frac{1.645 * \sigma}{\sqrt{n}}, \qquad \textbf{Eq. 2-31}$$

where σ is the standard deviation, n is the number of trials. The minus/plus sign indicates the true average value μ is in the range of (μ ± error bar). The constant is obtained from tabulated values for a confidence interval of 90%.

2.4.2 Fourier-Transform Infrared Spectroscopy (FTIR)

Infrared (IR) spectroscopy is a valuable tool for determining the organic or inorganic composition of a substance by analyzing the IR photon absorption peak spectrum [107]. IR spectroscopy utilizes the electromagnetic spectrum between the visible and microwave regions to scan the sample. More specifically, the range of wavelength of the light used in the analysis is from 2.5 μm to 25 μm. After scanning, IR spectroscopy provides a transmittance distribution of scanned lights. Currently, in academic research, the wavenumber of light is reported more frequently than the wavelength. The transformation equation for these two parameters is shown as follows:

$$Wavenumber = \frac{1}{wavelength(\lambda)}\ (cm^{-1}). \qquad \textbf{Eq. 2-32}$$

The range of the wavenumber used in FTIR is from 4000 to 400 cm^{-1}. This wavenumber is also known as the “frequency” because it is a calculation of the frequency of light c/λ. c is the speed of light which is a constant.

IR radiation can cause molecular bonds to vibrate when subjected to different wavenumbers of stimulation [107]. When the radiation is absorbed by the molecules, this radiation fails to pass (or transmit) through the sample. At this time, a light receiver behind the sample can only detect a small amount of light. After scanning the sample within a radiation range of 4000 cm^{-1} to 400 cm^{-1}, a spectrum that describes the radiation transmittances at the different wavenumbers is obtained. By comparing the spectrum of the sample with the spectrum of recognized substances, the chemical bonds of the sample can be identified.

Vibrations of chemical bonds when absorbing IR radiation are classified into two types – stretching and bending [107]. Stretching is the periodical movement of the atoms along the bond axis. When atoms are stretching, only the interatomic distances are changing periodically. Bending vibrations are the periodic rotation of the atoms around a center. Bending atoms exhibit the angle changing between bonds (but no change of interatomic distance). Figure 2-8 shows the two types of vibrations.

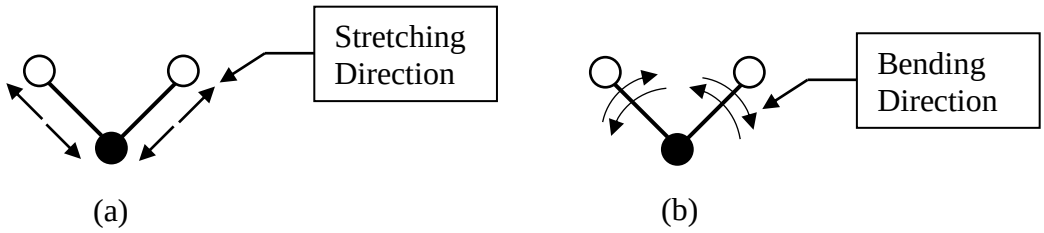

Figure 2-8: Two types of vibrations between atoms (stretching and bending) as a result of FTIR stimulation. The black atom is fixed.

Table 2-11 shows the wavenumbers and possible peak intensities of various chemical bonds when the sample is subjected to FTIR testing [108]. The absorption peaks are classified into three types – strong, medium, and weak. A strong peak means that the

minimum transmission of IR radiation is lower than 20%. Medium peak exhibits a minimum transmission of IR radiation that is in the region of (20-50%). A weak provides a minimum transmission of IR radiation in the range of (50-80%). Using Table 2-11 and similar resources, the chemical structure of an unknown sample can be approximately characterized.

Table 2-11: Wavenumbers and possible intensities of chemical bonds [108].

Approximate Wavenumber (cm^{-1})	**Bond Vibration**	**Description**
3500-3200	O-H	Broad, round
3400-3300	N-H	Weak, triangular
3300-2900	C-H	Weak-strong
2800 and 2700	C-H in O=C-H	Weak-Medium
2250	C=N	Medium
2250-2100	C=C	Weak-medium
1800-1600	C=O	Strong
1650-1450	C=C	Weak-medium
1450	H-C-H bend	Weak-medium
1300-1000	C-O	Medium-strong
1250-1000	C-N	Medium
1000-650	C=C-H	Strong

2.4.3 Energy Dispersive X-ray Fluorescence (EDXRF)

EDXRF is a non-destructive analytical tool used to obtain the identification of elements (within a liquid or solid). During the analysis, X-rays are irradiated onto a sample directly. Fluorescence is emitted by the sample. A detector measures and separates the fluorescence according to specific frequencies.

2.5 Electrophoresis

In a liquid system, the migration and separation of charged particles or ions when applying the electric field is referred to as electrophoresis [109]. Since the application of the electric field requires two electrodes (anode and cathode) in the system, the negatively and positively charged particles move towards the anode and the cathode, respectively. The moving particles are subjected to different forces in equilibrium as shown in Figure 2-9. Supposing the moving particle is positively charged, and it attracts negative ions (an ion cloud) surrounding it, the electric driving force is the force exerted by the electric field on the moving particle (positive). Retarding force is the force exerted by the electric field acting on the ion cloud (negative). This ion cloud also applies a force that resists the motion of the positive particle. The relaxation force is the force from the center of charge of the distorted ion cloud, which is negatively charged, acting against the charge of the particle or central ion. These negative charges apply a net force that pulls on the moving particle. The viscous drag force is the liquid friction force. When the viscosity of the liquid increases, so too does the viscous drag force, which tends to slow the particle/ion.

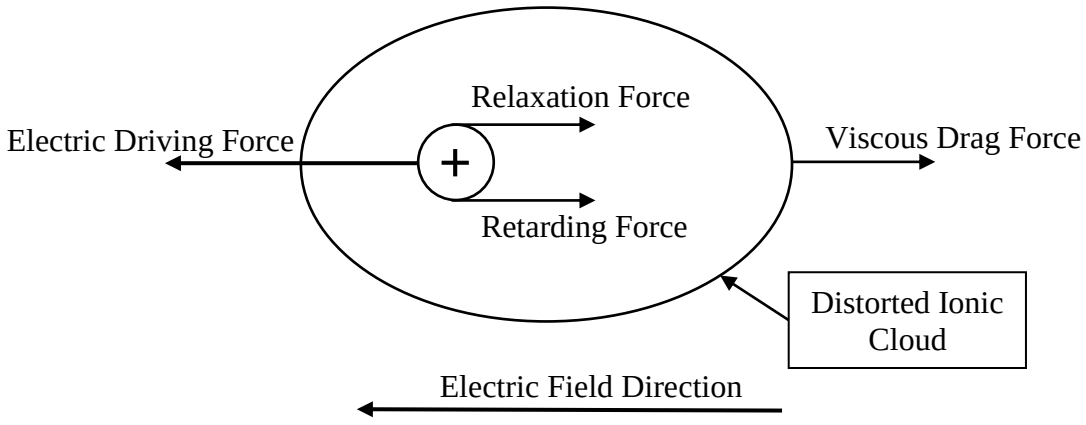

Figure 2-9: Model of forces acting on moving particle in liquid system.

When these forces reach equilibrium, the particle/ion moves at a constant speed. There is a relationship between the velocity of the particle (ν) and electric field intensity (E) as shown as follows [109]:

$$\nu = \mu E\ , \qquad \textbf{Eq. 2-33}$$

where μ the mobility of the particle. The mobility is determined in part by particle size, shape, charge, the solution chemistry, concentration and temperature. The electric field intensity is defined by Eq. 2-34 when two electrodes consist of infinitely large plates:

$$E = \frac{U}{d}, \qquad \textbf{Eq. 2-34}$$

where U is the applied voltage between two electrodes, and d is the distance between them. It can also be used to estimate the electric field intensity (roughly). Cardenas and Struble established a simple model (shown in Eq. 2-35) to predict the required time for the charged particles to penetrate hardened cement paste (HCP) under an applied electric field [110]:

$$P = \frac{\nu t}{N_D}, \qquad \textbf{Eq. 2-35}$$

where P is the penetration depth, ν is the net velocity of the particle, t is the time of particle transports, N_D is the degrees of freedom. When the particle is moving in the solution (not in HCP), the N_D is one. When the particle is moving in the pores of the HCP structure, the N_D is six. By substituting Eq. 2-33 and Eq. 2-34 into Eq. 2-35, one can obtain Eq. 2-36. Eq. 2-36 is used to predict the time needed to transport charged particles from an external solution to some distance within the interior of an HCP specimen.

$$t = \frac{P d N_D}{\mu U}. \qquad \textbf{Eq. 2-36}$$

2.6 Steel Corrosion Mechanism

According to the report from the National Association of Corrosion Engineers, the cost of corrosion was $451.3 billion in 2013 [111]. This cost occupied 2.7% of the gross domestic product. Apparently, any small breakthrough in the prevention of corrosion can have huge economic benefits. In this section, the basic electrochemistry corrosion will be introduced. Moreover, the concepts of polarization and corrosion rate calculation will be discussed. In addition, the Pourbaix diagram and concept of passivation of steel will be introduced.

2.6.1 Basic Concepts in Corrosion

When corrosion occurs on metal, the corrosion cell shown in Figure 2-10 must have 4 components – cathode, anode, electrolyte, and the metallic path between two electrodes [4]. Figure 2-10 shows a galvanic cell which describes the mechanism of a corrosion cell. The anode is one of two dissimilar metals in the cell. Since the anodic metal is more reactive than the cathodic metal, oxidization occurs at the anode where released electrons into the metallic path of the electric circuit that is connecting the two electrodes. The insoluble electrons have to move through the circuit to the cathode shown in Figure 2-10. The electric current can be monitored via the voltmeter. The cathode is the other less reactive metal in the cell, so the reduction occurs at this electrode and consumes the electrons that arrive (through the circuit) from the anode. When the reduction occurs at the cathode, the cations are consumed. This causes the concentration of cations to decrease. The oxidization of the anode release cations which slowly migrate towards the cathode in the electrolyte (and through the salt bridge). The electrolyte is the

medium that supports this ionic motion. It should be noted that the direction of electron flow is opposite to the conventional electric current (I) shown in Figure 2-10.

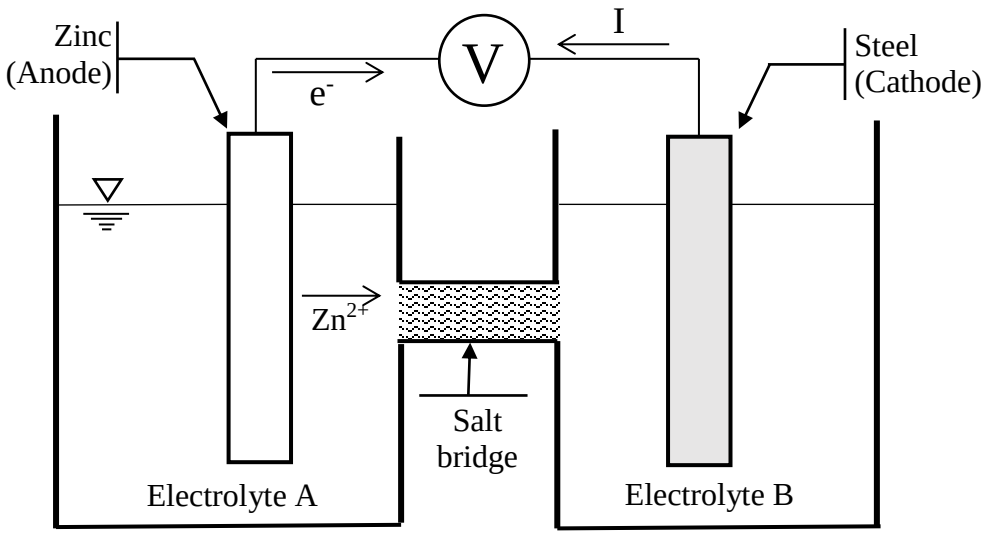

Figure 2-10: Galvanic cell.

Oxidization and reduction reactions may change when there is a change in electrolytes [4]. Supposing electrolytes A and B of Figure 2-10 are sodium chloride solutions (seawater). At the anode, the zinc bar oxidizes and releases zinc ions. At the cathode, water and oxygen react to produce hydroxide ions. If the electrolytes are acidic, (pH < 2), then hydrogen ions will be reduced at the cathode to produce hydrogen gas. Moreover, if the electrolytes A and B are 1 mol/L zinc sulfate and 1 mol/L ferrous sulfate, respectively, the cell can be referred to as Daniel cell. The electric potential measured is the corrosion potential. It is a reversible cell potential that is also referred to as the electro-motive force (EMF) of the two-chambered reaction cell.

In Figure 2-11, the zinc bar is replaced by a platinum bar in 1 mol/L H_2SO_4 solution. Hydrogen gas is purged into the platinum-electrode half of the cell at a pressure

of 1 atm. Also, the steel is replaced by a pure metal, and its solution set at 1 mol/L M^{n+}. The measured EMF is the reversible potential vs. the standard hydrogen electrode (SHE). When different metals are tested via this method, different potentials (EMF values with-respect-to SHE) can be obtained. Relatively noble (or less reactive) metals tend to have highly EMF values. For instance, zinc has an EMF of -0.763 V with respect to the SHE. This is more negative than the EMF of iron, -0.440 V vs. SHE [4]. This indicates that the zinc is less noble than the iron. When zinc and steel are put in the same corrosive environment, the zinc will corrode referentially. This is the reason why zinc is used as a sacrificial anode in the cathodic protection of steel structures.

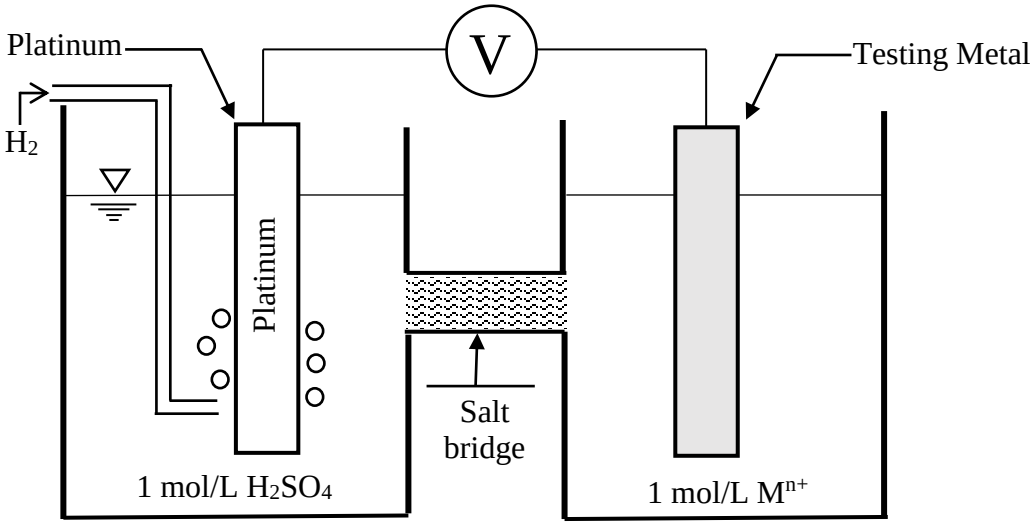

Figure 2-11: Standard hydrogen reference electrode (SHE) connected with pure metal in EMF testing.

In the corrosion industry, the standard hydrogen reference electrode is not used frequently because the setup is too complicated and requires pressurized hydrogen gas which may cause security issues during transports. A commonly used reference electrode is the copper/copper sulfate reference electrode (CSE) due to relative convenience, easy

setup, and good safety. The use and maintenance of the CSE are detailed in Section 3.2. This reference electrode consists of a saturated copper sulfate solution, copper sulfate crystals (that are used to maintain solution saturation), a pure copper metal rod and a porous plug.

Table 2-12 shows the corrosion potential of different metals vs. the standard hydrogen electrode (SHE), the copper/copper sulfate reference electrode (CSE), and the saturated calomel reference electrode (SCE) [4]. It should be noted that the EMF of the SHE vs. CSE is not -0.337 V because the copper sulfate solution in CSE is not equal to 1 mol/L (It is actually in a saturated state at 1.47 mol/L).

Table 2-12: Standard reduction potentials vs. SHE and CSE at 25 ℃. (partial)

Electrode Equation	**EMF vs. SHE (V)[1]**	**EMF vs. CSE (V)[2]**	**EMF vs. SCE (V)[3]**
$Au^{3+} + 3e = Au$	+1.500	+1.184	+1.256
$Ag^{+} + e = Ag$	+0.800	+0.484	+0.556
$Cu^{2+} + 2e = Cu$	+0.337	0.000	+0.133
$2H^{+} + 2e = H_2$	0.000	-0.316	-0.244
$Fe^{2+} + 2e = Fe$	-0.440	-0.756	-0.684
$Zn^{2+} + 2e = Zn$	-0.763	-1.079	-1.007
$Na^{+} + e = Na$	-2.71	-3.026	-2.954
$Ca^{2+} + 2e = Ca$	-2.87	-3.186	-3.114
$K^{+} + e = K$	-2.93	-3.246	-3.174

1. The reversible (corrosion) cell potential vs. standard hydrogen reference electrode.
2. The reversible cell potential vs. copper/copper sulfate reference electrode.
3. The reversible cell potential vs. saturated calomel reference electrode.

In general, a given metal with a higher EMF will tend to have higher corrosion resistance in corrosive environments. This is because the metallic atoms in these cases show less tendency to transform from solid state to an ionic state [4]. Moreover, the EMF can be used to predict which cations will tend to be electrodeposited on a given surface under a given potential. If a solution has silver and cupric ions, when a steel bar is immersed in this solution, the silver ions will tend to be reduced more quickly than the cupric ions as indicated by the more positive EMF of +0.8 V vs. SHE. Predicting system behavior via EMF has limitations. It cannot be used to predict the corrosion rate of the metal accurately, because the formation of corrosion depends on the chemistry of the corrosive environment. For example, the EMF of iron is -440 mV, but iron can form a passive film on the metal surface while in a high pH environment (pH > 12). Also, the pure metals listed in Table 2-12 are rarely applied in the industry because alloys are less expensive and provide greater strength-related benefits. By definition, EMF values cannot be assessed for alloys.

2.6.2 Polarization of Steel

Polarization is the application of external power to a cell (between the two electrodes) in order to change the reversible potential away from its equilibrium value. Figure 2-12 shows the polarization setup of a steel bar. Supposing the potential exerted by the power supply is V_a. The measured reversible potential is shown as follows:

$$E = E_o + V_a \,, \qquad \textbf{Eq. 2-37}$$

where E_o is the standard EMF vs. CSE, and E is the actual EMF. When the applied potential is zero ($V_a = 0$), it can be shown that $E = E_o$. When $V_a > 0$ or $V_a < 0$, the steel bar is being anodically or cathodically charged. The behavior of the anodically charged

steel bar was studied in Section 3.5 and 4.4. Anodically charged steel will tend to suffer corrosion.

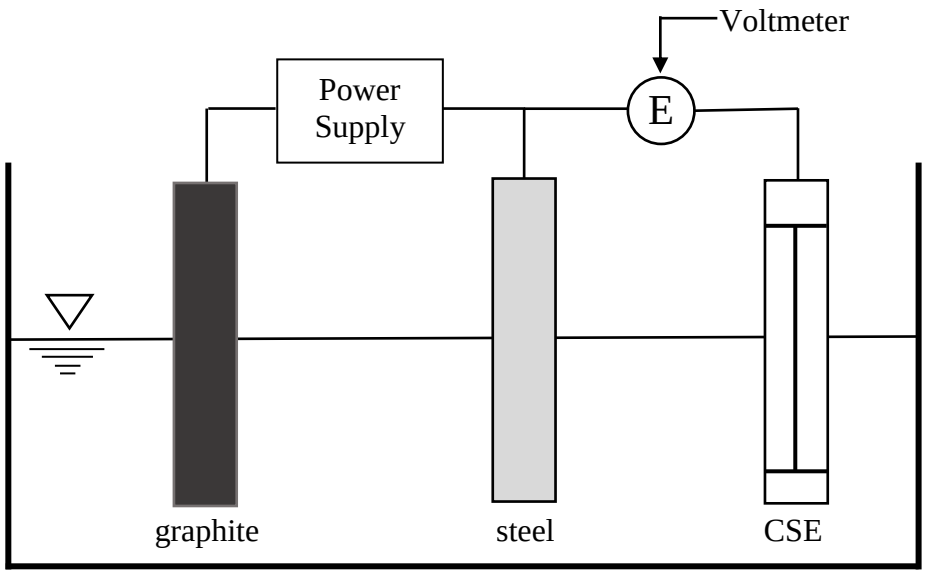

Figure 2-12: Polarization of steel bar. CSE is copper/copper sulfate reference electrode.

The reversible potential (EMF) is also referred to as the corrosion potential. When transition metals, such as Fe, Cr, Ni, and Ti, are subjected to the potentiodynamic polarization tests (this Setup is shown in Sec.3.5), S-shaped polarization curves can be observed if the solution contains acids such as H_2SO_4, HNO_3, H_2CrO_4 [4]. A general polarization curve is presented in Figure 2-13 [112]. This figure shows that when the applied potential slowly increases from zero, the steel bar is being driven into an increasingly active state under which the corrosion of steel occurs to accelerate [113]. When the corrosion potential increases to E_{pp}, which is called the primary passive potential, the steel bar transits into the passive state. At this point, a passive film starts to grow on the surface of the steel. In the passive region, the anodic current significantly

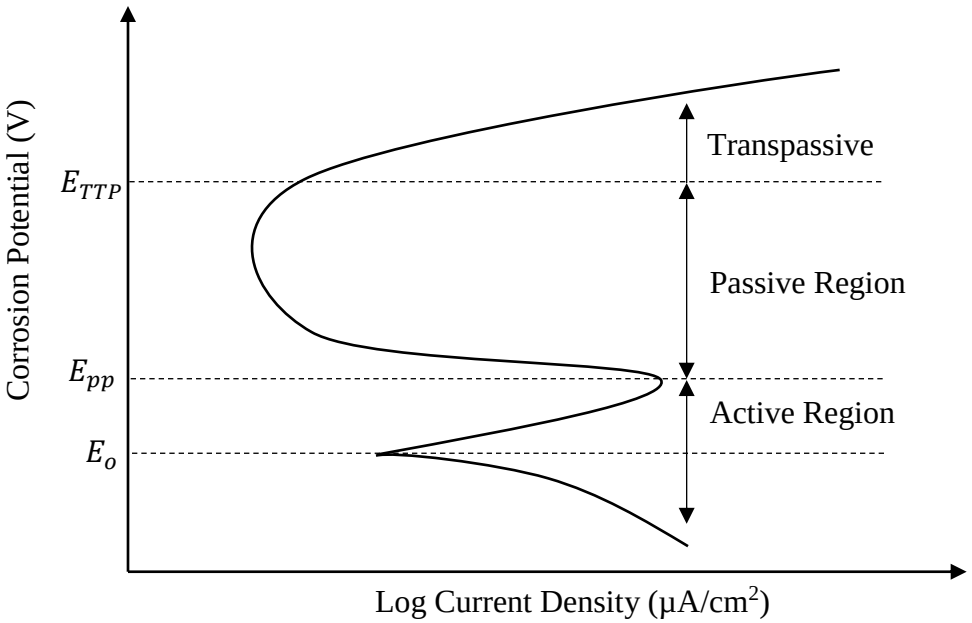

Figure 2-13: Polarization of steel in sulfuric acid.

decreases, and the corrosion of steel is hindered. When the corrosion potential increases to E_{TTP}, which is called the trans passive turning point, the steel is in the trans passive region where the corrosion acceleration re-starts. The study procedures in Section 3.5 were applied to determine the corrosion potential vs. CSE at the trans passive turning point. It should be noted that if the solution used in the polarization test contains a low concentration of sulfate acid or no acid, the passive region will disappear or become a vertical line (See Figure 4-29) [114].

When the reference electrode (RE) is applied to measure the corrosion potential, the distance between the tested electrode and the RE can significantly influence the measurement, especially during a polarization test. It is observed that when the RE is closer to a steel bar, the measured corrosion potential will be more negative at a constantly cathodic charging potential. The potential change depending on the distance is referred to as IR drop. IR drop is attributed to the electric current flow in the ionic

electrolyte. It is a function of the electrical resistance of this fluid path [115]. Eq. 2-38 describes the relationship between the exact corrosion potential $E_{applied}$, the measured corrosion potential E_m, and the IR drop iR:

$$E_m = E_{applied} - iR \, . \qquad \textbf{Eq. 2-38}$$

IR drop can significantly affect the corrosion potential measurements. In order to minimize the IR drop, some techniques can be adopted, such as increasing the concentration of conductive ions, shortening the distance between the RE and the tested metal, or using software to correct or compensate for the IR drop.

2.6.3 Corrosion Rate Calculation

One of the applications of potentiodynamic polarization is to calculate the corrosion rate at a specific environment [4]. The first step is to determine the polarization resistance. Figure 2-14 shows an example of a polarization resistance plot. E_o is the corrosion potential of the tested metals with no applied potential. This plot is also called a

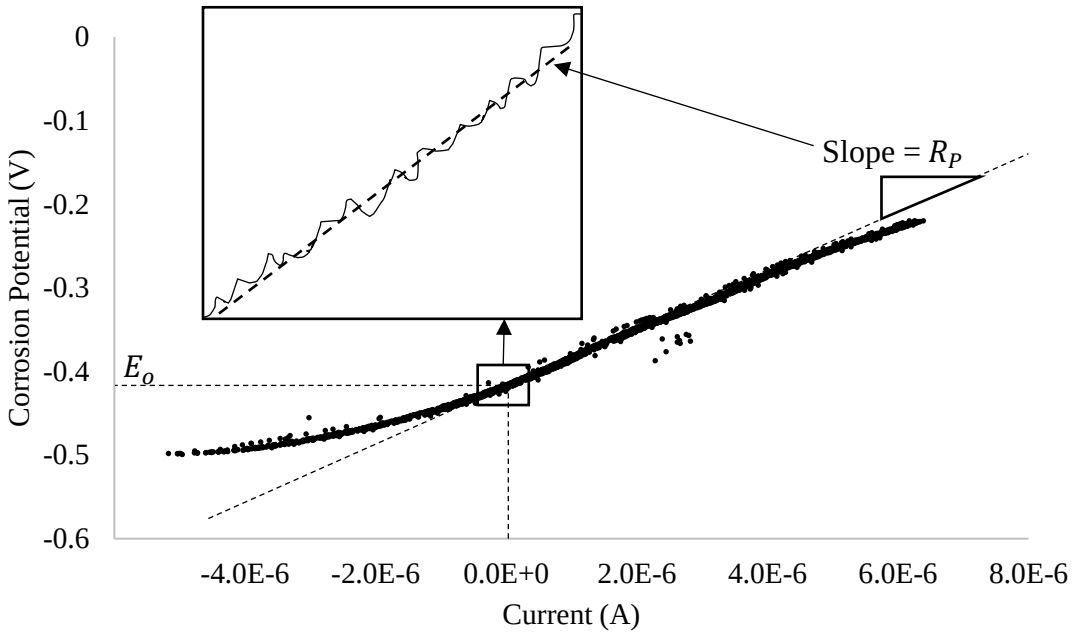

Figure 2-14: Linear polarization resistance plot. Rp is the polarization resistance.

linear polarization plot. In Figure 2-14, the slop of the zoomed-in dashed line is the polarization resistance, $\Delta E/\Delta I$. After calculating the polarization resistance, Figure 2-14 can be transformed into Tafel plot, as shown in Figure 2-15. The corrosion potential scan range in Figure 2-14 was from (E_o-300 mV) to (E_o+300 mV). After obtaining Tafel plot, the corrosion current, I_{corr}, can be calculated via Eq. 2-39 [116] [4]:

$$I_{corr} = \frac{\beta_a \beta_c}{2.3 R_P (\beta_a + \beta_c)}, \qquad \textbf{Eq. 2-39}$$

where β_a and β_c are the anodic and cathodic Tafel constants, $R_P = \Delta E/\Delta I$ is polarization resistance. Tafel constants are the slopes of the trend lines showed in Figure 2-15. I_{corr} is used to calculate the corrosion rate as follows [4]:

$$Corrosion\ Rate = 0.00327 \frac{I_{corr} M}{A \eta \rho}\ \ (mm/year), \qquad \textbf{Eq. 2-40}$$

where M is the equivalent weight of corroding metal, A is the area of the tested metal sample, η is the number of electrons involved in the electrochemical reaction, ρ is the

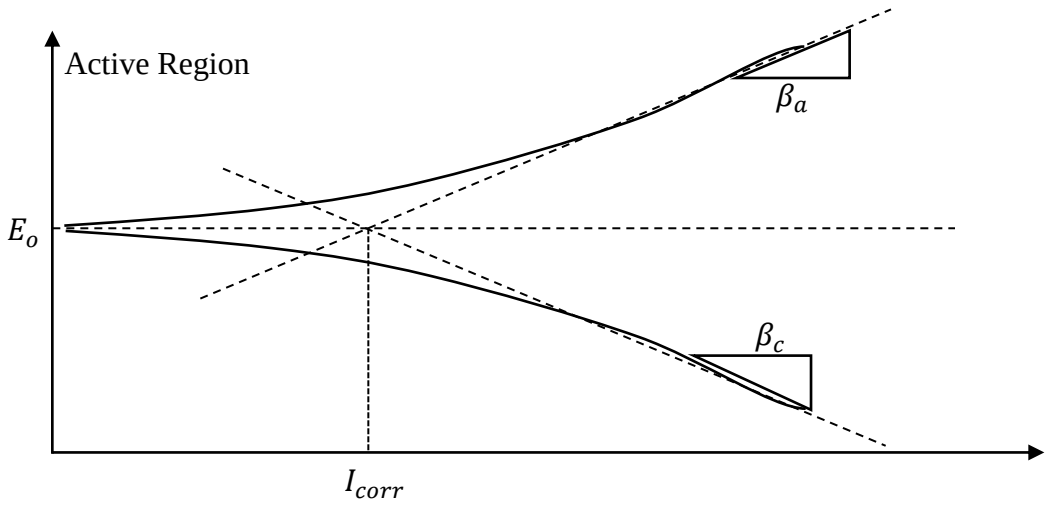

Figure 2-15: Hypothetical Tafel plot.

density of the metal. If a steel sample is subjected to an anodic polarization current, Eq. 2-39 can be used to estimate the corrosion rate on the surface of steel.

2.6.4 Passivation of Steel

It is introduced in Section 2.6.2 that when the steel metal is potentiodynamically polarized, it may enter the passive region where a thin film iron oxides form on the surface of the steel. This passive film consists of various iron oxides and can form in either acidic or alkaline environments. The Pourbaix diagram of iron summarizes the possible oxide formations or ions that tend to form on the surface of the metallic iron at the different potentials and pH values (as shown in Figure 2-16). These reactions are pH-independent, but potential-dependent. The vertical lines are potential-independent but

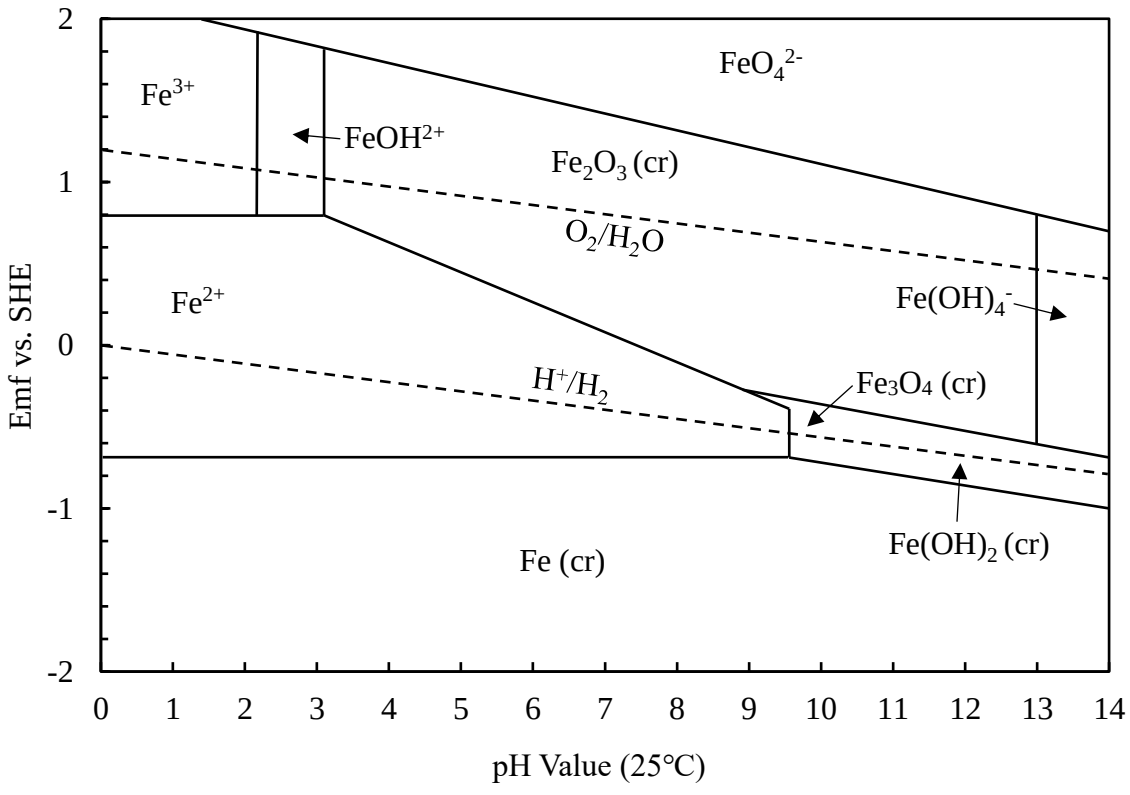

Figure 2-16: Pourbaix diagram for iron in a bath that contains 10^{-6} mol/L of ferrous ions at 25 °C [132] [4, p. 46]. Cr indicates the crystals. Ionic oxides indicate dissolution (corrosion) of iron.

pH-dependent reactions. For example, when the pH of the solution is 9.65, the ferrous ions will react with hydroxide ions to form a ferrous hydroxide (passive film). The sloping lines indicate the reactions or phase changes that are pH and potential dependent. The two sloping dash lines are oxygen and hydrogen lines which indicate the occurrence of electrolysis of water. For example, when the EMF is higher than the dashed line (O_2/H_2O), oxygen gas is produced via Eq. 2-41 and Eq. 2-42:

$$2H_2O \rightarrow O_2 + 4H^+ + OH^-(Low\ pH), \quad \textbf{Eq. 2-41}$$

$$4OH^- \leftrightarrow O_2 + 4H_2O + 4e^-(High\ pH). \quad \textbf{Eq. 2-42}$$

When the EMF is lower than the dashed line (H^+/H_2), hydrogen gas is produced via Eq. 2-43 and Eq. 2-44:

$$2H^+ + 2e^- \rightarrow H_2\ (Low\ pH), \quad \textbf{Eq. 2-43}$$

$$2H_2O + 2e^- \rightarrow H_2 + 2OH^-(High\ pH), \quad \textbf{Eq. 2-44}$$

The Pourbaix diagram of iron indicates that when the pH value of the solution is between 12 to 14, $Fe(OH)_2$ a passive film forms on the surface of iron in the EMF range from -0.4 to -1.0 V. The compositions of the passive film are complicated. One study found that, in the passive film, the anodic oxidation of $Fe(OH)_2$ produced Fe_3O_4, and Fe_3O_4 which further oxidized into Fe_2O_3 [117]. Moreover, since alloys are used more frequently than pure iron, the composition of the alloy will also affect the oxides of the passive film. Yao *et al.* stated that the Fe_2O_3, Fe_3O_4, FeOOH, and CrO_3 oxides are predominant in the passive film of 2205 duplex steel when the material was subjected to potentiodynamic polarization in the solution (0.1 mol/L H_3BO_3 and 0.025 mol/L $Na_2B_4O_7{\cdot}10H_2O$) from -0.4 to 0.1 V vs. a saturated calomel reference electrode (SCE) [118].

The Pourbaix diagram in Figure 2-16 also indicates that at pH 14, when the EMF of the iron vs. SHE increases to -0.7 V, the $Fe(OH)_2$/ Fe_3O_4 passive film dissolves and forms $Fe(OH)_4^-$. The dissolution of the passive film causes the passive film to become thinner, and the iron is then easier to corrode [119]. It was tested that when the independent steel sample was subjected to potentiodynamic polarization, the corrosion potential (E_o, no applied potential) of the steel sample became more negative with the increasing pH of the solution. Moreover, the polarizing current in the passive region increased when the pH increased.

CHAPTER 3

PROCEDURES

In this chapter, the methodology of the research is introduced. This research explored the possibility of producing electro-initiated polymerization of methyl methacrylate (MMA) in the pores of hardened cement paste (HCP) for the purpose of reducing porosity, increasing corrosion resistance, and enhancing mechanical strength. This research examined the application of sacrificial electrodeposition applied to 1018 steel. Before applying the MMA treatment on the HCP specimens, the feasibility of electropolymerization of MMA was tested in the beakers. Furthermore, Solartron Analytical Potentiostat was applied to locate a suitable corrosion potential to use in MMA treatments without causing deleterious side effects. After MMA treatment, the HCP specimens were subjected to indirect tension testing, direct compression testing, and porosity evaluation. The MMA and the production of poly(methyl methacrylate) (PMMA) were characterized using Fourier transform infrared spectroscopy (FTIR). The instruments, chemicals, and procedures required for these tasks are described in the following sections.

3.1 Instruments and Chemicals

This section presents all the instruments and materials utilized in this study. The chemicals used in this study are listed in Table 3-1. The instruments used in this study are listed in Table 3-2.

Table 3-1: List of chemicals used in the study.

Chemical Name	Manufacturer	Location	Purity (wt %)
Calcium Hydroxide	Acros Organics	Pittsburgh, PA	95
Sodium Hydroxide	Spi-chem	West Chester, PA	99
Potassium Hydroxide	Fisher Scientific	Pittsburgh, PA	99
Potassium Persulfate	Fisher Scientific	Pittsburgh, PA	99
Methyl Methacrylate	Polysciences, Inc.	Warrington, PA	99.5
Poly(methyl methacrylate)	Matheson Coleman and Bell	Norwood, OH	99
Cupric Sulfate	Tinker and Rasor	San Bernardino, CA	99
Ethanol	Decon labs, Inc.	King of Prussia, PA	100
Acetone	Fisher Scientific	Pittsburgh, PA	99.7
Deionized water (DI-water)	Mar Cor	Plymouth, MN	17.6 MΩ·cm[1]

1. The resistivity of deionized water.

Table 3-2: List of instruments used in the study.

Instrument Name	Manufacturer	Location	Model
DC power supply	AMETEK	San Diego, CA	LH 75-5
Multimeter	Innova	Irvine, CA	3300
Fourier-Transform Infrared Spectroscopy (FTIR)	Thermo Scientific	Grand Island, NY	Nicolet 6700
Attenuated Total Reflectance-FTIR	ThermoFisher Scientific	Grand Island, NY	Nicolet IR100
Centrifuge	Fisher Scientific	Pittsburgh, PA	228
Field Emission Scanning Electron Microscope	Hitachi	Tarrytown, NY	S-4800
Compression test machine	ADMET	Norwood, MA	CM-450-SF
$Cu/CuSO_4$ Reference Electrode	Tinker and Rasor	San Bernardino, CA	2-A
Mixer	KitchenAid	Benton Harbor, MI	Pro Line® Series 7 Quart
Concrete Mold	Paragon Products	Mount Pleasant, IA	2 x 4 Concrete Mold with Lid
Mass Balance	Sartorius	Goettingen, Germany	AL-64
Solartron Analytical Potentiostat	AMETEK	San Diego, CA	SI 1287
Electromagnetic Relay	Uxcell	Hong Kong, China	IEC255, DC, 12V, 8pin
Titanium Wire	Corrpro	Houston, TX	Wire anode 1.5±0.2 mm XXL coated
Titanium Mesh	Corrpro	Houston, TX	Mesh ribbon 20mm width
Energy Dispersive X-ray Fluorescence	ThermoFisher Scientific	Grand Island, NY	ARL™ QUANT'X

3.2 Corrosion Potential Measurements

The corrosion potential measurements were conducted in accordance with ASTM C 876 [120]. During a corrosion potential measurement, a Copper/Copper Sulfate ($Cu/CuSO_4$) reference electrode and the target object (reinforcement within the HCP specimen or bare steel bar) were connected to a voltmeter. Both the reference electrode and the target object were immersed in a test solution as shown in Figure 3-1. The voltage observed on the voltmeter was the corrosion potential. Preparation of the reference electrode was conducted in accordance with manufacturer's instructions (Tinker and Rasor) [121].

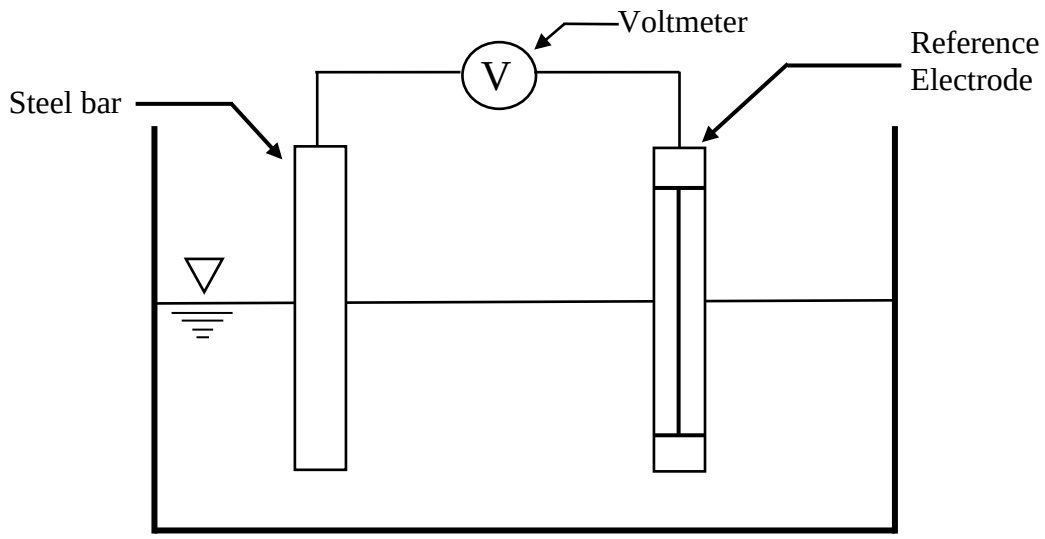

Figure 3-1: Setup of corrosion potential measurement.

Since the $Cu/CuSO_4$ reference electrode directly touched the treatment solution, it tended to be easily contaminated (especially in the case of high alkali solutions) and caused inaccurate results. To maintain its accurate performance, two reference electrodes were prepared to maintain accurate performance. One was the working reference

electrode which was used to take measurements. The other one was reserved as the lab standard electrode for checking calibration.

Calibration of the working reference electrode is shown in Figure 3-2. If the voltage difference was greater than 5 mV, the copper sulfate mixture in the working reference electrode was replaced, and the copper rod was polished with 150 grit sandpaper. Calibration was rechecked not less than 10 minutes following the mixture replacement.

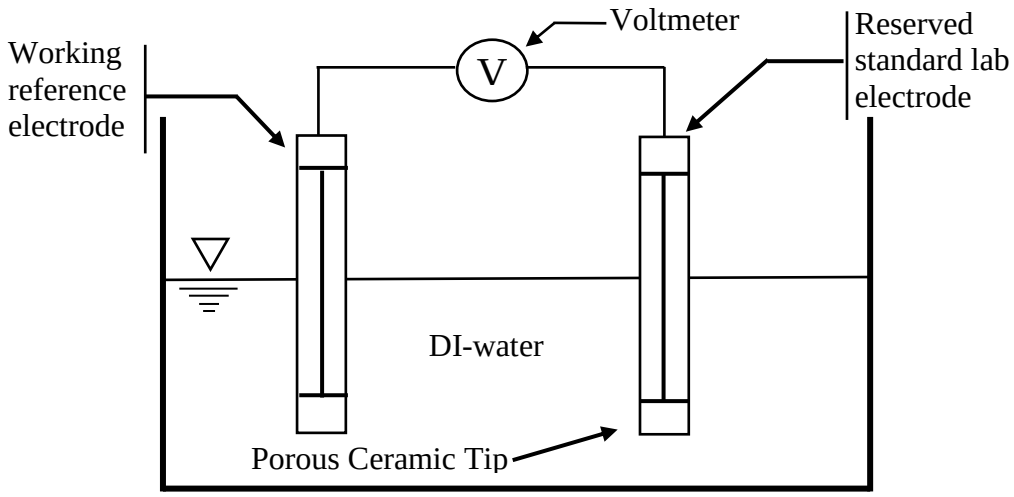

Figure 3-2: Setup of calibration of working reference electrode.

When the working reference electrode was used in alkali solutions, hydroxide ions tended to react with cupric ions in the electrode and produced cupric hydroxide (solid) which precipitated within the electrode cell or was embedded within the porous ceramic tip. The cupric hydroxide can tend to block the path (within the porous ceramic tip) between the solution and the working reference electrode. Under these circumstances, the divergence from calibration often exceeded 20 mV. To remedy this situation, the ceramic tip was soaked in an acetic acid solution (1 wt%) for one day to remove possible

cupric hydroxide. Subsequently, the tip was flushed with DI-water to remove acetic ions and soaked in DI-water for another day. If the above cleaning processes failed to reduce the calibration voltage to < 5 mV, the ceramic tip was replaced, and the copper rod in the working reference electrode was polished with 150 grit sandpaper.

Another factor that affected the precision of corrosion potential measurement was the power supply. When a power supply was connected to the circuit to conduct a treatment, the positive or negative charges were accumulating at the anode or cathode because these two electrodes naturally exhibited an electric capacitance. Even though the power supply was turned off and disconnected, the charges could tend to stay at these electrodes. These remnant charges tended to produce an electric potential on the working reference electrode or the rebar that could disturb the next corrosion potential measurement significantly. The most effective way to balance these potentials was to build a short circuit between the cathode and the anode. The electrons at the cathode were then moved towards the anode so that the charges' imbalance was removed. During the removal of charges, an ampere meter can be connected in the short circuit to monitor the decreasing current. After this current dropped to < 5 mA, the short circuit was removed, and the measurement of corrosion potential was taken.

3.3 Electropolymerization Proof of Concept Tests

In order to study the electropolymerization of MMA, a series of experiments were developed. In this section, the setup of an electro-polymerization experiment is presented. Apparent reaction products were subjected to a separation and purification process. The separated product was characterized by Attenuated Total Reflectance-Fourier-Transform Infrared Spectroscopy (ATR-FTIR).

3.3.1 Setup of Electro-Polymerization Experiments

As a preliminary exercise, Methyl methacrylate (MMA) solution was set up to induce polymerization in a beaker under an applied electric field. Figure 3-3 shows the setup of the polymerization process. Titanium mesh (the cathode) was located along the inside wall of the beaker to generate a uniform electric field. A 1 wt% solution (0.1 mol/L) of MMA monomer was placed into the beaker. The MMA monomers in the solution were expected to migrate toward the titanium wire (anode) and polymerize at the wire surface. A 200 ml beaker was used. The MMA monomer inhibitor was not removed

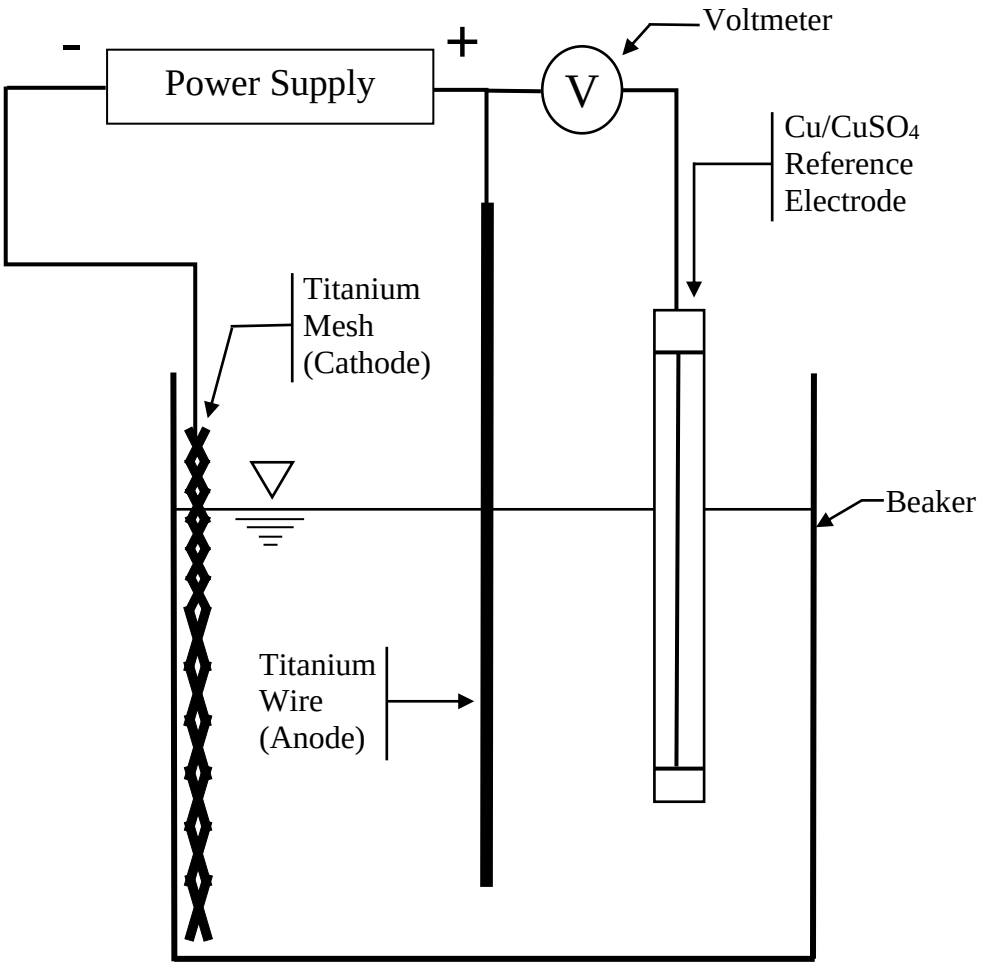

Figure 3-3: Beaker electro-polymerization setup. The titanium mesh occupied the entire interior perimeter of the beaker.

in order to promote a relatively slow reaction rate.

Previous research showed that MMA was polymerized in the pores of HCP under an applied electric field without the addition of an initiator [60]. The experiment in this section was conducted to examine MMA monomer transport and polymerization in a beaker solution when there is no HCP present. The experimental conditions applied to Figure 3-3 are listed in Table 3-3. Before starting each trial, the beaker and the titanium

Table 3-3: List of conditions applied in the polymerization proof of concept beaker test.

Trial	Solution[1] (g)	Treat time	PP[2] (g)	V_{corr}[3] (V)	C_{HCl}[4] (mol/L)	Ti-wire Polarity
1	100	10 min	0	0.70	0	Anode
2	100	10 min	0	0.80	0	Anode
3	100	10 min	0	0.90	0	Anode
4	100	10 min	0	1.00	0	Anode
5	100	10 min	0	1.10	0	Anode
6	100	10 min	0	1.50	0.2	Anode
7	100	10 min	0	1.50	0.4	Anode
8	100	24 h	0.1	1.50	0	Anode
9	100	24 h	0.1	1.50	0	Cathode[5]
10	100	24 h	0.001	1.50	0	Anode
11	100	24 h	0	1.00	0	Anode

1. Solution content: 1 wt% MMA monomer.
2. PP is the potassium persulfate initiator.
3. V_{corr} is the corrosion potential.
4. C_{HCl} is the concentration of hydrochloric acid. (For 0.2-0.4 mol/L HCl, pH ≈ 1)
5. In Trial 9, the central titanium wire acted as the cathode.

wire/mesh were flushed with DI-water for the removal of possible inorganic or organic contaminants. After cleaning, these components were rinsed with ethanol and air dried.

Trials 1-7 were designed to determine if polymerization would occur on the surface of the Ti-wire. Before and after each test, the masses of the Ti-wire electrodes were measured three times. The average masses were recorded. Trials 8-10 were designed to explore the possibility of polymerization in the solution (away from the Ti-wire). Trial 11 was designed to check if the electricity helped to initiate polymerization of MMA in 24 hours. Also, Trial 11 checked if the electric field slowed down the evaporation of MMA in 24 hours.

3.3.2 Separation and Purification of PMMA from Proof of Concept Tests

The treated solution from trials 8-10 was stirred for 10 seconds to suspend product sediments in the solution. The solution was immediately poured into 10 ml centrifuge tubes. Centrifugation was conducted at the 1500 rpm for 20 minutes. After centrifuging, a precipitate was observed at the bottom of each tube. The liquid above the precipitate was decanted.

After removal of the initial solution, an additional 10 ml of DI-water was added to each tube and shaken to rinse the sediment. This step served to dissolve possible positive ions from the precipitate into the water. These tubes were centrifuged again for 20 minutes to provide a 2nd separation rinse. The rotation speed was the same as before. A third separation rinse was also conducted. After the 3rd separation rinse was completed, the liquid was removed, and the product was collected from the tubes. The remaining precipitate was set at the 60 ℃ for 24 hours to evaporate the residual water and collect residual solids.

3.3.3 Characterization of PMMA

ATR-FTIR was applied to characterize the precipitate noted in Section 3.3.2. Before testing the precipitate sample, the ATR-FTIR components were cleaned using a lab tissue dampened with isopropyl alcohol (91%). The background spectrum was collected by ATR prior to loading the samples onto a zinc selenide (ZnSe) crystal lens. The spectra of the samples were collected in one minute. The transmittance-wavenumber plot was compared with a solid PMMA sample spectrum.

3.4 Characterization of Electro-deposited Ceramic Coating

In order to explore the production of a sacrificial ceramic coating formed prior to MMA treatment of reinforced HCP specimens, this experiment contained two phases. The first phase was referred to as the electrodeposition (ED) treatment for depositing the ceramic coating. The second phase was referred to as the anodic polarization (AP) test for testing the performance of the electrodeposits.

3.4.1 Electrodeposition Treatment

Electrodeposition treatment was applied to develop and characterize ceramic coatings formed onto a 1018 steel bar. Figure 3-4 shows the setup for this treatment. The experiment included six trials conducted with a target corrosion potential V_{corr} of -3.50 V. The components of the simulated pore fluid (SPF) are shown in Table 3-4. The plastic test container was covered and sealed with epoxy after installing experimental equipment, such as the 1018 steel bar, U-shape tube, and the other components shown in Figure 3-4. Since the electro-deposition process decomposes water into hydrogen and oxygen gases, the solution level would tend to drop during treatment. To counteract this issue, a refilling bottle with SPF was used to maintain the solution level. The U-shaped tube was used to

Table 3-4: Chemical components of simulated pore fluid (SPF).

Component	NaOH	KOH	$Ca(OH)_2$
Concentration (Mol/L)	0.08	0.24	0.03*

* This was dosed above the saturation limit of 0.02 mol/L **[122]**.

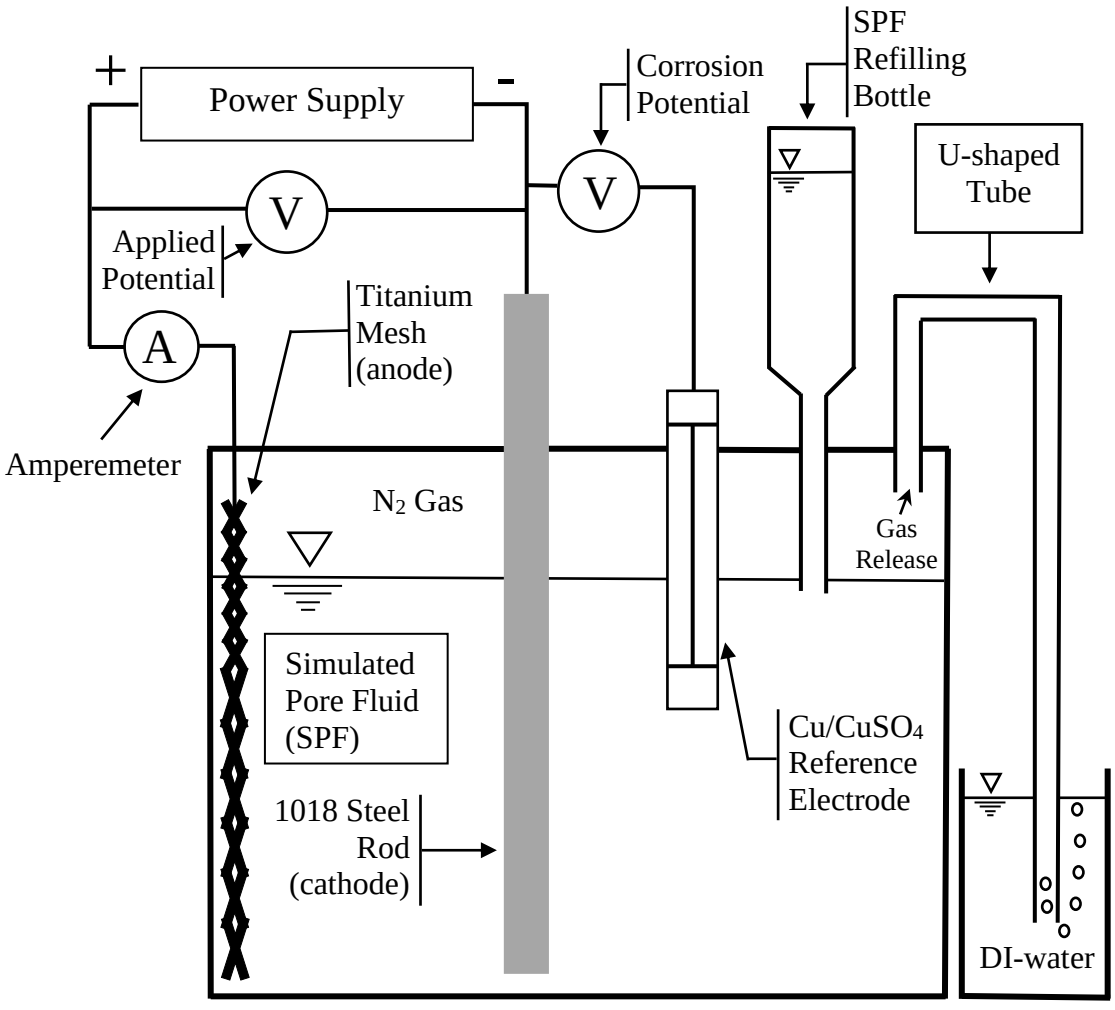

Figure 3-4: Setup of electrodeposition treatment.

release the generated gases and balance pressure while limiting atmospheric exposure that could cause CO_2 absorption. The 1018 steel bars were polished with 150 grit sandpaper to remove possible contamination and oxides prior to each test. The control bar was soaked in SPF separately during the 7-day ED treatment. The setup of the control bar exposure was similar to Figure 3-4 without the power supply and the SPF refilling bottle.

When the $Cu/CuSO_4$ Reference Electrode was placed in contact with the SPF, it was slowly releasing copper and sulfate ions and contaminating the solution. Also, positive metal ions and hydroxide ions entered the reference electrode cell and affected the precision of the corrosion potential measurement. To minimize this potential for contamination, the reference electrode was only placed in the SPF for less than 1 minute for measurement and then removed and rinsed. For this reason, the reference electrode was not permanently sealed to the chamber cover with epoxy. The reference electrode access hole was sealed with a rubber stopper during the deposition of the ceramic coating.

Before starting an ED treatment, the corrosion potential of the steel bar in the SPF was recorded while it was disconnected from the power supply. During treatment, the circuit was connected, and the voltage increased until the corrosion potential reached 3.50 V. Following corrosion potential measurement, the reference electrode was immediately extracted, and the access hole was sealed with a rubber stopper. The currents and the applied voltages were monitored daily during the 7-day treatment process.

After the 7-day treatment, the power supply was turned off, and the treatment chamber (with the steel bar) was moved to a nitrogen gas environment. At which point a reference electrode was introduced. The N_2 atmosphere was needed to avoid CO_2

contamination during corrosion potential measurement. During the corrosion potential measurement, the N_2 gas was pumped into the container through the U-shaped tube, and the gas was vented through a reference electrode access hole. Following treatment, the steel bars were then taken out of the chamber, and their images were recorded. After image collection, the specimens were returned to a nitrogen gas environment. Electrodeposits were collected from the treated steel bar surface and stored in a sealed glass bottle. Samples from six trials were examined via the Field Emission Scanning Electron Microscope (FESEM) and subjected to energy dispersive x-ray spectroscopy (installed in the FESEM) to obtain their elemental distribution.

3.4.2 Anodic Polarization (AP) Test

In the anodic polarization test, a positive potential was applied to the ceramic coated 1018 steel bars to check the corrosion resistance of the electrodeposits. The setup of the test is shown in Figure 3-5. The applied voltage was set at + 5.02 V for all six trials. During the AP test, the current, applied voltage, and corrosion potential were monitored daily over the five-day test period. After the AP test, images of the treated and control bars were taken for corrosion area estimation. The camera used for these images was the P20 Pro model, manufactured by Huawei, Shenzhen, China.

During the daily measurement of corrosion potential, N_2 gas was pumped into the treatment chamber to maintain inert conditions. When the corrosion potential of the treated bar was measured, the reading tended to require several minutes to become stable (unchanged in 10 seconds). The $Cu/CuSO_4$ reference electrode was removed promptly from the SPF following each measurement.

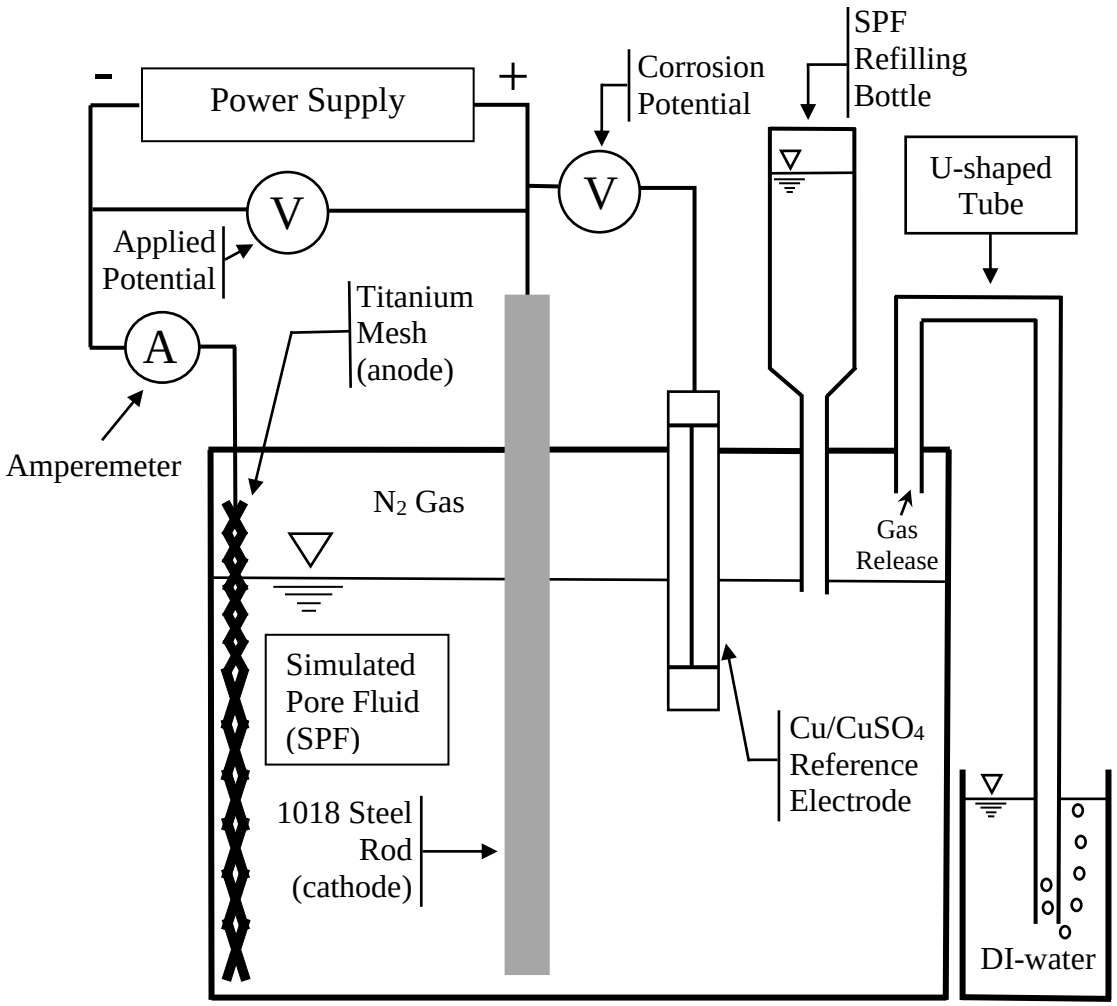

Figure 3-5: Setup of anodic polarization test.

After recording photos of the bars, they were transformed into grayscale images. The transformation of the raw image to the grayscale image was processed through a program written in Matlab (version R2018b, developed by Mathworks, Natick, MA). The program code is presented in Appendix C. The code was used to assign each pixel in the grayscale image a gray level magnitude in the range of 0 to 255. Based on the number of pixels at each gray level, a histogram of the grayscale image was obtained. From the histogram of the control bars, a threshold value (such as gray level = 100) was established

to coincide with a corroded area covering 99% of the surface. This same threshold was used in the histograms of the treated bars to estimate the corroded area in each trial. Section 4.2.2 illustrates how this estimation analysis was performed.

3.5 Potentiodynamic Polarization Scanning of 1018 Steel Bar

The purpose of this portion of the study was to locate the transpassive turning point (TTP) (discussed in Section 2.6.2) and to avoid it during treatments applied to the reinforcement of HCP. The polarization scan setup is shown in Figure 3-6. Twelve trials

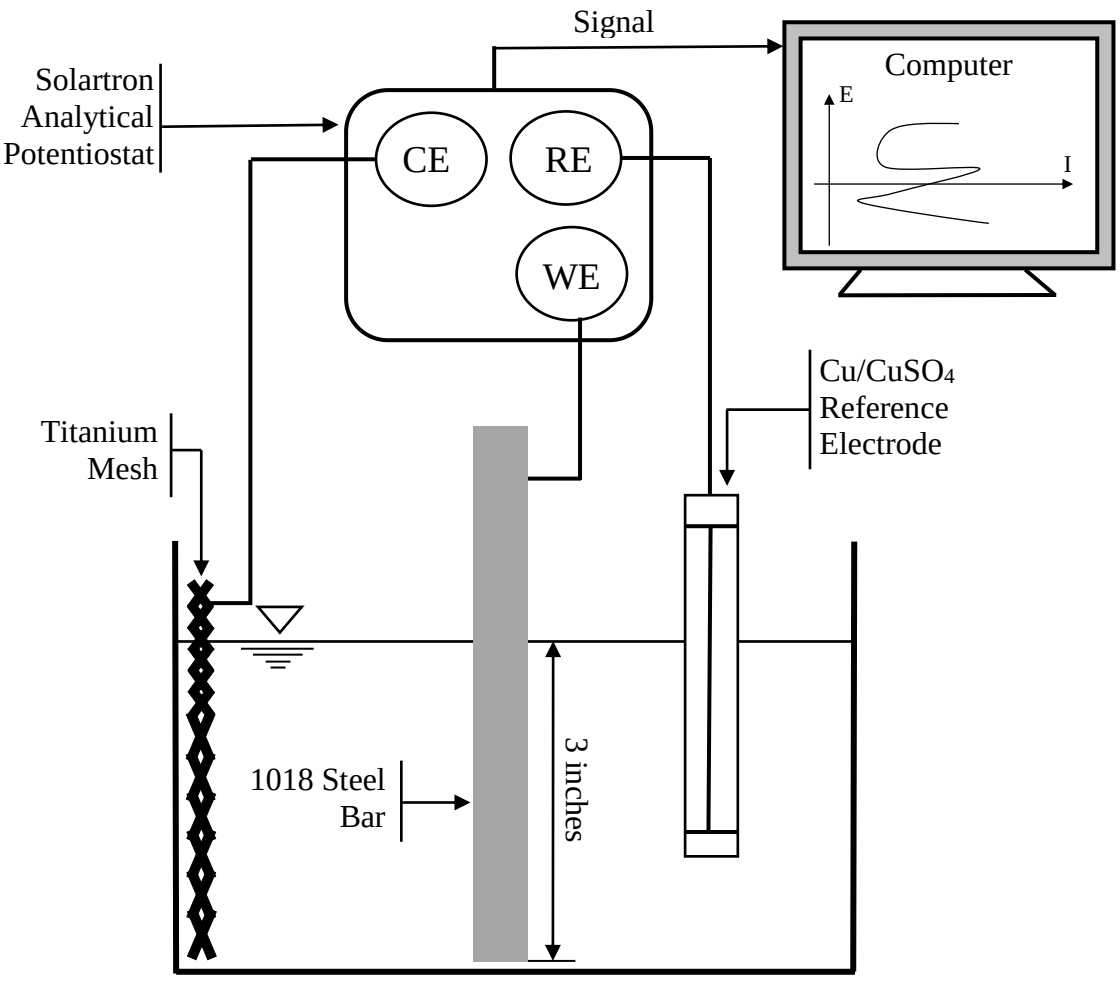

Figure 3-6: Setup for potentiodynamic polarization scan of 1018 steel bar. CE is the counter electrode, RE is the reference electrode, and WE is working electrode (1018 steel bar).

were conducted to determine the TTP. The test solutions and corrosion potentials are presented in Table 3-5. In Trials 1-6, the steel bars were directly exposed to the simulated pore fluid (Components shown in Table 3-4). The diameter of the 1018 steel bar was 1/4 inch. Three inches of the steel bar was immersed in the solution. In some cases, such as in Trials 7-12, 3-inch-high-reinforced HCP samples (20 days old) were

subjected to polarization scanning instead of the bare steel bars. The batching of HCP samples is introduced in Section 3.7. In Table 3-5, Start-V_{corr} and End-V_{corr} are the corrosion potentials where the polarization scanning starts and ends. The incremental rate of corrosion potential change with respect to the Cu/CuSO4 reference electrode was 0.122 mV per second.

Table 3-5: Applied conditions in the potentiodynamic polarization scans.

Trial	Solution	Start-V_{corr} (V)	End-V_{corr} (V)
1	SPF	-0.2	+1.5
2	SPF	-0.2	+1.5
3	SPF	-0.2	+1.5
4	SPF	-0.5	+1.0
5	SPF	-0.5	+1.0
6	SPF	-0.5	+1.0
7	2 g/L $Ca(OH)_2$	-0.5	+1.7
8	2 g/L $Ca(OH)_2$	-0.5	+1.7
9	2 g/L $Ca(OH)_2$	-0.5	+1.7
10	2 g/L $Ca(OH)_2$	-0.5	+1.7
11	2 g/L $Ca(OH)_2$	-0.5	+1.7
12	2 g/L $Ca(OH)_2$	-0.5	+1.7

1. SPF is simulated pore fluid.

Solartron analytical potentiostat was used to conduct the scans that monitored the current density changes while the corrosion potential was increasing. After the tests, the raw data from the tests was imported to an Excel document. On the E-I plots, there were two linear regression trend lines produced at either side of the TTP. Based on these two linear regression equations, the intersectional point was calculated to identify the TTP.

3.6 Uncertainty Evaluation

The purpose of this study was to evaluate and quantify the uncertainties of corrosion potential measurement and power supply behavior. The $Cu/CuSO_4$ reference electrode exhibited contamination problems when it was immersed in the simulated pore fluid (see Table 3-4). This contamination caused inaccurate corrosion potential scanning in potentiodynamic polarization tests. After each potentiodynamic polarization trial, the $Cu/CuSO_4$ working reference electrode was immediately connected to a voltmeter and compared with a standard reference electrode for rechecking the calibration voltage.

It was also observed that the treatment power supply exhibited voltage drift. The factors that caused this drift were unclear. This drift could have caused the corrosion potentials to become higher than the transpassive turning point (TTP), leading to higher than expected corrosion rates. To characterize this voltage drift, an applied voltage was set up, and after 24 hours the voltage was measured again. These two measurements were calculated through Eq. 3-1 to obtain a 24-hour voltage drift:

$$Daily\ Voltage\ Drift\ = V_{change} - V_{set}\ , \qquad \textbf{Eq. 3-1}$$

where V_{change} is the drifted voltage after 24 hours, V_{set} is the setting voltage. This drift test was repeated daily for 28 days. The average voltage drift was calculated.

The sum of the average voltage drift and the average corrosion potential error constituted the overall voltage uncertainty that was considered during interpretation of the results of the MMA treatment applied to the HCP specimens. This sum was also used to establish the corrosion potentials to avoid the trans passive region during the reinforced HCP polarization scans in Section 3.5. During the MMA treatments, the TTP was avoided by utilizing this sum to maintain the corrosion potential lower than TTP.

3.7 Hardened Cement Paste Specimen Batching

In order to make a batch of relatively uniform specimen properties, specific steps for mix design were followed. All the steps were conducted as per ASTM C 305-14 [123]. The following sections describe vital issues that governed batch uniformity.

The dimensions of the cylindrical cement specimens used in this study are shown in Figure 3-7. The water-cement ratio was 0.48. The Portland Cement type I/II and DI-water were used for batching. The chemical composition of the cement is shown in Table 3-6 (See Mill Test Report in Appendix A). Before mixing, it was confirmed that the bowl of the mixer was clean and damp with DI-water. The mixer (described in Table 3-2) was started at the lowest speed to minimize air entrainment in the cement paste. The cement powder was added continuously into the bowl at a rate of approximately 250 g per minute. If the mixture became too thick to mix effectively, the rate of water input was increased by an additional 300 g/min (for one minute) to re-establish adequate mixing workability. The above steps were repeated until all the cement and water were in the bowl, and the mixture was visually uniform. The cement paste was subsequently mixed for another 10 minutes.

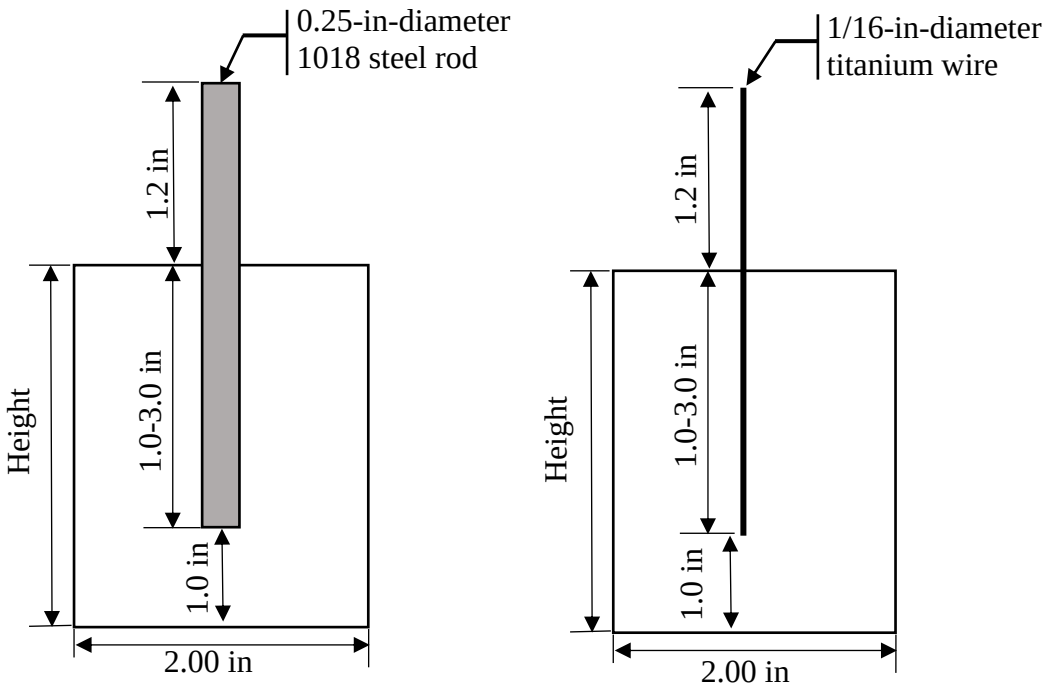

Figure 3-7: Schematic of reinforced HCP specimens. Specimen height ranged from 2 to 4 inches in various batches.

Table 3-6: Chemical composition of the Portland cement type I/II*

Item	SiO_2	Al_2O_3	Fe_2O_3	CaO	MgO	SO_3	Na_2O	K_2O
(%)	20.45	4.68	3.85	64.23	0.87	2.63	0.13	0.52

* Manufactured by Ash Grove, Little rock, AK

After mixing, the cement paste was poured into cylindrical molds (described in Table 3-2). The pouring process was divided into three portions. In each pour, only 1/3 of the mold was filled. The cement paste was rodded 20 times with a 0.25-inch-diameter steel bar to remove trapped air pockets or suspended bubbles. After these three pours, the molds were covered, and titanium wires or 0.25-inch-diameter 1018 steel bars were inserted into the mold lids so as to center the electrode placement as illustrated in Figure 3-7. After 24 hours, the hardened cement paste specimens were demolded and cured in

lime water (2 g/L of $Ca(OH)_2$ solution). If the HCP specimens were reinforced by 1018 steel rod, the lime water level was set to be just below the top edge of the specimens in order to avoid water line corrosion.

3.8 Tensile Strength Test

Tensile strength tests were conducted for HCP specimens following treatment. All the test steps were conducted as per ASTM C 496 [124]. The assembly of an indirect tensile test is shown in Figure 3-8. Masonite wood board (4.5" × 1" ×0.25") and rubber strips (4.5" × 1" ×0.05") were used to distribute the force uniformly along the specimen's load line shown in Figure 3-8. The harnesses of wood and rubber strips were 75.5 HD and 96 HC, respectively (the Shore C and D durometers were manufactured by AICE, China, Taizhou). The loading rate was 2,000 pounds per minute. After each test, the conditions of the rubber strips were checked and replaced if damaged or permanently

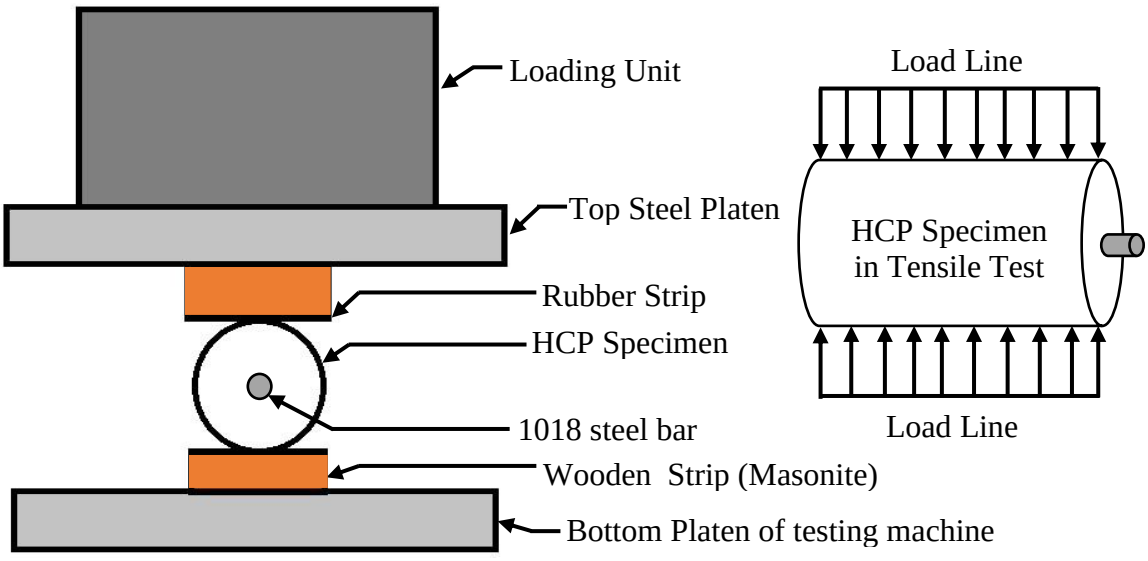

Figure 3-8: Setup of indirect tensile strength test.

deformed. After recording the peak load, the tensile strength was calculated according to Eq. 3-2 [123]:

$$T = \frac{2P}{\pi LD}, \qquad \textbf{Eq. 3-2}$$

where P is the peak load, T is tensile strength, L is the length of the specimen, and D is the diameter.

3.9 Compressive Strength Test

Some of the HCP specimens were subjected to compressive strength testing. The test was conducted as per ASTM C39/C39M-18 [125]. The specimens were equipped with an embedded titanium wire to facilitate treatment as shown in Figure 3-7. This wire was trimmed flush with the top surface, and the specimens were sulfate capped prior to loading. The capping process was conducted as per ASTM C617/C617M-15 [126]. The load rate was 2000 lb per minute. The peak load was recorded. The compressive strength was calculated based on

$$C = \frac{P}{\pi(\frac{D}{2})^2}, \qquad \textbf{Eq. 3-3}$$

where C is the compressive strength, P is the maximum load, and D is the diameter.

3.10 Porosity Test

Porosity tests were conducted after the indirect tensile strength measurements. Fragments (about 4 g each) from each test were selected and stored in deionized water at the start of porosity testing. The capacity and accuracy of the analytical mass balance (described in Table 3-2) was 60 g ± 0.1 mg. The HCP fragment masses were monitored daily to confirm full pore saturation. The saturation was considered complete if the mass

difference of the fragment over two days was lower than 0.2%. Eq. 3-4 illustrates how to calculate the mass difference rate:

$$D = \frac{M_2 - M_1}{(M_2 + M_1)/2}, \qquad \textbf{Eq. 3-4}$$

where D is the mass difference rate, M_1 is the mass of fragment on the first day, M_2 is the mass of fragment on the second day. The fragments were heated in the range of 100-105 ℃. Sample masses were monitored daily during the heating process. Once the mass difference rate (D) stabilized over the course of 3-7 days, this was taken to mean that the water in the pores of the HCP fragments was evaporated. After the evaporation process, the porosities of fragments were calculated through Eq. 3-5:

$$\mathrm{P} = \frac{M_{before\ heating} - M_{after\ heating}}{M_{before\ heating}}, \qquad \textbf{Eq. 3-5}$$

where P is the porosity of cement, $M_{before\ heating}$ is the mass of the fragment before heating, $M_{after\ heating}$ is the mass of fragment after it stopped losing water.

3.11 MMA Tests with Electrodeposit on Rebar

In this study, 1018-steel-reinforced HCP specimens (2-inch-high) were subjected to electrodeposition (ED) treatments and MMA polymerization treatments. The MMA dosage requirement was calculated in Appendix C. These treatments were conducted at selected corrosion potentials and treatment concentrations of alkaline species (Na^+, K^+, Ca^{++}). Some HCP specimens were treated electrochemically in various alkaline solutions to achieve deposition of sacrificial ceramic coatings on the rebar. The sacrificial ceramic coating was intended to protect the rebar in the MMA treatment. There were two batches of HCP specimens (3-month-old and 1-week-old) that were subjected to treatments. A listing of these two batches is shown in Table 3-7. Each group had 5 specimens. Groups

Table 3-7: Treatment conditions applied to specimens in 3-month and 1-week batches

Age of Batch	Specimen Group No.	Corrosion Potential (V)	Alkaline Species (Na^+, K^+, Ca^{++}) (mol/L)	Time of Electrodeposition Treatment (Days)	Time of MMA Treatment (Days)
3-Month	1	3.50	N/A	N/A	8
	2	1.75	1	8	8
	3	3.50	1	8	8
	4	3.50	3	8	8
	5*	N/A	N/A	N/A	N/A
1-Week	6	3.50	N/A	N/A	8
	7*	N/A	N/A	N/A	N/A

***** Control specimens were not subjected to any treatment.

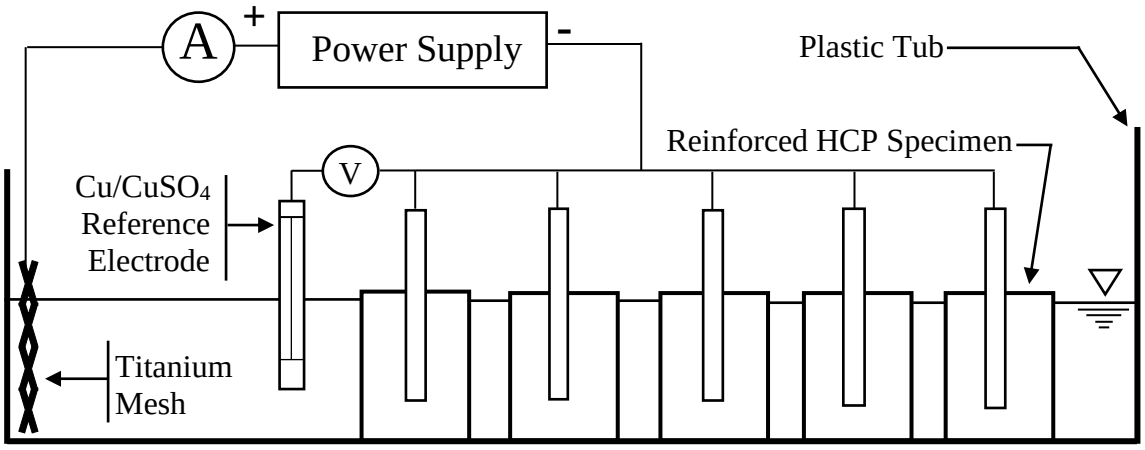

Figure 3-9: Setup of ceramic electrodeposition (ED) treatment.

1 and 6 were only subjected to MMA treatment while at 3.50 V corrosion potential. Groups 2, 3 and 4 were subjected to electrodeposition treatments and MMA treatments at various concentrations of alkaline species and corrosion potentials. Groups 5 and 7 were stored in the lime water (2 g/L calcium hydroxide). The setup of the ED treatment is shown in Figure 3-9. The solution contained concentrations of sodium hydroxide, potassium hydroxide, and calcium hydroxide as noted in Table 3-6. Titanium mesh was located all along the entire inside wall of the plastic tub.

Groups 2, 3 and 4 had 8-day electrodeposition treatments prior to 8-day MMA polymerization treatments. The concentrations of alkaline species in the electrodeposition treatment and the applied corrosion potentials are shown in Table 3-7. The current density in each treatment was not allowed to exceed 1 A/m^2 to avoid cement damage. MMA treatment was conducted after the electrodeposition treatments. Figure 3-10 shows the MMA treatment setup. The MMA monomer dosage and DI-water were added daily into the solution to maintain constant concentrations during treatment. During the

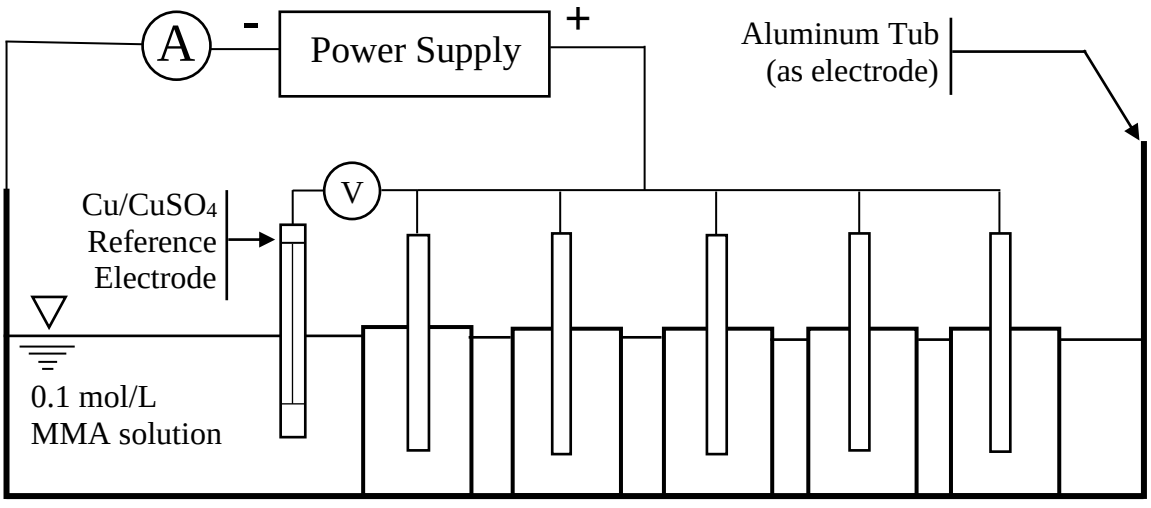

Figure 3-10: Setup of MMA polymerization treatment.

ceramic and MMA treatments, the electric current, applied voltage, and corrosion potential were monitored daily. After the treatments, treated and untreated HCP specimens were subjected to tensile strength and porosity tests. The tub composition was later changed to steel or glass in order to avoid aluminum degradation.

3.12 MMA Tests with Small Corrosion Potentials

It was calculated in the potentiodynamic polarization test (described in Section 3.5) that the trans passive turning point was +0.57 V. After some analysis of the uncertainty, a relatively safe lower limit was selected at +0.49 V. In the MMA treatments, the solution contained 0.15 mol/L of MMA monomer and 2 g/L of calcium hydroxide. The corrosion potentials were maintained for the four trials shown in Table 3-8. MMA dosage requirements were calculated as shown in Appendix F.

Table 3-8: Corrosion potentials utilized for MMA treatments of steel reinforced HCP (3-inch-high specimens).

Trial	Age of Batch (days)	Maintained Corrosion Potential (V)
1	32	0.57
2	34	0.57
3	72	0.57
4	41	0.49

The setup of MMA polymerization treatment was similar to the setup in Figure 3-10. The aluminum tub was replaced by a stainless-steel tub since the calcium hydroxide was causing aluminum corrosion. The treatment time was ten days. The MMA monomer was dosed to the solution every two days. Each trial had twelve steel-reinforced HCP

specimens (3-inch-high). Six of the specimens were controls that were cured in lime water. The other six specimens were subjected to MMA treatment. During the MMA treatments, the electric current, applied voltage, and corrosion potential were monitored daily. After the MMA treatments, the treated and untreated HCP specimens were subjected to tensile strength tests and porosity tests. Subsequently, the fragments of HCP specimens were ground with a mortar and pestle until the specimen powder was fine enough to pass through a No. 80 sieve. About 30 g of specimen powder was collected, soaked in a sealed container of 40 ml, high-purity, acetone (99.7%) for 24 hours to dissolve the PMMA polymer. Subsequently, the acetone liquid was centrifuged for 20 minutes to separate any undissolved HCP powder. If any HCP powder was still visible in the acetone liquid, the same centrifuging process was repeated. After centrifuging, the acetone liquid was evaporated in an oven at 80 ℃ for 24 hours. The residue from the acetone liquid was characterized by FTIR.

3.13 Reproducibility Check on MMA Treatment

Previous tests did not exhibit satisfying results on tensile strength. The Nayeem's experiment was repeated to reproduce results [60]. Two trials were conducted. MMA dosage requirement was calculated in Appendix G. The treatment solution in Trial NSR was not replaced during the MMA treatment, but the MMA monomer dosage was added daily. In Trial DSR, the solution and dosage were replaced daily during the MMA treatment. Each trial had twelve titanium-wire-reinforced HCP specimens (3-inch-high) which were stored in lime water for 28 days before MMA treatment. In each trial, six samples were treated separately in 0.1 mol/L MMA solution as shown in Figure 3-11. The other six samples were stored in lime water. Each HCP sample was treated with an

individually dedicated power supply. Each specimen was provided with a current density that was set at 1 A/m^2 on the first day as controlled by a constant direct current voltage. These currents and applied voltages were monitored and adjusted daily in the event of voltage drift. The pH values of the solution for each MMA-treated HCP specimen were monitored daily during the MMA treatments. The treatment solutions of Specimens 1-3 in Trials NSR and DSR were subjected to the pH value monitoring test. After the treatments, all the treated and untreated HCP specimens from two trials were subjected to indirect tensile strength testing and porosity measurement. Subsequently, the fragments were subjected to the same PMMA characterization test described in Section 3.12.

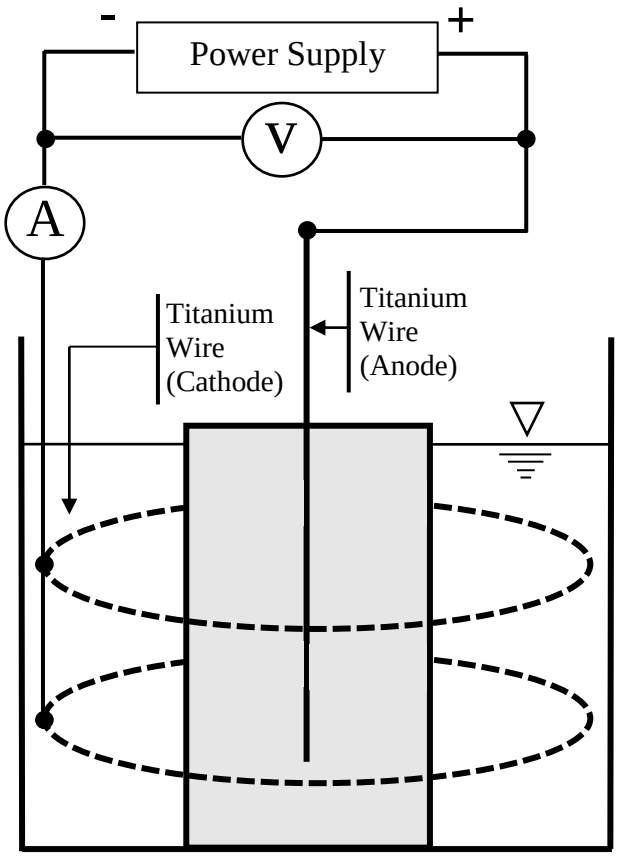

Figure 3-11: The setup of preliminary MMA treatment of HCP to establish reproducibility of prior work.

3.14 Electro-initiated Polymerization of MMA in HCP

In the current study, PMMA was produced using potassium persulfate ($K_2S_2O_8$) in a beaker solution, which was described earlier in Section 3.4. For enhancing HCP, four trials of MMA treatment applied to HCP samples (4-inch-high) were conducted. These trials were designed to transport monomer and persulfate ions into the HCP and to polymerize PMMA particles within the HCP pores. The treatment application schemes of each trial are shown in Table 3-9. The requirements of MMA dosage and applied potential were calculated in Appendix H.

Table 3-9: Transport process cycle parameters for application of $K_2S_2O_8$ in MMA electro-initiated polymerization treatment. The applied voltage was ±6.0 V.

Trial	$K_2S_2O_8$ Concentration (mol/L)	Cyclic Attract Time* (hours)	Cyclic Extract Time* (hours)	Polarity Reversal Cycles in 48-hour Segment
1	0.01	4	3.5	6
2	0.01	4	3.5	6
3	0.01	4	8	1
4	0.004	4	8	1

***** Each cycle "Attract and Extract" times are defined in Figure 3-12.

Each trial had 12 titanium-wire-embedded specimens as illustrated in Figure 3-7. Six companion control specimens were cured in lime water. The others were treated in 0.1 mol/L MMA solution with the persulfate initiator as prescribed in Table 3-9. The 10-day MMA treatment was divided into five, 48-hour segments at an applied voltage of ±6.0 V. The treatment solution was replaced every 48-hour segment.

As is shown in Figure 3-12, Trial 1 and 2 had six polarity reversal cycles in a 48-hour segment. Each polarity cycle contained a 4-hour attracting and a 3.5-hour extracting process aimed at controlling sulfate residence time within the HCP. During the attracting process, the central Ti-wires were set as the anode (+6.0 V) to attract persulfate ions and MMA monomers into the HCP pores. During the extracting process, the central Ti-wires were set as the cathode (-6.0 V) to initiate polymerization (as described in Section 2.3) and extract sulfate ions out of the HCP pores. The last 3 hours were used to keep the initiator in the HCP pores.

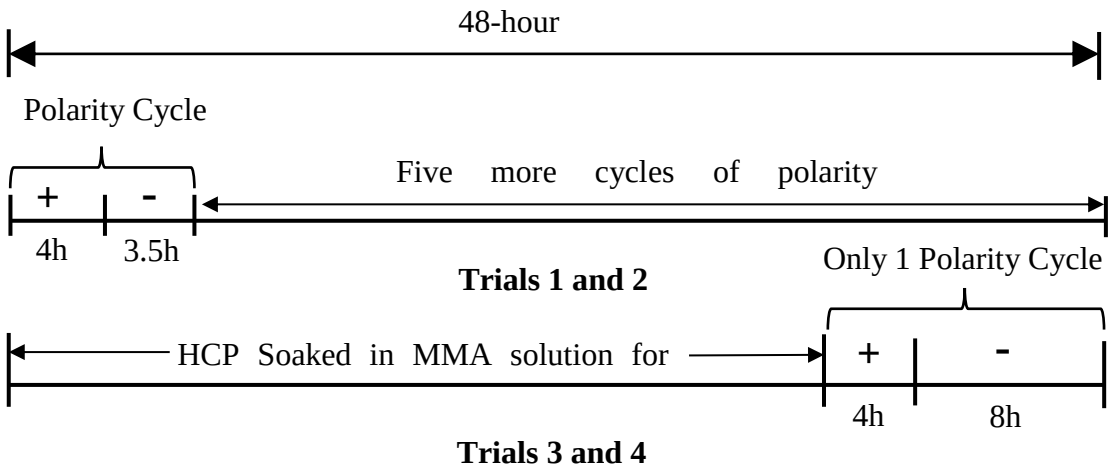

Figure 3-12: Treatment cycle timelines.

In order to avoid sulfate attack of the HCP, Trials 3 and 4 were designed to have a low sulfate residence time or a low persulfate concentration in the HCP pores. The treated HCP specimens in Trials 3 and 4 were soaked in the MMA solution (with no initiator or applied potential) during the first 36 hours of the 48-hour segment. Subsequently, the specimens were subjected to 4-hour (+6.0 V) persulfate attracting and 8-hour (-6.0 V) sulfate extracting processes (see Figure 3-12).

The electric circuit for controlling polarity reversals of the applied potentials is shown in Figure 3-13. The electromagnetic relay (described in Section 3.1) used to control two switches required a working DC voltage of 10 V. The Relay Power was the power supply for charging the electromagnetic relay, and the E-chem Power was the power supply for charging the MMA treatment. The timer controlled the relay on or off at the designed time. As shown in Figure 3-13, when the relay power supply was on, both switches were at position "1", and the central Ti-wires were charged anodically to attract persulfate ions and MMA monomers. When the relay power supply was off, the switches bounced to position "2" and the central Ti-wires were charged cathodically to extract negatively charged species out of the HCP pores. Figure 3-14 shows the setup of the electro-initiated polymerization treatment on the six HCP samples of a given trial. Titanium meshes were all wired to a single node, and the titanium wires in the HCP were wired to another single node. After treatment, all the HCP specimens were subjected to tensile strength tests and porosity tests.

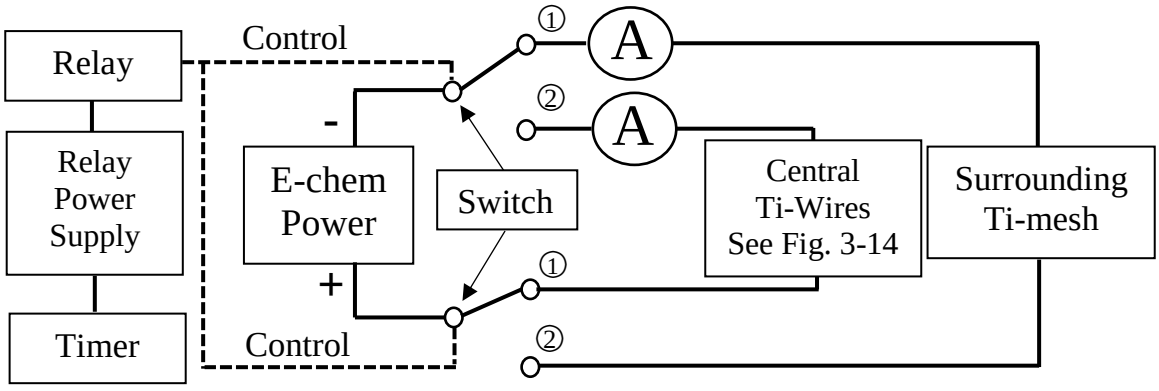

Figure 3-13: Electric circuit for applying treatment polarity reversal cycles as defined in Figure 3-12.

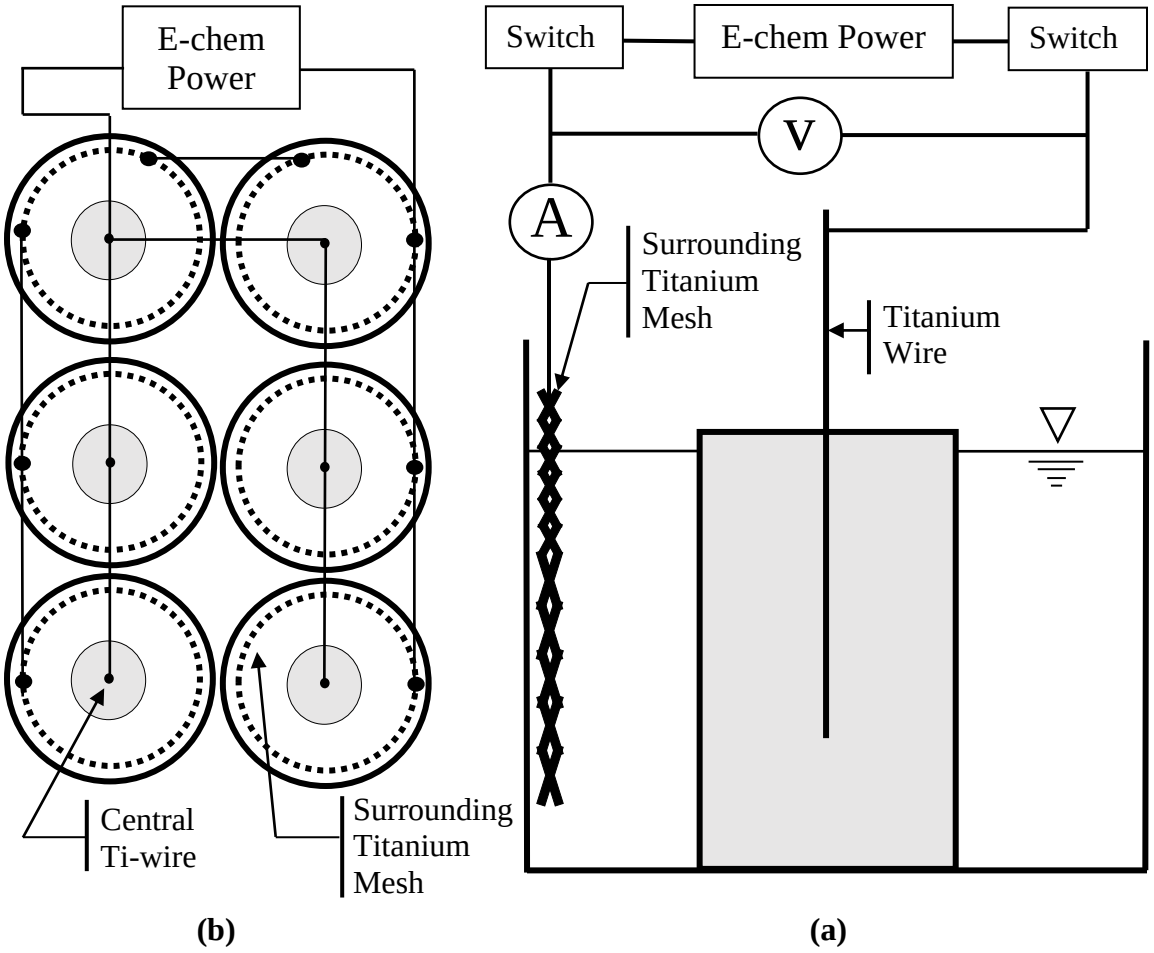

Figure 3-14: (a) The setup of the electro-initiated polymerization treatment of HCP specimens immersed in MMA solution. (b) Wiring scheme of six specimens subjected to the same applied voltage. Each specimen was treated in separate beakers.

After each 48-hour segment of the MMA treatment, approximately 50 ml of treated solution was collected from each beaker, and the mass of the solution sample was measured. These six solution samples were placed in an oven at 80°C for 24 hours to evaporate the water. After evaporation, the mass of the solid sample in the evaporation dish was measured. This solid mass was used to help estimate the resultant PMMA mass in the solution and in the MMA-treated HCP specimens following treatments. These

estimated calculations are presented in Section 4.7.6. This PMMA mass estimation was conducted for Trials 1-4.

Following treatment, selected specimens were evaluated to test to sulfate content. Fragments of HCP specimens were ground with a mortar and pestle until the specimen powder was fine enough to pass through a No. 80 sieve. Four grams of powder were collected from the HCP specimens and subjected to energy dispersive x-ray fluorescence (EDXRF) for the elemental characterization analysis. After obtaining the histogram, the signal intensity of the sulfur element was recorded. Each Trial had 12 specimens (6 control and 6 treated). Each specimen was tested 5 times. The average signal intensity of the elemental sulfur was calculated. Subsequently, the powder was subjected to the PMMA characterization test that was described in Section 3.12.

CHAPTER 4

RESULTS AND DISCUSSION

In this chapter, Section 4.1 discusses the results of the electro-polymerization proof of concept test of electro-polymerization in the aqueous system. Section 4.4 discusses the results of potentiodynamic polarization of 1018 steel. Section 4.2 discusses the results of electro-deposition and anodic polarization applied to the 1018 steel bars. Other sections discuss the results of MMA treatments on the HCP specimens with titanium wires (Ti-wire) embedded or 1018 steel bars reinforced.

4.1 Electropolymerization Proof of Concept Tests

This portion of the study investigated electropolymerization in a beaker. The intension was to apply lessons learned in this simple fluid system to the HCP system. Figure 4-1 shows the average masses of Ti-wire anode from Trials 1-5 following anodic charging in MMA fluid as described in Section 3.3.1. All the raw data in this section are listed in Appendix B. The average masses from Trials 1, and 5 were slightly lower than the average untreated mass.

It was possible that the Ti-wire had some amount of material dissolving in the methyl methacrylate (MMA) solution when it was anodically charged. After these Trials, no deposit was observed on the Ti-wire. Also, the nearly unchanged average masses reflected the fact that methyl methacrylate monomer did not polymerize on the surface of

the Ti-wire. Furthermore, the treated solution was clear and had a strong MMA smell, which indicated that the polymerization of MMA was not initiated.

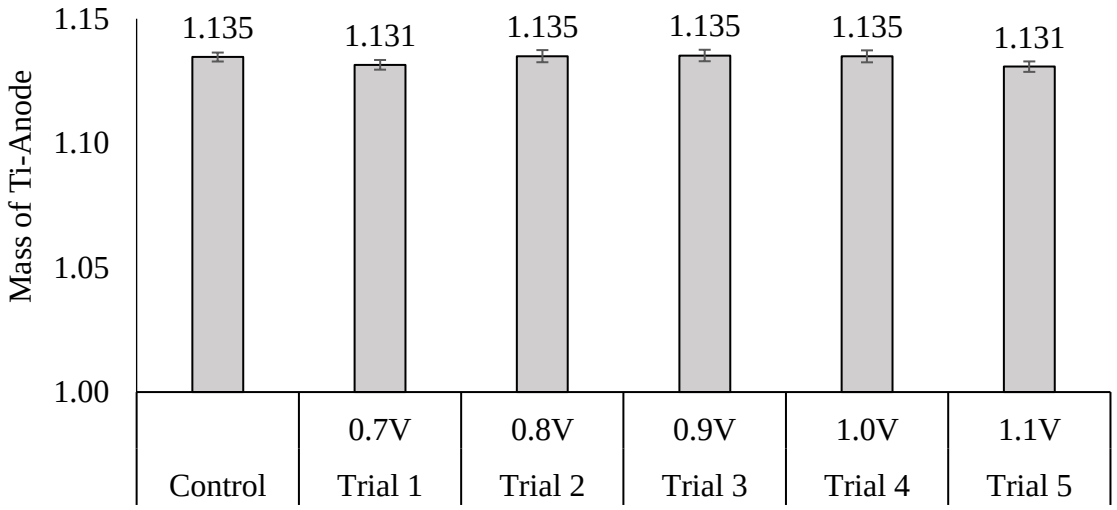

Figure 4-1: Titanium wire was charged anodically in a 0.1 mol/L MMA beaker test solution. The corrosion potential ranged from 0.7 V to 1.1 V. Treatment time was 10 minutes. After testing, the mass of the Ti-wire was measured.

Figure 4-2 shows the average masses of the Ti-wire anode from Trials 6 and 7 which involved highly acidic conditions as described in Section 3.3.1. The ending masses of the treated Ti-wire were 1.132 g and 1.131 g when the concentrations of hydrochloric acid were 0.2 mol/L (pH = 0.7) and 0.4 mol/L (pH = 0.4), respectively. After these 10-minute treatments, no deposits were observed on the Ti-wire or in the treated solutions.

The loss of mass was attributed to the strong acid, and the anodic polarization corroded the surface components of the Ti-wire. Also, the clear treated solution had a strong MMA odor after treatments, which indicated the MMA monomers did not polymerize. The literature indicated that the reduction of the hydrogen ions helped to initiate the polymerization of MMA [92] [100] [90]. However, the efficiency of the initiation was limited by the treatment time, half-life of initiator, and the concentrations

of the initiators and MMA. Ten minutes obviously were not enough for the completion of the polymerization of MMA in Trials 6 and 7.

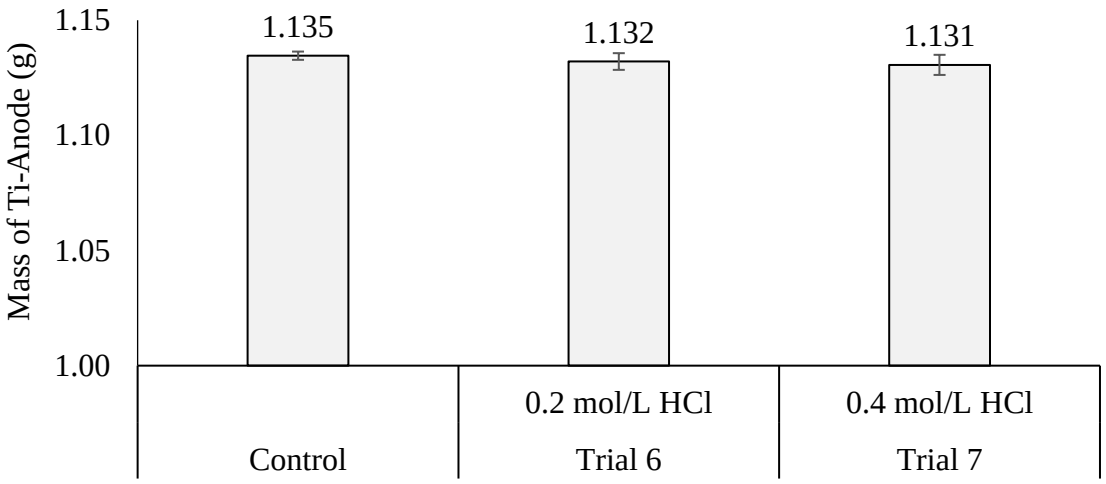

Figure 4-2: Anodic polarization treatment beaker test solution contained 0.1 mol/L MMA and hydrochloric acid. Concentrations of HCl in the two tests were 0.2 mol/L and 0.4 mol/L. The mass of Ti-wire was measured after each test. Each column represents five trials.

Trials 1-11 were conducted to examine the impact of the initiator and the treatment time. In Trials 1-7 which were conducted over a span of 10 minutes (with no initiator species present) exhibited no deposits. Trials 8-10 (spanning over 24 hours) were conducted to polymerize MMA with the use of potassium persulfate in a beaker as described in Section 3.3.1. Trial 11 was conducted to polymerize MMA without potassium persulfate (also in a 24-hour period). It was observed that, after Trials 8-9, the treated solution had white, micro-size deposits floating in the liquid. More white deposits were produced in Trial 10 as observed at the bottom of the beaker. The treated MMA solution in Trial 11 exhibited no deposits. A strong MMA odor from the treated solution of Trial 11 was detected. When the mass ratio of MMA monomer and potassium

persulfate was 10:1 (Trial 8 and 9), the yield of poly(methyl methacrylate) (PMMA) was approximately 1000% greater than that from Trial 10 when the ratio was 1000:1.

After the separation, purification, and evaporation of deposits from Trials 8-10 (described in Section 3.3) these materials were characterized by Attenuated Total Reflectance – Fourier Transform Infrared Spectroscopy (ATR). Figure 4-3 shows the ATR analysis of the white deposits, standard PMMA, and MMA monomer. The black

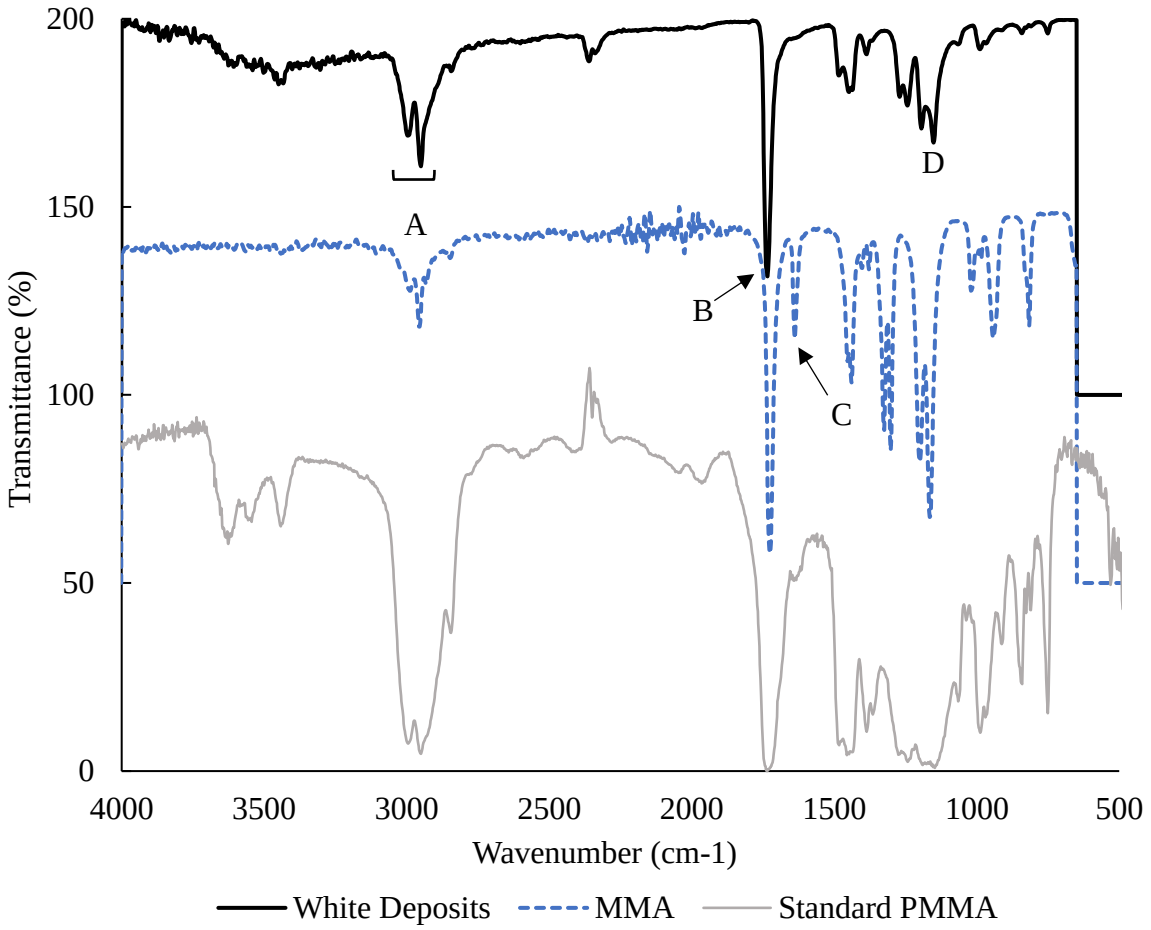

Figure 4-3: ATR analysis of MMA monomer, standard PMMA and the white deposits from beaker test trials 8-10. Peak identification: A. The C-H stretch, 2950 cm^{-1} [107]. B. The C=O stretch, 1762 cm^{-1}. C. The C=C stretch, 1640 cm^{-1}. D. The C-C(=O)-O stretch, 1164 cm^{-1}. It should be noted that the transmittances of spectrums of MMA and white deposits would need to be reduced by 50% and 100%, respectively, to obtain the exact transmittances for these trials.

line is the ATR analysis of the white deposits. The gray-dashed line is the MMA monomer. The gray line is the standard PMMA samples manufactured by Matheson Coleman and Bell, Norwood, OH.

The ATR analysis of these three samples had the three identical strong peaks which represented the C-H bond stretch (Peak A) at 2900-3100 cm^{-1} [107],], the C=O bond stretch (Peak B) at 1700-1800 cm^{-1} and the C-O bond stretch (Peak D) at 1000-1300 cm^{-1}. Also, the white sample and the MMA monomer had an identical medium peak at the wavenumber of 1164 cm^{-1}, which correlates to the stretch of the C-C(=O)-O molecular structure. Furthermore, The MMA monomer and standard PMMA both had a medium-strong peak at a wavenumber of 1640 cm^{-1}, which indicated that they had significant C=C bond. The white-deposits graph did not show a peak indicating the presence of carbon double bonds, so the white deposits were apparently saturated organic compounds. These four transmittance peaks A-D in Figure 4-3 indicated that the white deposits were chemically similar to PMMA.

It was found in the literature that the disproportionation (polymer contains significant C=C bonds as described in Section 2.2.2) was predominant in the termination of polymerization at 25 ℃ [71]. Apparently, a long treatment time (24 hours) helped to produce sufficient radicals (SO_4*, eq.2-23) to break the C=C bonds and re-initiate the terminated polymers. Therefore, the results from Trials 8-10 appeared to show that the MMA monomer could electropolymerize in the presence of potassium persulfate (initiator). It was possible that if the sufficient time was provided in Trials 6-7 (these were the only acidic environment trials), the hydrogen ions would possibly be able to initiate the polymerization of MMA. It also demonstrated that adequate initiator content

could overcome the inhibition provided by mequinol, which is one of the inhibitors that is packed into MMA liquids for shipping. Without the potassium persulfate initiator, the electricity alone was unable to initiate polymerization in trials involving Ti-wire and near-neutral solutions (Trials 1-5).

4.2 Protective Electrodeposits and Anodic Polarization on 1018 Steel Bars

In this section, the electrodeposition of alkaline metals on 1018 steel bars was examined. The protective capacity of these alkali-metal films was evaluated using anodic polarization. The estimated corrosion area of the steel samples was presented. The corrosion currents, the corrosion potentials, and the calculated coulombs of the charge's passage were also examined. After the electrodeposition of alkali-metal-ceramic coating, coated samples were examined by FESEM and analyzed by Energy Dispersive X-ray Spectroscopy (EDS). All the images of the samples and monitored data are presented in Appendix C.

4.2.1 Electrodeposition (ED) Mechanism

Figure 4-4 shows the important reactions that were anticipated at the cathode and anode during the electrodeposition treatment. It was observed that both the anode and cathode exhibited bubble formation. At the anode (Ti-mesh), the hydroxide ions were expected to lose electrons and produce oxygen gas and water according to the reaction:

$$4OH^- - 4e^- \rightarrow O_2(\uparrow) + 2H_2O\ , \qquad \textbf{Eq. 4-1}$$

At the cathode (1018 steel rod), it was anticipated that sodium, potassium, and calcium ions could be reduced to pure sodium, potassium and calcium as follows:

$$Na^+ + e^- \rightarrow Na\ , \qquad \textbf{Eq. 4-2}$$

$$K^+ + e^- \rightarrow K\,, \qquad \textbf{Eq. 4-3}$$

$$Ca^{++} + 2e^- \rightarrow Ca\,. \qquad \textbf{Eq. 4-4}$$

An additional electrolysis reaction:

$$2H_2O + 2e^- \rightarrow 2OH^- + H_2(\uparrow) \qquad \textbf{Eq. 4-5}$$

was also anticipated. In a high pH environment (pH > 13), the corrosion potential (EMF) vs. standard hydrogen electrode (SHE) for the occurrence of Eq. 4-5 is -0.828 V. After converting this voltage as per Table 2-12, the EMF vs. the copper/copper sulfate

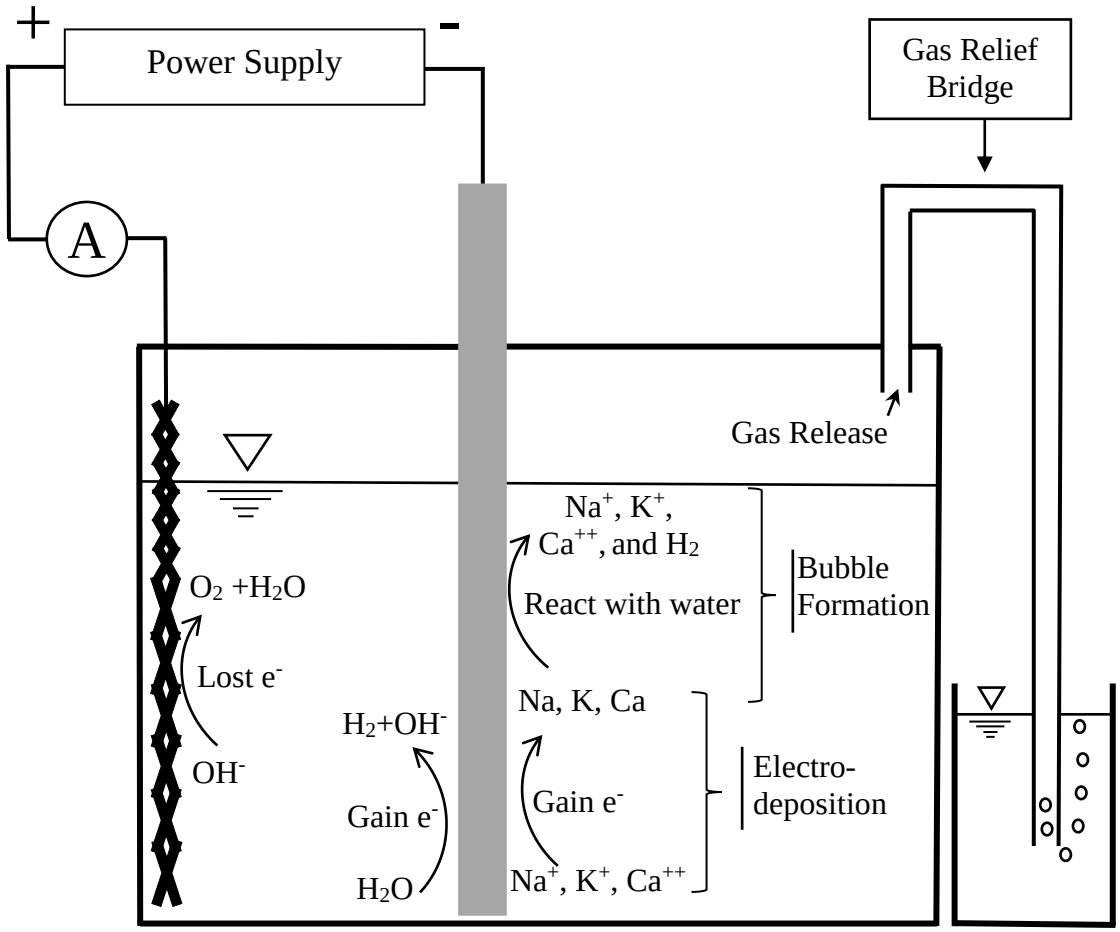

Figure 4-4: The reactions of electrodeposition at the cathode and the oxidization at the anode in simulated pore fluid.

reference electrode (CSE) is -1.144 V. Apparently, the EMF vs. CSE (-3.50 V) during the ED treatment was significantly more negative than -1.144 V and -3.174 V (K^++e = K). The water electrolysis and the reductions of K^+, Na^+, and Ca^{2+} shown in equations 4-2 to 4-5 are thus considered very likely to occur. Furthermore, the EMF vs. SHE for the occurrence of Eq. 4-1 is +0.6 V (+0.284 V vs. CSE), which is lower than the EMF during the ED treatment. This indicated the occurrence of Eq. 4-1, too.

Pure sodium, potassium, and calcium tend to be very active metals. For this reason, they tend to react rapidly with water to produce sodium hydroxide, potassium hydroxide, calcium hydroxide, and hydrogen as follows:

$$2Na + 2H_2O \rightarrow 2Na^+ + OH^- + H_2(\uparrow)\,, \qquad \textbf{Eq. 4-6}$$

$$2K + 2H_2O \rightarrow 2K^+ + OH^- + H_2(\uparrow)\,, \qquad \textbf{Eq. 4-7}$$

$$Ca + 2H_2O \rightarrow Ca(OH)_2(cr) + H_2(\uparrow)\,, \qquad \textbf{Eq. 4-8}$$

Since sodium hydroxide and potassium hydroxide are highly soluble, they would be expected to ionize into sodium, potassium and hydroxide ions. Moreover, the simulated pore fluid was saturated with calcium hydroxide, so the calcium hydroxide produced would tend not to dissolve and thus form the discrete electrodeposits at the cathode. The following electrolysis equation (shown in eq.4-9) can be obtained by combining the equations from Eq. 4-1 to Eq. 4-8:

$$Ca^{2+} + 2OH^- + H_2O \xrightarrow{\substack{Alkaline\ Species,\\ and\ Electricity}} O_2(\uparrow) + 2H_2(\uparrow) + Ca(OH)_2(cr)\,, \qquad \textbf{Eq. 4-9}$$

In the SPF solution, the sodium and potassium ions were not significantly depleted by an ED treatment conducted by Bahman Horri *et al*. [127]. Similarly, in the current work, the

calcium ions were depleted from the solution as they formed white deposits on the surface of the steel rod.

4.2.2 Corroded Area Analysis

After the steel was alkali-metal coated, the polarity was reversed to see the extent to which this coating protected the steel from corrosion while it was anodically charged. After the anodic polarization tests, images of steel bars were used for corrosion area estimation. Figure 4-5 shows sample images of bars after the electrodeposition treatment (left) and the anodic polarization tests (right). The right pair of images in Figure 4-5 was the raw images which were transformed into grayscale images in Figure 4-6. Every pixel in a raw image consists of three independent primary colors: red, green and blue. The degree of each primary color ranges from 0 to 255. These three colors can be transformed

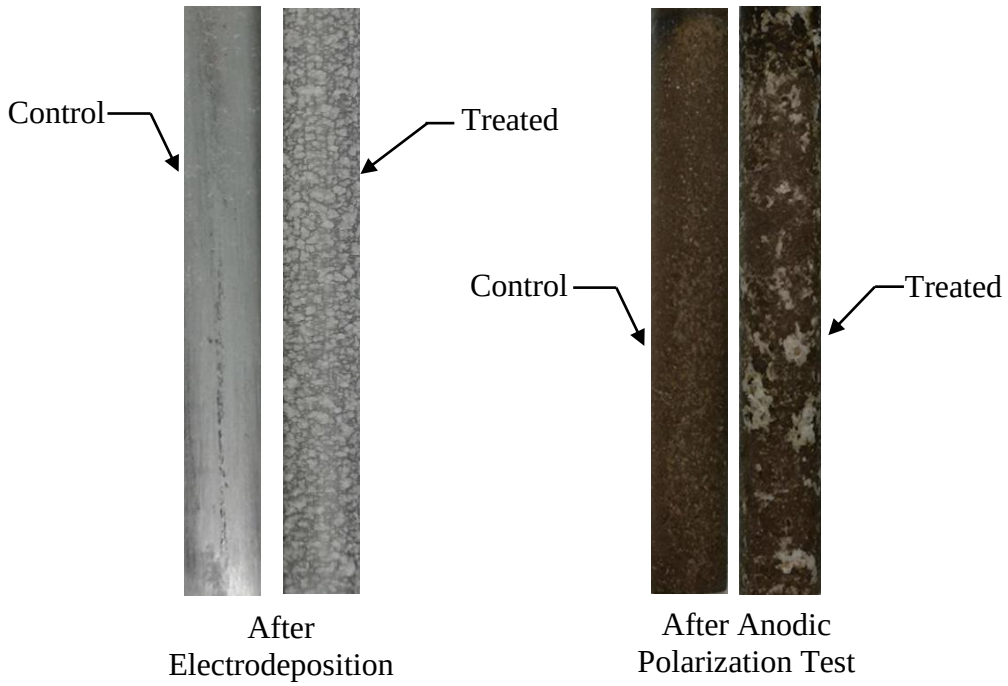

Figure 4-5: The corrosion area analysis image example (Trial 2) from anodic polarization tests. The left pair of images is the bars after the electrodeposition treatment. The right pair of images is the bars after the anodic polarization tests.

into a simple image parameter that is referred to as the gray level. The transformation of these colors to a gray level is given by [128]:

$$Gray\ Level = 0.2989 \cdot Red + 0.587 \cdot Green + 0.114 \cdot Blue\ , \qquad \textbf{Eq. 4-10}$$

where the Gray level is the degree of gray in a pixel after the gray-level transformation, Red is the degree (also known as intensity or brightness) of primary red, Green is the degree of primary green, and Blue is the degree of primary blue. The degree of color may range from 0 to 255. After the gray-level transformation, the grayscale versions of the original images were obtained as illustrated the example in Figure 4-6.

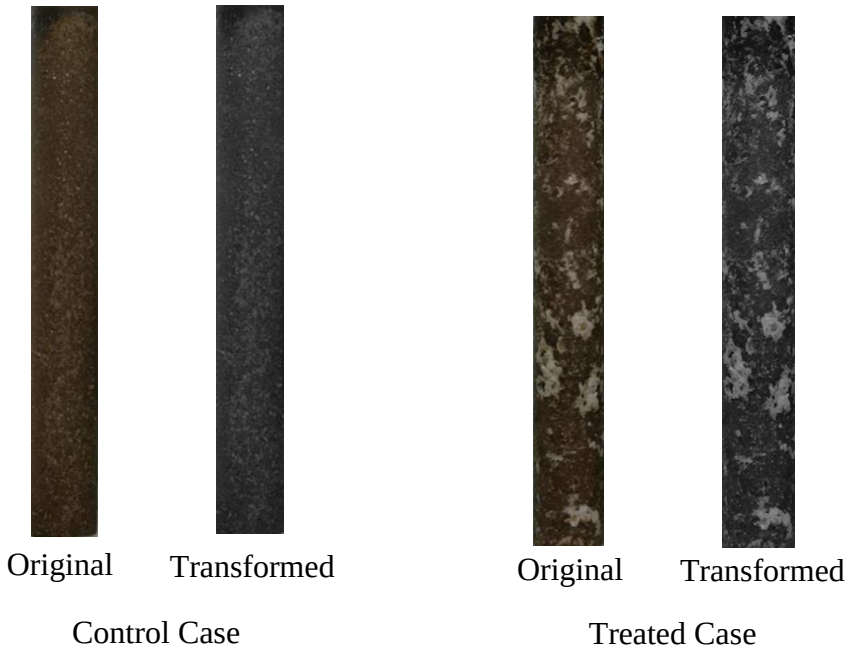

Figure 4-6: The gray-level transformed images of control and treated bars from electrodeposition followed by anodic polarization (Trial 2).

After counting the number of pixels at each gray level in the grayscale images, the histograms of the images were compared as shown in Figure 4-7. In the histogram of a completely corroded control bar (100% surface-corroded) in Figure 4-7, a threshold was

selected at the gray level of 81 to distinguish between a corroded and un-corroded area. Each pixel represented an element of the steel area. When the gray level of pixel in the grayscale image was lower than 81, this pixel represented a corroded area. In Figure 4-7 (left side), 99% of the pixels were lower than the gray level of 81, which correlated to 99% of the area of the control bar being corroded. The same threshold (level 81) with the control bar was applied in the histogram analysis of the treated steel bar shown in Figure 4-7 (right). It was obtained in this particular case that 83.7% of the area was corroded.

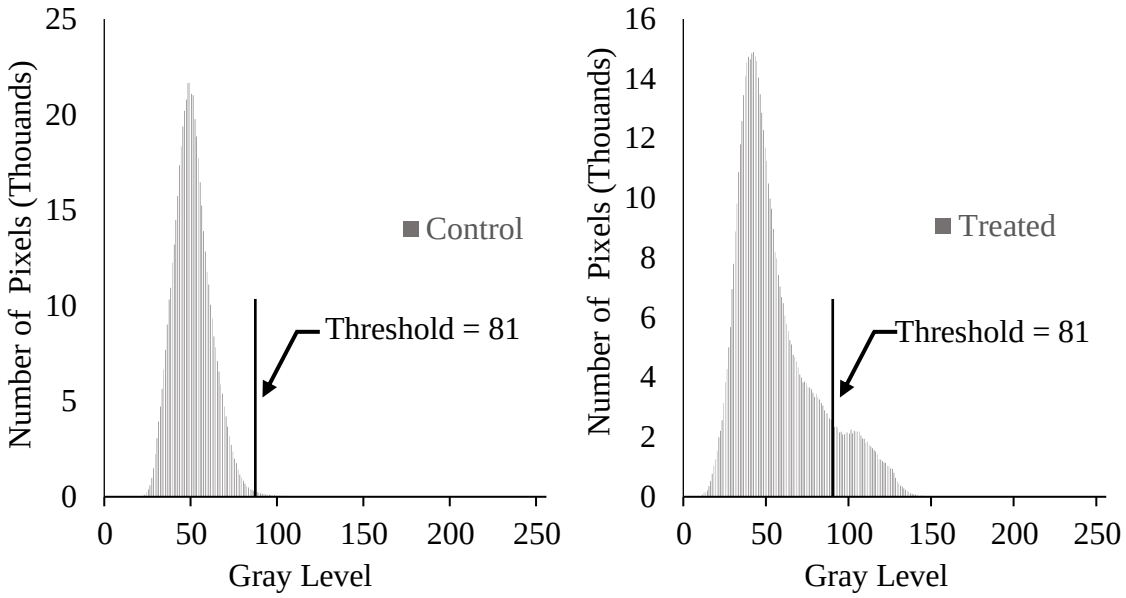

Figure 4-7: Grayscale histograms of the control bar's grayscale image (Left) and the treated bar's grayscale image (right). These bars are shown in Figure 4-6 and Figure 4-8.

The problem with a grayscale analysis was that it yielded an image that did not give a clear visual indication of the relative amount of corrosion present on a surface. This was remedied by transforming the gray scale image to a binary (black and white) image in which black is the corroded area and white is the un-corroded area shown in Figure 4-8. In Figure 4-6 (treated case), the white area was the un-corroded area and the

brown area was the corroded area. When the threshold was more than 81, the binary image of the treated steel bar in Figure 4-8 showed a corroded area which was visually bigger than the real corroded area shown in Figure 4-6. At the gray level of 81, the binary image of the control steel bar in Figure 4-8 exhibited 99% of the corroded area. Meanwhile, the binary image of the treated steel bar in Figure 4-8 was the most similar to the real image in Figure 4-6. Therefore, the threshold which caused the control bar exhibited 99% corroded area was applied in Trials 1-4.

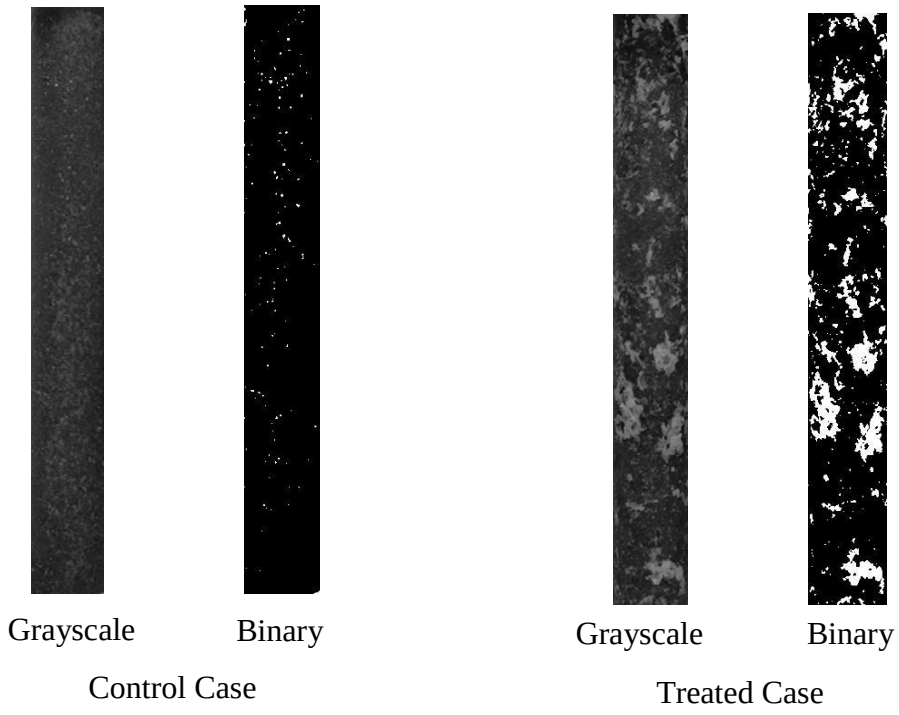

Figure 4-8: The grayscale images of the bars in Figure 4-6 were transformed into binary images which more clearly show the corroded (black) and un-corroded (white) areas.

The estimated corroded area from other trials (Excluding Trials 5 and 6) was calculated based on the same procedure, and the results are shown in Figure 4-9. At Day 10 of Trials 5 and 6, it was observed that a significantly black electrodeposition which were possibly magnetite on the treated and control steel bars. The black electrodeposition

was shown in Figure C-2 (Appendix C), and it was unable to analyze the corroded area, so Trial 5 and 6 were excluded from the estimation of the corroded area. Moreover, it was observed that the surfaces of the control steel bars in the AP test were covered thoroughly by a brown coating (Fe_2O_3) after Days 8 and 9. Meanwhile, the treated steel bars only had part of their areas corroded. This indicated the electrodeposits appeared to protect the steel bars from some of the corrosion that occurred during the anodic polarization.

Therefore, when the threshold of the control image for the corroded area was set at 99%, the average estimation of all the treated samples in this study was found to be 88%. The electrodeposits reduced the corrosion of the steel bars by approximately 12% during the anodic polarization (AP) tests (see Figure 4-9).

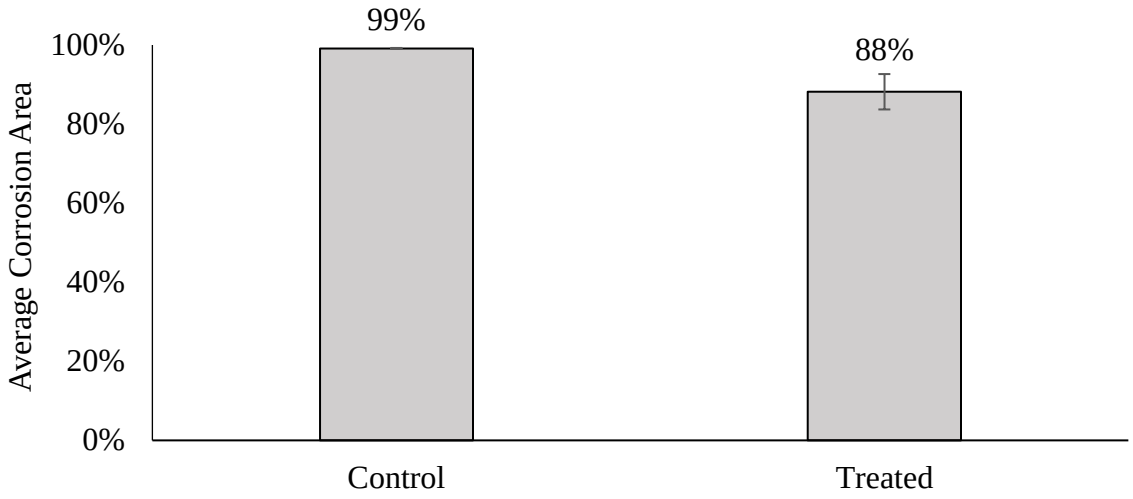

Figure 4-9: The Average Corrosion Area of the 1018 Steel Bars after the Anodic Polarization Tests.

4.2.3 Average Current Analysis

Figure 4-10 shows the average current profile of six electrodeposition and anodic polarization Trials in 12 days. In the 7-day electrodeposition treatments, the average current dropped from 2.47 to 0.74 A. After Day 5, the decreasing trend tended to be slow. In the 5-day anodic polarization tests, both the control and the treated bars exhibited a rising current over Days 8-10. From Day 8 to 12, it was observed that the average current of the control bars increased from 1.36 to 1.90 A, and the average current of the treated bars increased from 0.35 to 1.84 A. The increasing trend of the average current of the control bars tended to be flat after Day 9. The trend of the treated bars tended to be flat after Day 11. It was observed that a significantly black electrodeposition (magnetite)

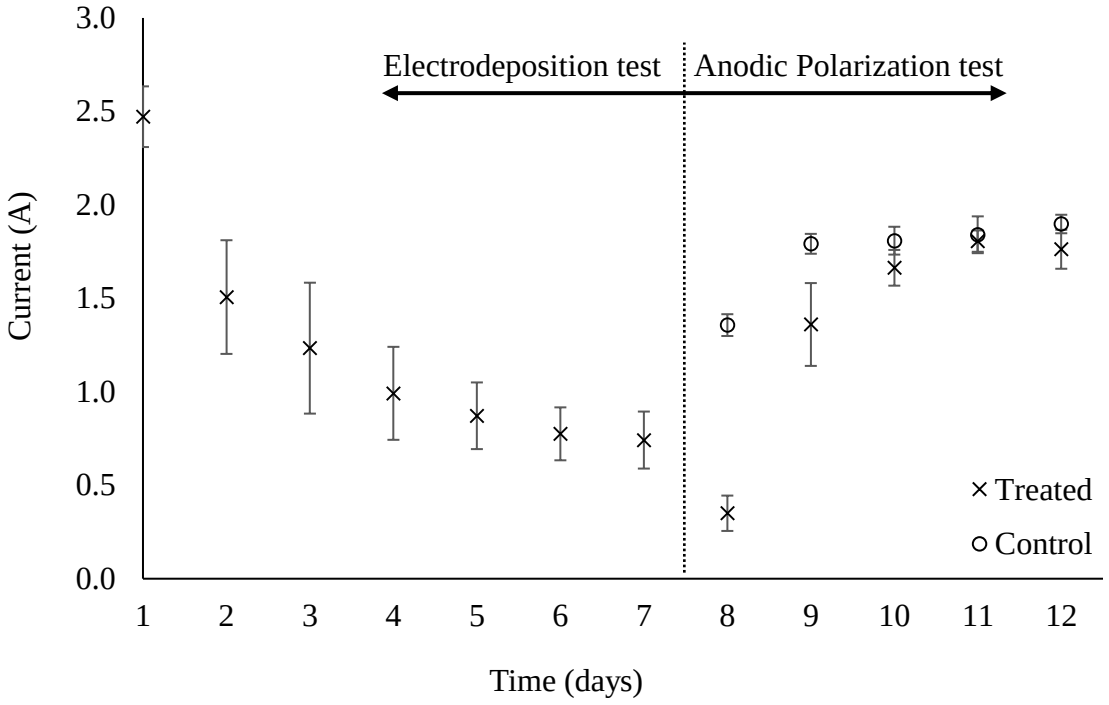

Figure 4-10: Current profile of electrodeposition and anodic polarization tests. The average current was monitored daily during the 12-day treatment period. Each point represents the average current of six trials. The control steel bars were subjected to anodic polarization only for five days. (1 A of the electric current correlated to 0.64 A/cm^2 of the current's density).

occurred on both the treated and the controlled samples in Trial 5 and 6. Also, the magnetite caused the currents in Trials 5 and 6 on Days 11 and 12 were significantly lower than the other trials. Therefore, the currents from Day 11 to 12 in Trial 5 and the currents at Day 12 in Trial 6 were excluded from the calculation of the average currents shown in Figure 4-10.

As shown in Figure 4-10, it was clear that the decreasing average currents in the 7-day electrodeposition treatments indicated that the surface of the treated bars was gradually covered by the white deposits shown in Figure 4-11. In Figure 4-11, some regions of the treated bars were not covered by the deposits. This may possibly be due to the white deposits exhibiting less conductivity than the steel. It was researched by Surplice [129] that the conductivity of calcium oxide was 10e-8 $w^{-1}cm^{-1}$, which was extremely lower than the conductivity of 1018 steel (6.29 × 10e4 w^{-1} cm^{-1}) [130]. As more treated areas became covered by electrodeposits, fewer areas would tend to be exposed to the alkaline solution. It would be anticipated that electrons from the power supply would tend to accumulate at these more-conductive regions because of their relative low resistance. Higher electron density at these regions may tend to cause the

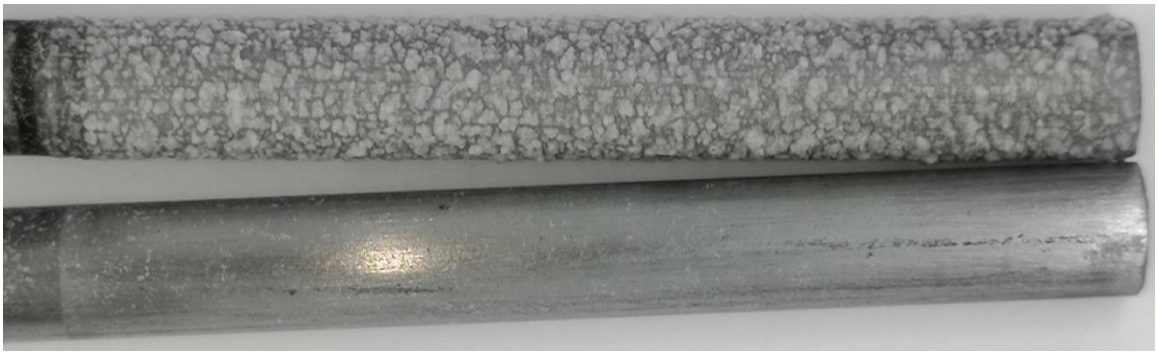

Figure 4-11: Image of treated steel bar (upper image) and control bar (lower image) after the electrodeposition treatment. The current and corrosion potential data for this example (Trial 2) is located in Appendix C, Tables C-1 and C-4.

localized reduction of sodium, potassium and calcium ions to become more intense.

Moreover, the concentrations of these cations would be expected to cause an increase in the production rate of hydrogen gas [127]. In the study about the generation of hydrogen gas using alkaline zinc hydroxide solution was conducted by Bahman Horri et al. Their study showed that the sodium and potassium ions acted as the catalyst to produce hydrogen gas at the cathode in the electrolysis system. When the sodium and potassium ions were 0.2 and 0.3 mol/L, respectively, the production rate of hydrogen gas peaked. The concentrations of Na^+ and K^+ (Shown in Table 3-4) in the electrodeposition treatment were very close to the concentrations which induced the highest production of hydrogen gas in Horri's study, so it was possible that the reductions of Na^+ and K^+ and bubble formation also reached the peaks. This increase of hydrogen gas could hinder the reduction of calcium ions so that a uniform coating could not be achieved.

It was observed in Figure 4-10 that the average current of the control bars at Day 8 was significantly lower than the average currents on other days. The origin of this spike may be due to the control bars being soaked in simulated pore fluid for 7 days. A thin layer of passive film may have formed on the surface of steel bars [131]. During the anodic polarization test, this passive film would tend to dissolve rapidly to form a rusty coating at Day 9. The average currents of the treated bars on Days 8, 9 and 10 were significantly lower than those of the control bars. This may be because the relatively high-resistance electrodeposition limited the treated bars from passing high current. Meanwhile, the active chemical compositions of the deposits, consisting of sodium, potassium, and calcium oxides, may have acted as a high-resistance barrier to protect the

bars. After the dissolution of the electrodeposits, the average currents of the treated bars were significantly increased and relatively close to the control bar values.

4.2.4 Corrosion Potentials Analysis

Figure 4-12 shows the average corrosion potentials of the treated and control bars before the electrodeposition treatments. The average corrosion potentials vs. the copper/copper sulfate reference electrode (CSE) of the controls and treated bars in simulated pore fluid (See Table 3-4) were -0.49 V and -0.50 V, respectively. It can be observed from the error bars in Figure 4-12 that the average corrosion potentials of two bars were not significantly different.

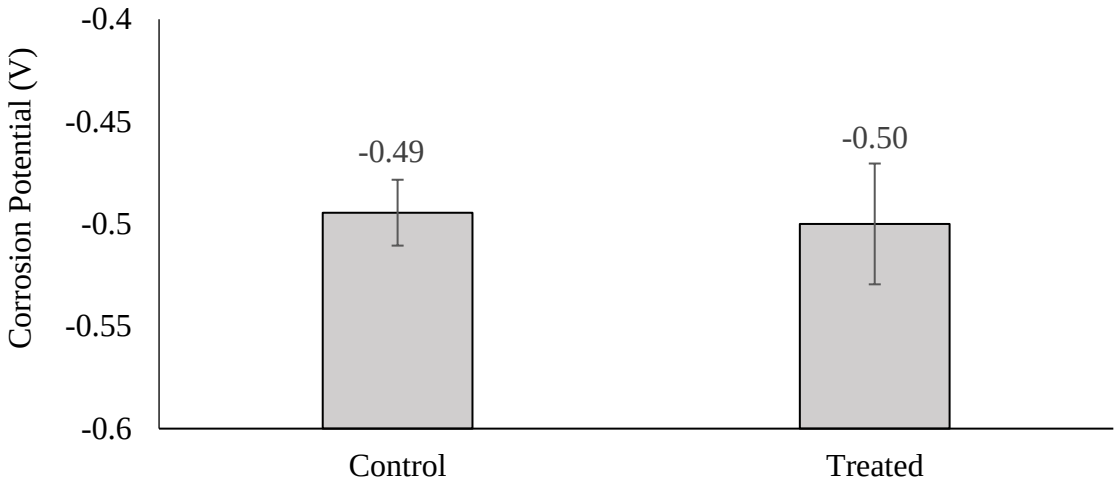

Figure 4-12: The corrosion potentials of the treated and control bars prior to electrodeposition treatments. Each point represents the average value of six trials. The error bars represent a 90% confidence interval.

Figure 4-13 shows the average corrosion potentials of the treated and control bars with respect to the CSE during the anodic polarization tests. Each point represents the average corrosion potential of six trials. The corrosion potential of the control bar in Trial 1 at Day 9 was unreasonably smaller than other values, so it was excluded. It is shown in

Figure 4-13 that the average corrosion potential of the control bars was -0.32 V at Day 8 and it stabilized around -0.8 V from Day 9 to 13. The average corrosion potentials of the treated bars were -0.57 V and -0.50 V at Days 8 and 9, respectively, and they arrived in the vicinity of -0.8 V by Day 10. At Day 13, the corrosion potentials of the control and treated bars were nearly identical.

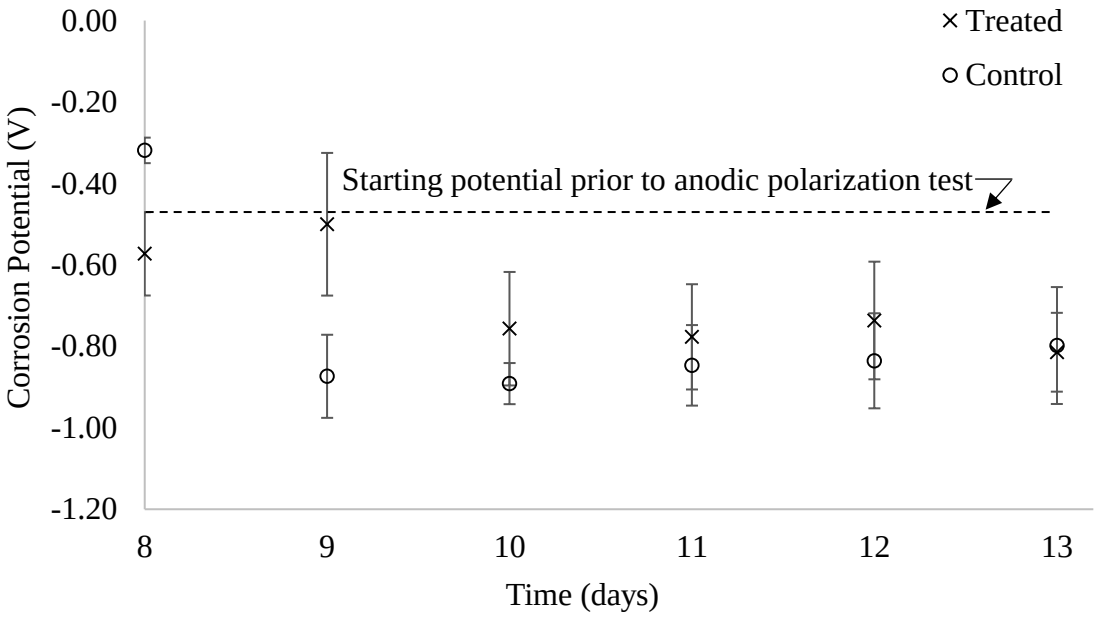

Figure 4-13: The average corrosion potentials of treated and control bars during the anodic polarization phase of the electrodeposition and anodic polarization tests. Each point represents the average value of six trials.

Based on Figure 4-12 and Figure 4-13, it is observed that after the electrodeposition treatment the average corrosion potential of the control bars became more positive from -0.49 to -0.32 V, and the average corrosion potential of the treated bars became more negative from -0.50 to -0.57 V. In the high pH solution at 25 °C, the surface of control bars were expected to be passivated while forming $Fe(OH)_2$ [132], Fe_3O_4, and FeOOH at the surface [118] [131]. A thin passive film would be expected to

increase the corrosion resistance on the control bars, so the average corrosion potential became more positive at Day 8 [119]. At Day 9 the average corrosion potential of the control bars decreased to -0.86 V. This may be due to the thin passive film dissolving quickly as a result of anodic polarization.

The treated bars had a lower average corrosion potential than the control bars on Day 8. Apparently, this indicated that the electrodeposits contained sodium, potassium and calcium oxides which were more corrosive than the steel passive film. This was because the electrodeposits contained potassium, sodium, and calcium oxides, which were more active than the steel and the passive film. It is introduced in Section 2.6.1 that the reduction potentials of iron, potassium, sodium, and calcium are -0.756 V, -3.25 V, -3.03 V, and -3.19 V with respect to CSE. When the corrosion potential is more negative, the metal has more tendencies to corrode. As the corrosion potentials of the treated bars were measured, it was the electrodeposits that were providing the signal. This more negative corrosion potential of the treated steel bars indicated the electrodeposits would tend to corrode prior to the steel material.

It appears that the electrodeposits were more protective than the passive film of the uncoated controls because after the first-day anodic polarization, the average corrosion potential of the treated bars was significantly more positive than that of the control bars. The electrodeposits acted as a sacrificial coating until Day 10 when the two average corrosion potentials were not significantly different. Moreover, the trends of the average corrosion potentials are consistent with that of the average currents shown in Figure 4-10 (except Day 8). When the average corrosion potential of the treated bars was more positive than that of the control bars, the average current of the treated bars was

lower than that of the control bars. Therefore, these electrodeposits appeared to act as a sacrificial coating defending against the anodic polarization during AP tests.

4.2.5 Coulomb Passage Analysis

Based on the average current analysis in Sec. 4.2.3, the coulomb passage of each day through the bars was calculated based on Eq. 4-10 and shown in Figure 4-14:

$$Q = I \cdot t\,, \qquad \textbf{Eq. 4-11}$$

where Q is the average daily charge passage (C), I is the average current (A), t is the treatment time (s). Exhibiting the same tendency with the average currents observed in Figure 4-10, the average daily coulomb passage appeared to decrease with the development of electrodeposits. Figures 4-10 and 4-13 indicate that the treated bars lost the corrosion protection significantly after Day 9. Moreover, after Day 9 the treated bars

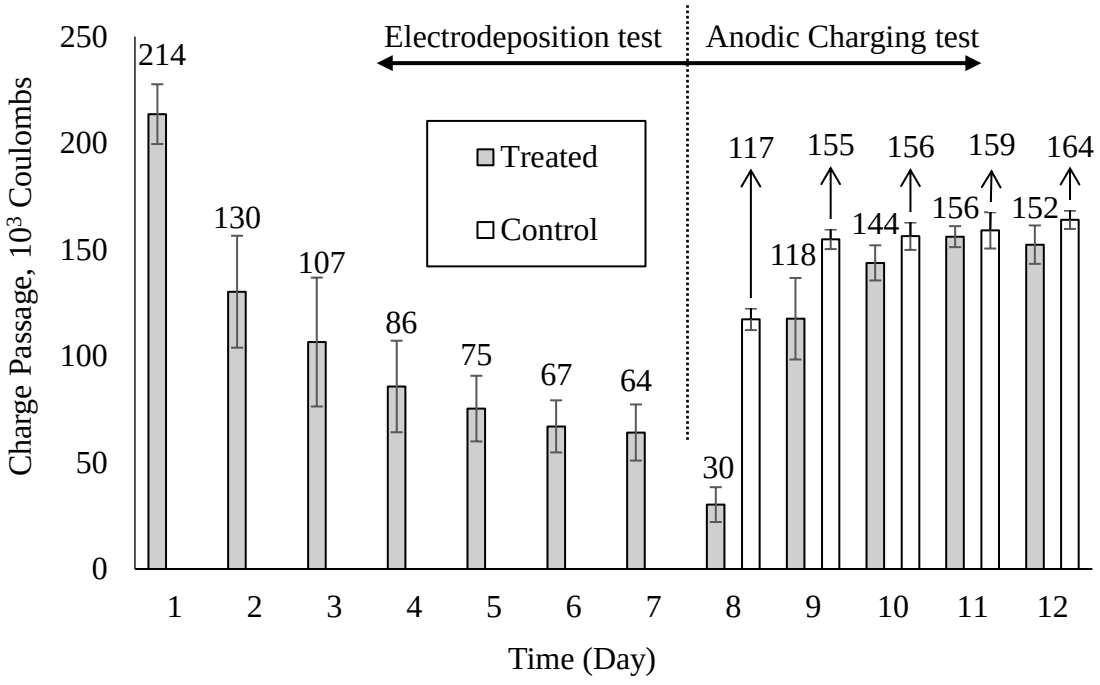

Figure 4-14: The average daily electric charge passage observed during electro-deposition treatments and the anodic polarization tests. Each point represents the average charge passage of six trials.

exhibited significantly corroded areas. Also, the corroded area of the treated bars appeared to be proportional to the charge passage. In Figure 4-11, the average charge passage of the treated bars on Days 8 and 9 are 30 and 118 coulombs, respectively. Therefore, if a significantly corroded area was expected to be avoided, the charge passage during an anodic polarization test would be lower than 148 coulombs (30 + 118 = 148).

Figure 4-15 shows the average total coulomb passage of the bars in the electrodeposition treatments and the anodic polarization tests. It was observed that the treated bars had lower average total charge passage (613 C) than the control bars (758 C) in the anodically charged tests and the average total charge passage of the treated bars in electrodeposition treatments (820 C). These results indicated that the treated bars may exhibit a lower corroded area than the control bars.

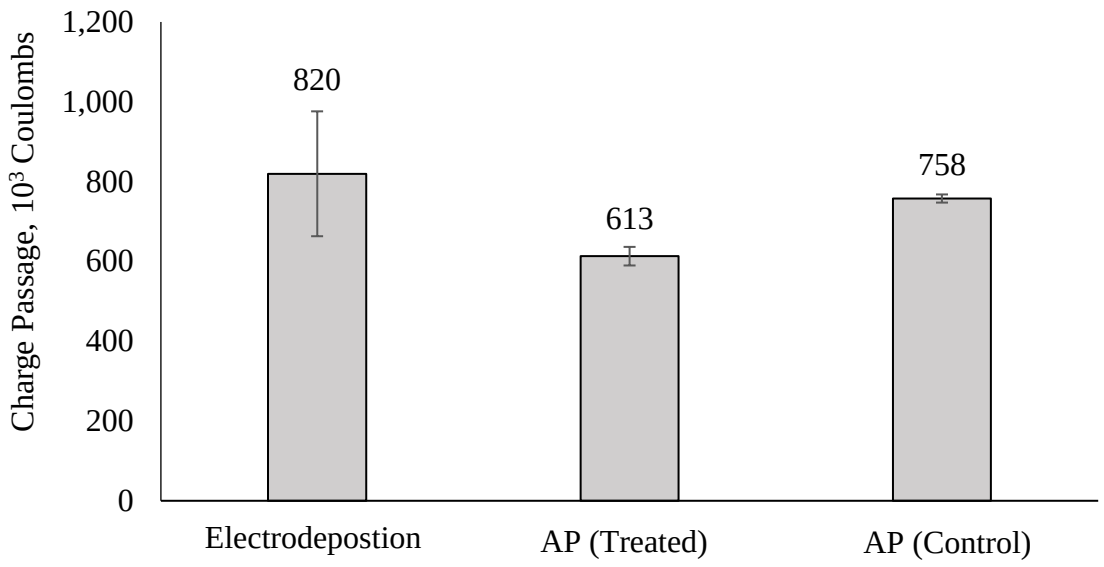

Figure 4-15: The average total electric charge passage during the electrodeposition treatments and the anodic polarization (AP) tests on 1018 steel bars in simulated pore fluid. Each value represents the average value of trials 1-4.

4.2.6 Characterization of Electrodeposits

The white electrodeposits were characterized by Field Emission Scanning Electron Microscope (FESEM) and energy dispersive X-ray spectroscopy (EDS). The results are shown in Figure 4-16. Results in Table 4-1 showed that the electrodeposits exhibited approximately 60 atomic percent (AT%) oxygen, 30 AT% Ca, 2 AT% K, and 1 AT% Na. The SEM image demonstrated that the majority of the crystalline deposits exhibited a morphology that is typical of calcium hydroxide. During the SEM observation of the electrodeposits, EDS analysis at several locations was conducted, and the elemental results are shown in Table 4-1.

SEM Image

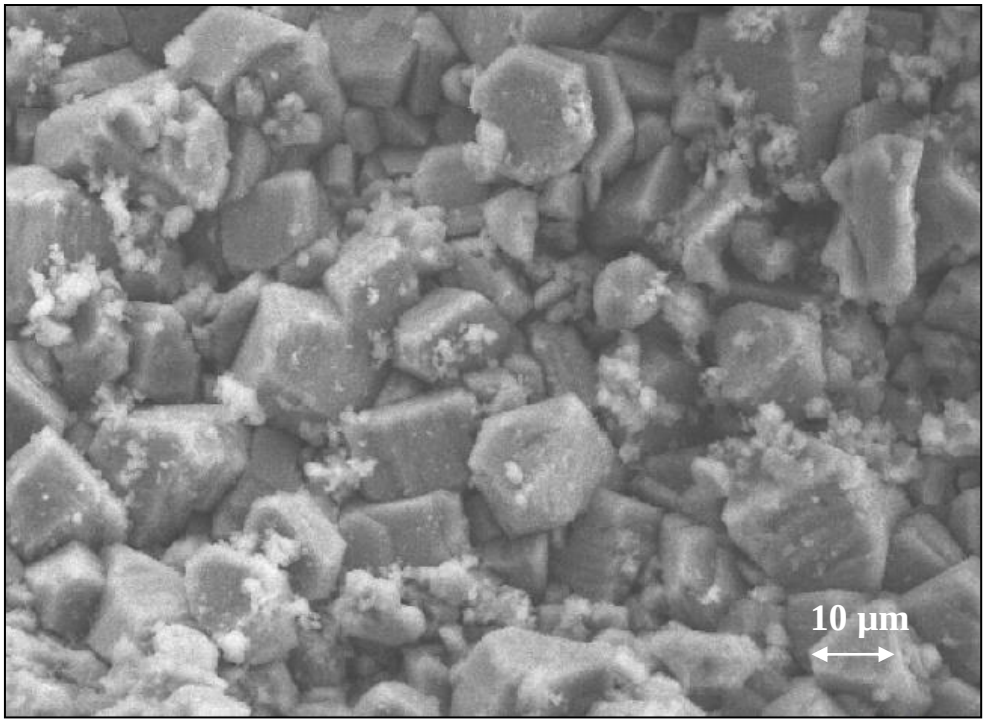

EDS Analysis

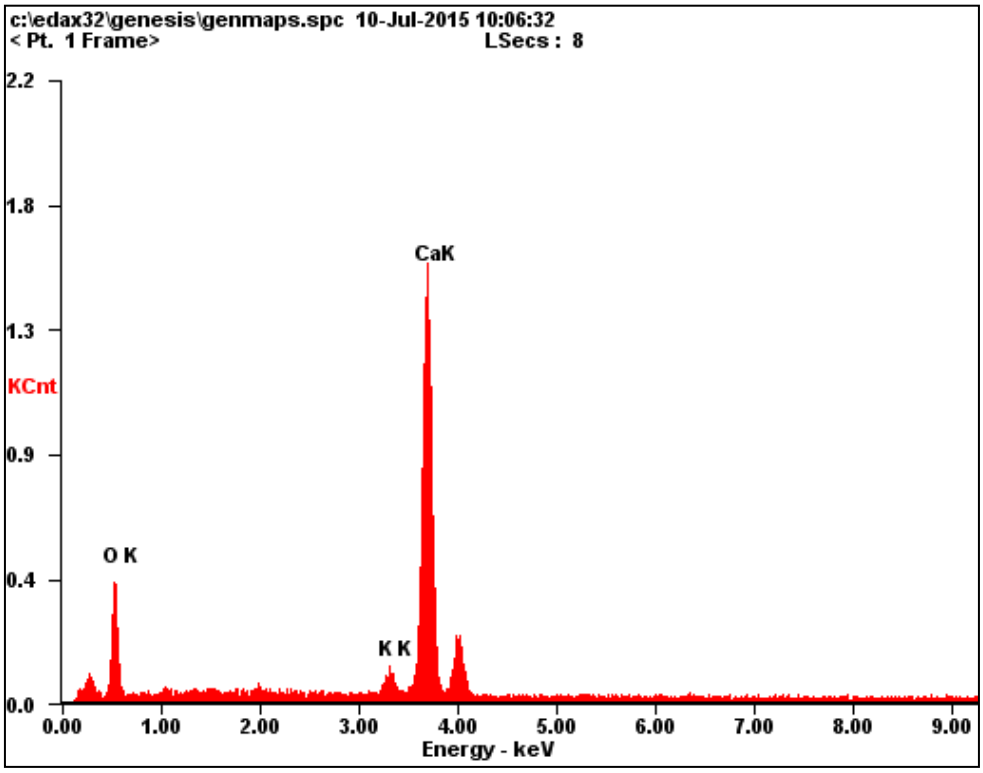

Figure 4-16: SEM image and EDS analysis of electrodeposits observed on treated specimens such as shown in Figure 4-9.

Table 4-1: EDS analysis of electrodeposits at 5 different places during SEM observation. (atomic percent, AT%)

Location	Oxygen AT%	Calcium AT%	Potassium AT%
1	59.6	39.9	0.5
2*	56.2	14.4	3.8
3	68.7	30.4	0.8
4	67.8	30.7	1.4
5	54.3	44.9	0.7

*Sample from Trial 2 contained other elements, such as 15.05% of carbon, 3.84% of sodium, 0.61% of aluminum, and 6.18% of silicon.

4.3 MMA Treatment with Electrodeposits on Rebar

The current density, applied voltage, and corrosion potential during the electrodeposition (ED) and MMA treatments are presented in Section 4.3.1. Corroded areas for the reinforcement (steel bars) are estimated in Section 4.3.2. Depending on the electric current recorded in the ceramic and MMA treatments, the electric charges passed in the treatment circuits were calculated and shown in Section 4.3.3. The tensile strength and porosity of each specimen were achieved and calculated according to the Eq. 3-2 and Eq. 3-5, respectively. These are presented in Sections 4.3.4 and 4.3.5. Statistical analysis was applied to examine the significance of tensile strength and porosity between the treated and untreated specimens.

4.3.1 Current Density, Applied Voltage and Corrosion Potential Profile

In order to distinguish groups conveniently, the notations for each group are established in Table 4-2. As described in Table 3-7, Groups 1-5 used the 3-month-old HCP specimens. Groups 6 and 7 used the 1-week-old HCP specimens. Groups 1 and 6

were only subjected to MMA treatment administered under a corrosion potential of +3.50 V vs. the $Cu/CuSO_4$ reference electrode (CSE), so they were termed as Group O-MMA (old batch) and Group Y-MMA (young batch), respectively. Groups 5 and 7 were the control groups which were cured in lime water and received no other treatment, so they were termed as Group O-Control (old batch) and Group Y-Control (young batch), respectively. Group 2 had a low concentration of the alkaline species in the ED treatment and a low corrosion potential in the ED and MMA treatments, so Group 2 was termed as Group LCLV (low concentration low voltage). According to the similar reasons, Groups 3 and 4 were termed as Groups LCHV and HCHV (high concentration high voltage).

Table 4-2: Notations of groups subjected to electrodeposition treatments and MMA treatments as described in Table 3-7.

Group No.	1	2	3	4	5	6	7
Notation	O-MMA	LCLV	LCHV	HCHV	O-Control	Y-MMA	Y-Control

Figure 4-17 shows the daily current density profile of Groups (LCLV), (LCHV) and (HCHV) during the 8-day electrodeposition treatments. The current density was calculated according to the area of the HCP sample. It is observed that the current density of Groups (LCHV) and (HCHV) decreased during Days 1 and 2, and increased during Days 3, 4 and 5. At Day 3 the solution level was lower than the labeled line, so an extra 100-ml DI-water was added into these two groups. The addition of DI-water permitted additional calcium hydroxide dissolution and increased the treated area of the HCP samples so that current density increased from Day 3 to 5. The water electrolysis rates of

Groups (LCHV) and (HCHV) apparently were higher than that of Group (LCLV) due to the need of additional water in these cases.

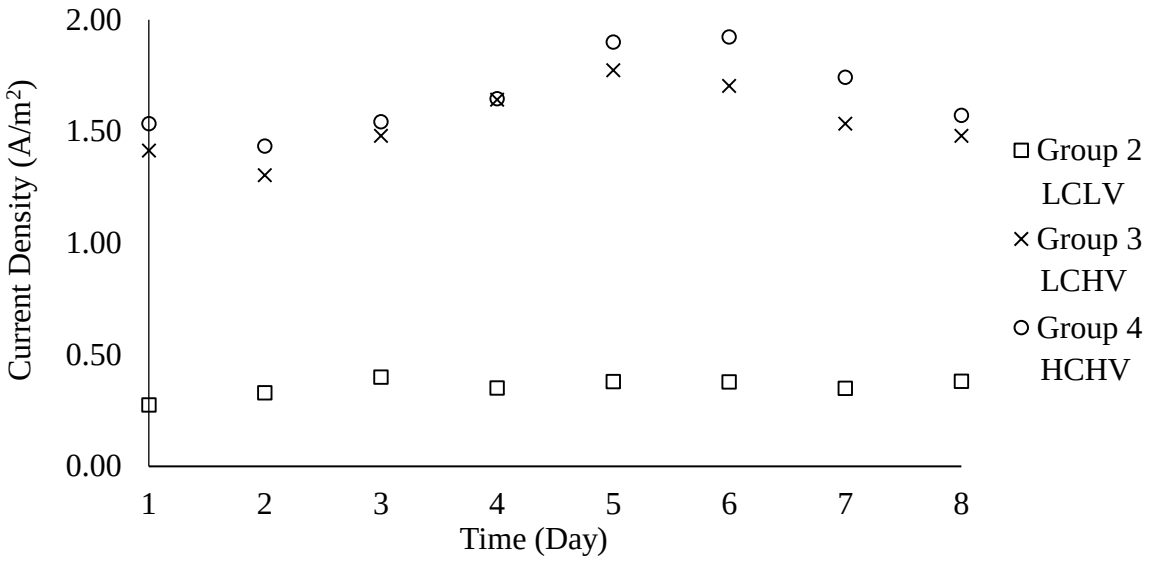

Figure 4-17: Average daily current densities of electrodeposition treatments on three-month-old HCP batches. Each point represents the average current density of a group of five specimens at a single node in the treatment circuit setup (shown in Figure 3-8). Group 1 was a control group that was not included here since it was not subjected to electrodeposition treatment. Treatment parameters for these cases are listed in Table 3-7.

It is observed in Figure 4-17 that the current densities of Groups (LCHV) and (HCHV) were nearly four times those of Group (LCLV). The concentrations of cations and the corrosion potential applied in the ED treatment were the main factors influencing the current densities.

As mentioned in Section 4.2.1, it was mentioned that the corrosion potential of -3.50 V vs. CSE was able to reduce the cations and produce significant hydrogen gas. Section 2.6.3 introduces that the standard reduction potentials of potassium, calcium and sodium ions at the cathode are -2.93 V, -2.87 V and -2.71 V vs. the standard hydrogen electrode (SHE), respectively. If these potentials are measured versus the CSE, these

potentials should be -3.174 V, -3.114 V and -2.954 V for the reductions of K^+, Na^+, and Ca^{2+}, respectively. Clearly, the corrosion potential of Groups (LCHV) and (HCHV) (-3.50 V) in the ED treatments was more negative than the standard reduction potentials of those cations. The corrosion potential of Group (LCLV) in the ED treatment was -1.75 V vs. the CSE, which was more positive than the standard reduction potentials of those cations. This indicated that the reduction of cations was not expected to occur in the ED treatment of Group (LCLV). Therefore, the electrodeposition treatments had significant reductions of cations when the corrosion potential vs. CSE was -3.50 V. This reduction caused the current increased significantly in Groups (LCHV) and (HCHV) during ED treatments.

Moreover, the concentrations of the ions also affected current density. In Figure 4-17, the current densities of Group (HCHV) were slightly higher than the current densities of Group (LCHV) because the concentrations of cations in Group (HCHV) (3 mol/L) were higher than those in Group (LCHV) (1 mol/L) during the ED treatment.

Group (LCLV) still had detectable currents during the ED treatment even though its corrosion potential was lower than the corrosion potential of the cations vs. the CSE. This was because the following reaction was occurring at the cathode:

$$2H_2O + 2e^- = H_2 + 2OH^-, \qquad \textbf{Eq. 4-12}$$

The corrosion potential of Eq. 4-12 is -0.828 V vs. the SHE [4]. The corrosion potential is -1.144 V vs. the CSE. This electrolysis of water caused the current density to be detectable in Group (LCLV).

Figure 4-18 shows the distributions of current densities of the ED treatments (+3.50 V vs. the CSE) when the 1018 steel bars were directly exposed to the alkaline

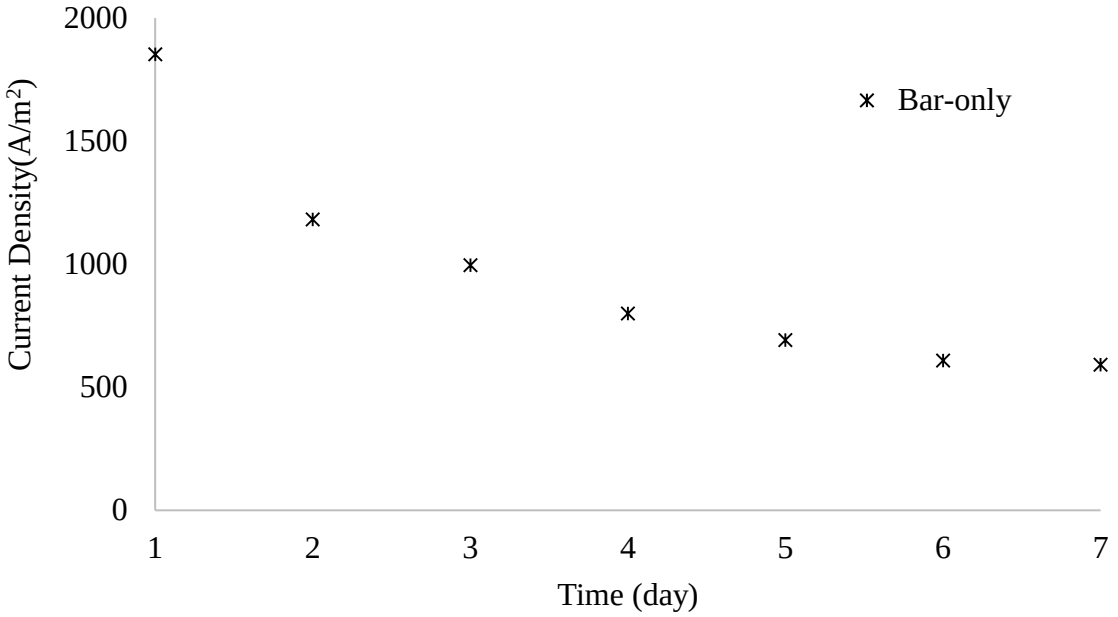

Figure 4-18: Average current density profile of ED treatments when 1018 steel bars were directly exposed to simulated pore fluid. The average current density was calculated according to the electric current profile shown in Figure 4-10. Each point represents the average current density of six trials.

solution. These current densities in Figure 4-18 were calculated based on the electric current profile of the ED treatment from Figure 4-10. Each point in Bar-only group represents the average current density of six trials. It is clear to see that the average current densities (> 500 A/m^2) of Bar-only group in Figure 4-18 were significantly higher than the current densities (< 2 A/m^2) of the HCP groups in Figure 4-17 during the ED treatments. Moreover, the distributions of current densities in Figure 4-17 do not exhibit a similar trend as the average current density distribution observed in Figure 4-18.

The hardened cement pastes in Groups 2, 3 and 4 (See Table 3-7) hindered the motion of positive ions, so the speed of electrodeposition was similarly limited. The decreasing trend in Figure 4-18 indicates that the increasing electric current resistance with time. In Figure 4-17, the low current densities caused the electrodeposits on the bars

to be probably not enough to increase the current resistance significantly. It may take a longer time to observe a significant current drop as shown in Figure 4-18 during the ED treatment on the reinforced HCP specimens.

Another possible reason for the relatively insignificant current drop in Figure 4-17 is the development of bubble formation, which can lead to the discrete and non-homogeneous distribution of electrodeposits as discussed in Sec. 4.2.3. The intense bubble formation on the metal surface may have hindered the electrodeposition of calcium hydroxide and caused the non-uniform electrodeposits shown in Figure 4-11. It was possible that the hardened cement paste attached to the steel surface may have acted as distributed field of high-resistance deposits that could have caused the localized bubble formation to be relatively intense. For these reasons it is conceivable that the current profiles of the treatments plotted in Figure 4-17 may have been dominated by electrolysis and thus less likely to exhibit significant current drop associated with electrodeposition.

Figure 4-19 contains the current densities of MMA-HCP specimen Groups 1-4 (See Table 4-2) that were monitored daily during the MMA treatments. The current densities were calculated according to the surface area of the HCP sample. It was observed that each group had a higher current density on Day 1 than the rest of the time. In Figure 4-19, these decreasing current densities indicated the decreasing concentration of ions in the solution and the reducing porosities of the HCP specimens that were undergoing treatment.

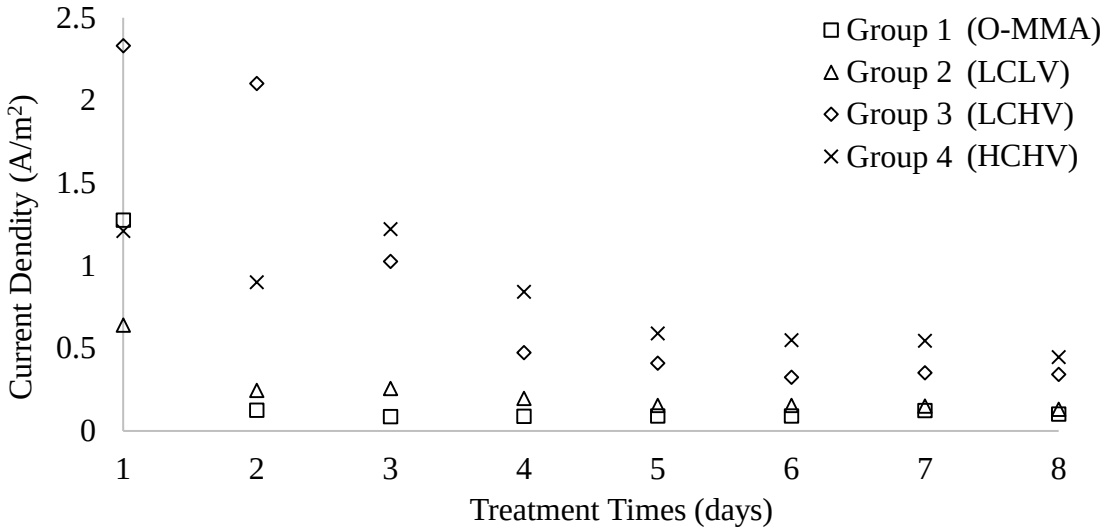

Figure 4-19: Current densities monitored daily during the 3-month-batch MMA treatments of HCP specimens. The specimens were retained in lime water for 10 days prior to the start of the MMA treatments.

Figure 4-20 shows that the applied potentials of MMA-HCP Groups 1-4 (See Table 4-2) were monitored and adjusted daily during the MMA treatments. The corrosion potentials of rebar were set at the +3.50 V (Groups 1, 3 and 4) and +1.75 V (Group 2)

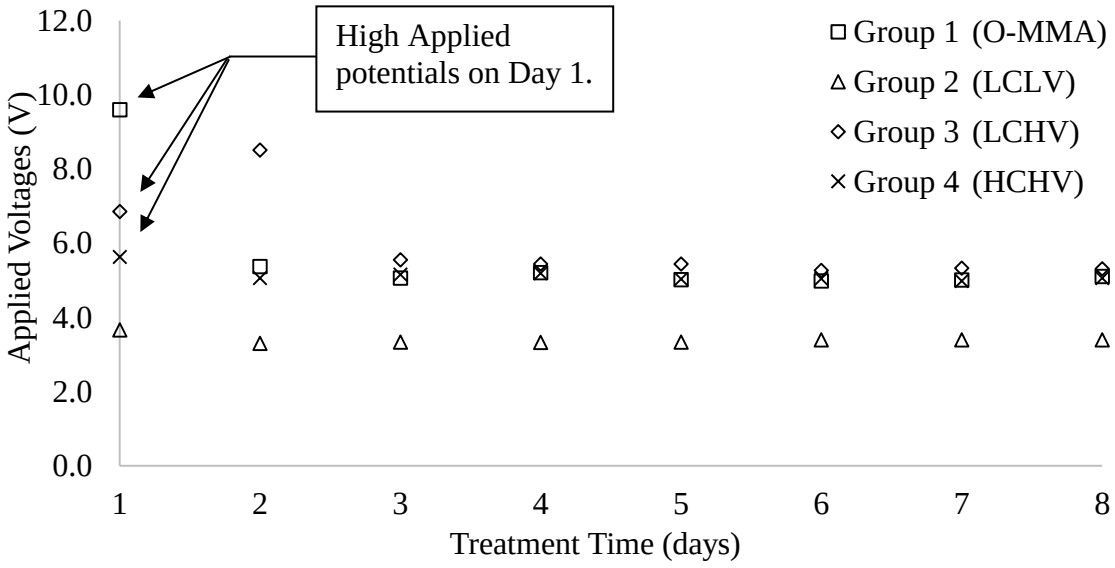

Figure 4-20: Applied potentials of bar in specimens undergoing MMA treatments in 3-month batch. After day 2 the applied potentials became stable.

with respect to the $Cu/CuSO_4$ reference electrode (CSE).

It was expected that a flat applied-voltage distribution would be observed for each MMA treatment in Figure 4-20. However, it was observed that all groups had a significantly higher applied potential on Day 1. The applied potential of Group (O-MMA) at Day 1 (+9.60 V) was significantly higher than other groups. This was because, at the beginning of MMA treatment, the low conductivity of the solution due to a relative lack of ions required a higher applied voltage to achieve the corrosion potential of +3.50 V. After Day 1, significant numbers of cations (Na^+, K^+, Ca^{2+}) in the pores of HCP samples were being extracted (by both diffusion and the electric field) into these solutions. This would have caused the conductivity of the solutions in Groups 1-4 to increase during Day 1. Therefore, this low conductivity of the treatment solution can be mitigated by increasing the concentration of ions in the solution at the beginning of the MMA treatments.

This study examined the influence of the HCP batch age with respect to the treatment outcome. Figure 4-21 shows the current densities of Groups (O-MMA) and (Y-MMA) that were subjected to the MMA treatment while held to a corrosion potential of +3.50 V. The ages of Groups (O-MMA) and (Y-MMA) were 3-month and 1-week, respectively. It was observed that the current densities of Group (O-MMA) were significantly higher than those of Group (Y-MMA). The profiles of applied voltage and corrosion potential of the 1-week batch are shown in Appendix D.

In Figure 4-21, the HCP specimens in Group (Y-MMA) were expected to have more capillary pores than Group (O-MMA) because the hydration of the cement paste was not complete (as illustrated to Figure 2-1). Capillary pores provided the accesses for

the ions to reach the steel bar in the HCP. The availability of more capillary porosity would be expected to cause the current density to increase. As shown in Figure 4-20, Group (Y-MMA) also had a relatively high applied potential on Day 1 during the MMA treatment due to the low conductivity of the solution.

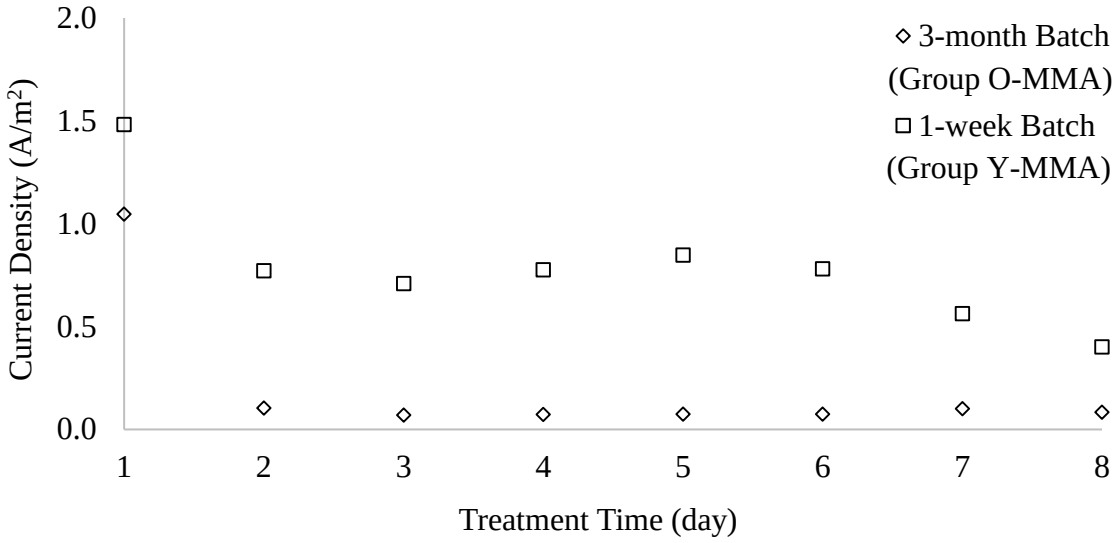

Figure 4-21: Current density distributions of the 3-month and 1-week batches which were only subjected to MMA treatment while held to a corrosion potential of +3.50 V.

For the 1-week batch, the hydration of cement and water was not complete, and the pore fluid would have been expected to contain a relatively high concentration of alkaline species. These alkaline species would be expected to have a pH value of 13.5 [3] [119]. For the 3-month-old batch, the HCP samples were soaked in lime water (2 g/L $Ca(OH)_2$) for three months prior to the MMA treatment. This length of soaking time could have made the pH value in the HCP pores drop to 12.5 or lower (the carbonation of calcium hydroxide). For these reasons, it would not have been surprising 1-week batch would have contained a higher concentration of ions which could have resulted in the higher current density distribution observed in Figure 4-21.

4.3.2 Corroded Area Analysis of Treated HCP Specimen Bars

After the indirect tensile strength tests, the bars embedded in the HCP specimens were subjected to an image analysis similar to those conducted on the bare bar tests of Section 4.2.2. The original images of the bars were transformed into the grayscale images based on 3q. 4-10. Matlab software was used to calculate the histograms of these grayscale images and produce binary images (the Matlab codes are in Appendix C). It was different from Section 4.2.2 to determine the threshold applied in the histograms from Groups 1, 2, 3, 4, and 6 (See Table 4-2). There were two thresholding methods (global and manual) applied to analyze the approximate corroded area on the treated samples. This was because single thresholding could not guarantee the achievement of satisfying binary image, which was visually similar to the raw image of the MMA-treated bar.

The first thresholding method was the global thresholding method that was obtained from the analysis of the histograms of the grayscale images from the control groups. Since the HCP specimens from the control groups were cured in lime water during the treatments, the steel bars were passivated by the alkaline water and had no corroded areas as shown in Figure 4-22. The threshold of each control sample in Figure 4-22 was defined to be a 1% corroded area (99% in Section 4.2.2). The average gray levels for thresholding were 100 for Groups 1-5 (3-month batch), and 68 for Groups 6 and 7 (1-week batch). These two thresholding gray levels were applied to determine the corroded areas from the histograms of the treated samples. If the gray level of a pixel was more than 100 (for Groups 1-5) or more than 68 (for Groups 6 and 7), then this pixel

would be considered un-corroded. These two gray levels are here-after referred to as the global threshold values for corrosion.

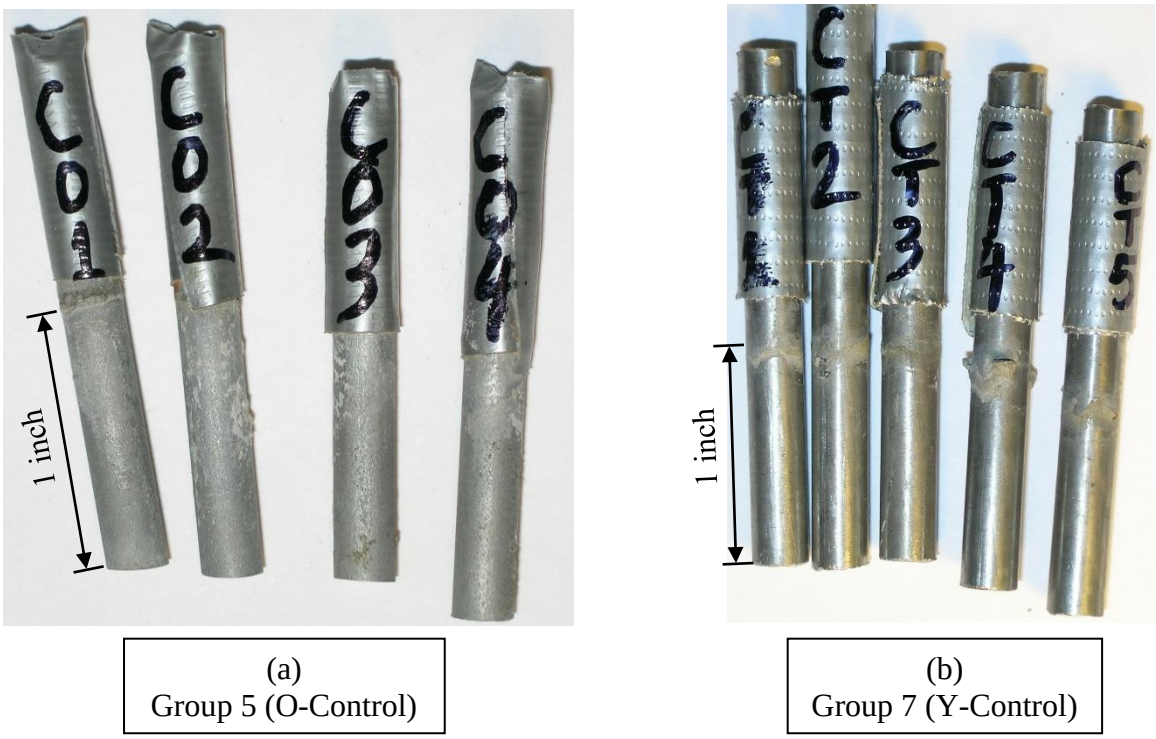

Figure 4-22: Images of control specimens of groups 5 (a) and 7 (b) after the indirect tensile strength testing.

The second thresholding method was a manual determination. This approach was examined because, sometimes, when the global thresholding was applied, the corroded area in a binary image was significantly different from the raw image. Figure 4-23 shows the images of Sample 5 from Group 3. Figure 4-23(b) was the binary image based on the global thresholding value (100), and Figure 4-23(c) was the binary image based on the manual thresholding value (124). From a visual perspective, the binary image (threshold = 100) exhibited a more incorrect un-corroded area than the binary image (threshold = 124). This was because if the threshold was too small, more areas could be misjudged as

un-corroded areas. Therefore, the global thresholding was not appropriate for the analysis of the corrosion area in this case.

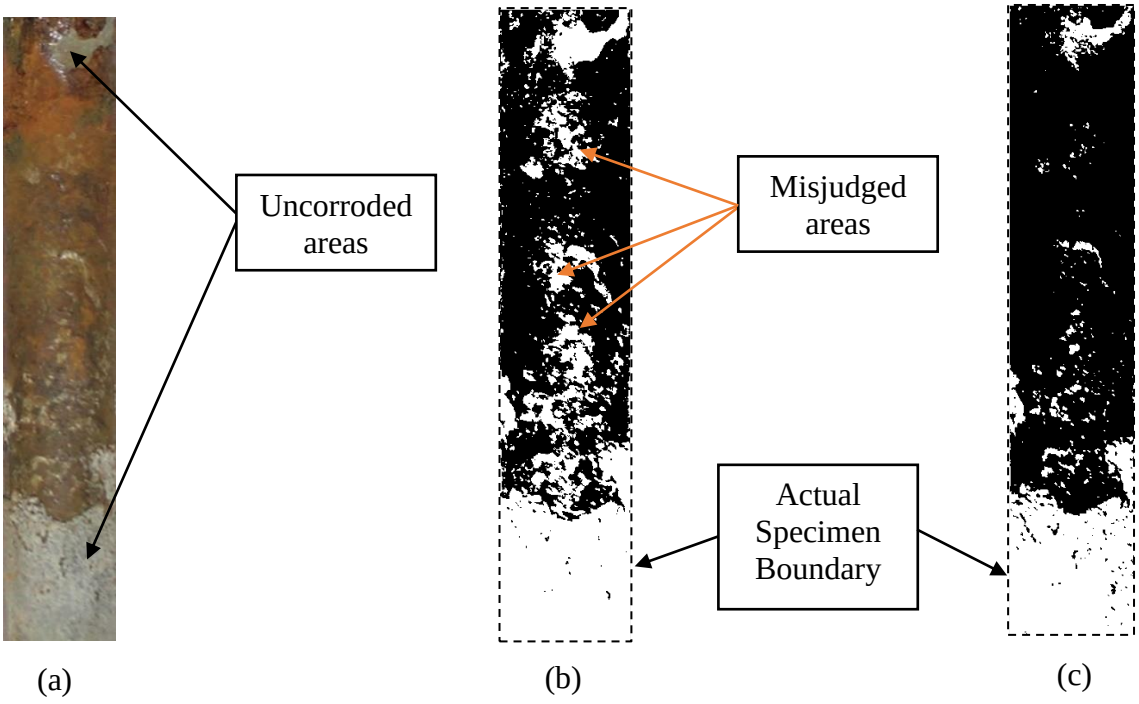

Figure 4-23: An example of the raw and binary images of specimen 5 from HCP group 3. (a) Raw image; (b) Binary image when the global threshold was equal to a gray level of 100, (c) Binary image when the manual threshold was equal to a gray level of 124.

In order to confirm that the uncorroded areas in the binary image were more similar to the raw image, the manual thresholding method was applied on some images whose histograms had two peaks shown in Figure 4-24. The manual thresholding was applied according to the shape of the histogram of the analyzed grayscale image. Figure 4-24 shows the histogram of the grayscale image of steel bar in the MMA-treated HCP Specimen 5 from Group (LCHV). The graph has two peaks which represent two different major colors in the raw image (Figure 4-23(a)). If the color difference is more significant, the two peaks can become sharper in the histogram. The gray level (124) in the middle of

the valley between two peaks was the threshold chosen to identify the corroded or un-corroded area. Some histograms had only one peak which indicated that the bars were thoroughly surface-corroded. In this condition, the corroded area was 100%. Therefore, in some cases, in order to obtain an excellent binary image that simulated un-corroded areas of the raw image, the threshold was manually selected.

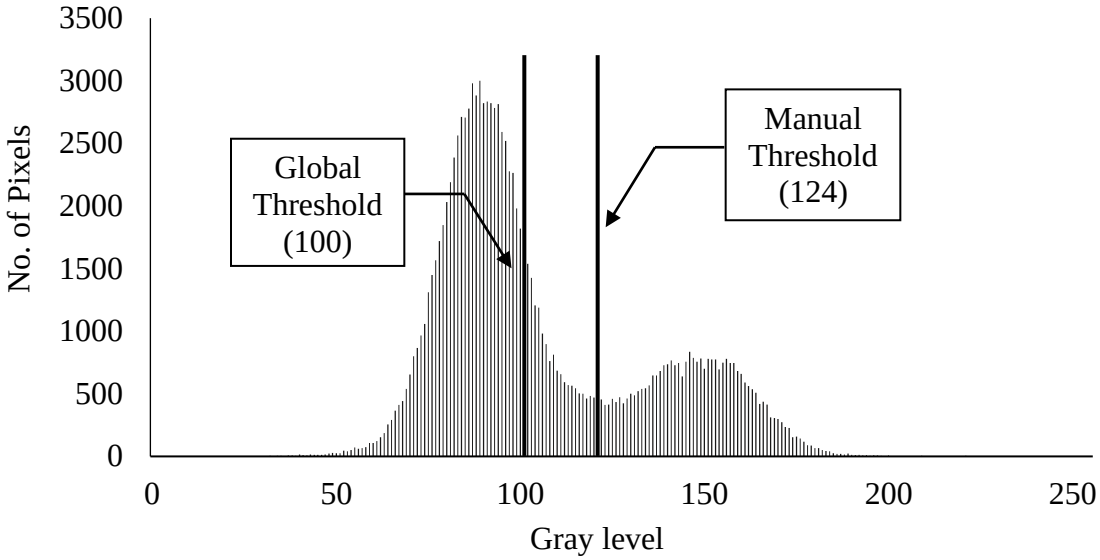

Figure 4-24: Histogram of grayscale image of steel bar in MMA-treated HCP specimen 5 from Group (LCHV).

Based on the previous thresholding methods, the average corrosion areas of the steel bars in the HCP specimens of Groups 1-7 (See Table 4-2) were calculated and shown in Figure 4-25. It was observed that the rebars in Group (LCHV), (HCHV), and (Y-MMA) nearly corroded. The bars in Group (O-MMA) and (LCLV) had 10% and 7% corroded area. The error bars represent a 90% confidence interval. It was observed that the average corroded area of Groups 1 and 2 was approximately 1/10 of Group 6.

It was discussed in Section 4.3.1 that the pH value of the pore fluid in the HCP specimens in Group (O-MMA) was likely to be in the vicinity of 12.5, which was lower

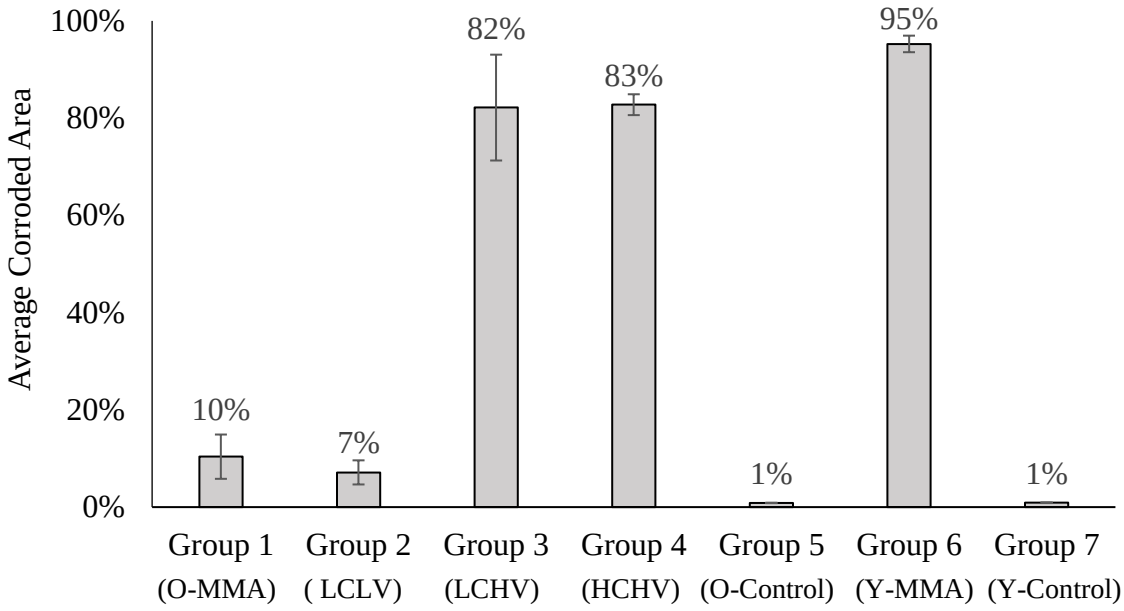

Figure 4-25: Corroded image analysis results of each HCP group after electrodeposition and MMA treatment.

than what would be expected (13.5) for the Group (Y-MMA) due to diffusion [3] [119]. The pH value correlates to the concentration of hydroxide ions in the pore fluid. For this reason, the concentration of ions in the pore fluid of the HCP specimens in Group (O-MMA) was likely to be nearly 1/10 of that in Group Y-MMA (the 1-week batch). Eq. 2-41 describes how the oxidation of hydroxide ions produces oxygen gas and water when the applied corrosion potential is higher than the O_2/H_2O line as shown in Figure 2-16. These two products are reactants which support steel corrosion. Figure 4-21 shows that the current densities of the MMA treatment of Group (Y-MMA) were higher than those of Group (O-MMA). This indicated that the oxidation rates of hydroxide and iron at the anode (steel bar in HCP) of Group (Y-MMA) was likely to be higher than those of Group (O-MMA). Groups (O-MMA) and (LCLV) exhibited a low-oxygen environment around the bars and the low current densities which caused less corroded areas. Groups (LCHV),

(HCHV) and (Y-MMA) had an oxygen-rich environment and the high current densities which caused more corroded area. Therefore, the low concentration of alkaline species applied in the ED treatment and the low corrosion potential during MMA treatments may have contributed to the low corroded area on the steel bars.

4.3.3 Electric Charges in Electrodeposition and MMA Treatment

Figure 4-26 shows the electric charges passed during the electrodeposition (ED) and MMA treatment for the MMA-treated HCP specimens in each group. Each value represents the sum of 8-days of electric charges passed in each group of five specimens. It was observed that the electric charges passed in the MMA treatments of Groups (LCLV), (LCHV), and (HCHV) were nearly half of the coulombs passed during the respective ED treatments that preceded them. Moreover, the electric charges passed in the

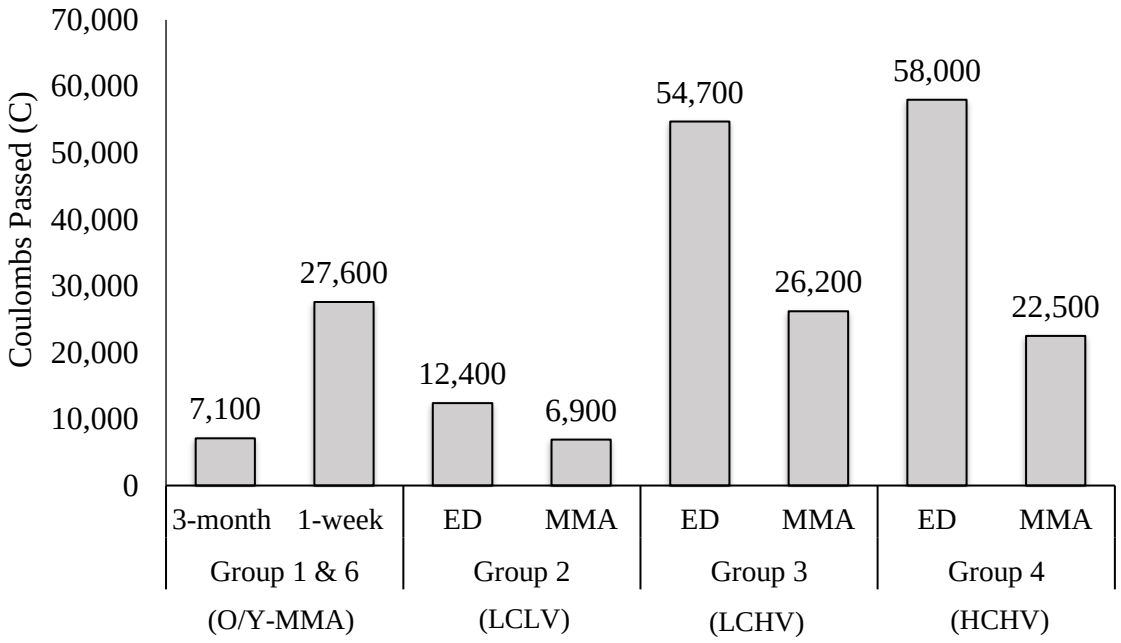

Figure 4-26: Electric charge passed in electrodeposition (ED) and MMA treatment for MMA-treated HCP specimens in each group (5 specimens were wired together in each group). Groups 5 and 7 are not shown here because they are the untreated HCP control groups.

MMA treatments of Group (O-MMA) were significantly less than that of Group (Y-MMA).

Theoretically, if the coulombs in the ED treatment were used to electrodeposit the calcium hydroxide on the bar, the steel bar would start to corrode after the deposits completely dissolved. However, it was analyzed in Figure 4-25 that the steel bars in MMA-treated HCP specimens in Groups 1-4, and 6 exhibited significantly corroded areas even though the electric charges passed in the ED treatments were more than those in the MMA treatments. Moreover, when the corrosion potential was more negative than the -1.144 V vs. the CSE, the electrolysis of water was expected to occur at the steel bar during the ED treatments (discussed in Section 4.3.1). Based on the previous observations and discussions, the electrolysis of water seemed to be predominant during the ED treatments so that the protection provided by the electrodeposits was probably not significant in the MMA treatments.

4.3.4 Indirect Tensile Strength

Figure 4-27 shows the average tensile strength ratio of each MMA-treated HCP group compared with the companion specimens in Groups (O-Control) and (Y-Control). The error bars represent a 90% confidence interval. After the MMA treatments, the average tensile strengths of Groups (O-MMA), (LCLV), and (LCHV) were greater than that of the control Group 5 by 69%, 50%, and 17%. All the specimens in Group (HCHV) cracked during the MMA treatment, so the average tensile strength was zero. The average tensile strength ratio of Group 6 was less than that of Group 7 by 76%.

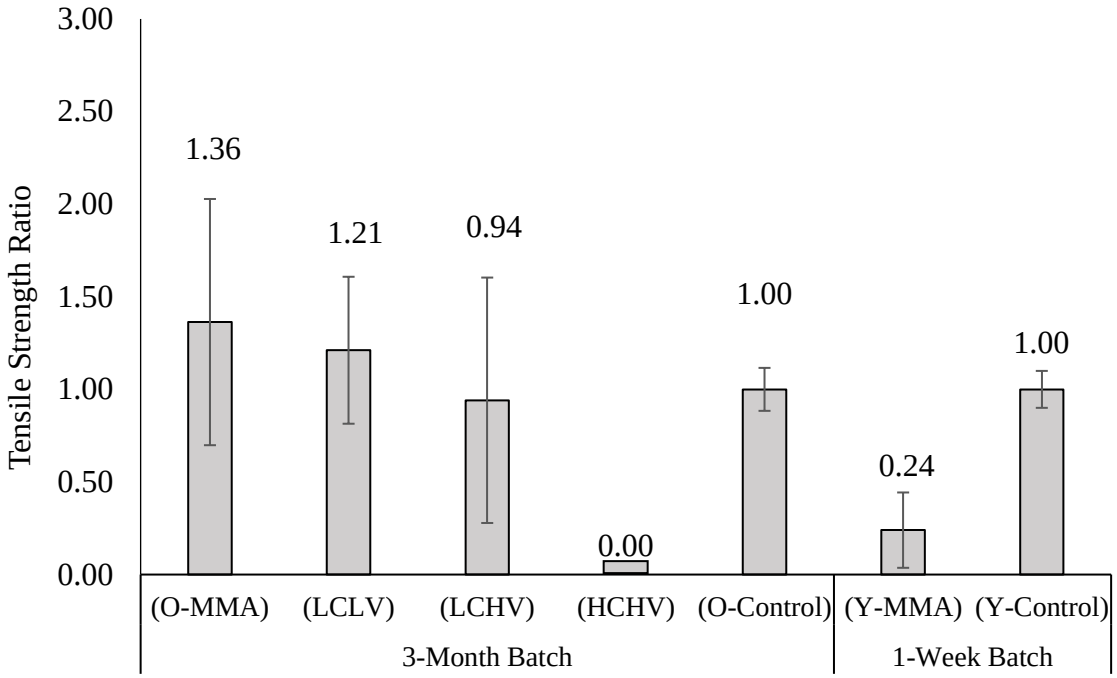

Figure 4-27: Average tensile strength ratio of the reinforced HCP samples which were subjected to the electrodeposition and MMA treatments. Treatment details of each group are located in Table 3-7.

Although the average tensile strengths of Groups (O-MMA), (LCLV), and (LCHV) were higher than Group (O-Control), the statistical analysis in Table 4-3 indicated that their mean tensile strengths were not significantly different. A statistical analysis (F and T tests) on the average tensile strength was conducted and shown in Table 4-3. Table 4-3 shows the tensile strength of each specimen and the results of F-tests and Student's T-tests. In Table 4-3, the MMA-treated HCP Groups 1-4 are compared with Group (O-Control), and the MMA-treated HCP Group (Y-MMA) is compared with the Group (Y-Control). It can be observed in Table 4-3 that the F-test value (40.8) of Group (LCHV) is more than the F-table value (19.2), and the F-test values of other groups are less than the F-table value. This indicated that the variances between the MMA-treated

Table 4-3: Tensile strength and statistical analysis of MMA treated specimens.

	3-month Batch (psi)					1-week Batch (psi)	
Specimen NO.	Group 1 (O-MMA)	Group 2 (LCLV)	Group 3 (LCHV)	Group 4 (HCHV)	Group 5 (O-Control)	Group 6 (Y-MMA)	Group 7 (Y-Control)
1	200	69	0*	0*	254	240	437
2	239	306	0*	0*	201	185	305
3	393	369	269	0*	201	54	431
4	587	246	326	0*	-	0*	415
5	72	334	434	0*	-	0*	415
Average	298	265	343	-	220	160	400
Statistical Analysis+							
F-test	41	14.6	40.8	-	-	4.1	-
F-table	19.2	19.2	19.2	-	-	6.3	-
T-test	0.9	1.24	0.14	-	-	5.5	-
T-table	2.1	1.9	2.1	-	-	1.9	-
Significance Result	No	No	No	-	-	Yes	-

* Specimens cracked during the MMA treatments.
+ 95% confidence for F-test, 90% confidence for T-test.

and control HCP Groups were statistically equal at a 95% confidence interval except Group (LCHV). The T-test values of Groups (O-MMA), (LCLV), and (LCHV) were less than the T-table values. Average tensile strengths of treated HCP specimens (3-month-aged) were higher than that of control specimens, but the statistical analysis indicated that the two mean values were not significantly different. The T-test value of Group (Y-MMA) is more than the T-table value in Table 4-3. This indicated that the average tensile strength of Group (Y-MMA) was significantly lower than that of Group (Y-Control).

It was discussed in Section 4.2 that the anodic polarization was able to corrode the steel bars with or without the electrodeposits in the simulated pore fluid. Moreover, the corrosion of steel produces iron oxides which have a bigger volume than iron. This expansion of volume on the surface of the steel bars appeared to cause the cracking of the MMA-treated HCP specimens [1]. This is because the expansion of steel bars exerts tensile stresses at the center of HCP specimens which are vulnerable to tensile forces. When the cracks propagated from the center of the MMA-treated HCP specimens to the surface, the specimens cracked and could be split into two pieces by hand. Because of the corrosion products on the surfaces of steel bars, Groups (LCHV), (HCHV), and (Y-MMA) exhibited cracked specimens which were considered to have zero tensile strength presented in Table 4-3. The cracked specimens caused the steel bars to be directly exposed to the solutions so that the current density was increased in these cases.

It was observed in Figure 4-19 that the current density of Group (HCHV) increased at Day 3 when the first crack was observed. This cracked specimen was removed immediately to stop the available ions from accumulating around the exposed steel bar of the cracked specimen. Moreover, Group (Y-MMA) had a similar current density increase at Day 5 in Figure 4-21 when the first crack was observed here as well. During the MMA treatments, the current density of the treatment circuit dropped after the removal of the broken specimens. Therefore, these current-density increases observed after the MMA-treated HCP specimens cracked indicated that these specimens failed during the MMA treatments.

4.3.5 Porosity Results

Figure 4-28 shows the average porosity of the HCP specimens that were subjected to electrodeposition and MMA treatments. Error bars represent the 90% confidence interval of each result. It was observed that, compared with the control groups, all the treated groups had increases in the average porosity. However, the overlapping of the error bars indicated that the results were very similar. Table 4-4 shows the statistical analysis of the porosity. The results in Table 4-4 indicated that the average porosities (25.2% and 24.3%) of Group (O-MMA) and (Y-MMA) were statistically greater than those (22.5% and 22.9%) of the control groups, respectively. The average porosities of Groups (LCLV), (LCHV), and (HCHV) had no significant difference compared to their respective control group.

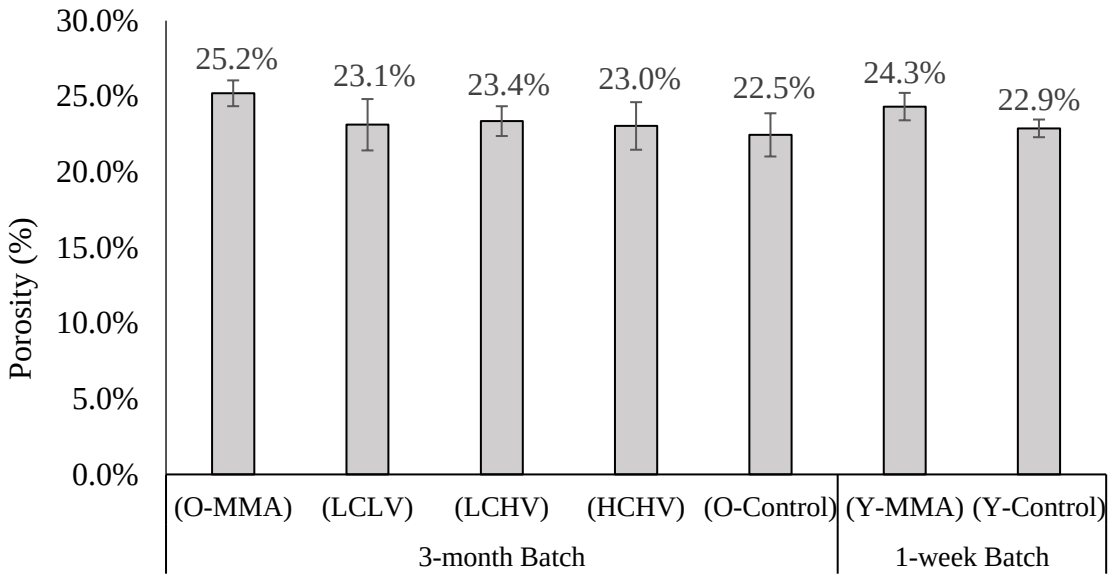

Figure 4-28: Average porosity of the HCP specimens which were subjected to the electrodeposition and/or MMA treatments. Groups (O-MMA) and (Y-MMA) were subjected to the MMA treatment only.

Apparently, when the HCP specimens in Groups (O-MMA) and (Y-MMA) were subjected to the MMA treatments, their porosities slightly increased. The anodic polarization of the steel bar in HCP specimens extracted the cations (Na^+, K^+, and Ca^{2+}) from the pores of HCP specimens and into the surrounding solutions during the MMA treatments. The loss of these cations caused the pores to lack sodium, potassium, and calcium solids when the water evaporated in the 105 ℃ oven. The lack of these solids may have caused the porosity to increase somewhat as presented in Table 4-4.

Table 4-4: Statistical analysis of average porosities of MMA-treated HCP specimens in groups 1-4 (Compared with Group 5), and 6 (Compared with Group 7).

	3-month Batch				1-week Batch
	(O-MMA)	(LCLV)	(LCHV)	(HCHV)	(Y-MMA)
F-test	2.81	1.41	2.11	1.21	2.40
F-table	6.59	9.12	6.59	9.12	6.39
T-test	2.65	0.46	0.83	0.43	2.20
T-table	2.36	2.36	2.36	2.36	2.3
Significance Result	Yes	No	No	No	Yes

95% confidence for F-test, 90% confidence for T-test

Groups (LCLV), (LCHV) and (HCHV) were subjected to the electrodeposition (ED) treatments prior to the MMA treatments. During the ED treatments, the cations were attracted into the pores of the MMA-treated HCP specimens from the solutions. The increased concentrations of cations in the pores during the ED treatments may have compensated for the loss of cations during the MMA treatments. This may have caused

the porosities of the MMA-treated HCP specimens in Groups (LCLV), (LCHV) and (HCHV) not to increase significantly as presented in Table 4-4. Therefore, the MMA treatments appeared to cause the porosities of only Groups (O-MMA) and (Y-MMA) to increase significantly.

4.4 Potentiodynamic Polarization Scanning on Rebar

This section examines the trans-passive turning points of the 1018 steel bars which were subjected to the potentiodynamic polarization tests. The steel bars were embedded in HCP or directly exposed to the simulated pore fluid (SPF) (See Table 3-4). Subsequently, the results of uncertainty analysis regarding power supply and the reference electrode performance will be presented.

4.4.1 Potentiodynamic Polarization Tests of Steel Bars

The results of the corroded area analysis shown in Figure 4-25 indicated that if the corrosion potential is too high during the MMA treatment, the embedded steel bars in the HCP specimens may corrode. Figure 2-13 shows that when a steel bar enters the trans-passive region from the passive region, the polarization current will significantly increase. The point where the current starts to increase significantly is termed as the trans-passive turning point (TTP). Apparently, if the corrosion potential in MMA treatments is lower than TTP, it will be expected to see no corrosion growth on the surface of the steel bars would take place during these treatments. This portion of the study was conducted to locate the TTP via the potentiodynamic polarization of the 1018 steel bars. In this section, one example scan is presented. Other scans are presented in Appendix E.

Figure 4-29 shows an example scan of Trial 4 from the -0.5 V to +1.0 V (corrosion potential). Trials 1-6 (See Table 3-4) were the potentiodynamic polarization tests to scan the corrosion potential and electric current behavior when the 1018 steel bars were directly exposed to SPF. When the steel bar entered the trans-passive region (discussed in Section 2.6.2), the significantly increased current indicated oxygen production from the oxidization of hydroxide ions—the breakdown of the passive film—and so the beginning of severe corrosion [119] [133] [134]. It was observed in Figure 4-29 that the electric current increased significantly when the corrosion potential was approximately +0.5 V. This potential was referred to as TTP. The TTP was taken as the intersection of the two trend lines shown in Figure 4-29. Two sections of the curve beside

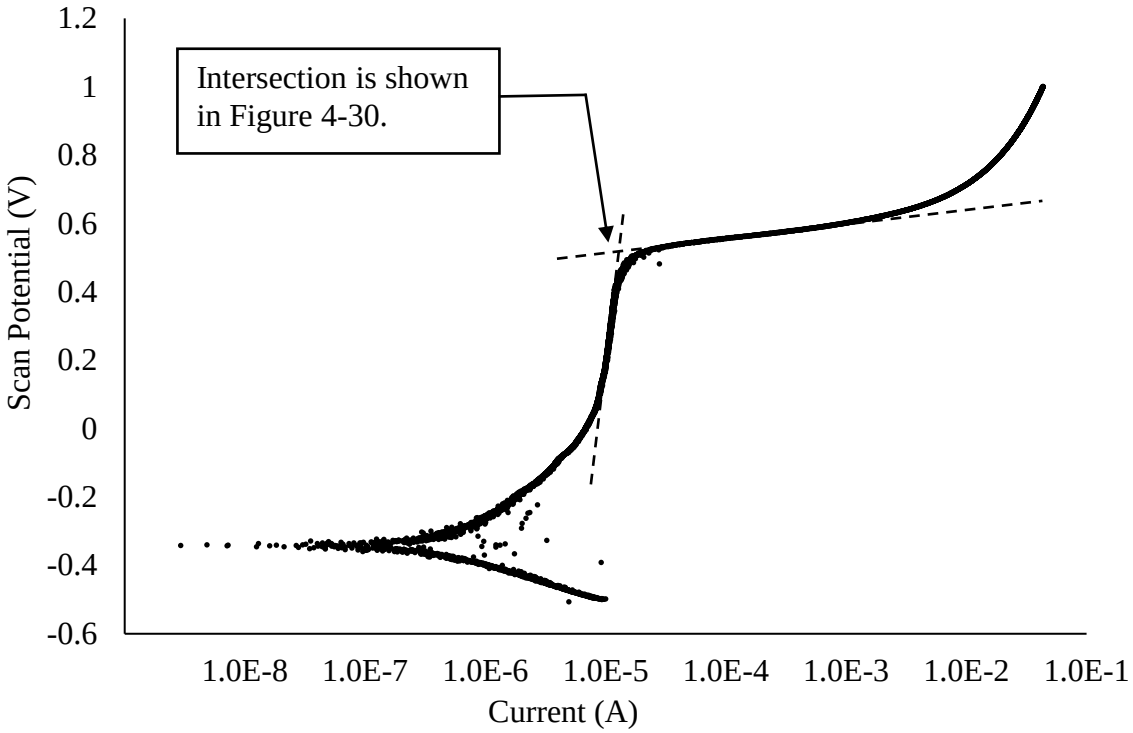

Figure 4-29: Potentiodynamic polarization curve of 1018 steel bar scanned in simulated pore fluid (See Table 3-4). The scanning corrosion potentials ranged from -0.5 V to +1.0 V. The current was monitored during scanning. The 0.1A current corresponds to a current density of 64.4 A/m^2.

the TTP were selected and shown in Figure 4-30. The functions of the two trend lines were calculated. These two functions consisted of a system of linear equations of two unknowns. After solving these equations, the values of the TTP (+0.523 V) were obtained. Potentiodynamic polarization tests indicated that the average corrosion potential at the transpassive turning point were 0.53 V as shown in Figure 4-31 when the steel bars were exposed directly to the SPF solution.

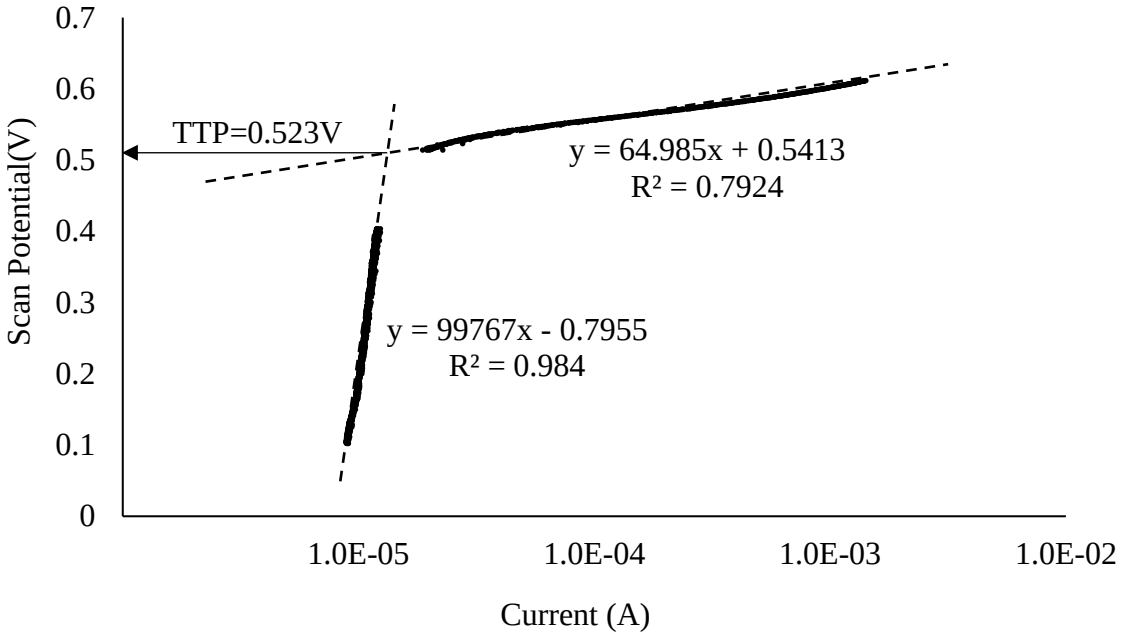

Figure 4-30: Two sections of curve were selected from Figure 4-29 to calculate the critical point at which the current began increasing significantly in the transpassive region. The intersection of these two dash lines is TTP.

Figure 4-32 shows the potentiodynamic polarization plot when the steel bars acted as the rebar embedded in the HCP specimens. Following the same procedures as described in the prior paragraph, two sections of the curve beside the TTP were selected as shown in Figure 4-33. The corrosion potential of the reinforced HCP specimen in

Figure 4-33 at the TTP was 0.649 V. Potentiodynamic polarization tests indicated that the average corrosion potential at the trans passive turning point were 0.67 V as shown in Figure 4-31 when the steel bars were exposed directly to the SPF solution.

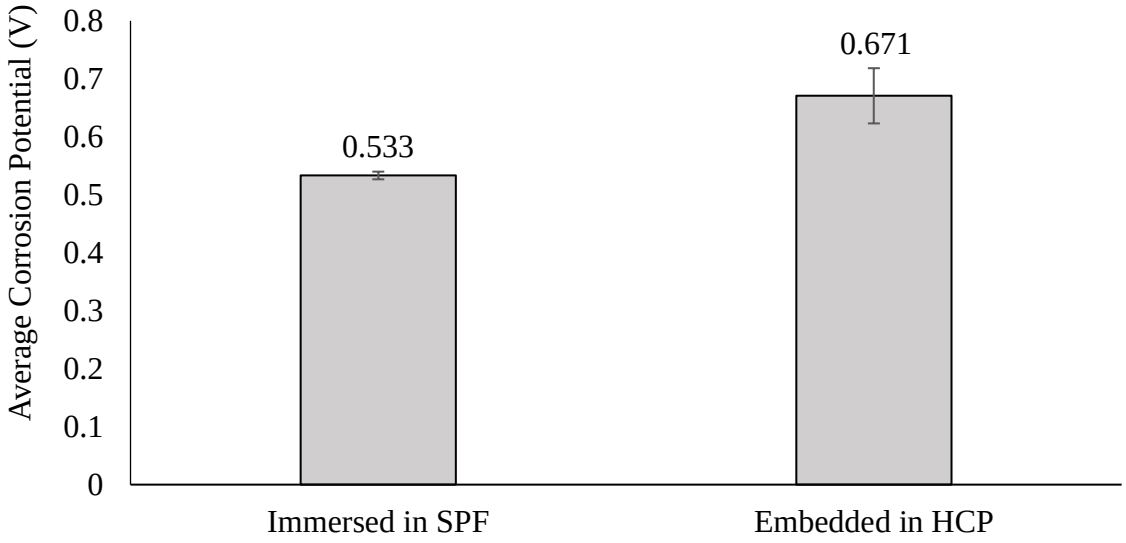

Figure 4-31: Average corrosion potentials when the 1018 steel bars reached the transpassive turning point (TTP). Each value was an average of six trials.

Figure 4-31 shows that the average TTP corrosion potentials of the bars in HCP are higher than the bare bars. This was probably because the embedded bars had been passivated in the HCP specimen for 20 days. This passive film on the surface of the bar would likely have been less conductive than the iron, so the currents of the bars in HCP (Figure 4-32) in the corrosion potential region (0-0.5 V) would be expected to be lower than those of the bare bars exposed to the SPF (Figure 4-29). The measurement of the corrosion potential of the bar in HCP specimen was expected to be more positive than the actual corrosion potential because of the IR drop (discussed in Section 2.6.2) between the reference electrode and the steel bar.

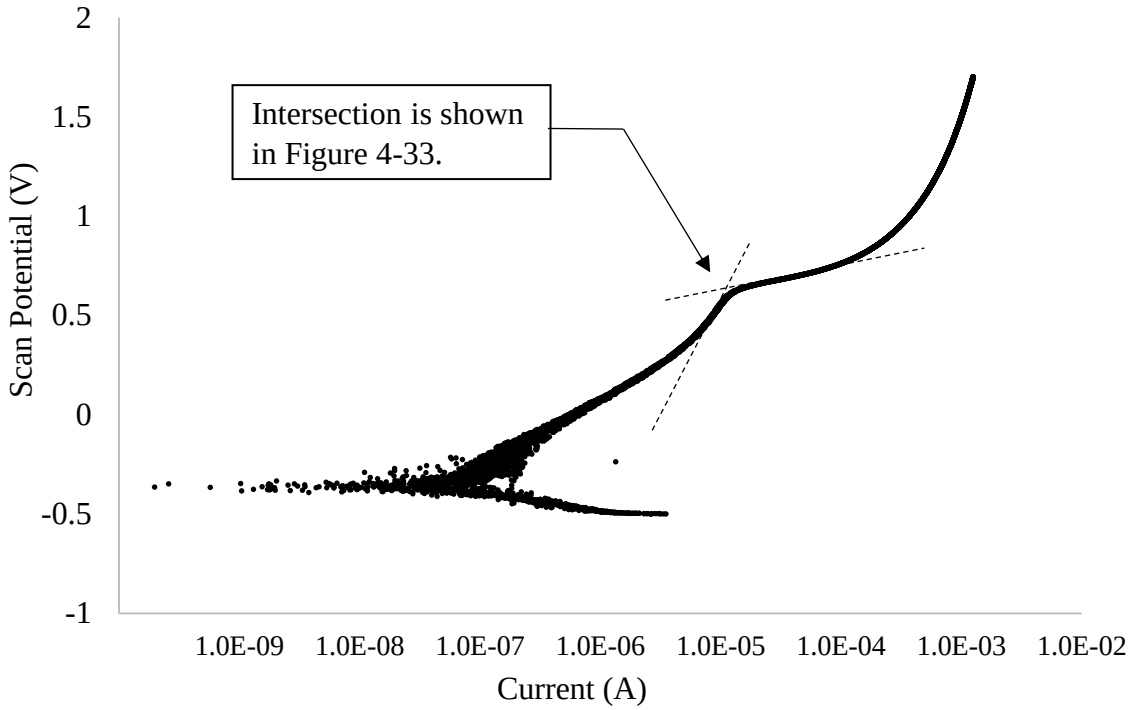

Figure 4-32: Potentiodynamic polarization curve of 1018 steel bar embedded within HCP specimen scanned in lime water (Trial 7 as described in Table 3-4). Scanning potential ranged from -0.5 V to +1.7 V. Electric current was monitored during scanning. The 0.01A current corresponds to a current density of 0.705 A/m^2.

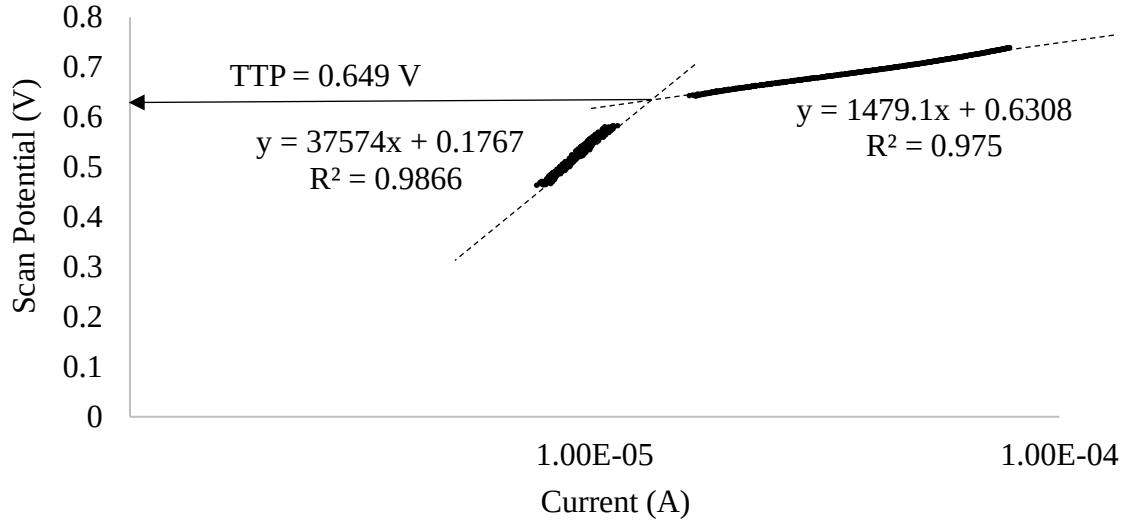

Figure 4-33: Two sections of curve were selected from Figure 4-32 to calculate the transpassive turning point (TTP) at which the current began increasing significantly (see Trial 7 as described in Table 3-4). The intersection of these two dash lines is the TTP.

The error bar of the average corrosion potential of the bars in HCP specimens in Figure 4-31 was 0.048 V according to Eq. 2-31 at the 90% confidence level. In order to prevent severe corrosion of bars during MMA treatments, the target corrosion potential was calculated as follows:

$$V_{Treat} = V_{TTP} - 2 \times V_{uncertainty}\,, \qquad \textbf{Eq. 4-13}$$

where the V_{Treat} is the corrosion potential applied in the MMA treatment discussed in Section 4.5, V_{TTP} is the average TTP corrosion potential of the bars embedded in the HCP specimens, and $V_{uncertainty}$ is the uncertainty that may cause the corrosion potential to scatter. When the error bar was the only factor of the uncertainty that may cause the scattering, the corrosion potential applied in the MMA treatment was 0.671-0.048 x 2 = 0.57 V via Eq. 4-13.

4.4.2 Uncertainty Analysis

After a corrosion potential of 0.57 V (calculated in Section 4.4.1) was applied to reinforce HCP specimens for MMA treatments, it was observed that the bars corroded in two of three trials. It was deemed possibly that instrument error could have been at fault. In this Section, the errors associated with the Cu/$CuSO_4$ reference electrode and the power supplies that are used for maintaining this low corrosion potential were quantified. The raw data for this error analysis is located in Appendix E.

Figure 4-34 shows the power supply uncertainty and reference electrode uncertainty observed. The average drift error of the power supply after a one-day treatment was 11 mV. The maximum observed drift error was 17 mV. The average error of the reference electrode after the potentiodynamic polarization tests was 18 mV. The maximum observed error was 24 mV. The sum of the error bar value (48 mV) of the TTP

of bars in HCP (shown in Figure 4-31), the maximum power supply error (17 mV), and the maximum reference electrode error (24 mV) was (48 + 24 + 17 = 89) mV, constituted was the total uncertainty in the MMA treatment. After substituting this total uncertainty into equation 4-13, the new corrosion potential selected for application of MMA treatments was adjusted 0.671-0.089 x 2 = 0.49 V, which protected against trans passive corrosion.

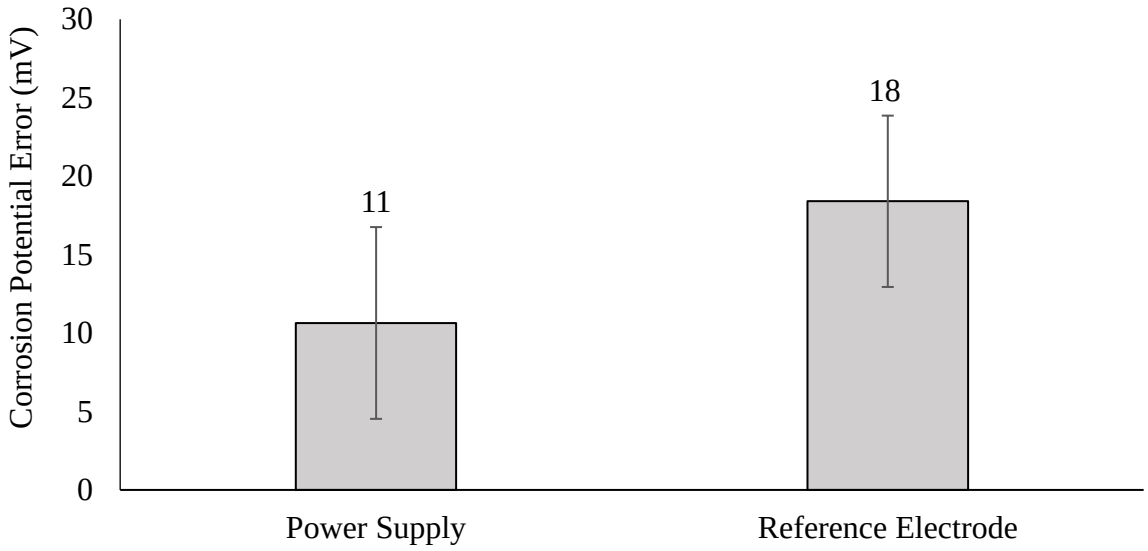

Figure 4-34: Errors due to power supply (PS) and reference electrode (RE) uncertainty. This represents the average value of voltage drift of the PS after one-day of treatment. The average error of the PS was obtained from 28 trials. After each potentiodynamic test, the tested $Cu/CuSO_4$ RE was compared with another standard RE that was stored in de-ionized water. In the RE column (above), the RE uncertainty is the average value of 10 trials.

MMA Treatment with Small Corrosion Potentials

In this section, two corrosion potentials, +0.57 V and +0.49 V, were applied in the MMA treatments in order to evaluate the effectiveness of the lower potential. Trials 1-3 were subjected to MMA treatments when the corrosion potential was +0.57 V vs. the

copper/copper sulfate reference electrode (CSE). Trial 4 was subjected to MMA treatment when the corrosion potential was +0.49 V vs. CSE. The electric current distribution, corrosion potential, applied voltage, tensile strength, and porosity of each trial are discussed in the following sections. After porosity tests, the possibility of poly(methyl methacrylate) formation was examined by attenuated total reflectance Fourier-transform infrared spectroscopy (ATR).

4.4.3 Current Density Profile and Corrosion Rate

In this study, there were four trials conducted on reinforced HCP specimens. The MMA-treated HCP specimens in Trials 1-3 were subjected to the MMA treatments with the corrosion potential of +0.57 V. The MMA-treated HCP specimens in Trial 4 were subjected to the MMA treatment with the corrosion potential of +0.49 V. Each trial contained 12 HCP specimens. Six of them were subjected to the MMA treatment, and the others were retained as controls that were soaked in lime water. During the MMA treatments, six MMA-treated HCP specimens were wired together. The electric currents, applied voltages, and corrosion potentials were monitored daily.

Figure 4-35 shows the current density profile of MMA treatments in 10 days. It was observed that the current densities were overall lower than the 20 $\mu A/cm^2$ with respect to the surface area of the steel bars. Only the current densities on Days 3 and 4 in Trial 3 were higher than 20 $\mu A/cm^2$. This was because one of the HCP specimens cracked at Day 3 and caused the bar to be exposed directly to the solution. However, the cracked specimen was observed and removed from treatment on Day 4. Trial 1 had one extra treatment day because the fuse of ampere meter melted at Day 5.

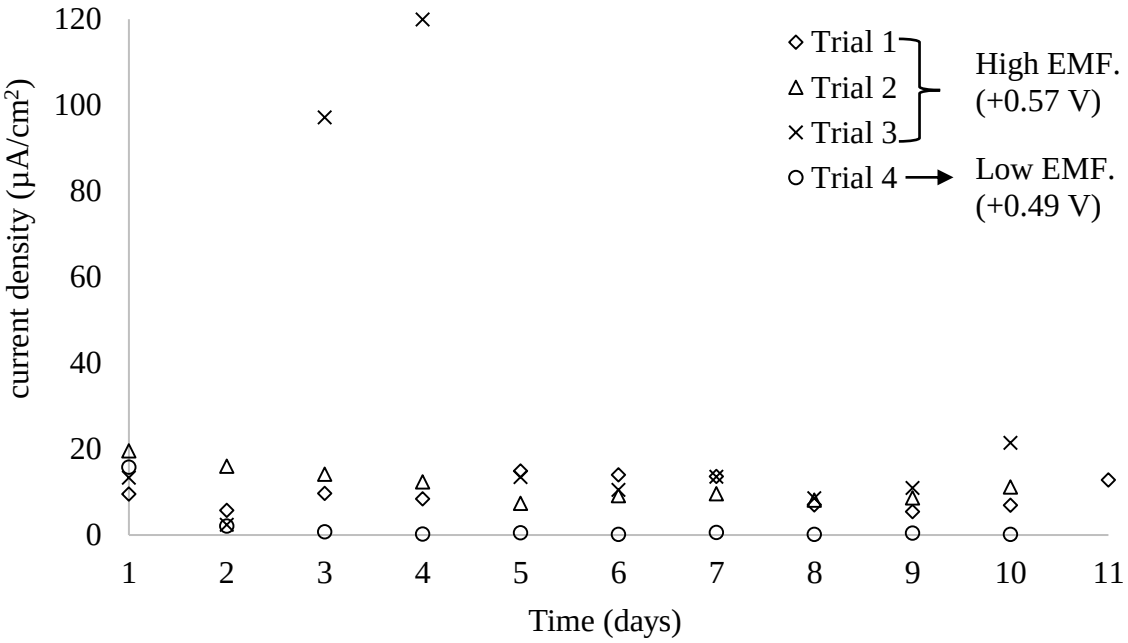

Figure 4-35: Steel rebar surface current density profiles for Trials 1-4. Trial 1 had one extra treatment day because of the occurrence of an open circuit on day 6. Trial 3 had a cracked specimen at day 3, causing the rebar of the specimen to be exposed to solution and draw an increased current.

In figures 4-32 and 4-33, it was observed that the current of the reinforced HCP specimen was approximately 10 µA at the trans-passive turning point (TTP). At that time, the current density was 0.64 µA/cm^2 (at steel rebar surface). With the 0.64 µA/cm^2 value taken as the TTP current density, all the current densities in Trials 1-3 were significantly higher than this TTP (0.64 µA/cm^2) in Figure 4-35. The current densities from Day 4 to Day 10 in Trial 4 (shown in Figure 4-36) were lower than this TTP current density.

Figure 4-37 shows the applied voltage profiles of MMA treated HCP specimens for Trials 1-4 during the MMA treatments. It was observed that at Day 1 the applied voltages of all trials were not significantly higher than those on other days. Unlike the applied potential profile in Figure 4-20 (involving high applied potentials at Day 1), the applied potential at Day 1 was significantly higher than other days because of the low

conductivity of the solution. With the addition of calcium hydroxide during the MMA treatments presented in Figure 4-37, the conductivity of the solution increased in order to solve the problem of the high applied potential at Day 1.

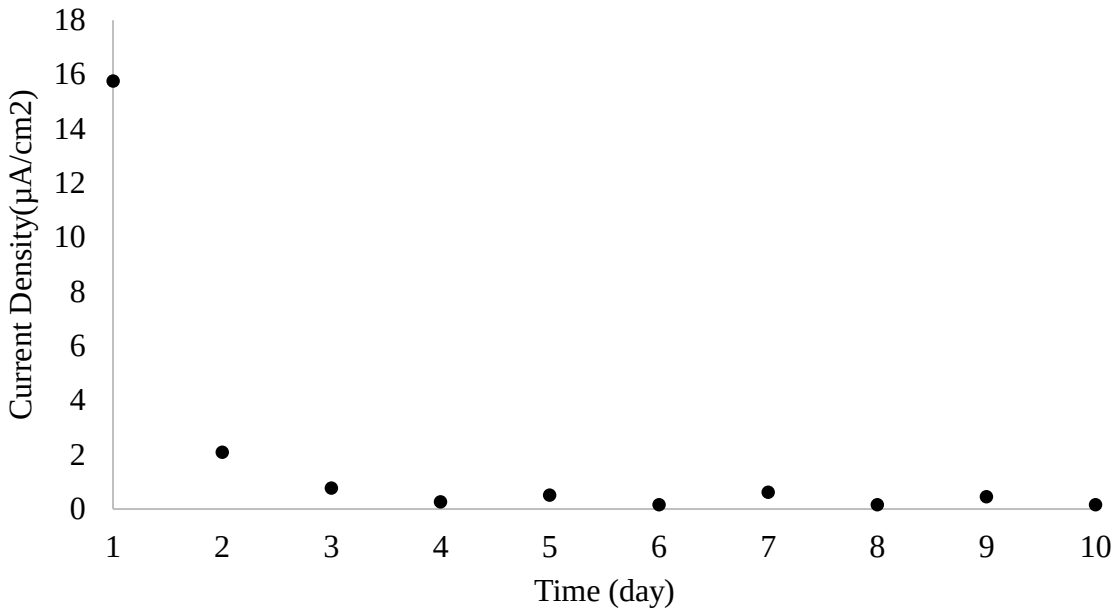

Figure 4-36: Steel bar surface current density profiles for HCP-MMA treatment applied with corrosion potential of 0.49 V in Trial 4.

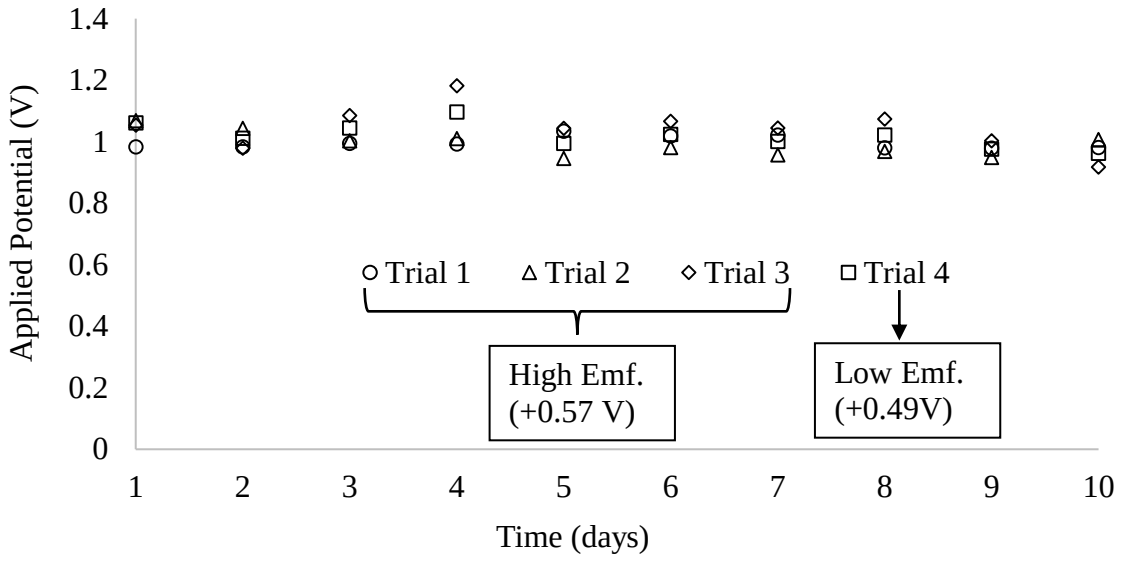

Figure 4-37: Applied voltage profile of Trials 1-4 (as described in Table 3-7). Trials 1-3 were subjected MMA treatments when the corrosion potential of the rebar was maintained at +0.57 V. Trial 4 was subjected MMA treatment when the corrosion potential was maintained at +0.49 V to avoid transpassive activation.

Using the current densities in Figure 4-35, the corrosion rates of the reinforcement in the MMA-treated HCP specimens can be calculated via Eq. 2-39. The equivalent weight of steel is 27.92 g/equiv [135]. The density of steel is 7.87 g/cm^3. The number of electrons involved in the reaction is 2. The calculated corrosion rates are presented in Table 4-5. It can be observed that the estimated corrosion depths on the steel bars in Trials 1-4 were 1.56, 1.85, 4.95, and 0.33 µm, respectively. The corrosion rate of the control HCP specimens was estimated based on the Tafel plot shown in Figure 2-15. By examining the potentiodynamic polarization plots (Appendix E-Figures E-13 to E-23), it can be estimated that the corrosion current, I_{corr}, was lower than 10^{-6} A, which indicated the current density of 0.1 µA/cm^2. Therefore, by using Eq. 2-40, the corrosion rate of the control specimens was lower than 0.1 µm.

Table 4-5: Corrosion rate of 1018 steel bars during MMA treatments**.**

	Trial 1	Trial 2	Trial 3	Trial 4	Control
Average Current Density (μm/cm^2)	9.8	11.6	31.1	2.1	0.1
Corrosion Rate (mm per year)	0.0570	0.0674	0.1806	0.0121	0.0004
Corrosion Rate (μm per day)	0.156	0.185	0.495	0.033	0.001
Corroded Depth (μm)	1.562	1.847	4.948	0.333	0.010

It should be noted that the corroded depth calculated for the steel bars in Trials 1-4 was significantly higher than that of steel bars in the control specimens. When the reinforced HCP specimens were subjected to the MMA treatments, the steel bars were subjected to anodic polarization. The polarization currents at or below the TTP caused the oxidation of iron which tends to produce $Fe(OH)_4^-$ based on the Pourbaix diagram in Figure 2-16. The formation of $Fe(OH)_4^-$ consumes the hydroxide ions significantly, the pH value of the environment decreases, and $Fe(OH)_4^-$ may transform into Fe_2O_3. The density of Fe_2O_3 is 5.24 g/cm^3 [136]. This density is significantly lower than the density of iron. This indicated that the corrosion of iron induced an expansion of the space occupied by the iron and its oxide. Expansion of reinforcement was expected to exert tensile stress originating at the centers of HCP specimens. This tensile stress apparently caused the cracks that were observed in some of the HCP specimens in Trial 3. Moreover, if the applied potential caused the steel bars to enter the trans-passive region shown in Figure 2-13, the oxidation of hydroxide ions can produce oxygen gas (Eq. 2-42) that could tend to accelerate the corrosion of steel [134]. Apparently, the cracked

specimen in Trial 3 at Day 3 indicated that this accelerated corrosion due to the anodic polarization could damage the HCP specimens.

4.4.4 Image and Coulomb Passage Analysis

Current density analysis in the previous section indicated that Trials 1-3 may exhibit the signs of corrosion on the steel bars of the MMA-treated HCP specimens. It was observed that the bars in the MMA-treated HCP in Trial 3 had significant corrosion as shown in Figure 4-38. Trials 1, 2 and 4 did not exhibit visible corrosion on the steel bars in the MMA-treated HCP specimens. These results indicated that when the bars were subjected to the corrosion potential at or exceeding +0.57 V, the passive film was possibly transformed into Fe_2O_3 during the MMA treatments due to the anticipated decrease of pH (discussed in Section 4.5.1). Moreover, in Table 4-5, it can be observed

Figure 4-38: Comparison of bars from the MMA-treated group (Left) and the control group (Right) in Trial 3. The steel bars in the MMA-treated HCP exhibited a brown corroded coating (Left). The target corrosion potential for treatment was maintained at +0.57 V. Trials 1, 2, and 4 exhibited no sign of corrosion on the MMA-treated bars.

that the corroded depths (1.6, 1.8, and 0.3 μm) of the bars from Trials 1, 2 and 4, respectively, were significantly lower than that (4.9 μm) from Trial 3. These corrosion rates were consistent with the images of the bars in MMA-treated HCP cases from Trials 1-4 (significant corroded bars in Trial 3 are shown in Figure 4-38).

Figure 4-39 shows the cumulative electric charges passed per MMA-treated HCP specimen during the MMA treatment. Apparently, Trials 1-3 had more electric charge passage than Trial 4 most likely because the treated specimens in Trials 1-3 were subjected to a higher corrosion potential (0.57 V compared to 0.49 V). When the corrosion potential increased from 0.49 V to 0.57 V during the MMA treatments, the cumulative electric charges of Trial 4 were 1/5 of that of Trials 2 and 3, and 1/4 of that of Trial 1.

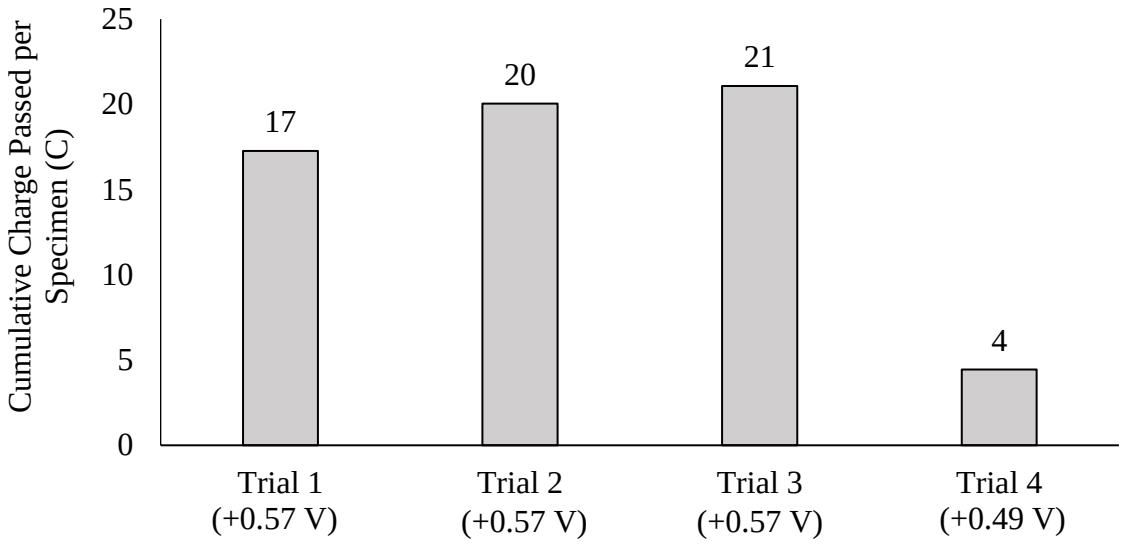

Figure 4-39: Cumulative electric charge passed per HCP specimen during MMA treatments. The passed charges in Day 3 and 4 were excluded from the calculation because Trial 3 developed a cracked specimen during those days.

The cumulative passage electric charges are related to the corrosion severity of the MMA-treated bars. If a steel bar has more cumulative electric charges, it will tend to have a more extensive corroded coating. However, the bars in the MMA-treated HCP cases from Trial 2 did not exhibit a similar coating like that of Trial 3 even though Trials 2 and 3 had nearly the same cumulative electric charges shown in Figure 4-39. This may be attributed to the age difference of the HCP specimens in Trials 2 and 3. The ages of the HCP specimens in Trials 2 and 3 were 34 and 72 days, respectively. The older HCP specimens were expected to exhibit a lower pH value of the pore fluid because the older HCP specimens were soaked in lime water for a longer time. When the alkaline ions in the specimens diffused from the pores, the pore fluid in older HCP specimens were expected to exhibit a more similar pH value with lime water (pH = 12.5) (discussed in Section 4.3.2). Moreover, the older specimens were exposed to carbon dioxide for a longer time. This may also cause the pH value of the pore fluid to decrease. When the pH value of the environment around the steel bar is below 13, the $Fe(OH)_4^-$ will transform into Fe_2O_3 shown in Figure 2-16. Apparently, the older HCP specimens (72 days) in Trial 3 exhibited a less basic (pH < 13) environment which may also cause the brown coating (Fe_2O_3) that was observed after tensile testing. The younger HCP specimens in Trial 1 and 2 (32 and 34 days-old, respectively) likely exhibited a more basic (pH > 13) environment which would be less likely to form Fe_2O_3, thus permitting better strength than observed in older specimens.

4.4.5 Indirect Tensile Strength

Figure 4-40 shows the average tensile strength of the MMA-treated reinforced HCP specimens from Trials 1-4. Trials 2-4 exhibited decreases in the tensile strength

after the MMA treatment. The tensile strength of treated specimens decreased by 44% in Trial 2, 27% in Trial 3, and 33% in Trial 4. Apparently, the treated specimens were not strengthened by the MMA treatment, and on the contrary, were apparently impaired.

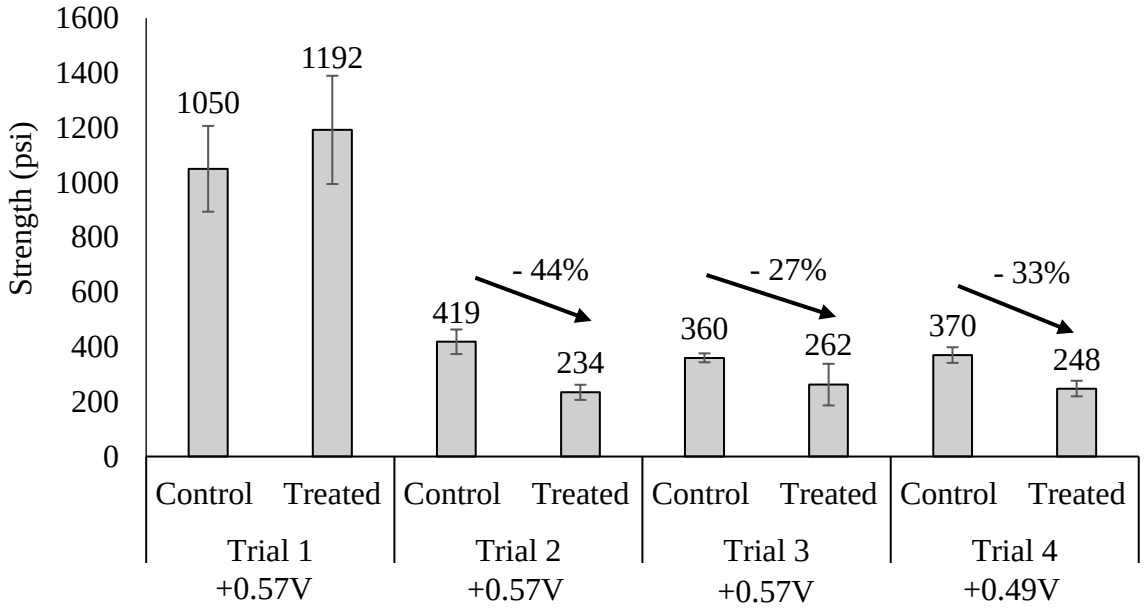

Figure 4-40: Average indirect tensile strength of MMA-treated HCP (trials 1-4). Each value represents the average tensile strength of six specimens. (One of specimens in Trial 3 cracked when subjected to the MMA treatment.)

Trial 1 exhibited an increase on the tensile strength, but this result could possibly be attributed to specimen defects (oblique oriented bars at center) which caused the tensile strength to be nearly twice that of the tensile strength of other trials. During the batching of Trial 1, the steel bars were not fixed firmly and vertically at the center of the specimens to prevent an oblique orientation. Oblique bar orientation possibly caused the bars to be unparalleled with the surface of the HCP specimens. When these specimens were subjected to indirect tensile strength testing, the load line was not consistently parallel with the bars so that the apparent tensile strength of specimens would have been

raised higher than the normal tensile strength of the control specimens in Trials 2-4. After the correction of this batching defect, the average tensile strength decreased significantly, and the scatter (error bar size) of the data was smaller. It was observed that the tensile strengths of the control specimens in Trials 2-4 did not vary significantly, even though their ages were different (34 days for Trial 2, 72 days for Trial 3, and 41 days for Trial 4). This is not surprising since all the batch ages were beyond 28 days at the time of tensile testing.

Table 4-6 shows the statistical analysis of the tensile strength between the treated and control specimens. The results of the Student's t-test indicated that the average tensile strengths of the treated specimens of Trials 2-4 were significantly different from those of the control specimens (90% confidence). This was because the values of T-test in Trials 2-4 were more than the values of T-table. The value of T-test in Trial 1 was less than the value of T-table. This result indicated that the average strengths of the treated and control specimens were not significantly different.

Table 4-6: Statistical analysis of average tensile strength of trials 1-4.

	Trial 1	**Trial 2**	**Trial 3**	**Trial 4**
F-test	1.6	2.6	18	1
F-table	5.1	5.1	5.2	5.1
T-test	0.9	5.8	2.1	5.0
T-table	1.8	1.8	2.1	1.8
Significance Result	No	Yes	Yes	Yes

95% confidence for F-test, 90% confidence for T-test.

The expansion of trans-passive (corroded) steel bars in the MMA-treated HCP specimens in Trials 2 and 3 caused the cracking to occur at the center of HCP specimens. These microscopic cracks probably caused elevated stress concentrations during the indirect tensile strength testing. The stress concentration caused by this damage probably caused the tensile strength to decrease for the MMA-treated HCP specimens in Trials 2-4. This loss of strength due to the corrosion on the steel bars of the MMA-treated specimens was apparently not compensated by the electropolymerization of MMA.

4.4.6 Porosity Results

Figure 4-41 shows the average porosities of the MMA-treated HCP specimens in Trials 1-4. It was observed that the average porosities of the treated specimens were higher than those of the controls. However, the statistical analysis shown in Table 4-7

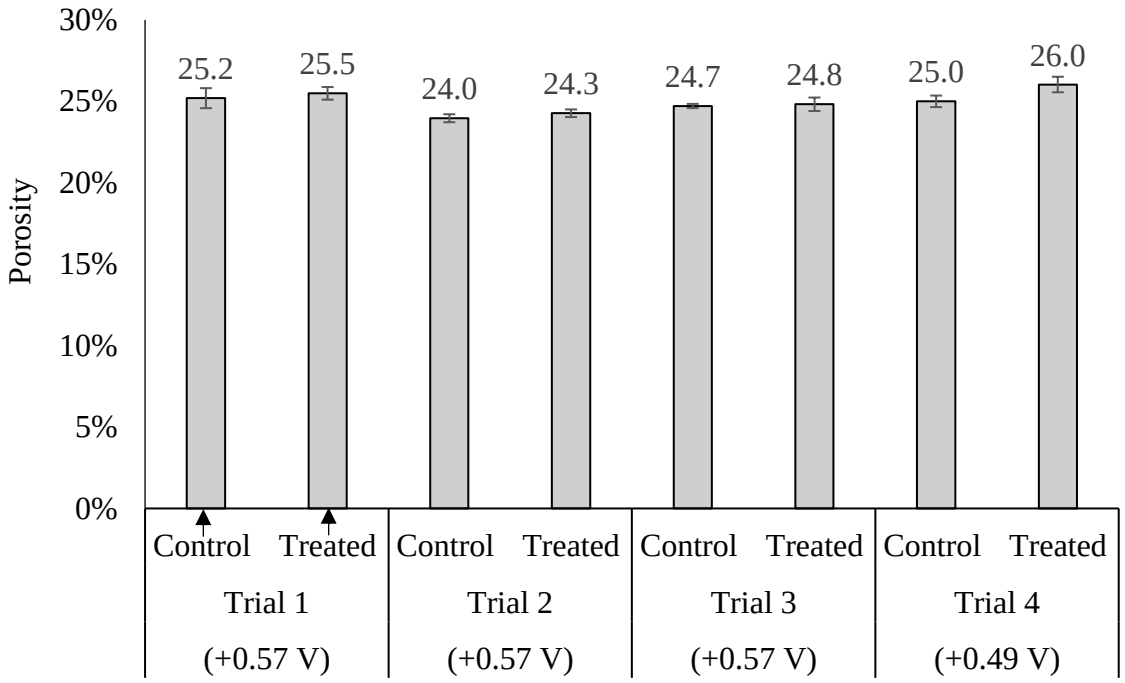

Figure 4-41: Average porosities of the HCP specimens in trials 1-4. Each value represents the average porosity of six specimens. (One of specimens in Trial 3 cracked when subjected to the MMA treatment.)

indicated that only the average porosity of the treated samples in Trial 4 was significantly higher than that of the control specimens at the 90% confidence level. Apparently, the porosity was not reduced by the MMA treatments in contrast to what was anticipated.

Table 4-7: Statistical analysis of the average porosities of the MMA-treated HCP specimens in trials 1-4.

Analysis Values	Trial 1 (+0.57 V)	Trial 2 (+0.57 V)	Trial 3 (+0.57 V)	Trial 4 (+0.49 V)
F-test	2.5	1.1	8.4	1.8
F-table	5.1	5.1	5.2	5.1
T-test	0.7	1.5	0.4	2.9
T-table	1.4	1.8	1.5	1.8
Significance Result	No	No	No	Yes

95% confidence for F-test, 90% confidence for T-test.

The significantly increased porosities in Trial 4 indicated that the decreased tensile strengths (from 370 to 250 psi) could possibly be attributed to these increased porosities because the increased porosity generally causes the strength of HCP and concrete to decrease somewhat linearly [137]. However, the unchanged average porosity in Trials 2 and 3 did not support this opinion since the average tensile strength of the treated HCP specimens also decreased significantly. Therefore, the decreased tensile strength of the MMA-treated specimens in Trial 4 seemed to be attributed to the cracking that occurred at the interface of steel and HCP because of the bar's expansion.

4.4.7 PMMA Characterization Results

The porosity analysis in the previous section seemed to indicate that no PMMA formation had occurred in the pores of MMA-treated HCP specimens in Trials 1-4. This

was because no porosity decrease was observed after the MMA treatments. The experiments in this section were conducted to verify the existence of PMMA in the MMA-treated HCP. After evaporating the acetone solvent in 24 hours, a clear, odorless, oil-like liquid was obtained from the MMA-treated HCP powder of Trial 3 (+0.57 V). Figure 4-42 shows the characterization result of the liquid analyzed by the Attenuated Total Reflectance-Fourier-Transform Infrared Spectroscopy (ATR). Peaks B-F in Figure 4-42 indicate that the extracted liquid is PMMA. This is because the molecular structure of PMMA contained C-H, C-C(=O)-O, and C=O bonds.

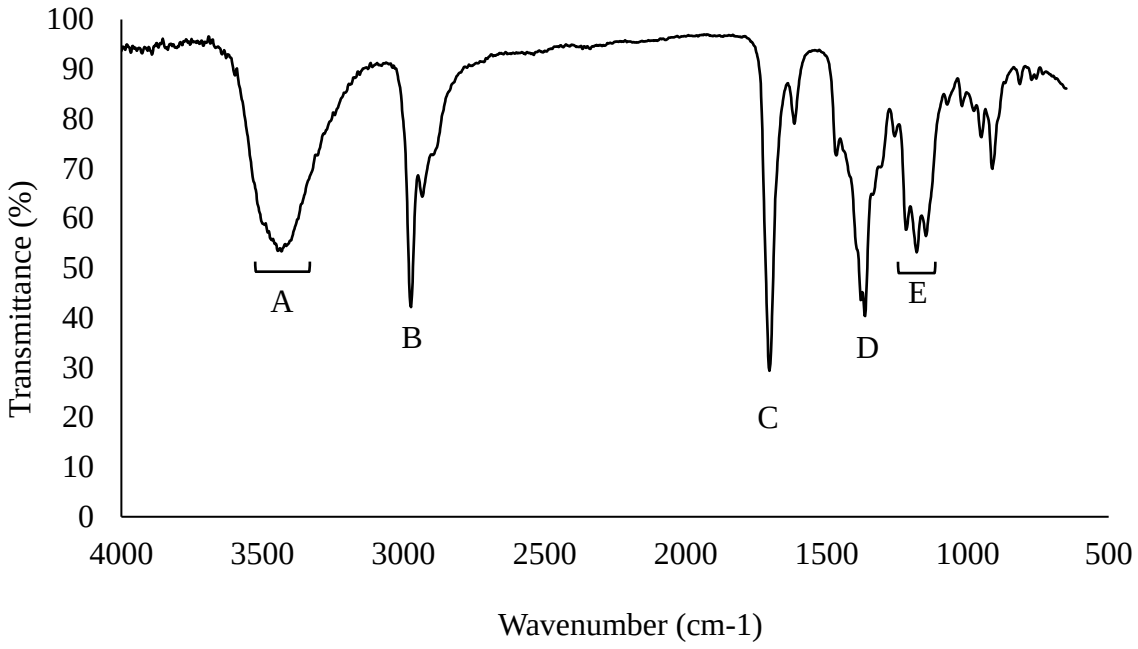

Figure 4-42: ATR analysis of the extracted liquid from the MMA-treated HCP specimens of Trial 3 (+0.57 V). Peak identification: A. The O-H stretch, intermolecular hydrogen bonding 3444 cm^{-1} [107]. B. The C-H stretch, 2972 cm^{-1}. C. The C=O stretch, 1702 cm^{-1}. D. The C-H bend, 1365 cm^{-1}. E. The C-C(=O)-O stretch, 1180 cm^{-1}. These are compared with standard PMMA and acetone in Figure 4-44.

PMMA extraction of the control specimens was also conducted, and no liquid or solid residue was observed. Moreover, no significant volume of residue sample (sufficient to conduct an FTIR test) was obtained from Trial 4. After the PMMA extraction in Trial 4, it was observed that the wall of the beaker was dampened with an uncollectable layer of oil-like materials. This result indicated that the production of PMMA in Trial 4 was significantly lower than that of Trials 1-3. The MMA-treated HCP specimens in Trial 4 were subjected to the corrosion potential of +0.49 V. The electric current densities during the MMA treatment were significantly lower than those of Trials 1-3. The lower currents appeared to correlate the result in the low conversions of the MMA monomer during the MMA treatment [138].

Figure 4-43 shows the ATR characterization result of the acetone fluid (99.7%) that was used to extract the PMMA out of the HCP powder in Trials 3 and 4. It is observed that figures 4-42 and 4-43 have several identical signal peaks that represented

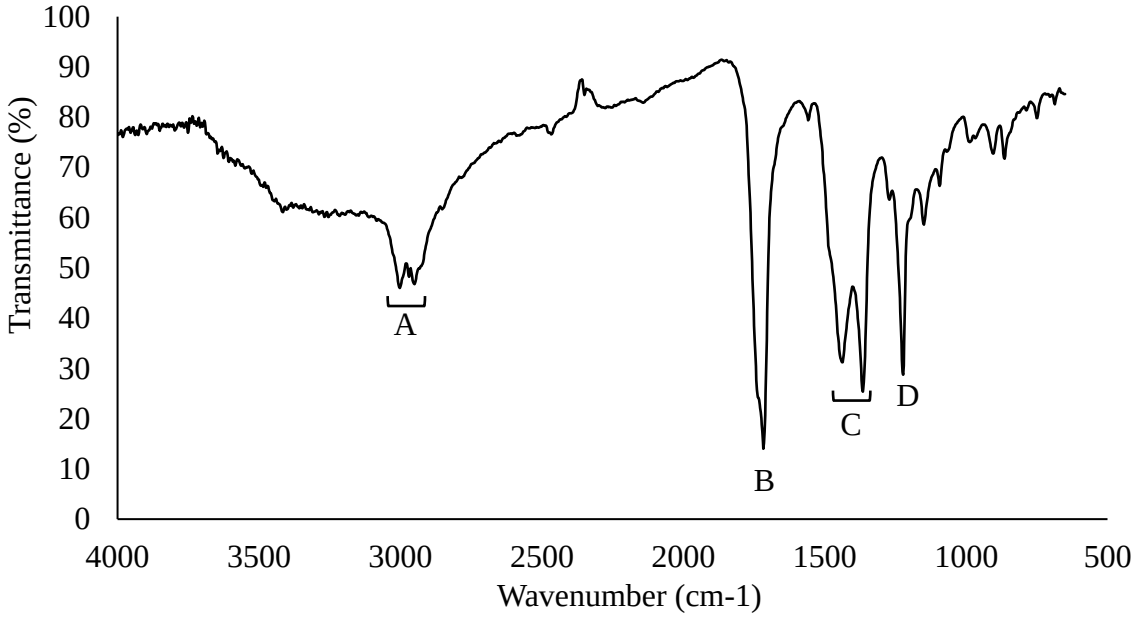

Figure 4-43: ATR analysis of acetone. A. C-Hs, 3000 cm^{-1}. B. C=O stretch, 1716 cm^{-1}. C. C-H bend, 1365 cm^{-1}. D. C-C-C asymmetric stretch, 1222 cm^{-1}.

the C-H bond and C=O bond. This is because acetone has similar molecular structures (C=O, C-H) with the PMMA. Because of the similarities of these molecular structures, acetone can dissolve a significant amount of PMMA.

Since acetone and PMMA have similar bonds that appear in the ATR spectrum, it was suspected that the extracted liquid with a clear, oil-like, appearance was acetone. Several pieces of evidence indicated that the liquid was not acetone. First, after 24 hours of evaporation, no liquid residue was obtained from the PMMA extraction tests of the untreated control samples. This indicated that the acetone had completely evaporated in 24 hours. The acetone used in the extraction process of PMMA of the treated specimens would similarly be expected to evaporate in 24 hours. Second, the extracted liquid did not exhibit an acetone odor. Moreover, in Figure 4-42, there are three peaks that occurred in the E region (~1200 cm^{-1}). In Figure 4-43, there is only one peak at 1222 cm^{-1}. This is because the molecular structures of the liquid product contained both the C-C-C bond and C-O-C bond. The stretches of these two bond systems occurred in the same region, thus yielding a peak in Figure 4-42 that was split into three peaks [107]. Figure 4-44 shows the overlapped ATR results of the liquid product, acetone, and the standard PMMA solids. Therefore, based on these descriptions of the evidence, the extracted organic liquid was not acetone but a species chemically similar to PMMA.

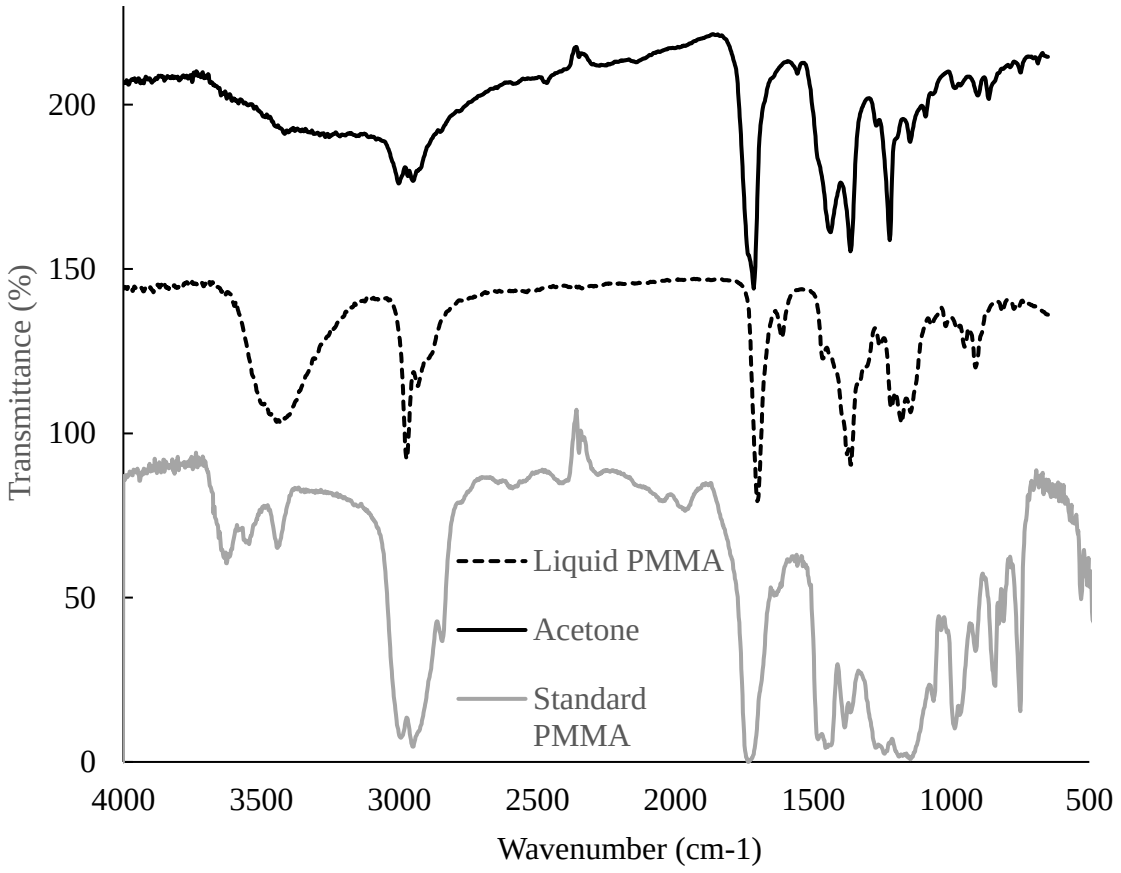

Figure 4-44: Overlapping of ATR results of the liquid product, acetone and the standard PMMA. It should be noted that the transmittances of spectrums of liquid product and acetone would need to be reduced by 50% and 130%, respectively, to obtain the exact transmittances.

4.5 Reproducibility Check on Strength Benefit of MMA Treatment

Nayeem's study indicated that the MMA-treated HCP specimens exhibited an increase of 50% in tensile strength. In order to check the reproducibility of this strength benefit, his experiment was conducted again in the current study [60]. In this section, the results of repeating Nayeem's experiments are discussed. The average electric current profile, average tensile strengths, and average porosities are presented in the following sections. Moreover, the ATR characterization results of the samples extracted from the

MMA-treated HCP samples are discussed. The pH value monitoring is discussed in the final section.

4.5.1 Current Density Time Profiles

Two trials were conducted to examine strength benefits of MMA treatment. The first one was a “No Solution Replacement" Trial (NSR), the other one was Daily Solution Replacement Trial (DSR). The only difference between these two trials was whether the MMA solutions were replaced daily. These two cases were examined because a significant pH drop that was anticipated for the NSR Trial could possibly damage the MMA-treated HCP specimens.

Figure 4-45 shows the average electric current densities (HCP surface) profile when the area of HCP surface is used in the calculation of the electric current density. Trials DSR and NSR exhibited significant decreases in the current densities during the MMA treatments. Also, when the solution was replaced daily in Trial DSR, the current densities were significantly lower than those of Trial NSR when the solution was not replaced.

It was possible that the polymerization of MMA caused the electrical resistance to increase during the MMA treatments. It was not surprising to observe that the current densities of Trial DSR were significantly lower than those of Trial NSR. This was because the solution in the DSR trial was replaced daily. Every daily replacement caused a proportion of ions coming from the MMA-treated HCP specimens to be lost. The loss of ions in the DSR trial was likely higher than that in NSR trial and may have caused the current densities of the DSR trial DSR be lower than in the NSR trial. Decreasing current

densities observed in both MMA-treated trials indicated that the concentration of available ions decreased during the MMA treatments.

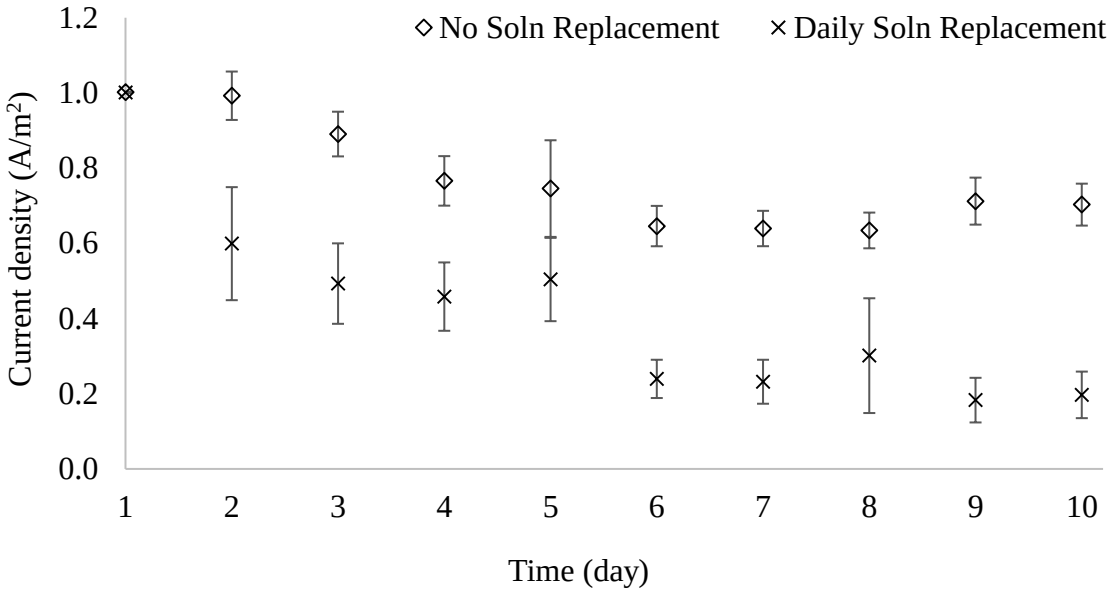

Figure 4-45: Average electric current densities profiles of trials NSR and DSR at constant voltages. The solution of Trial NSR was not replaced during the treatment. Each value represents the average current density of six trials.

4.5.2 Average Tensile Strength

Figure 4-46 shows the average tensile strength of the treated and control HCP specimens in Trials NSR and DSR. It was observed that after the MMA treatments, the average tensile strengths of Trials NSR and DSR decreased by 29% and 14%, respectively. Apparently, these tests failed to duplicate Nayeem's experimental result of the tensile strength benefit (50% increase) on the treated specimens. Table 4-8 shows the statistical analysis results by comparing the treated and control HCP specimens in each trial. It was calculated that in both trials, the average tensile strength of the treated HCP specimens was significantly lower than that of the control specimens at the 90% confidence interval.

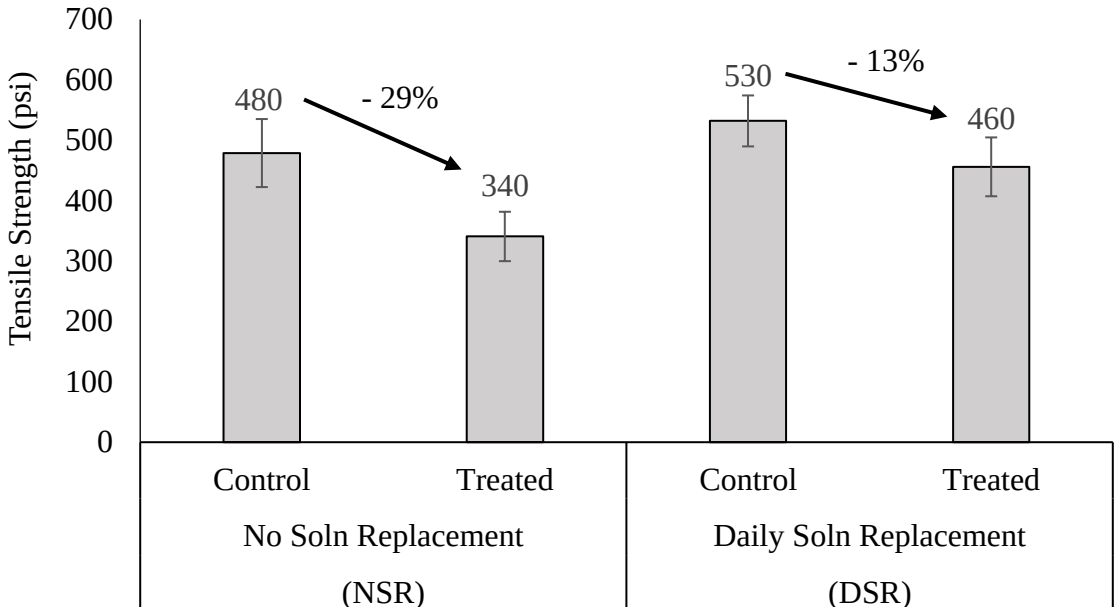

Figure 4-46: Average tensile strength of the HCP specimens of trials NSR and DSR. Each value represents the average tensile strength of six trials.

Table 4-8: Statistical analysis of the average tensile strength of the MMA-treated HCP specimens in trials NSR and DSR.

Analysis Values	NSR No Soln Replacement	DSR Daily Soln Replacement
F-Test	1.9	1.3
F-Table	5.1	5.1
T-Test	3.3	1.9
T-Table	1.8	1.8
Significance Result	Yes	Yes

95% confidence for F-test, 90% confidence for T-test.

The reduction in tensile strength of the MMA-treated HCP specimens could be attributed in part to the high current density at the center of the specimens. It was calculated that the applied current density during the MMA treatments was 1 A/m^2 with respect to the HCP surface. However, when the surface area was selected at the Ti-wire,

the current density was 55.7 A/m^2. It is recommended in the Concrete Repair Manual that the current density is in the range of 1-5 A/m^2 (steel surface) when the current is used for cathodic protection [139]. Apparently, the central current density at the beginning of the MMA treatment was 11 times the recommended current density. These results of tensile strength indicated that high current density may have caused micro cracks in the HCP specimens. These invisible micro cracks did not propagate to the surface of the specimen like the cracks caused by the corrosion of steel, but they can still cause the tensile strength to decrease significantly. This appeared evident when these specimens were subjected to the indirect tensile strength testing. Micro cracks or related damage due to high current density in the MMA-treated HCP specimens probably caused stress concentrations that lowered down the tensile strength.

4.5.3 Porosity Results

Figure 4-47 shows the average porosities of the HCP specimens in Trials NSR and DSR. It was observed that the average porosities of the MMA-treated specimens were higher than those of the control specimens in both trials. Table 4-9 shows the results of a statistical analysis of Trials NSR and DSR. Apparently, the average porosity of the MMA-treated specimens in Trial NSR was significantly higher than that of the control specimens at the 90% confidence interval. As is discussed in Section 4.6.2, the high current density resulted in the micro cracking in the center of the MMA-treated HCP specimens. These micro cracks may have increased the average porosity of the specimens.

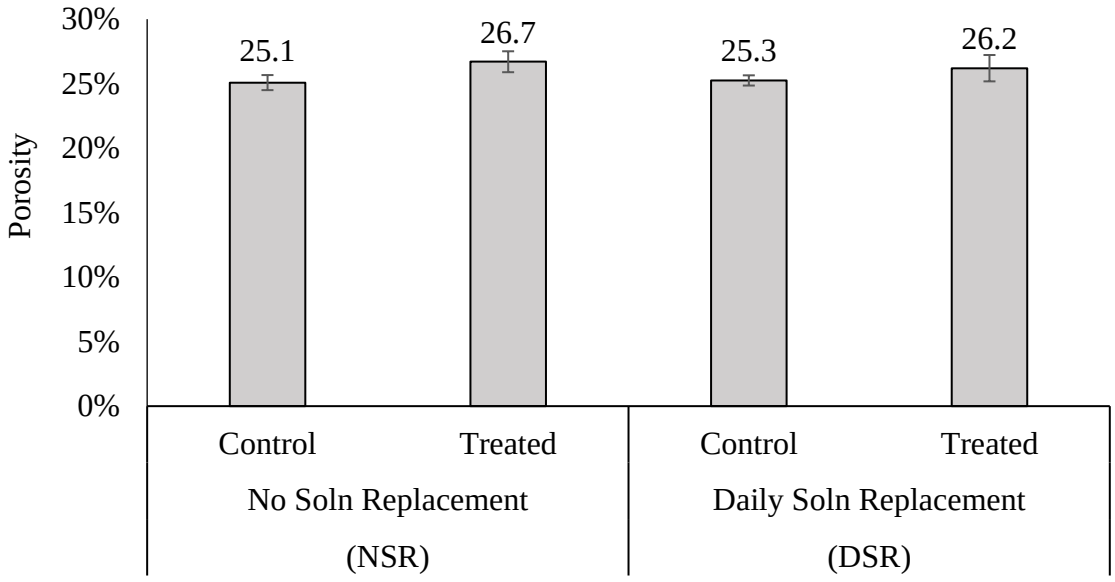

Figure 4-47: Average porosity of MMA-Treated HCP specimens in trials NSR and DSR. Each value represents the average porosity of six trials.

Table 4-9: Statistical analysis of the average porosity of the MMA-treated HCP specimens in trials 1 and 2.

Analysis Values	(NSR) No Soln Replacement	(DSR) Daily Soln Replacement
F-Test	1.9	6.7
F-Table	5.1	5.1
T-Test	2.7	1.4
T-Table	1.8	1.8
Significance Result	Yes	No

95% confidence for F-test, 90% confidence for T-test.

4.6.4. PMMA Characterization Results

Porosity test results appeared to indicate that no PMMA formation occurred in the pores of the MMA-treated HCP specimens because no reduction in porosity was observed after the MMA treatments. The experiments in this section were conducted to

extract organic samples from the MMA-treated HCP samples and subject them to chemical analysis. After the PMMA extractions were conducted on the MMA-treated HCP samples from the NSR and DSR trials, a clear, odorless, oil-like liquid was obtained. Figure 4-48 shows the ATR characterization results of these liquid samples from the NSR and DSR trials. Moreover, the spectrum of the PMMA liquid from the MMA-treated HCP samples (Trial 3, +0.57 V, in Section 4.5) is presented in Figure 4-48 for the comparison of the spectrums of liquid samples from related trials. The observed peak positions of the spectrums of liquid samples from the NSR, DSR trials and Trial 3 were nearly identical as shown in Figure 4-48. This result indicated that the extracted treatment liquid in this section was the same as the PMMA liquid discussed in Section 4.5.5.

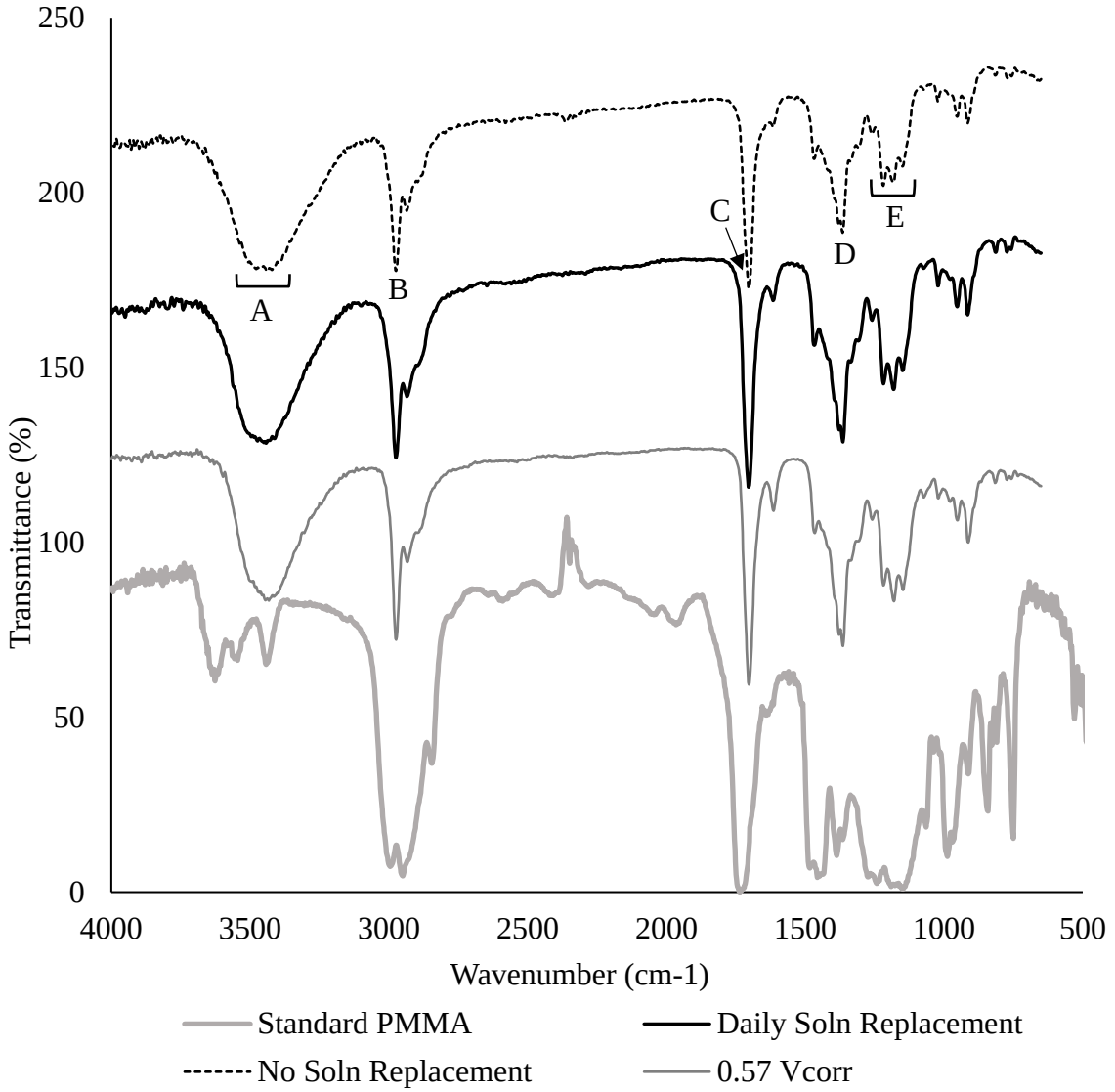

Figure 4-48: ATR characterization results of the extracted liquid from MMA-treated HCP specimens of trials NSR and DSR. Peak identification: A. The O-H stretch, intermolecular hydrogen bonding 3428 cm^{-1} [107]. B. The C-H stretch, 2973 cm^{-1}. C. The C=O stretch, 1702 cm^{-1}. D. The C-H bend, 1365 cm^{-1}. E. The C-C(=O)-O stretch, 1180 cm^{-1}. It should be noted that the transmittances of spectrums of 0.57 V_{corr}, daily soln replacement, and no soln replacement would need to be reduced by 30%, 100%, and 150%, respectively, to obtain the exact transmittances for these trials.

4.5.4 pH Monitoring

It was suspected that decreasing pH values may have damaged the MMA-treated HCP specimens in the NSR and DSR trials. It was observed that the tensile strength dropped significantly in both of these trials after the MMA treatments. The micro-cracking caused by the high current density could have been responsible for this damage. However, the acidic environment could also have damaged the HCP because the concentrated hydrogen ions were available to react with the calcium hydroxide in HCP, thus decomposing the HCP phases. The tests in this section were conducted to monitor the pH values of the solution in the NSR and DSR trials during MMA treatments.

Figure 4-49 shows the daily pH values of the solutions for Trials NSR and DSR during the MMA treatments. Each value represents the average pH of three trials. It can be observed that after the first-day treatment, both solutions in Trials NSR and DSR had an average pH of 10.8. After the 10-day treatments, both solutions in Trials NSR and

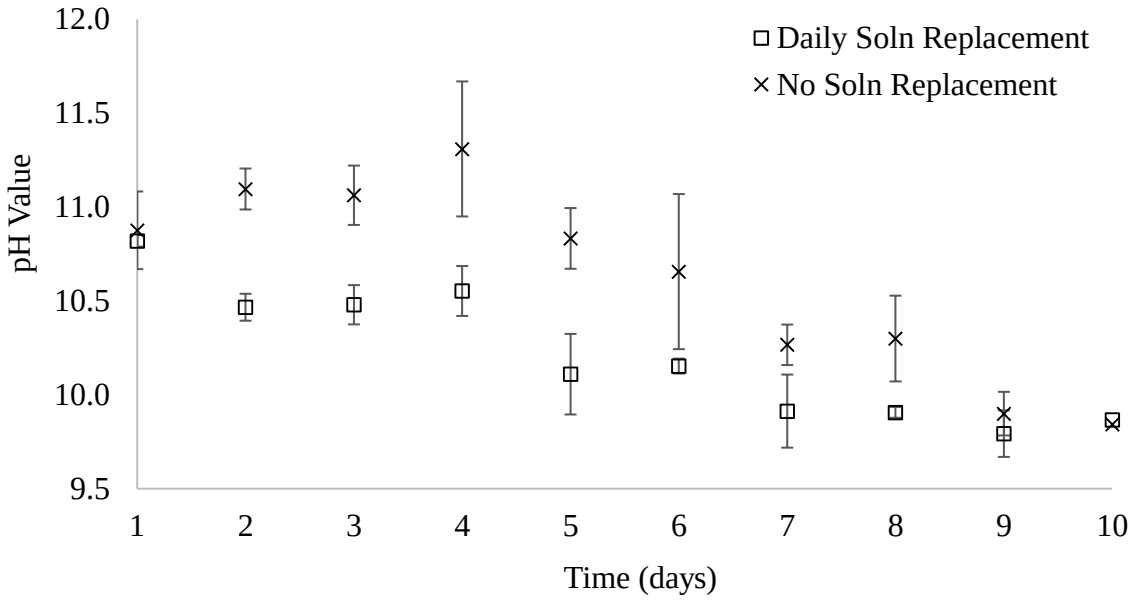

Figure 4-49: The pH values of solutions were monitored after the daily MMA treatments. Each point represents the average value of three trials.

DSR also had a similar average pH of 9.8. Moreover, the pH values of the solution in Trial DSR were significantly lower than those of Trial NSR after Day 1.

Daily solution replacement apparently caused the pH of the solution in Trial DSR to drop more quickly than Trial NSR. Moreover, decreasing pH from Day 1 to Day 10 in both trials indicated that the hydrogen concentrations increased 10 times after MMA treatments. The increase in the concentration of hydrogen ions indicated the decrease of concentration of hydroxide ions. During a treatment, the tendency is that OH^- would be getting oxidized at the anode (Ti-wire in HCP) to produce water and oxygen (described in Section 2.6.4), thus depleting hydroxide ions. In contrast, the electrolysis of water at the cathode would tend to produce OH^- (which was being depleted at the anode (Eq. 2-43)). In the meantime, it was possible for hydroxide ions to participate in the polymerization of MMA, providing a net depletion of hydroxide. This may be why (as shown in Figure 4-48) the ATR analysis of PMMA liquid from the NSR and DSR trials exhibited a strong signal of O-H bond stretch. These considerations suggest that the electrolysis of water may not be the primary reason for decreased hydroxide ions (as evidenced by the pH drop noted earlier). The apparent reason for the pH drop was that the hydroxide ions may have participated in the polymerization of MMA in the MMA-treated HCP specimens.

4.6 MMA Treatment with Potassium Persulfate Initiator

As noted earlier, previous MMA treatments exhibited no reduction in the porosity of the MMA-treated specimens. This may be attributed to a lack of initiators. In Section 4.1, solid PMMA was successfully electro-synthesized with the use of potassium persulfate, and the PMMA was characterized by ATR. In this section, potassium persulfate was applied in the MMA treatments to promote more polymerization, and thus

obtain a strength benefit and a porosity reduction (setup shown in Section 3.14). In this section, the current density profile of each trial is presented. The masses of the suspended solids in solution are discussed. The average tensile (compressive) strength and the average porosities of the MMA-treated HCP specimens are discussed and compared with the control specimens. The indirect sulfur concentration difference between the treated HCP specimens and control specimens are discussed. The characterization of PMMA in the MMA-treated HCP specimens are also addressed. All the raw data are put in Appendix H.

4.6.1 Current Density Profile

Figure 4-50 shows the current density time profile of Trials 1-4. The letter "L" in the label of Trials 1 and 2 indicates the long persulfate-penetration time. The letter "S" in the label of Trial 3 indicates the short persulfate-penetration time. The letters "LC" in the label of Trial 4 indicate the low centration of persulfate ions and the short persulfate-penetration time. The current densities were calculated with respect to the surface of the HCP specimen. It was calculated in Section 4.6.2 that the current density of the HCP specimens at the center electrode was significantly higher than at the HCP surface. In Figure 4-50, the minimum current density among these cases was approximately 0.5 A/m^2 at the HCP surface, and the central electrode current density was 18.6 A/m^2 (> 5 A/m^2).

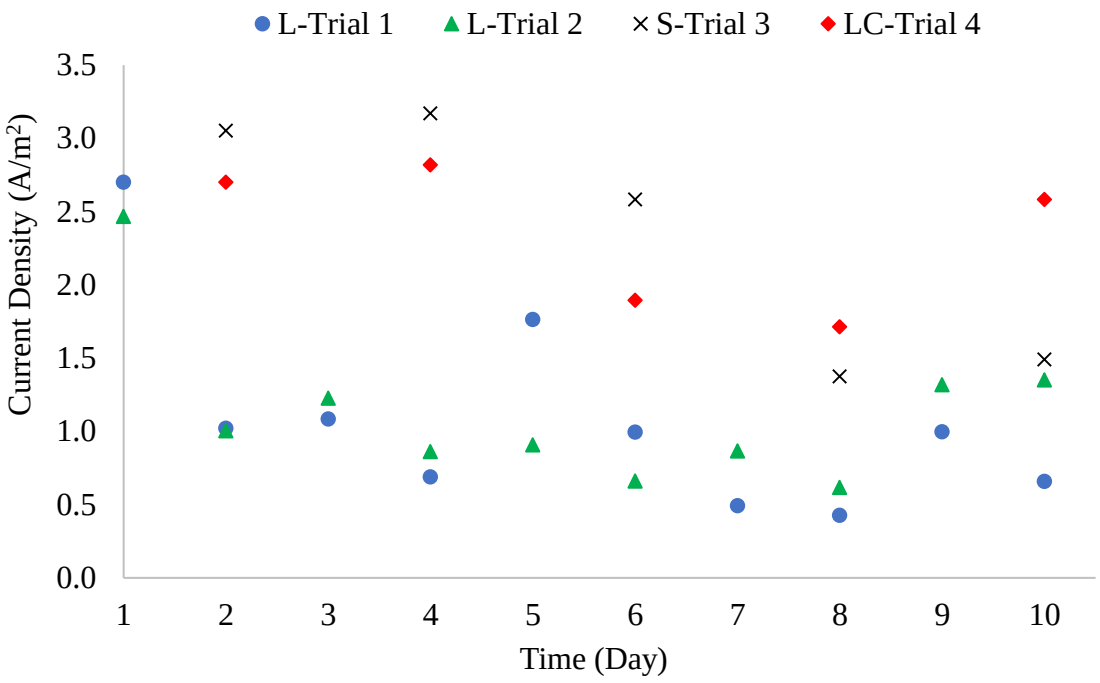

Figure 4-50: Current density time profile of MMA-treated HCP trials 1-4. L-Trials 1 and 2 were subjected to the same MMA treatment (described in Table 3-9). S-Trial 3 was subjected to a shorter treatment time (12 h) than that of S-Trial 1 (48 h). LC-Trial 4 was subjected to a shorter treatment time (12 h) and lower initiator concentration (0.004 mol/L) than those of S-Trials 1-3 (0.01 mol/L).

Because of the high current density (> 5 A/m^2) at the central electrode, it was likely that all the MMA-treated HCP specimens in the four trials suffered some degree of high-current-density damages (possibly micro cracking) at the center of the specimens. This damage was expected to cause the strength of the MMA-treated HCP specimens to decrease.

4.6.2 Average Tensile and Compressive Strength

Figure 4-51 shows the average tensile or compressive strength of the MMA-treated HCP specimens. Table 4-10 shows the statistical analysis of the MMA-treated and control specimens in all trials using initiators. Based on the Figure and table, it is observed that the average tensile strength of the MMA-treated HCP specimens was

significantly (90% confidence) lower than that of the control specimens in L-Trials 1 and 2. Moreover, the average tensile strength of the MMA-treated HCP specimens in the S-Trial 3 and LC-Trial 4 were higher than those of the control specimens. However, the statistical analysis indicated that there was no significant difference on the average tensile strength between the MMA-treated and untreated HCP specimens.

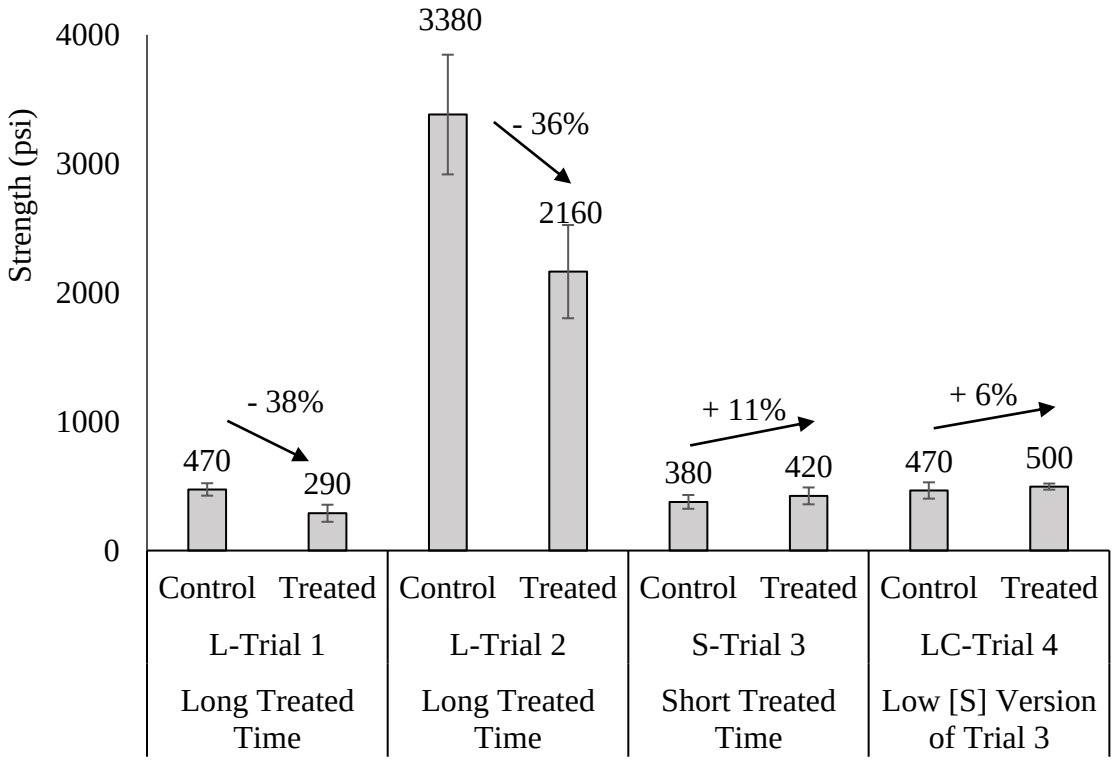

Figure 4-51: Average tensile strength of MMA-treated HCP specimens. The strength in L-Trial 2 is average compressive strength. Each value represents the average of six trials.

Table 4-10: Statistical analysis of the average strengths of the MMA-treated HCP specimens in trials 1-4.

	L-Trial 1	L-Trial 2	S-Trial 3	LC-Trial 4
F-test	1.9	1.6	1.5	7.2
F-Table	5.1	5.1	5.1	5.1
T-test	3.7	3.4	0.9	0.7
T-Table	1.8	1.8	1.8	1.8
Significance Result*	Yes	Yes	No	No

*95% confidence for F-test, 90% confidence for T-test.

Decreased strength in L-Trials 1 and 2 could also be attributed to the fact that the initiation of the polymerization of MMA produced sulfate ions, which can damage HCP [100]. Although efforts were made to limit sulfate exposure, it appears that sulfate ions may have damaged the HCP (through sulfate attack) and cause the compressive strength to decrease [13]. The sulfate attack in the MMA-treated HCP specimens appeared to cause decreases in both the tensile and compressive strengths. Moreover, it is discussed in Section 4.6.2 that high central current density may have caused the strength to decrease. Therefore, the sulfate attack and the high current density were two factors that likely contributed to the strengths of MMA-treated HCP specimens to decrease in L-Trials 1 and 2.

In order to mitigate or eliminate the adverse effect of persulfate ions during the MMA treatment, the treatment time in a 48-hour segment (See segment definition in Figure 3-12) or the concentration of the potassium persulfate was reduced in S-Trial 3 and LC-Trial 4. Firstly, reducing the treatment time mitigated the damage of the high

current density. Moreover, after reducing the resident time of the persulfate ions from 24 hours (L-Trials 1 and 2) to 4 hours (S-Trial 3 and LC-Trial 4), the damages of sulfate on the HCP specimens was reduced because the average tensile strength of the MMA-treated HCP specimens increased by 12%. It should be noted that the statistical analysis in Table 4-7 shows that the average tensile strengths between the control and treated HCP specimens are not significantly different (at a 90% confidence). Based on the above discussions, it was concluded that reducing sulfate-residence time mitigated 100% of the damage in HCP specimens that was observed in earlier trials.

Trial 4 was intended to cause the damage of persulfate ions to decrease further. However, the reduced concentration of persulfate ions may have caused the production of PMMA in LC-Trial 4 to decrease significantly (shown in Figure 4-57). This resulted in the benefit of the tensile strength on the MMA-treated HCP specimens reduced (12% to 6%). However, the average tensile strengths between the control and MMA-treated HCP specimens are not significantly different (90% confidence).

4.6.3 Porosity Result

Porosity tests for each HCP specimen was conducted immediately after the strength tests. Figure 4-52 shows the average porosity of the MMA-treated HCP specimens from Trials 1-4 with the application of potassium persulfate. It is observed that the average porosities between the MMA-treated and control specimens were not significantly different. Moreover, the statistical analysis in Table 4-11 shows that average porosities between the control and MMA-treated HCP specimens are not significantly different in all trials using initiators (90% confidence). Apparently, the porosity of HCP specimens was not reduced after the MMA treatments.

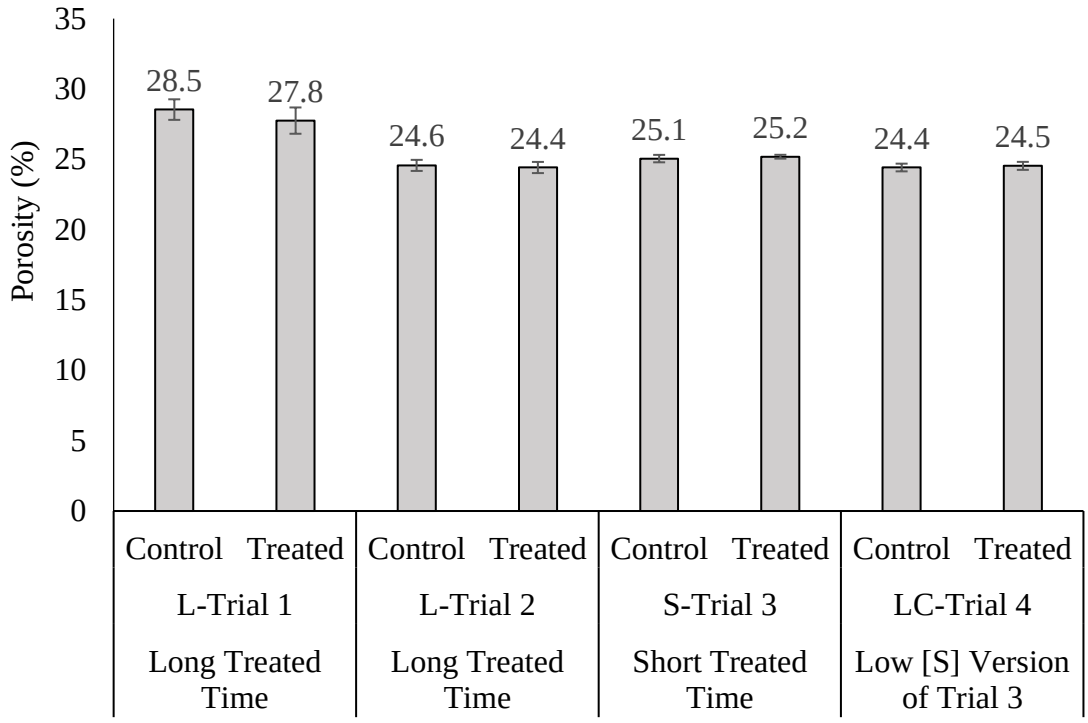

Figure 4-52: Average porosities of the persulfate-induced, MMA-treated HCP specimens. Each value represents the average porosity of six trials. Treatment times are defined in Table 3-9. [S] Refers to the concentration of potassium persulfate.

Table 4-11: Statistical analysis of average porosities of MMA-treated HCP specimens in all trials using initiators.

	L-Trial 1	**L-Trial 2**	**S-Trial 3**	**LC-Trial 4**
F-test	1.6	1.0	3.7	1.1
F-Table	5.1	5.1	5.1	5.1
T-test	1.1	0.4	0.7	0.5
T-Table	1.4	1.4	1.4	1.4
Significance Result*	No	No	No	No

***95% confidence for F-test, 90% confidence for T-test.

4.6.4 Sulfate Percentage Analysis

After the porosity tests, the MMA-treated HCP samples from L-Trial 1, S-Trial 3, LC-Trial 4 were ground enough to pass through a No. 80 sieve. The collected HCP powders were subjected to sulfur characterization tests. After utilizing the energy-dispersive X-ray fluorescence (EDXRF) to analyze the elements in the MMA-treated HCP powder, a histogram of the elements was obtained as shown in Figure 4-53. It was observed that the detected count of the sulfur element was 20415. This value was used to represent the concentration of sulfate in the HCP specimen indirectly.

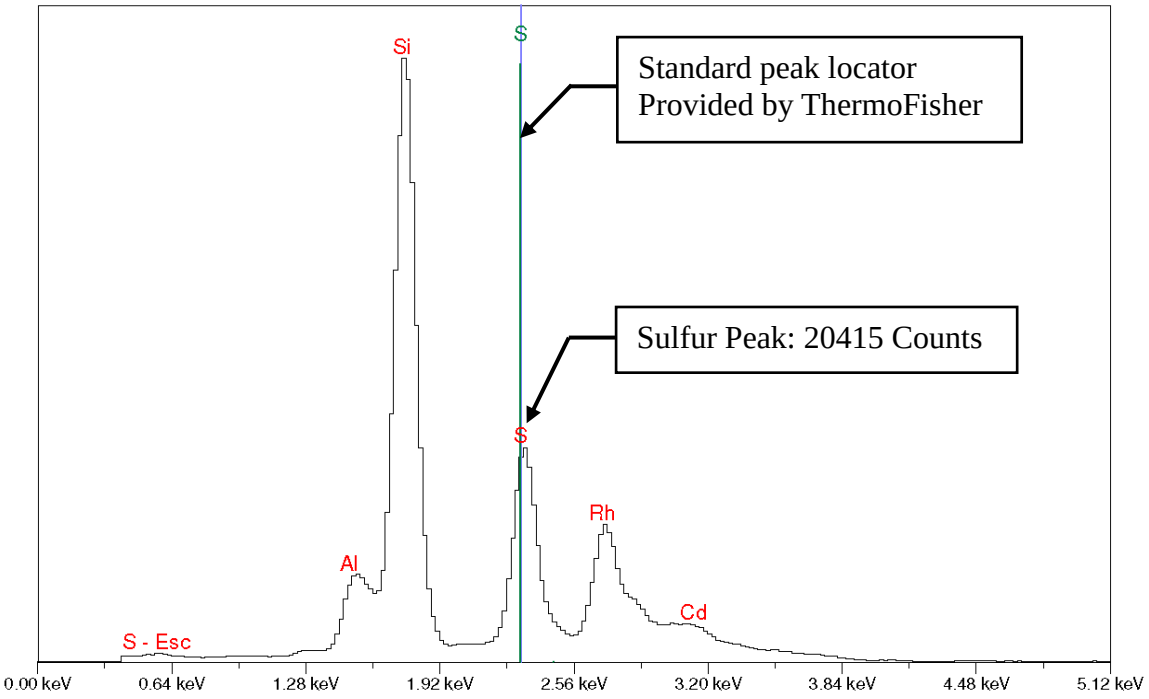

Figure 4-53: The elemental distribution of HCP specimen powder from Trial 1 analyzed by energy-dispersive X-ray fluorescence (EDXRF).

Figure 4-54 shows the average couvc5nts of the sulfur found in the MMA-treated and control HCP specimen powder from L-Trial 1, S-Trial 3, and LC-Trial 4 via the

XRF. It was calculated that the concentration of sulfur in the HCP specimens increased by 3.0%, 1.6%, and 7.4% following the MMA treatments in L-Trial 1, S-Trial 3, and LC-Trial 4, respectively.

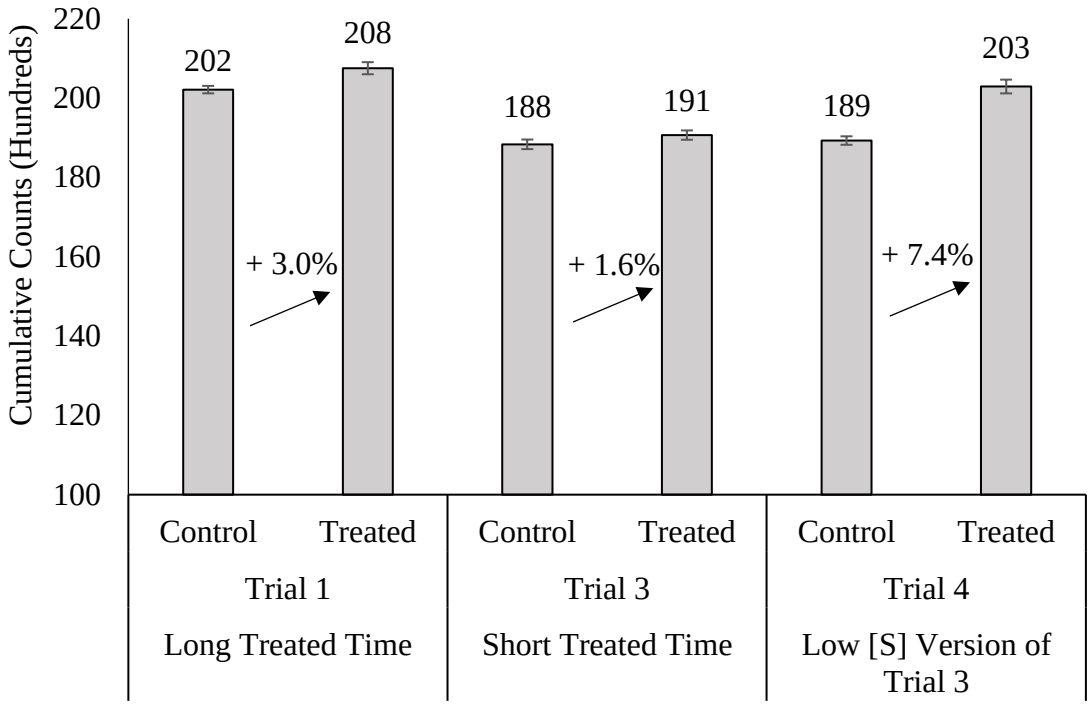

Figure 4-54: Average detected counts of elemental sulfur in MMA-treated HCP specimen powder via EDXRF analysis. Each reported average value represents the average count of 30 trials. Trial 2 was not analyzed since it did not differ from Trial 1 conditions.

Table 4-12: Statistical analysis of the average counts of sulfur element in the MMA-treated HCP specimens in trials 1, 3, and 4.

	L-Trial 1	S-Trial 3	LC-Trial 4
F-test	2.6	1.1	2.6
F-Table	1.9	1.9	1.9
T-test	4.9	2.3	11
T-Table	1.7	1.7	1.7
Significance Result*	Yes	Yes	Yes

*95% confidence for F-test, 90% confidence for T-test.

Table 4-12 shows the average sulfur counts between the control and MMA-treated HCP specimens are significantly different in L-Trial 1, S-Trial 3, and LC-Trial 4 (at a 90% confidence). One of the reasons for conducting S-Trial 3 and LC-Trial 4 was the observation of surface softening of the treated HCP specimens in L-Trials 1 and 2. Between each 48-hour segment of MMA treatments, it was found that the surface of the treated HCP specimens exhibited a slippery, gray film. This gray fluid film appeared to contain the HCP powder and could be easily removed by hand. This appeared to indicate that the HCP surface was damaged. As discussed in Section 2.1.5, the increased concentration of sulfate ions in the HCP could cause the decalcification, which constitutes a decomposition of the C-S-H gel of HCP, and cause the formation of ettringite, which was observed to expand the capillary pores and cause the micro cracks [41]. The loss of C-S-H gel and the damage from the ettringite's needle growth can significantly affect the strength. The results of sulfur content analysis and the decreased tensile strength indicated that the decomposition (softening) of the HCP surface could likely have been attributed to the increased sulfate content in the treated HCP specimens.

The sulfur contents in the treated HCP specimens in S-Trial 3 and LC-Trial 4 were also significantly higher than the controls. However, the decrease in tensile strength did not occur. Compared with L-Trials 1 and 2, the attraction time of persulfate ions decreased from 24 hours (L-Trials 1 and 2) to 4 hours (S-Trial 3 and LC-Trial 4) in a 48-hour segment (described in Figure 3-12). After reducing the persulfate-penetration time, the average tensile strengths in S-Trial 3 and LC-Trial 4 increased slightly. Therefore, by limiting the sulfate interaction time and concentration, the impact of sulfate ions on the MMA-treated HCP specimens appeared to be minimized or compensated by the MMA treatment.

4.6.5 PMMA Characterization Results

After the sulfur content tests, the MMA-treated HCP powder from all trials were subjected to the PMMA extraction tests. After the extraction, the slightly yellowish, transparent and oil-like liquid sample was obtained from all trials using initiators. It may be possible that the application of initiators (potassium persulfate) caused the liquid sample to be yellowish. Figure 4-55 shows the ATR and FTIR characterization results of the extracted samples from the MMA-treated HCP powder in all trials using initiators. Since L-Trials 1 and 2 had the identically experimental conditions shown in Table 3-9, the PMMA extraction analysis was only conducted for L-Trial 1. The liquid samples from Trial 3 and the standard PMMA sample were characterized by the FTIR. Based on the descriptions of peak identification in Figure 4-55, it was concluded that the extracted liquid samples from L-Trial 1, S-Trial 3, and LC-Trial 4 were chemically similar to PMMA.

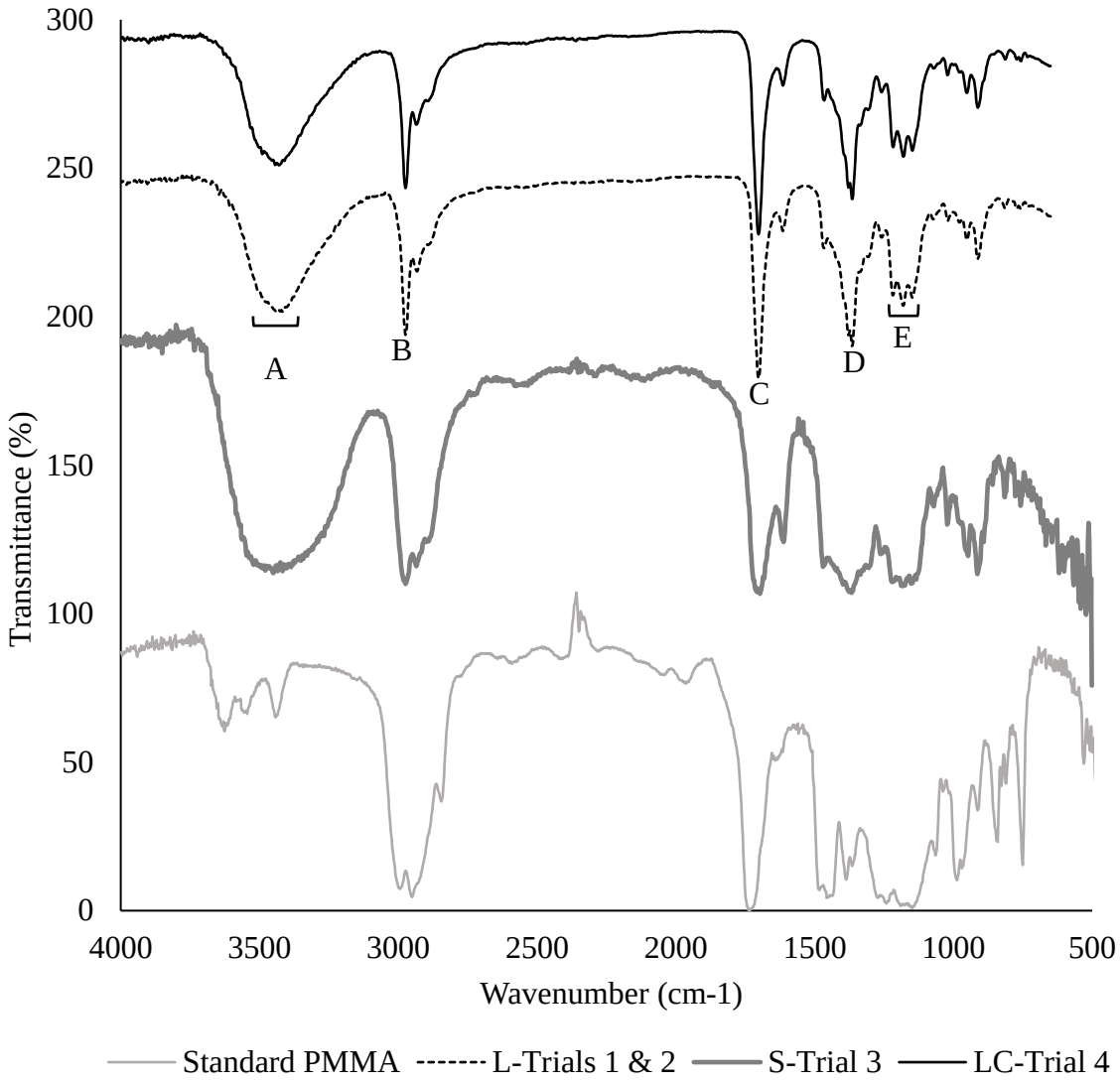

Figure 4-55: ATR/FTIR analysis of extracted liquid from MMA-treated HCP specimens of trials 1-4. The samples from L-Trial 1 and LC-Trial 4 were characterized by ATR. The samples from S-Trial 3 and standard PMMA were characterized by FTIR. Peak identification: A. The O-H stretch, intermolecular hydrogen bonding 3428 cm^{-1} [107]. B. The C-H stretch, 2973 cm^{-1}. C. The C=O stretch, 1702 cm^{-1}. D. The C-H bend, 1363 cm^{-1}. E. The C-C(=O)-O stretch, 1180 cm^{-1}. It should be noted that the transmittances of spectrums of L-Trials 1 & 2, S-Trial 3, and LC-Trial 4 would need to be reduced by 150%, 100%, and 200%, respectively, in order to obtain the exact transmittances for these trials.

4.6.6 Estimated Masses of PMMA in MMA-treated HCP Specimens

During the MMA treatments of all trials, the mass measurements of the solids in the MMA solutions were conducted at a 48-hour interval to indirectly calculate the estimated masses of solids in the pores of the MMA-treated HCP specimens in all trials using initiators. After evaporating the water in the tested solution sample (~50 g) from the MMA-treated solution of each segment, the mass of solids was measured (m_{solids}). The concentration of the suspended and dissolved solids in the MMA-treated solution was calculated through Eq. 4-14:

$$M_{sample} = \frac{m_{solids}}{m_{sample}}, \qquad \textbf{Eq. 4-14}$$

where the M_{sample} is the mass of solids per gram of solution, m_{solids} is the mass of solids after the evaporation process, and m_{sample} is the mass of tested solution sample (~50 g). Because the solution and the pore fluid were connected, the system contained the treatment solution, and pore fluid was treated as an integrated volume shown in Figure 4-56. When the potassium persulfate was added in the solution, its concentration was calculated via Eq. 4-15:

$$M_{PP} = \frac{m_{pp}}{(m_{water} + m_{pore})}, \qquad \textbf{Eq. 4-15}$$

where M_{PP} is the mass of potassium persulfate per gram in the integrated system, m_{pp} is the mass of potassium persulfate dosage in each 48-hour segment, m_{water} is the mass of DI-water applied in each 48-hour segment, and m_{pore} is the mass of water in the pores of MMA-treated HCP specimen. It was measured that the mass of one 4-inch-high HCP specimen was about 410 g (m_{HCP}).

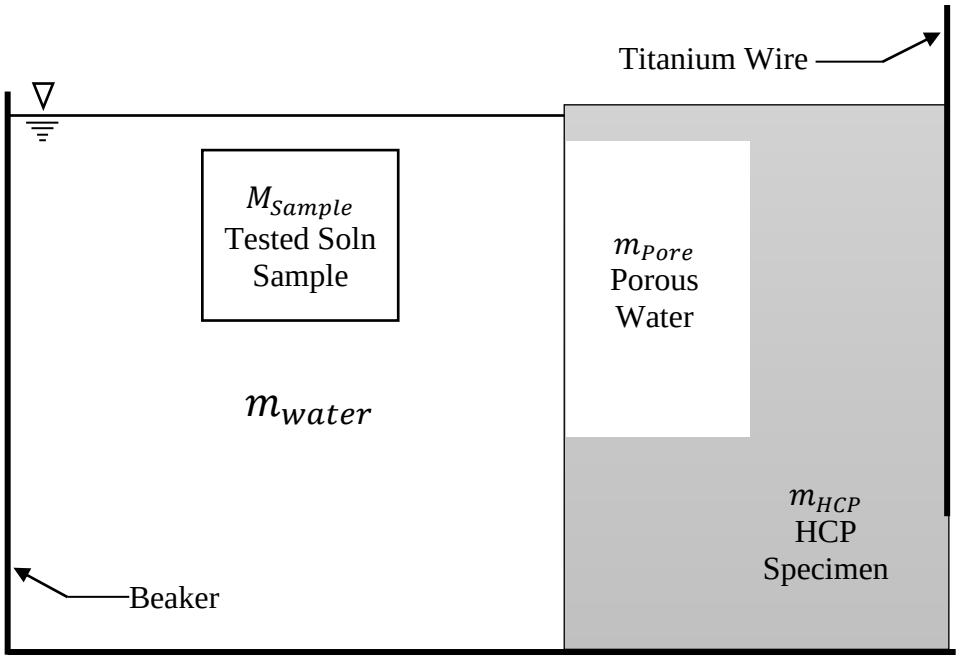

Figure 4-56: Sectional view of an MMA-treated HCP specimen in a beaker.

Based on the results of the porosity test in Section 4.7.4, the m_{pore} was calculated through Eq. 4-16:

$$m_{pore} = m_{HCP}(410\ g) \times Average\ Porosity\ , \qquad \textbf{Eq. 4-16}$$

where the average porosity is the average of six porosities of the MMA-treated HCP specimens in all trials using initiators. The porosity testing is described in Section 3.10.

Based on equations 4-14 to 4-16, the mass of PMMA in the MMA-treated HCP specimen was calculated via Eq. 4-17:

$$m_{PMMA} = \left(M_{sample} - M_{PP}\right) \times m_{pore}\ , \qquad \textbf{Eq. 4-17}$$

where m_{PMMA} is the mass of PMMA in the pores of the MMA-treated HCP specimens. With the application of Eq. 4-17, Figure 4-57 shows the average estimated mass of PMMA in the pores of six MMA-treated HCP specimens after each 48-hour segment. It was observed that the masses of estimated PMMA decreased from Segment 1 to 5 in

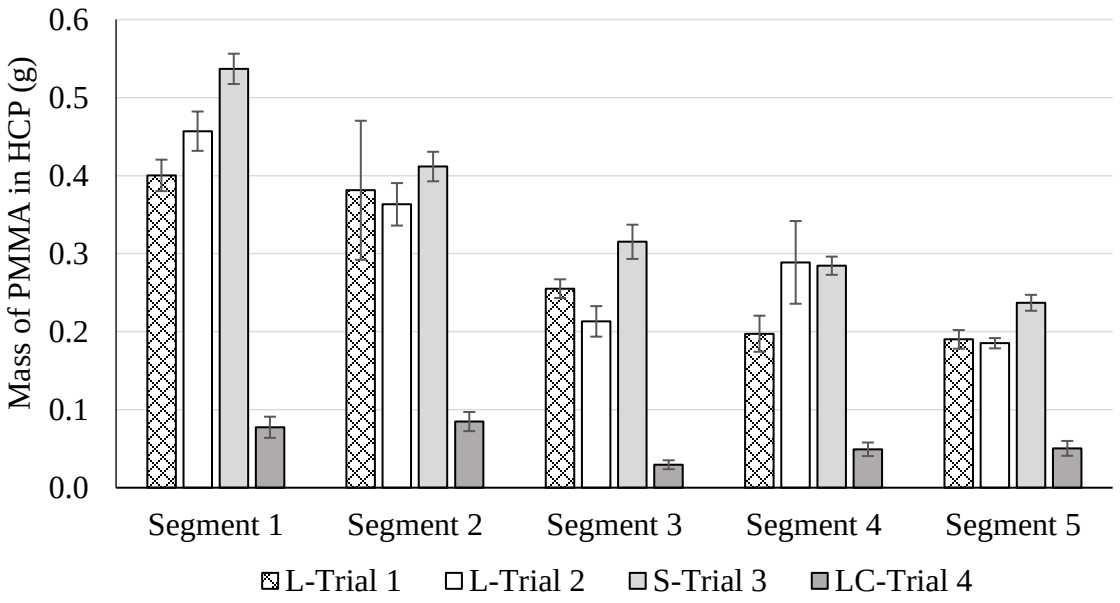

Figure 4-57: Average masses of PMMA in the MMA-treated HCP specimens for each 48-hour segment of each trial. Each value represents the average mass of the estimated PMMA from six MMA-treated HCP specimens. The raw data is located in Appendix H.

Figure 4-57 in L-Trials 1 and 2, and S-Trial 3. This was because, after the replacement of the solution at the beginning of each segment, the concentration of the OH^- tended to decrease (as observed in Figure 4-49). The reduction in hydroxide ions (as noted from pH monitoring) would be expected to slow down and reduce the production of PMMA (as observed in Segment 4 and 5 of Figure 4-57).

After decreasing the treatment time (from 48h to 12h) in S-Trial 3, the average masses of PMMA in the MMA-treated HCP increased significantly during Segments 1-5 as compared with L-Trials 1 and 2. Reducing the treatment time in S-Trial 3 as compared to L-Trials 1 and 2 suggests that the negatively charged particles (MMA monomer and persulfate ions) may have lacked the time needed to migrate into the pores of HCP specimens. As a result, more of these species would have reacted in the solution instead

of in the HCP pores. Therefore, reducing the treatment time caused the charged particles were less likely to migrate into the pores of HCP specimens.

After reducing the concentration of the initiators in LC-Trial 4, the PMMA mass in each segment was reduced significantly as compared with S-Trial 3. This indicated that the reduced persulfate ions caused the PMMA was reduced.

Based on Figure 4-56, the total mass of PMMA in the pores of the MMA-treated HCP specimens was calculated through Eq. 4-18:

$$m_T = \sum_{1}^{5} m_{PMMA,Segment\ n}\ , \qquad \textbf{Eq. 4-18}$$

where the m_T is the total mass of PMMA in each MMA-treated HCP specimen, the $m_{PMMA,Segment\ n}$ is the average mass of PMMA in the MMA-treated HCP specimens delivered via treatment Segment n. The results are shown in Figure 4-58.

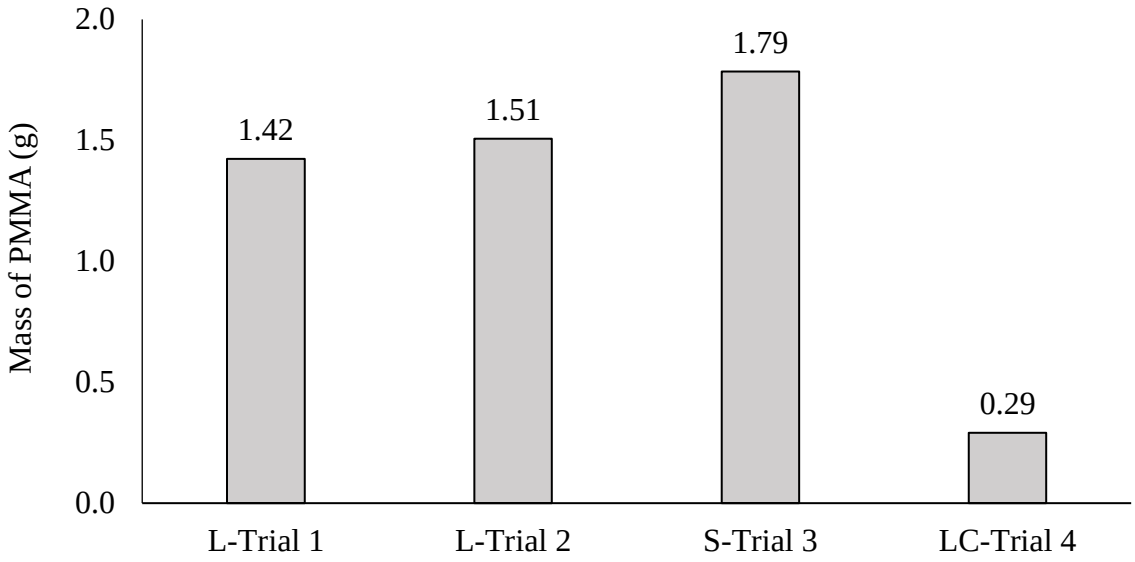

Figure 4-58: Estimated mass of PMMA in the pores of one MMA-treated HCP specimen.

Figure 4-58 shows that the mass of the mass of PMMA estimated to be in one MMA-treated HCP specimen was lower than 2 g. The PMMA content in the HCP from LC-Trial 4 was estimated to be lower than 0.3 g. The mass of porous water in an HCP specimen was ~100 g (Eq. 4-16). If two grams of porous water in the MMA-treated HCP specimen was replaced in the PMMA, the volume change is only 2% (Densities of PMMA and water are 1.20 g/cm^3, and 1.00 g/cm^3). This was the reason why the porosities of the MMA-treated HCP specimens in all trials using initiators did not reduce significantly as compared to the control groups shown in Figure 4-52.

The lack of a significant reduction of porosity seemed to indicate that the conversion of MMA in the pores of the MMA-treated HCP specimens was not significant. However, in the PMMA characterization process discussed in Section 4.7.5, it was observed that the volume of the extracted PMMA containing liquid from the 30-gram powder sample of the MMA-treated HCP was approximately 1-2 ml in all Trials using initiators. If it was assumed that one milliliter of PMMA liquid was extracted from every 30 g of MMA-treated HCP powder, a 410-gram HCP specimen could contain 13.7 ml of PMMA liquid (total dosage of MMA was ~30 ml). The results of porosity testing in Section 4.7.3 indicated that the liquid product could not reduce the porosity and may have actually evaporated during the porosity testing. In the liquid extraction tests, each extracted sample was obtained after 24 hours of evaporation at 80°C. However, the MMA-treated HCP samples in the porosity tests experienced a longer heating time (5-7 days) and higher temperatures (105°C). During the porosity testing, the extracted liquid in the MMA-treated HCP samples was slowly evaporated, and the porosities in all trials using initiators between the MMA-treated and control HCP specimens were not

significantly different. Therefore, the conversion of MMA monomers in the MMA-treated HCP specimens in all trials using initiators was significant, but liquid phase reaction product was unable to provide strength and porosity benefit to HCP.

4.7 Mechanism of Electroinitiated Polymerization of MMA

Many studies indicated that the electropolymerization of MMA occurred via free radical polymerization [90] [100] [93]. This type of polymerization utilizes highly active radicals to initiate the polymerization of MMA. The electropolymerization of MMA in HCP is divided into three steps – transportation, initiation, and polymerization. Transportation of the MMA monomer was attempted via electrical conduction into the HCP pores. Initiation was attempted by introducing production of highly active free radicals (OH^* and SO_4* production) to initiate the polymerization.

For electrical transport, one of the most important requirements was that the polymer precursors being positively or negatively charged. For instance, it is introduced in Section 2.1.6 that the electrochemical chloride extraction and the electro kinetic enhancement of concrete structures utilize the electric field to extract negatively charged chloride ions and attract positively charged alumina-coated silica nanoparticles, respectively. If MMA monomers are transported via electrical conduction, they need to have charges attached. However, as an ester compound, MMA monomers cannot be ionized when dissolved into water. This results in low water solubility. Moreover, volatile MMA evaporates rapidly from the water in 3 hours when the electric field is not applied [60]. It is mentioned in Section 2.3.4 that the inhibitor in MMA monomer shipments is added to prevent the spontaneous polymerization of MMA. The mechanism

of inhibition is unclear. It is conceivable that the inhibitor may interfere with the transport of MMA under the electric field.

Successfully extracted PMMA liquid indicated that the MMA monomer could be migrated via electrical conduction. Two mechanisms are in charge of this movement. The first one is the hydrolysis of the ester function on the MMA monomer. The other one is the formation of the OH-Complex. Either one involves the interaction with electronegativity of the oxygen atom in the MMA molecule. When an oxygen atom forms a covalent bond (a pair of electrons) with a hydrogen ion, the pair of electrons will be held close to the oxygen [140]. As is shown in Figure 4-59(a), if the OH^- ion is treated as the combination of two square boxes forming a covalent bond, the pair of electrons that constitute this bond will be held close to the oxygen. The left box will then exhibit a slightly negative charge ($\delta -$), and the right box will exhibit a slightly positive charge ($\delta +$). The ability of an atom to retain a bonding pair of electrons is termed as electronegativity [141]. The oxygen atom has a strong electronegativity (3.5) compared with the hydrogen (2.1). Figure 4-59(b) shows that MMA monomer contains a pair of covalent bonds between the carbon and the oxygen in the middle of the molecular structure. The of oxygen atom in the C=O bond of MMA exhibits slightly negative

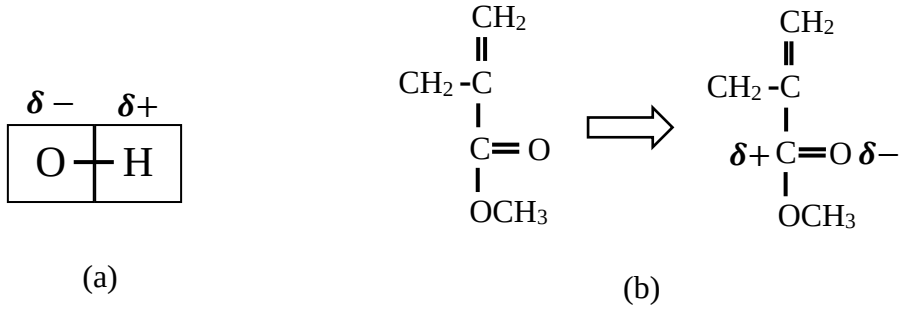

(a) (b)

Figure 4-59: Electronegativity of oxygen in hydroxide ion (a) as compared to the MMA monomer (b).

charge. This charge imbalance causes the molecule to exhibit polarity which is measured by the dipole moment [142]. If a molecule is non-polar, the dipole moment will be zero, such as oxygen gas and carbon dioxide [143]. Some examples show that polar molecules exhibit dipole moments. Water exhibits the dipole moment of 1.85 debyes, hydroxyl radical exhibits the dipole moment of 1.66 debyes, and sodium chloride exhibit the dipole moment of 9.00 debyes. A research shows the dipole moment of poly(methyl methacrylate) is in the range from 1.3 to 1.5 [144]. This result may indicate that the MMA monomer is a polar molecule.

When dipoles are placed in an electric field, the dipoles will tend to align themselves shown in Figure 4-60 [145]. If the electric field is more intense, the alignment of the dipoles will be more significant. After alignment, the positive end of one dipole will develop electrostatic attractive force with the negative end of the neighboring dipole as shown in Figure 4-60. When the solution contains only water and MMA, it is likely that they will form dipole-dipole complex under the electric field [100]. This complex formation significantly slows down the evaporation of MMA. An experiment was conducted to apply two titanium electrodes in the MMA solution (0.1 mol/L) at 2.0 V for 24 hours (See Figure 3-3). The results of MMA evaporation tests are presented in Appendix B. After 24 hours, a strong MMA odor could still be detected. If no electric

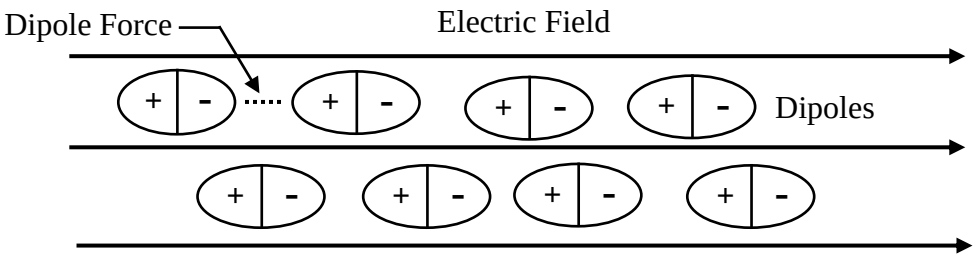

Figure 4-60: Alignment of dipoles in electric field.

field was applied, the MMA was evaporated within 3 hours, as indicated by a lack of odor being detected. This experiment appeared to indicate that MMA was being retained in the solution by a dipole-dipole complex formation.

MMA dipoles can form a complex with any positive ion such as hydrogen, sodium, potassium or lithium [98]. Electropolymerization studies found in the literature indicated that hydrogen ions were able to form a complex with MMA monomer under an electric field [100]. This was because the addition of sulfuric acid together with potassium persulfate significantly increased the conversion of MMA as compared with adding potassium persulfate alone. Apparently, the hydrogen ions were weakly bonding with the MMA dipoles under the electric field. The H-MMA complex exhibited a positive charge which enabled the MMA to move toward the cathode. If hydrogen ions are replaced to Na^+, K^+, or Ca^{2+}, then it is anticipated that positively charged Na-MMA, K-MMA, or Ca-MMA complexes would form.

It is recognized in the literature that esters, such as oil or fat, can react with alkaline species to produce organic salts (soap) [146] [147]. This process is termed as saponification or the hydrolysis of esters. A similar mechanism for the hydrolysis of MMA is described in the literature and is shown in Figure 4-61. Step 1: The MMA monomers and hydroxide ions form hydroxide-MMA complex $(OH\text{-}MMA)^-$. Step 2: The complex splits into two particles, methacrylic acid and a methyl radical. Step 3: Methyl radical has strong negative potential which attracts hydrogen ions to form methanol and methacrylic ion.

Steps 1 and 2 are reversible. It is anticipated that the hydrolysis of MMA in a basic solution may consume hydroxide ions and thus would lower the pH. The

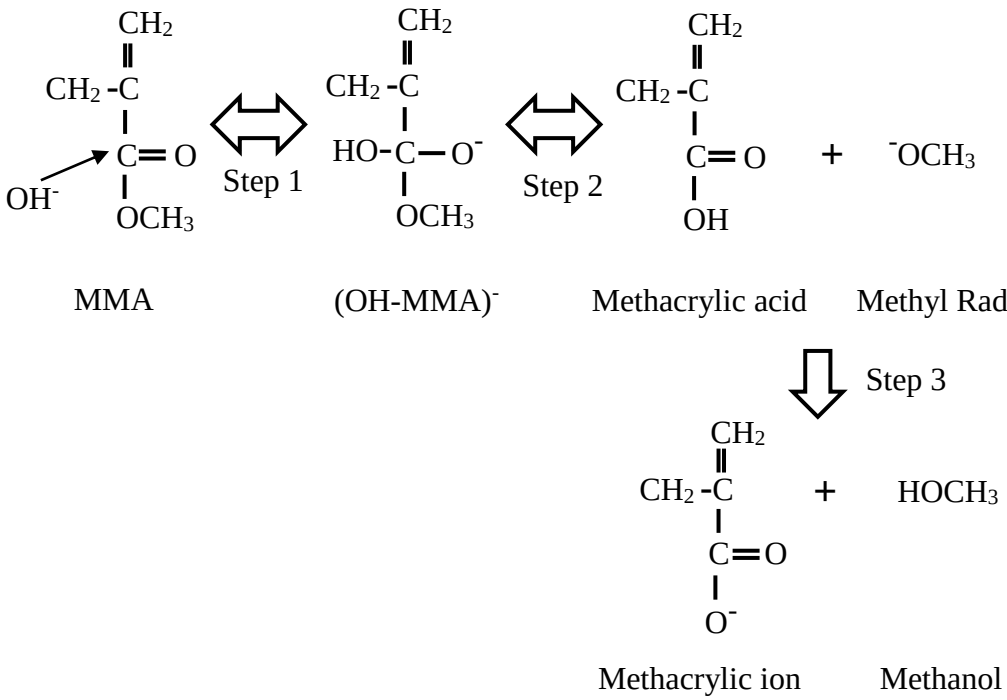

Figure 4-61: Hydrolysis of MMA.

methacrylic ion and the (OH-MMA) complex are negatively charged, which indicates they can be attracted to the anode during an MMA treatment. This theory seems to match the decreasing pH observed in the treatment solutions during the MMA treatments as presented in Section 4.6.5.

In Figure 4-61, it was noted that the $(OH\text{-}MMA)^-$ complex is negatively charged, which indicates this complex can be transported by the electric field. When the complex reaches the anode, the OH- ions lose electrons and form OH* radicals which can initiate the polymerization of MMA [148] [60]. Several results indicated that the OH* radicals likely initiated the polymerization. In Section 4.5, the extracted PMMA liquid (~0 ml) from the MMA-treated HCP powder in Trial 4 (+0.49 V) was significantly less than those (1~2 ml) in Trials 1-3 (+0.57 V). This was because the MMA treatment in Trial 4 with the corrosion potential of +0.49 V exhibited significantly lower current densities than

those of Trials 1-3 (+0.57 V). Lower current densities indicated that the oxidation of hydroxide ions at the anode in Trial 4 (+0.49 V) was less intense than Trials 1-3 (+0.57 V). Since oxidation of hydroxide ions produced OH* radicals which could initiate the polymerization of MMA, less radicals during the MMA treatment in Trial 4 (+0.49 V) caused less PMMA liquid to be produced as compared to Trials 1-3 (+0.57 V). Moreover, in Figure 4-56 from Section 4.7, the decreasing average mass in 48-hour Segments 1-5 (from ~0.45 g to ~0.2 g) indicated that the reducing radicals caused the conversion of MMA to decrease. This was because the solution replacement at the end of each segment during the MMA polymerization caused the loss of hydroxide ions. Also, in Section 4.6, during the MMA treatments in Figure 4-49 when the solution was not replaced daily, the pH of the solution dropped from 10.8 to 9.8, which indicated the consumption of hydroxide ions during the MMA treatments. The consumption of the hydroxides could be attributed to the initiation of polymerization of MMA, or the hydrolysis of MMA/poly(MMA). Therefore, based on the above observations and considerations, the hydroxide ions appeared to participate the electro-polymerization of MMA as initiators.

Section 4.1 demonstrated that potassium persulfate was an effective initiator at the cathode [100]. Since the persulfate ion was also negative, it can form a negative complex with MMA monomer as well as could the hydroxide ion. In Section 4.7, Figure 4-56 shows that LC-Trial 4 had significantly decreased conversion of MMA when less potassium persulfate was added. However, the extracted PMMA liquid from Trial 4 still had O-H bonds detected by ATR as shown in Figure 4-54. It was possible that the produced sulfate radicals reacted with hydroxide ions to form hydroxyl radicals as shown in Eq. 2-21 [79]. Moreover, when persulfate ions were reduced at the cathode in the

MMA-treated HCP, this reduction produced sulfate radiacals and sulfate ions as shown in Eq. 2-23 [92]. Sulfate ions can cause decalcification in the pores of HCP and produce hydroxide ions as shown in Eq. 2-9. These hydroxide ions can then be oxidized at the anode in the MMA-treated HCP to produce hydroxyl radicals. Alternatively, these hydroxide ions and MMA monomers can form (OH-MMA) complexes which would then be attracted to the anode. The extra produced hydroxyl radicals and increased hydroxide ions were possibly responsible for the relatively more effective polymerization yields in L-Trials 1-2 and S-Trial 3 shown in Figure 4-57. Based on these theoretical considerations, the reduction of potassium persulfate from 0.01 mol/L to 0.004 mol/L in LC-Trial 4 was reasonably expected to reduce the production of active radicals and thus the conversion of MMA.

Because of the similarity of molecular structures between poly(methyl methacrylate) (PMMA) and poly(methacrylic acid) (PMAA), ATR analysis was insufficient to distinguish if the extracted liquid from MMA-treated HCP in various trials was PMMA or PMAA. Solubility in water can be used as a tool to distinguish between them because PMAA is highly soluble in water while PMMA is insoluble in water [149]. The results of the solubility test are presented in Table 4-13. It was observed that the extracted liquid from the MMA-treated HCP from Trial 3 (+0.57 V) and L-Trials 1 and 2 were highly soluble in water at the volume ratio of 1:1. The white deposits from the beaker tests (discussed in Section 4.1) remained apparently insoluble after they were collected from the solution and washed with DI-water 3 times (described in Section 3.3.2).

In contrast, the solubility test results (Table 4-13) of the extracted liquid and the ATR characterization of figures 4-42, 4-48, and 4-55, apparently indicated that the liquid was poly(methacrylic acid) (PMA) and it was soluble. As is shown in Figure 4-61, hydrolysis of MMA or PMMA can produce MAA and PMAA. It was possible that after MMA migrated into the HCP pores, it could have hydrolyzed to produce MAA, and MAA monomers that could then be polymerized to produce PMA. Alternatively, after MMA monomers had polymerized into PMMA, the PMMA could have hydrolyzed to produce PMA. The polymerization of MAA or MMA was possibly initiated by hydroxyl radicals as indicated by the O-H bonding detected in ATR spectrums (figures 4-42, 4-48, 4-55).

Table 4-13: Comparison of materials solubility in water.

Materials	**Solubility in Water**
Extracted Liquid from Trial 3 (+0.57 V, no potassium persulfate)	Highly Soluble (1:1 ratio)
Extracted Liquid from L-Trial 1&2 (with potassium persulfate)	Highly Soluble (1:1 ratio)
Methyl Methacrylate	Slightly Soluble (1.5g/100g)
White Deposits Obtained from Beaker Tests Described in Section 3.3 (with potassium persulfate)	Not Soluble
Standard PMMA	Not Soluble
Methacrylic acid (MA)/ Poly(methacrylic acid) (PMA)	Soluble

The pore fluid in harden cement paste was highly alkaline. The produced PMAA in the MMA-treated HCP appeared to react with the NaOH, KOH, and $Ca(OH)_2$ in the HCP pores to produce water and poly(sodium/potassium/calcium methacrylate) (PMA-

Na, PMA-K, and PMA-Ca, respectively). These species are referred to as poly(methacrylate) salts in later sections.

Another possible product in the HCP pores following MMA treatment is a copolymer of MMA and MAA. A copolymer is the product of a polymerization system which contains two or more types of monomers [60]. Several studies successfully developed methods to obtain copolymers of MMA and MAA (poly(MMA-MAA)) in various polymerization systems [150] [151]. Since MMA and MAA (after MMA is hydrolyzed) monomers were all possibly driven into the HCP pores, after initiating polymerization, poly(MMA-MAA) was produced. The MAA portions of such a polymer would tend to make it somewhat soluble in water.

Based on previous discussions and the solubility results, the extracted liquid from the MMA-treated HCP was likely to be PMAA, poly(methacrylate) salts or poly(MMA-MAA). However, after using the acetone solvent to extract polymer from the MMA-treated HCP, if the acetone extracted poly(methacrylate) salts (PMA-Na, PMA-K, and PMA-Ca), the remnant materials after evaporating acetone should be solid instead of liquid [152]. This is because the solid state of poly(methacrylate) salts is independent of the molecular weight. Therefore, the extracted liquid from the MMA-treated HCP in various trials was likely to be poly(MMA-MAA) copolymer as opposed to just PMAA.

In the HCP pores, copolymers would tend to provide strong negative charges which could repel the negatively charged complex (OH-MMA) or methacrylic ion. This repelling force could have caused the polymer to have limited long-chain growth of a solid phase polymer, thus yielding a liquid. This short-chain polymer is referred to as oligomers. Moreover, it was observed in Figure 4-55 that there was a small peak (C=C

peak) beside Peak C (C=O peak), which indicated that there was some small amount of unpolymerized carbon-carbon double bonding in the copolymer samples. If the copolymer had a long-chain structure, the intensity of C=C peak shown in the ATR spectrum would not be easily detectable. For instance, the ATR spectrum of the solid white deposit (PMMA) in Figure 4-3 does not have a noticeable C=C peak, since the polymer chains of a solid polymer would tend to be long, making these double bonds relatively rare. Therefore, based on the above observations and discussions, the liquid copolymers appeared to be oligomers.

According to the discussion in this section, the polymerization schemes is shown in figures 4-62 and 4-63. Scheme I indicates the polymerization path appeared to apply in MMA treatments without the use of potassium persulfate. Scheme II indicates the polymerization path appeared to apply in MMA treatments with the use of potassium persulfate.

Scheme I

(No potassium persulfate, HCP, V_{corr} = +0.57 V or higher)

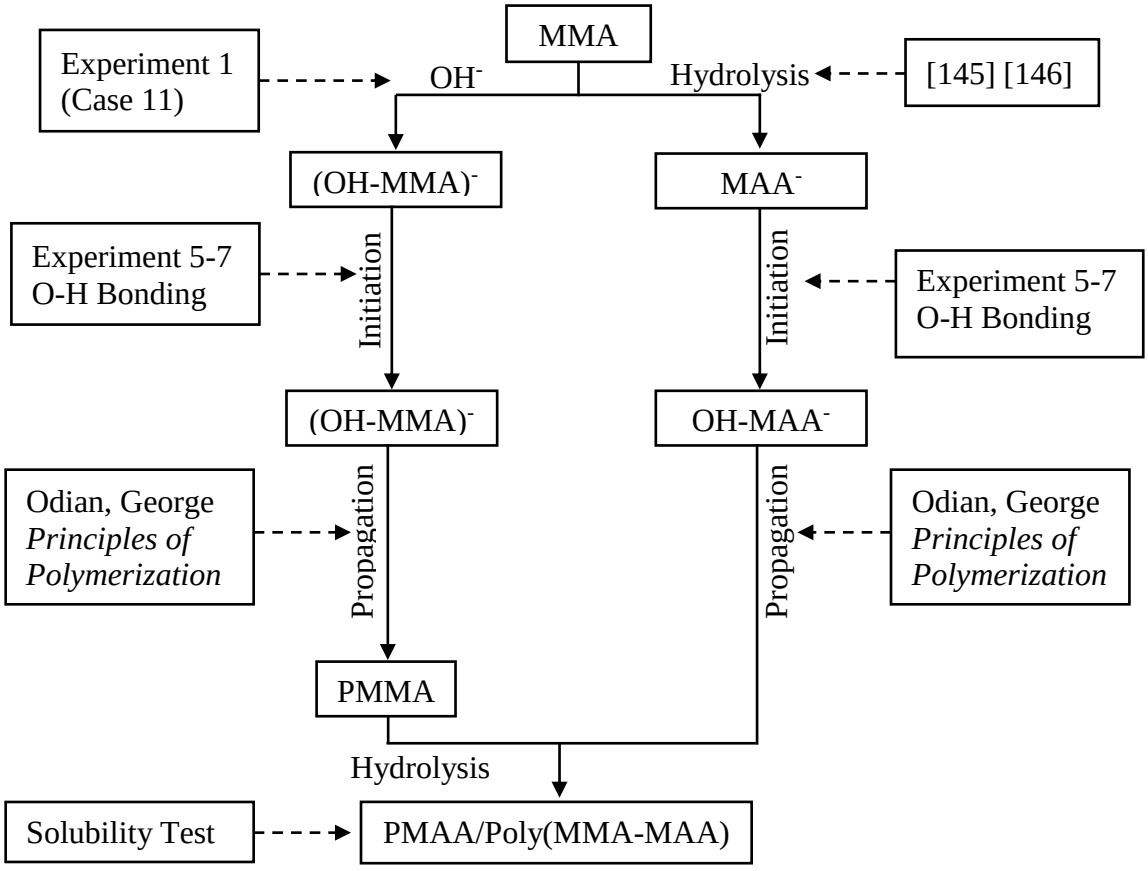

Figure 4-62: Scheme of electroinitiated polymerization of MMA in HCP specimens without the use of potassium persulfate. Dashed lines indicate sources of references.

Scheme II

(Potassium persulfate, HCP, $V_{applied}$ = 6.00 V)

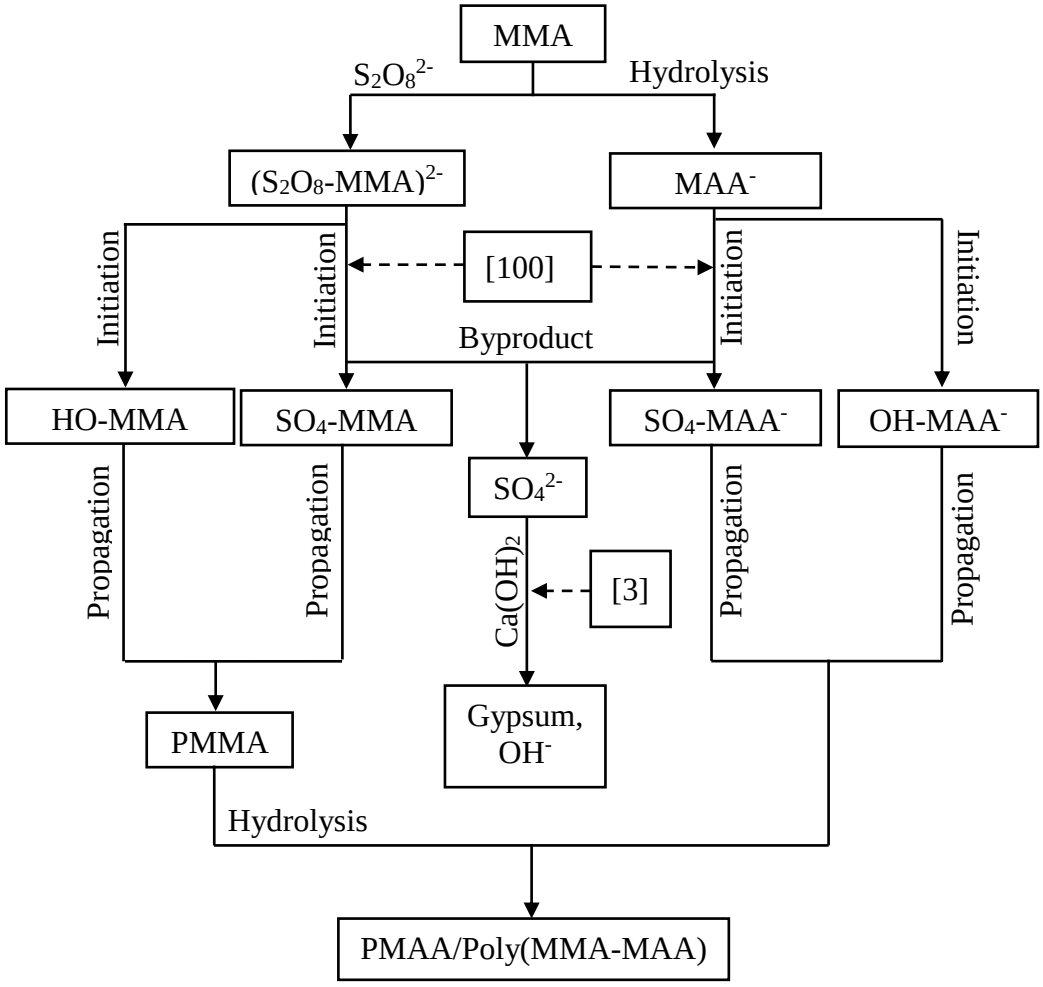

Figure 4-63: Scheme of electroinitiated polymerization of MMA in HCP specimens with the use of potassium persulfate. Dashed lines indicate sources of references. References noted for scheme I (Figure 4-62) also apply to this scheme.

4.8 Recommendations in Future Work

Previous sections show that the PMMA-related liquid was obtained from the pores of the MMA-treated HCP specimens. This organic liquid failed to increase tensile strength and reduce the porosity of the HCP specimens. In the future, several research

directions are worthy to explore in order to change the liquid phase of the PMMA-related product to a solid phase.

The emulsification of MMA or PMMA has a great potential to increase the efficiency of polymerization of MMA [152]. Surfactants (such as tetradecyl-trimethyl-ammonium bromide) are used to coordinate with the MMA monomers or PMMA particles. This surfactant has a hydrophobic and hydrophilic group. During the mixing process, the hydrophobic functional group of a surfactant is attached to the MMA/PMMA species. The hydrophilic group would tend to show affinity to water. Once the MMA/PMMA species have sufficient surfactant attached, the particle surface would tend to exhibit a net charge. This process is referred to as the emulsification of MMA/PMMA. Emulsified particles tend to be highly soluble. With the use of a surfactant, Gan *et al.* successfully obtained a 10-wt% MMA solution [153]. After increasing the solubility of MMA in an aqueous system, the MMA treatment on the HCP specimens can be conducted in a shorter time, with a lower applied potential and more yields of PMMA in the pores of the HCP. Moreover, after polymerization, the emulsified PMMA particles may also be charged and suspended in the solution, which means that they could be driven into the pores effectively under the electric field. Therefore, for strengthening the concrete structures, the electro-polymerization of the emulsified MMA and the electrophoresis of the emulsified PMMA needs to be explored.

The literature indicated that the addition of PMMA solid particles in a polymerization system can increase the conversion of MMA [82]. It is possible that the solid PMMA particles still have the potential to participate in the polymerization because the active radicals are hidden in the PMMA particles. Therefore, the addition of PMMA

in the cement paste during the batching (or driven electrophoretically) may facilitate the electro-polymerization of MMA in the pores.

Mequinol, as an inhibitor in MMA monomers, was not removed prior to the MMA treatments in this study. It is unclear if mequinol had an influence on the electro-polymerization of MMA. So, the inhibitor mechanism of mequinol and other potential inhibitors in MMA monomers and its impact on polymerization need to be explored.

In this work, electrodeposition treatments effectively formed a calcium-hydroxide barrier on the surface of steel bars. This barrier was tested under the anodic polarization and showed some positive results aimed at protecting the reinforcement during a given treatment. This protective electrodeposit in concrete structures needs to be further tested in the simulated seawater environment.

CHAPTER 5

CONCLUSION AND FUTURE WORK

The conclusions from Sections 4.1 to 4.8 are presented in the following sections. Moreover, a final conclusion and future work are presented.

5.1 Electropolymerization Proof of Concept Tests

1. The ATR analysis indicated that the reaction products (white deposits) were chemically similar to PMMA.
2. Adequate initiator content (mol/L) of persulfate could overcome the inhibition provided by mequinol (which is one of the inhibitors that is packed into MMA liquids for shipping).
3. Without the potassium persulfate initiator, the electricity alone was unable to initiate polymerization in trials involving Ti-wire and near-neutral solutions (Trials 1-5).

5.2 Electrodeposits and Anodic Polarization on 1018 Steel Bars

1. Calcium ions were depleted from the treatment solution and formed white deposits on the surface of the steel rod.
2. The electrodeposits reduced the corrosion of the steel bars by approximately 12% during the anodic polarization tests.

3. Intense bubble formation hindered the electrodeposition of $Ca(OH)_2$, which increased the difficulty to form a uniform coating.
4. High-resistance calcium hydroxide barrier protected the steel bar from corroding rapidly.
5. Therefore, this electrodeposit appeared to act as a sacrificial coating defending against the anodic polarization during AP tests.
6. If the anodically passed charges on the treated bar were less than 148 coulombs, the bar tended to exhibit a significantly lower corroded area.
7. The SEM image demonstrated that the majority of crystalline deposits exhibited a morphology that is typical of calcium hydroxide.

5.3 MMA Treatment with Electrodeposits on Rebar

1. The electrodeposition treatments (ED) had significant reductions of cations when the corrosion potential vs. CSE was -3.50 V. This reduction caused the current to increase significantly in Groups (LCHV) and (HCHV) during ED treatments.
2. The current profiles of the ED treatments may have been dominated by electrolysis and thus less likely to exhibit significant current drop associated with electrodeposition.
3. One-week batch would have contained a higher concentration of ions which could have resulted in the higher current density distribution.
4. The low concentration of alkaline species applied in the ED treatment and the low corrosion potential during MMA treatments may have contributed to low corroded area on the rebar.

5. The electrolysis of water seemed to be predominant during the ED treatments so that the protection provided by the electrodeposits was probably not significant in the MMA treatments.
6. Average tensile strengths of treated HCP specimens (3-month-aged) were higher than those of the control specimens, but the statistical analysis indicated that the two mean values were not significantly different.
7. The statistical analysis indicated that the average tensile strength of Group (Y-MMA) was significantly lower than that of Group (Y-Control).

5.4 Potentiodynamic Polarization Scanning on Rebar

1. Potentiodynamic polarization tests indicated that the average corrosion potentials at the trans-passive turning point were 0.671 (±0.048) V or 0.53 (±0.007) V, respectively, when the steel bars were embedded in the HCP specimens or exposed directly to the solution.
2. According to the calculations of uncertainties, the new modified corrosion potential used for the MMA treatment applications was 0.49 V, which protected against trans-passive corrosion.

5.5 MMA Treatment with Small Corrosion Potential

1. The younger HCP specimens in Trials 1 and 2 (32 and 34 days-old, respectively) likely exhibited a more basic (pH > 13) environment which would be less likely to form Fe_2O_3, thus permitting better strength than observed in older specimens.
2. The loss of strength due to corrosion on the steel bars of the MMA-treated specimens was not compensated by the electropolymerization of MMA.

3. Unchanged porosities after the MMA treatment indicated that the formation of PMMA-like compound did not decrease the porosity of HCP.
4. ATR analysis of the extracted liquid from the treated HCP specimens indicated that the liquid was chemically similar to PMMA.

5.6 Reproducibility Check on Strength Benefit of MMA Treatment

1. Decreasing current densities in both trials indicated that the concentration of available ions decreased during the MMA treatments.
2. Micro cracks or related damage due to high current density in the MMA-treated HCP specimens probably caused stress concentrations that lower the tensile strength.
3. Micro cracks may have increased the average porosity of the specimens.
4. ATR analysis of the extracted liquid from the treated HCP specimens indicated that the liquid was chemically similar to PMMA.
5. Decreased pH value of the treatment solution indicated the hydroxide ions may have participated in the polymerization of MMA in the MMA-treated HCP specimens.

5.7 MMA Treatment with Potassium Persulfate Initiator

1. High-current-density damage was expected to cause the strength of the MMA-treated HCP specimens to decrease.
2. MMA treatments caused the average tensile strength to increase by 12% in S-Trial 3, but the statistical analysis indicated that the strength between the MMA-treated and untreated HCP specimens were not significantly different.

3. Reducing sulfate-residence time mitigated 100% of the damage in the HCP specimens that were observed in L-Trials 1 and 2.
4. The porosity of HCP specimens was not reduced after the MMA treatments with the application of potassium persulfate.
5. By limiting the sulfate interaction time and concentration, the impact of sulfate ions on the MMA-treated HCP specimens appeared to be minimized or compensated by the MMA treatment.
6. ATR analysis of the extracted liquid from the MMA-treated HCP specimens indicated that the liquid was chemically similar to PMMA.
7. The reduction in hydroxide ions (as noted from pH monitoring) would be expected to slow down and reduce the rate of polymerization.
8. Reducing the treatment time caused the charged particles to be less likely to migrate into the HCP specimens.
9. Reduced concentration of potassium persulfate caused the conversion of MMA to decrease.
10. The conversion of MMA monomers in the MMA-treated HCP specimens in all trials using initiators was significant, but liquid phase reaction product was unable to provide strength and porosity benefits to the HCP.

5.8 Mechanism of Electro-initiated Polymerization of MMA

1. MMA appeared to be retained in the solution by a dipole-dipole complex formation.

2. The hydrolysis of MMA generated the hydroxide-MMA complex and caused the pH value of the solution to decrease. Charged complexes can be driven into the HCP pores under the electric field.
3. Hydroxide ions appeared to participate in the electro-polymerization of MMA as initiators.
4. The reduction of potassium persulfate from 0.01 mol/L to 0.004 mol/L in LC-Trial 4 was reasonably expected to reduce the production of active radicals, and thus the conversion of MMA.
5. The extracted liquid from the MMA-treated HCP in various trials was likely to be poly(MMA-MAA) copolymer as opposed to just PMAA.

5.9 Future Work

1. For strengthening the concrete structures, the electro-polymerization of the emulsified MMA and the electrophoresis of the emulsified PMMA need to be explored.
2. The addition of PMMA in the cement paste during the batching (or driven electrophoretically) may facilitate the electro-polymerization of MMA in the pores.
3. The inhibitor mechanism of mequinol and other potential inhibitors in MMA monomers and its impact on polymerization need to be explored.
4. This protective electrodeposit in concrete structures needs to be further tested in the simulated seawater environment.

APPENDIX A

CERTIFIED MILL TEST REPORT OF PORTLAND CEMENT

ASH GROVE CEMENT COMPANY

4343 Highway 108
Foreman, Arkansas 71836
Phone: 870-542-3040

Type I/II (Low Alkali)

Production Period: October 1 thru October 31, 2018

Date: 11/7/2018

The following information is based on average test data during the production period. The data is typical of cement shipped from the Foreman, Arkansas plant. Individual shipments may vary.

STANDARD REQUIREMENTS
ASTM C150/C150M-09

CHEMICAL

Item	A.S.T.M. Test Method	Spec. Limit	Test Result
SiO_2 (%)	C114	*A*	20.45
Al_2O_3 (%)	C114	*A*	4.68
Fe_2O_3 (%)	C114	*A*	3.85
CaO (%)	C114	*A*	64.23
MgO (%)	C114	6.0 max	0.87
SO_3 (%)	C114		2.63
Loss on ignition (%)	C114	3.5 max	2.93
Na_2O (%)	C114	*A*	0.13
K_2O (%)	C114	*A*	0.52
Insoluble Residue (%)	C114	1.50 max	0.50
CO_2 (%)	C114	*A*	1.86
Limestone (%)	C114		4.8
$CaCO_3$ in limestone (%)	C114		86.73
Potential compounds (%)[D]			
C_3S	C114	*A*	54
C_2S	C114	*A*	14
C_3A	C114		5
C_4AF	C114	*A*	11
$C_3S + 4.75\ C_3A$	C114		78

PHYSICAL

Item	A.S.T.M. Test Method	Spec. Limit	Test Result
Air content of mortar (volume %)	C185	12 max	8
Fineness (cm^2/g):			
Air permeability	C204	2800 min	4261
Autoclave expansion (%)	C151	0.80 max	0.00
Compressive strength (psi)			
1 Day	C109	*A*	2506
3 Days	C109	1740 min	4295
7 Days	C109	2760 min	5133
Time of setting (minutes) (Vicat)			
Initial: Not less than	C191	45	139
Not more than		375	139
Mortar Bar Expansion (%)	C1038	0.020 max	0.002

OPTIONAL REQUIREMENTS
ASTM C150/C150M-09, Tables 2 and 4

CHEMICAL

Item	A.S.T.M. Test Method	Spec. Limit	Test Result
$C_3S + C_3A$ (%)	C114	*A*	
Equivalent alkalies (%)	C114	0.60	0.47

PHYSICAL

Item	A.S.T.M. Test Method	Spec. Limit	Test Result
False set (%)	C451	*B*	62
Heat of hydration (kJ /kg)			
7 days	C186	*A*	

A = Not applicable.
B = Limit not specified by purchaser, test result provided for information only.
C = Test results for this period not available.
D = Adjusted per Annex A1.6 M85

We certify that the above described cement, at the time of shipment, meets the chemical and physical requirements of ASTM C150/C150M-09 (Types I/II) and AASHTO M85-07 (Type I/II), or (other)_____specification.

Signature: Floyd Arnold

Floyd Arnold
Title: Chief Chemist

APPENDIX B

PMMA PROOF TESTS

Table B-1: The masses (in Grams) of Ti-wire after trials 1-5 described in Section 3.3.1.

Measurement	Control	0.7V	0.8V	0.9V	1.0V	1.1V
1	1.1375	1.1304	1.1382	1.1366	1.1304	1.1316
2	1.1366	1.1337	1.1296	1.1359	1.1340	1.1328
3	1.1343	1.1275	1.1345	1.1374	1.1383	1.1325
4	1.1317	1.1319	1.1355	1.1297	1.1379	1.1310
5	1.1329	1.1339	1.1370	1.1365	1.1338	1.1258
Average	1.1346	1.1315	1.1350	1.1352	1.1349	1.1307
Standard Deviation	0.0024	0.0026	0.0033	0.0031	0.0033	0.0029
Error Bar Limit	0.0018	0.0019	0.0024	0.0023	0.0024	0.0021

Table B-2: The masses (in Grams) of Ti-wire after trials 6 & 7 described in Section 3.3.1.

	Untreated	0.2 mol/L	0.4mol/L
Mass 1	1.1375	1.1242	1.1342
Mass 2	1.1366	1.1338	1.1352
Mass 3	1.1343	1.1307	1.1265
Mass 4	1.1317	1.1349	1.1350
Mass 5	1.1329	1.1368	1.1222
Average	1.1346	1.1321	1.1306
Standard Deviation	0.0024	0.0049	0.0059
Error Bar Limit	0.0018	0.0036	0.0044

Table B-3: Three beaker tests of polymerization of MMA with different treatment times. Setup is described in Section 3.3.1.

	Trial 4 (10 mins)	**Trial 11 (24 hours)**	**Control* (No Power Supply in 24 hours)**
MMA odor	Yes	Yes	No
Deposits	No	No	No

*Data of control Group derived from Nayeem's study **[60]**.

APPENDIX C

ELECTRODEPOSITION ON 1018 STEEL ROD

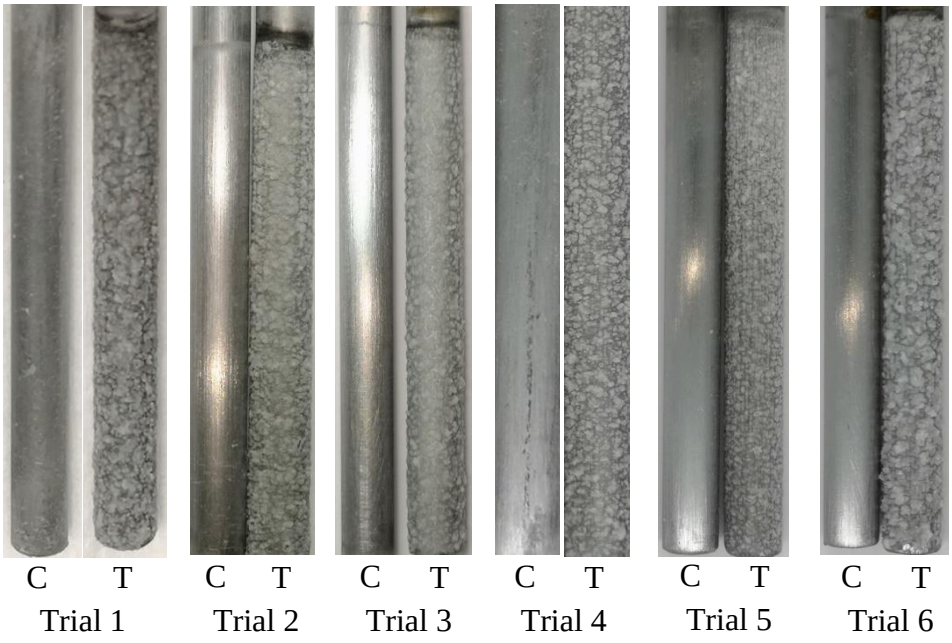

Figure C-1: Steel bars after electrodeposition treatments in trials 1-6. C Refers to the control bars. T refers to the treated bars.

Figure C-2: Steel bars after anodic polarization test in trials 1-6. C refers to the control bars. T refers to the treated bars.

Matlab Program for Grayscale Transformation and Calculation of corroded area:

(Matlab version R2018b, developed by Mathworks, Natick, MA)

```
A = imread('Local address of the raw image');   % Read local raw image
B = rgb2gray(A);                                % Grayscale transformation
thres1 = 122/255;                               % Setting Threshold
I2 = imbinarize(B,thres1);                      % Binarize grayscale image
C = imhist(B);                                  % Obtain histogram of grayscale image
figure(1)
imshow(B)                                       % Show the grayscale image
figure(2)
imshow(I2)                                      % Show the binary image
figure(3)
imhist(B)                                       % Show the histogram of grayscale image
White = 0;                                      % Calculate the corroded area
Black = 0;
for i = 1:N                                     %     (N = long edge)
   for j = 1:M                                  %     (M = wide edge)
      if I2(i,j) = 1
         White = White + 1;
      else
         Black = Black + 1;
      end
   end
end
Ratio = Black/(Black + White);                  % Rate of the corroded area
```

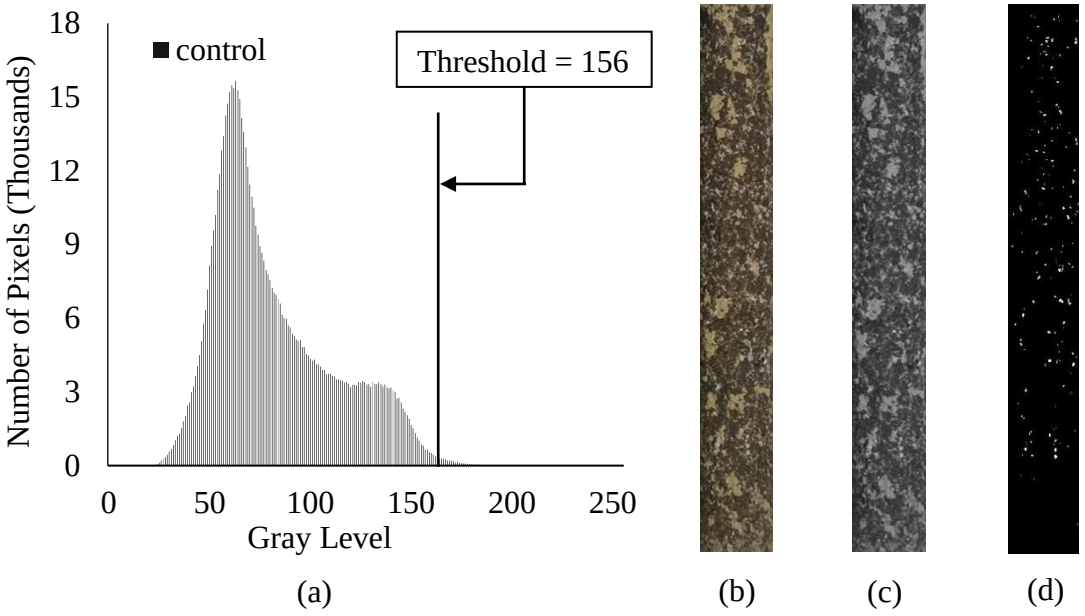

Figure C-3: Image analysis results of control bar in Trial 1. (a) Histogram of grayscale image of control bar. (b) Raw image of control bar. (c) Grayscale image of control bar. (d) Binary image of control bar.

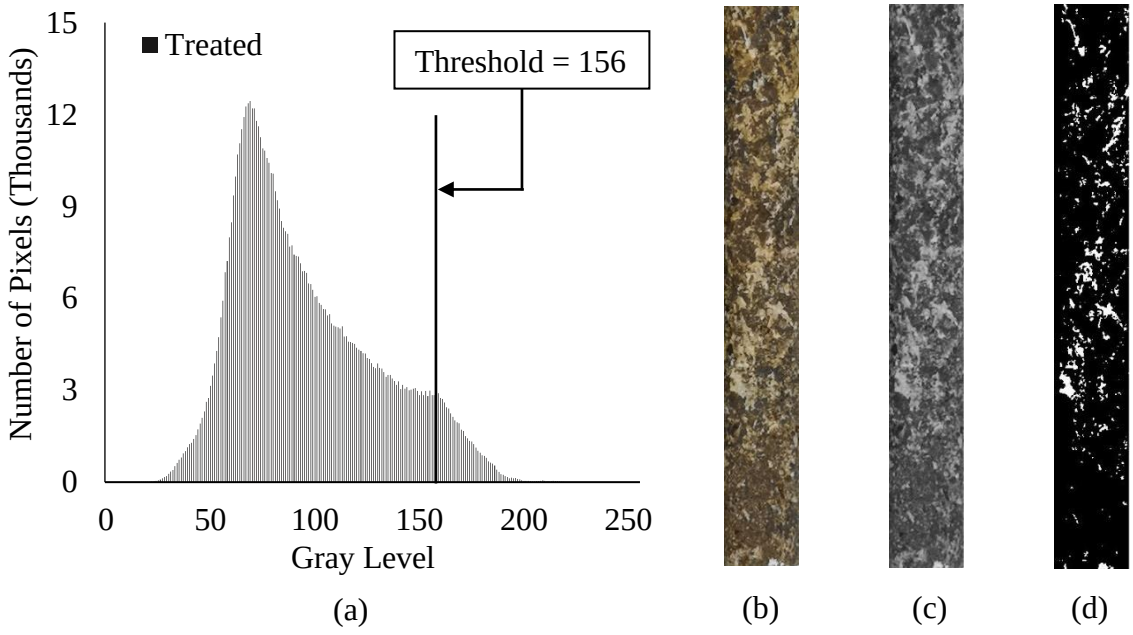

Figure C-4: Image analysis results of treated bar in Trial 1. (a) Histogram of grayscale image of treated bar. (b) Raw image of treated bar. (c) Grayscale image of treated bar. (d) Binary image of treated bar. 92.8% area corroded.

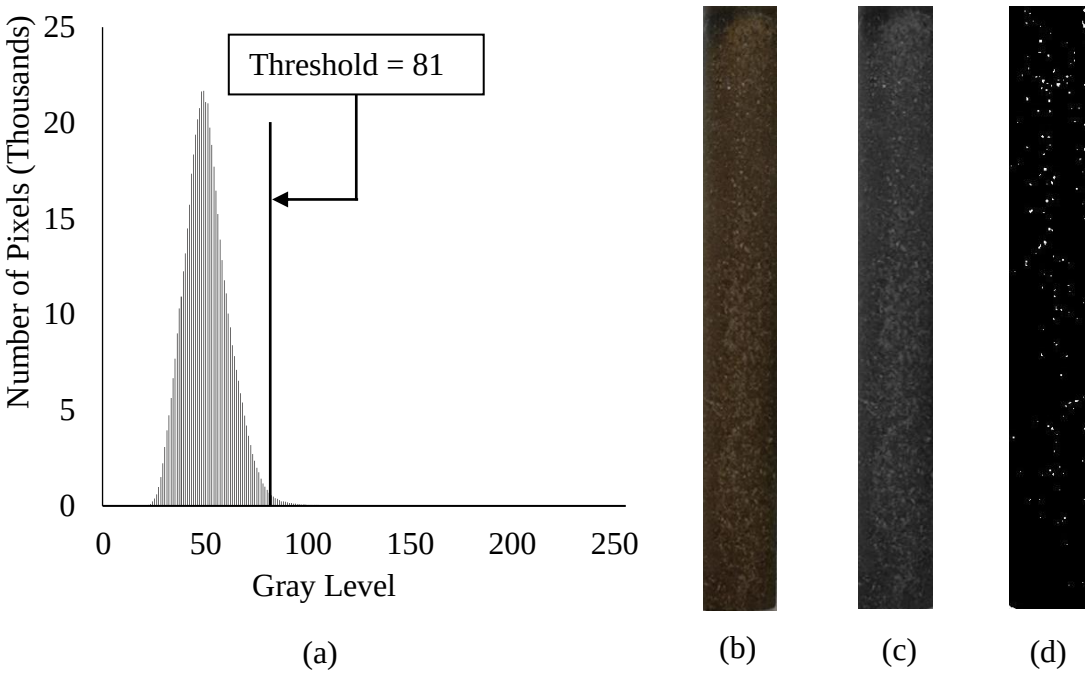

Figure C-5: Image analysis results of control bar in Trial 2. (a) Histogram of grayscale image of control bar. (b) Raw image of control bar. (c) Grayscale image of control bar. (d) Binary image of control bar.

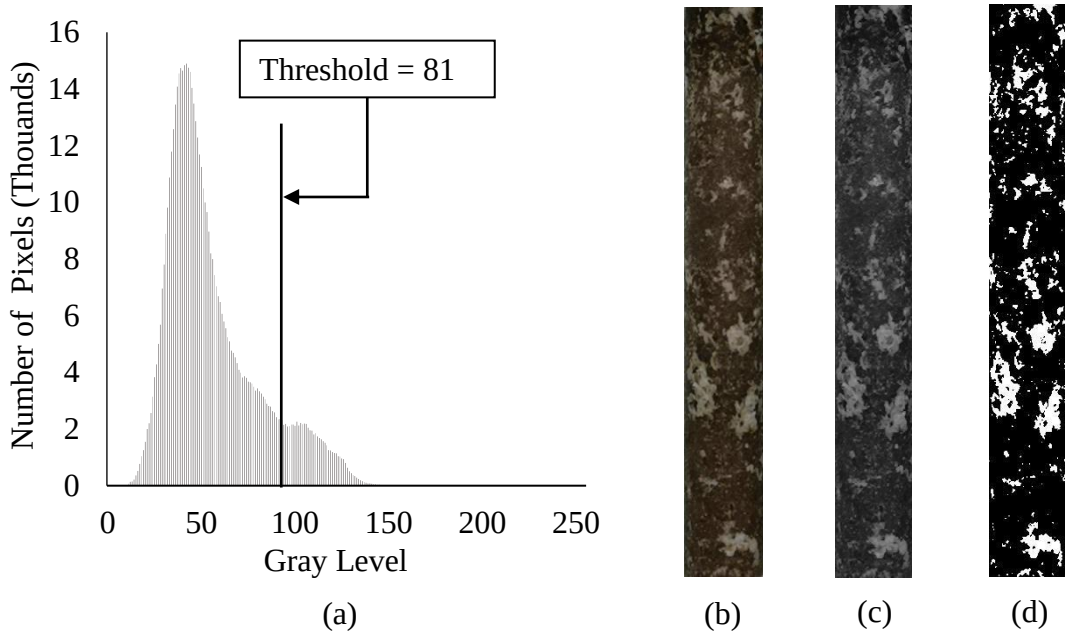

Figure C-6: Image analysis results of treated bar in Trial 2. (a) Histogram of grayscale image of treated bar. (b) Raw image of treated bar. (c) Grayscale image of treated bar. (d) Binary image of treated bar. 83.7% area corroded.

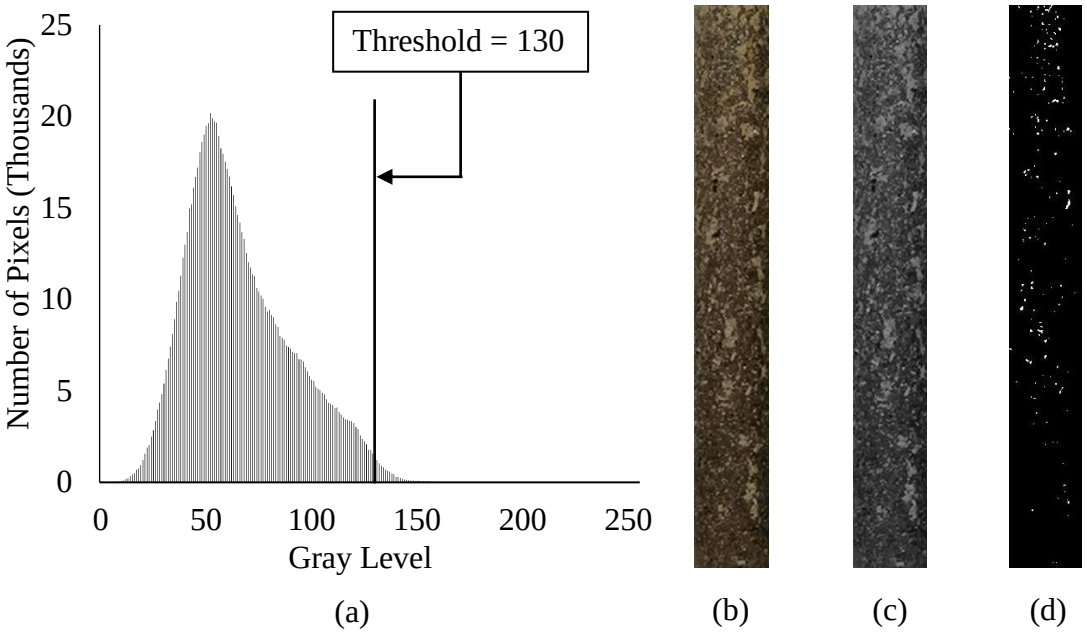

Figure C-7: Image analysis results of control bar in Trial 3. (a) Histogram of grayscale image of control bar. (b) Raw image of control bar. (c) Grayscale image of control bar. (d) Binary image of control bar.

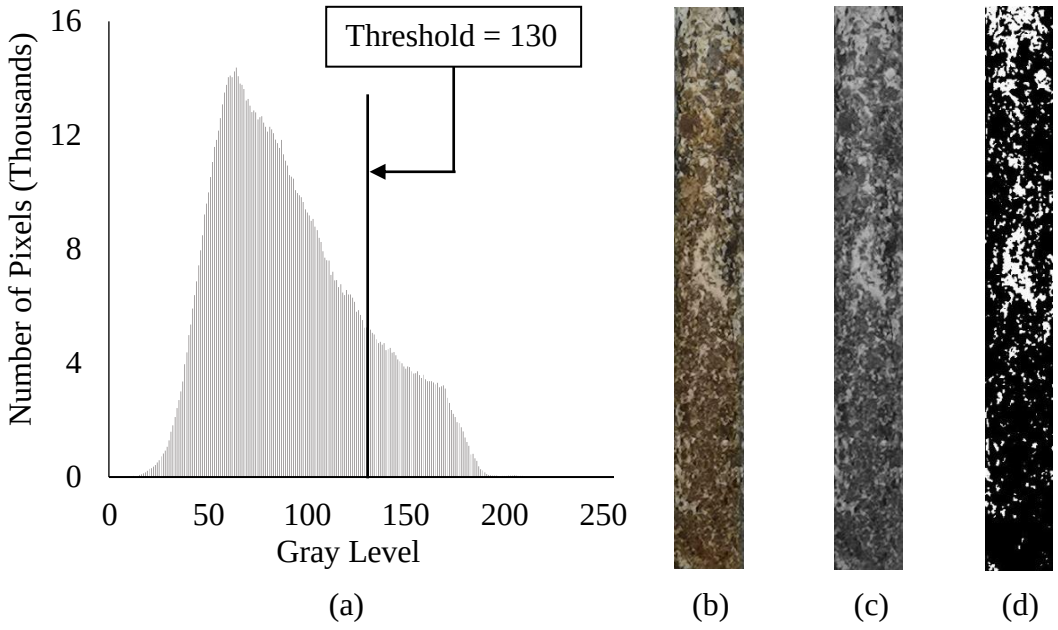

Figure C-8: Image analysis results of treated bar in Trial 3. (a) Histogram of grayscale image of treated bar. (b) Raw image of treated bar. (c) Grayscale image of treated bar. (d) Binary image of treated bar. 83.3% area corroded.

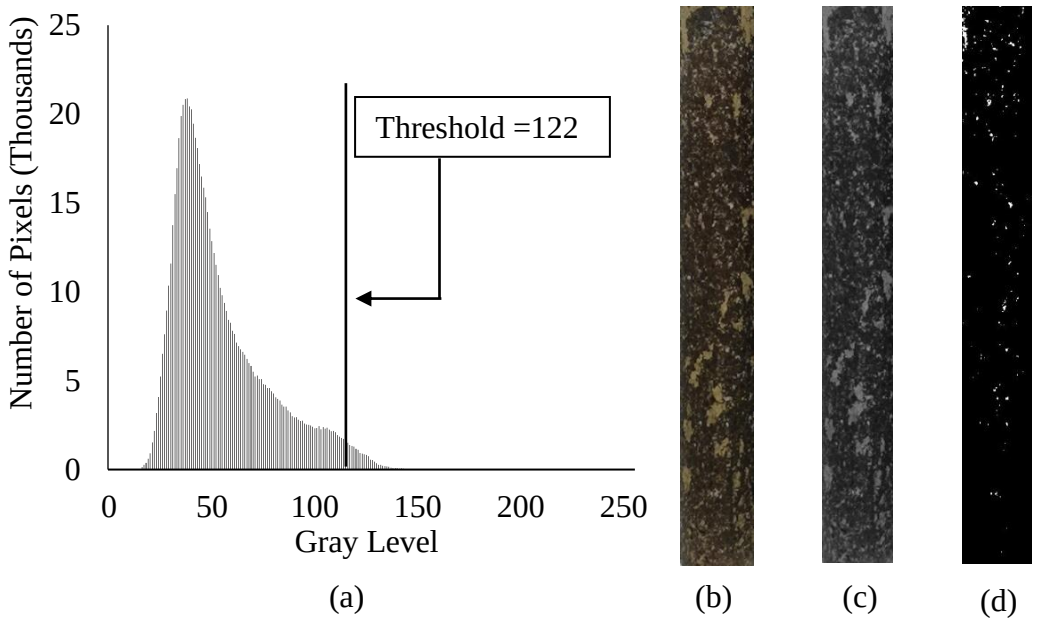

Figure C-9: Image analysis results of control bar in Trial 4. (a) Histogram of grayscale image of control bar. (b) Raw image of control bar. (c) Grayscale image of control bar. (d) Binary image of control bar.

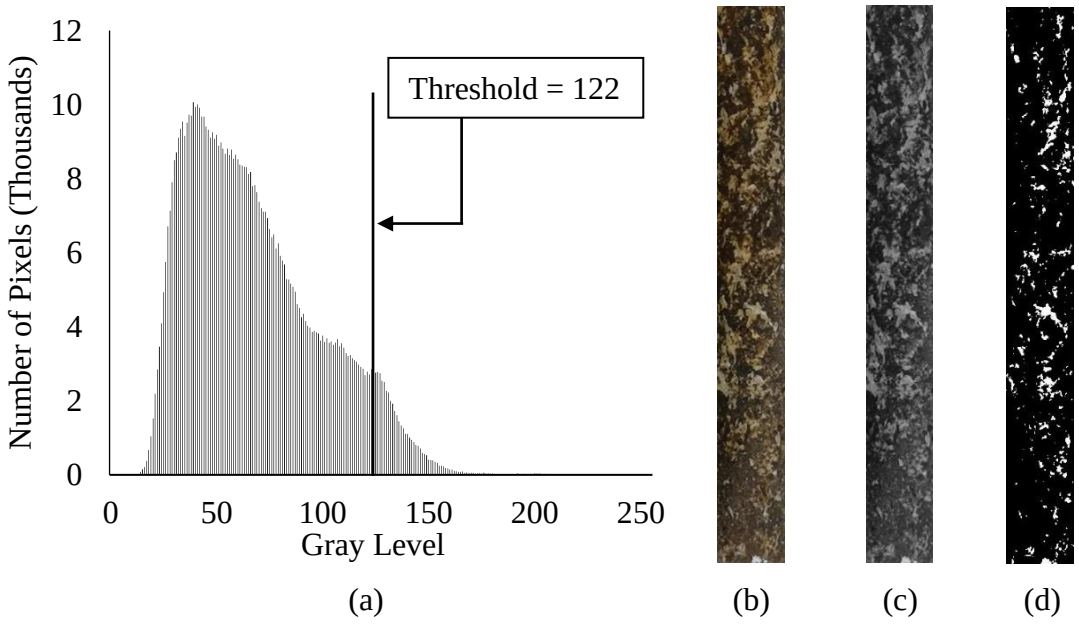

Figure C-10: Image analysis results of treated bar in Trial 4. (a) Histogram of grayscale image of treated bar. (b) Raw image of treated bar. (c) Grayscale image of treated bar. (d) Binary image of treated bar. 92.9% area corroded.

Table C-1: Currents of treated steel bars monitored in electrodeposition and anodic polarization treatments in trials 1-6. (Unit: Amperes)

Time (day)	Trial 1	Trial 2	Trial 3	Trial 4	Trial 5	Trial 6	Average	STDEV*	Error Bar
1	2.84	2.2	2.65	2.33	2.3	2.51	2.47	0.24	0.16
2	2.32	1.32	1.61	1.56	1.05	1.18	1.51	0.45	0.30
3	2.21	1.06	1.34	1.17	0.84	0.78	1.23	0.52	0.35
4	1.7	0.98	0.95	0.91	0.78	0.63	0.99	0.37	0.25
5	1.36	0.77	0.94	0.86	0.67	0.63	0.87	0.27	0.18
6	1.17	0.82	0.75	0.7	0.61	0.6	0.78	0.21	0.14
7	1.12	0.83	0.78	0.69	0.51	0.52	0.74	0.23	0.15
8	0.44	0.54	0.23	0.25	0.44	0.2	0.35	0.14	0.09
9	1.43	1.61	1.46	1.13	1.71	0.82	1.36	0.33	0.22
10	1.72	1.8	1.72	1.65	1.7	1.39	1.66	0.14	0.10
11	1.81	1.87	1.8	1.87	0.12	1.68	1.81	0.08	0.06
12	1.61	1.71	1.89	1.84	0.89	0.07	1.76	0.13	0.10

***** STDEV is the standard deviation.
Underlined currents were excluded from the calculations of average currents, standard deviation and error bar limit.

Table C-2: Currents of control steel bars monitored in anodic polarization treatments in trials 1-6. (Unit: Amperes)

Time (day)	Trial 1	Trial 2	Trial 3	Trial 4	Trial 5	Trial 6	Average	STDEV*	Error Bar
8	2.84	2.2	2.65	2.33	2.3	2.51	2.47	0.24	0.16
9	2.32	1.32	1.61	1.56	1.05	1.18	1.51	0.45	0.30
10	2.21	1.06	1.34	1.17	0.84	0.78	1.23	0.52	0.35
11	1.7	0.98	0.95	0.91	0.78	0.63	0.99	0.37	0.25
12	1.36	0.77	0.94	0.86	0.67	0.63	0.87	0.27	0.18

***** STDEV is the standard deviation.
Underlined currents were excluded from the calculations of average currents, standard deviation and error bar limit.

Table C-3: Corrosion potentials of treated and control bars prior to electrodeposition treatments. (Unit: Volts)

	Trial 1	Trial 2	Trial 3	Trial 4	Trial 5	Trial 6	Average	STDEV*	Error Bar
Control	-0.47	-0.47	-0.48	-0.51	-0.52	-0.52	-0.49	0.02	0.02
Treated	-0.50	-0.47	-0.50	-0.59	-0.46	-0.49	-0.50	0.04	0.03

***** STDEV is the standard deviation.

Table C-4: Corrosion potentials of steel bars monitored during anodic polarization tests in trials 1-6. (Unit: Volts)

Time (day)	Trial 1	Trial 2	Trial 3	Trial 4	Trial 5	Trial 6	Average	STDEV*	Error Bar
Corrosion Potentials of Treated Bars									
8	-0.38	-0.65	-0.50	-0.45	-0.65	-0.80	-0.57	0.15	0.10
9	-0.33	-0.85	-0.32	-0.32	-0.82	-0.36	-0.50	0.26	0.18
10	-0.65	-0.89	-1.01	-0.74	-0.85	-0.42	-0.76	0.21	0.14
11	-0.95	-0.90	-0.88	-0.84	-0.63	-0.45	-0.78	0.19	0.13
12	-0.45	-0.93	-0.93	-0.92	-0.62	-0.57	-0.74	0.22	0.14
13	-0.94	-0.96	-0.85	-0.87	-0.62	-0.66	-0.81	0.14	0.10
Corrosion Potentials of Control Bars									
8	-0.35	-0.33	-0.34	-0.25	-0.27	-0.37	-0.32	0.05	0.03
9	$\underline{-0.10^{+}}$	-0.68	-0.97	-0.78	-1.02	-0.91	-0.87	0.14	0.10
10	-0.95	-0.96	-0.97	-0.82	-0.85	-0.81	-0.89	0.08	0.05
11	-0.96	-0.92	-0.96	-0.86	-0.57	-0.81	-0.85	0.15	0.10
12	-0.96	-0.93	-0.97	-0.91	-0.56	-0.68	-0.84	0.17	0.12
13	-1.00	-0.95	-0.95	-0.82	-0.60	-0.48	-0.80	0.21	0.14

***** STDEV is the standard deviation.

+The underlined electric current was excluded from the calculations of average corrosion potential, standard deviation and error bar limit.

Table C-5: Electric charge passage on treated steel bars as monitored during electrodeposition and anodic polarization treatments in trials 1-6. (Unit: Coulomb)

Time (day)	Trial 1	Trial 2	Trial 3	Trial 4	Trial 5	Trial 6	Average	STDEV*	Error Bar
1	245k	190k	229k	201k	199k	217k	214k	21k	14k
2	200k	114k	139k	135k	91k	102k	130k	39k	26k
3	191k	92k	116k	101k	73k	67k	107k	45k	30k
4	147k	85k	82k	79k	67k	54k	86k	32k	21k
5	118k	67k	81k	74k	58k	54k	75k	23k	15k
6	101k	71k	65k	60k	53k	52k	67k	18k	12k
7	97k	72k	67k	60k	44k	45k	64k	20k	13k
8	38k	47k	20k	22k	38k	17k	30k	12k	8k
9	124k	139k	126k	98k	148k	71k	118k	29k	19k
10	149k	156k	149k	143k	147k	120k	144k	12k	8k
11	156k	162k	156k	162k	10k	145k	156k	7k	5k
12	139k	148k	163k	159k	77k	6k	152k	11k	9k

***** STDEV is the standard deviation.

Table C-6: Electric charge passages on control steel bars as monitored during anodic polarization treatments in trials 1-6. (Unit: Coulomb)

Time (day)	Trial 1	Trial 2	Trial 3	Trial 4	Trial 5	Trial 6	Average	STDEV*	Error Bar
8	128k	112k	115k	108k	124k	116k	117k	8k	5k
9	168k	150k	156k	149k	154k	152k	155k	7k	5k
10	157k	161k	163k	152k	165k	139k	156k	10k	6k
11	157k	170k	164k	163k	29k	140k	159k	12k	9k
12	157k	162k	168k	168k	49k	8k	164k	5k	4k

***** STDEV is the standard deviation.

APPENDIX D

MMA TREATMENT WITH ELECTRODEPOSITION ON REBAR

Methyl Methacrylate (MMA) Dosage Calculation for MMA Treatments with Electrodeposition on Rebar:

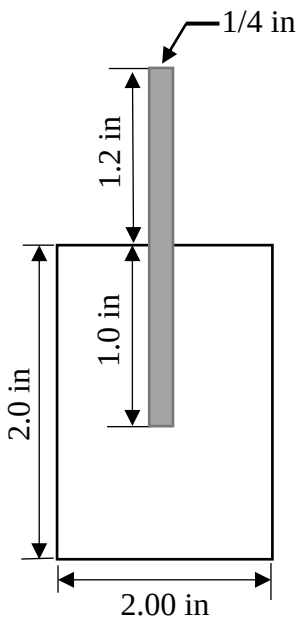

Volume of HCP Specimen:

$$V_{HCP} = \pi\left(\frac{D}{2}\right)^2 \cdot Height = \pi\left(\frac{2}{2}\right)^2 \cdot 2 = 6.283\ in^3$$

$$\approx 103\ cm^3$$

Assuming the porosity of the HCP specimen was 20%, the volume of the pores in an HCP specimen was:

$$V_{pore} = V_{HCP} \cdot 20\% = 103 \cdot 0.2 = 20.6\ cm^3$$

The density [154] of Poly(methyl methacrylate) was:

$$\rho_{PMMA} = 1.20\ g/cm^3$$

The required MMA monomer to fill the pores of HCP specimen:

$$m_{MMA} = \rho_{PMMA} \cdot V_{pore} = 1.20 \times 20.6 = 24.7\ g$$

Each group (described in Table 3-7) contained five HCP specimens. The required MMA monomer to fill the pores of 5 HCP specimens:

$$m_{Total} = 5 \cdot m_{MMA} = 5 \times 24.7 = 123.5\ \text{g}$$

The volume of the solution applied in the MMA treatment was 3172 cm^3. The concentration of MMA monomer was 0.1 mol/L. The capacity of dissolved MMA monomer in the solution was:

$$m_{MMA\ in\ Container} = 0.1\frac{mol}{L} \times 3.172\ L \times 100.12\frac{g}{mol} = 31.7\ g$$

In order to ensure the pores of HCP specimens were filled with PMMA because the porosity of HCP specimens might not be accurate, double dosages of MMA were applied

in the MMA treatment. This meant the required MMA monomer to fill the pores of 5 HCP specimens was:

$$m_{MMA,dosage} = 2 \times m_{Total} = 123.5 \times 2 = 247\ g$$

It was assumed that all the MMA monomer in the container would polymerize and evaporate in one day. A new MMA dosage ($m_{MMA\ in\ Container}$) was added daily in the solution during MMA treatment to maintain the concentration of MMA monomer. The MMA treatment time was calculated:

$$Time = \frac{m_{MMA,dosage}}{m_{MMA\ in\ Container}} = \frac{247g}{31.7g} = 7.79\ days \approx 8\ days$$

Figure D-1: Raw image of steel bars in MMA-treated HCP specimens of Group 1 (O-MMA).

Figure D-2: Raw image of steel bars in MMA-treated HCP specimens of Group 2 (LCLV).

Figure D-3: Raw image of steel bars in MMA-treated HCP specimens of Group 3 (LCHV).

Figure D-4: Raw image of steel bars in MMA-treated HCP specimens of Group 4 (HCHV).

Figure D-5: Raw image of steel bars in control HCP specimens of Group 5 (O-Control).

Figure D-6: Raw image of steel bars in MMA-treated HCP specimens of Group 6 (Y-MMA).

Figure D-7: Raw image of steel bars in control HCP specimens of Group 7 (Y-Control).

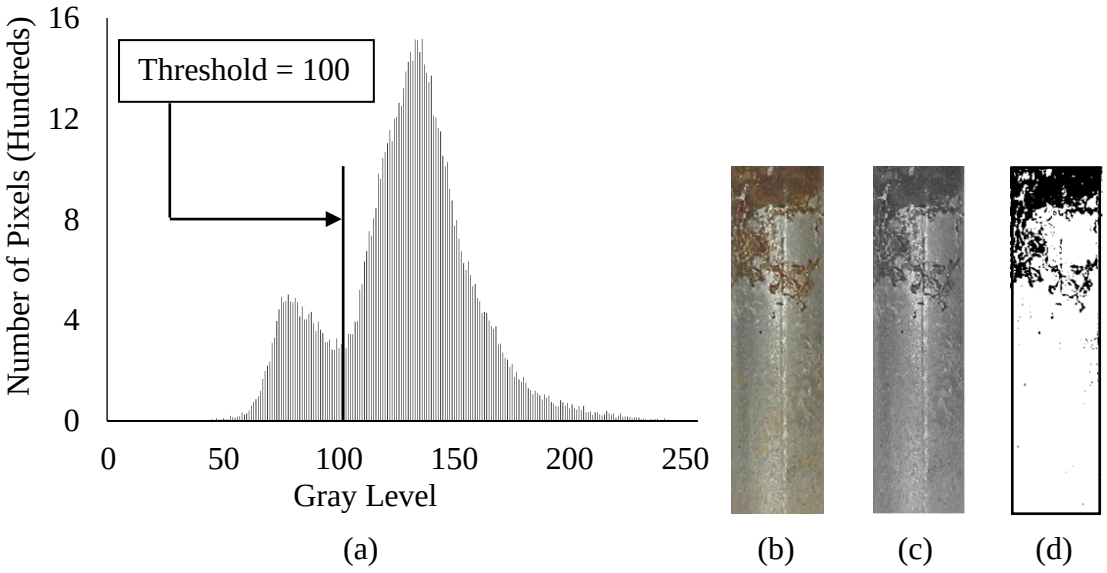

Figure D-9: Image analysis results of steel bar in MMA-treated HCP specimen 1 of Group 1 (O-MMA). (a) Histogram of grayscale image of control bar. (b) Raw image of control bar. (c) Grayscale image of control bar. (d) Binary image of control bar (exclude the black boundary).

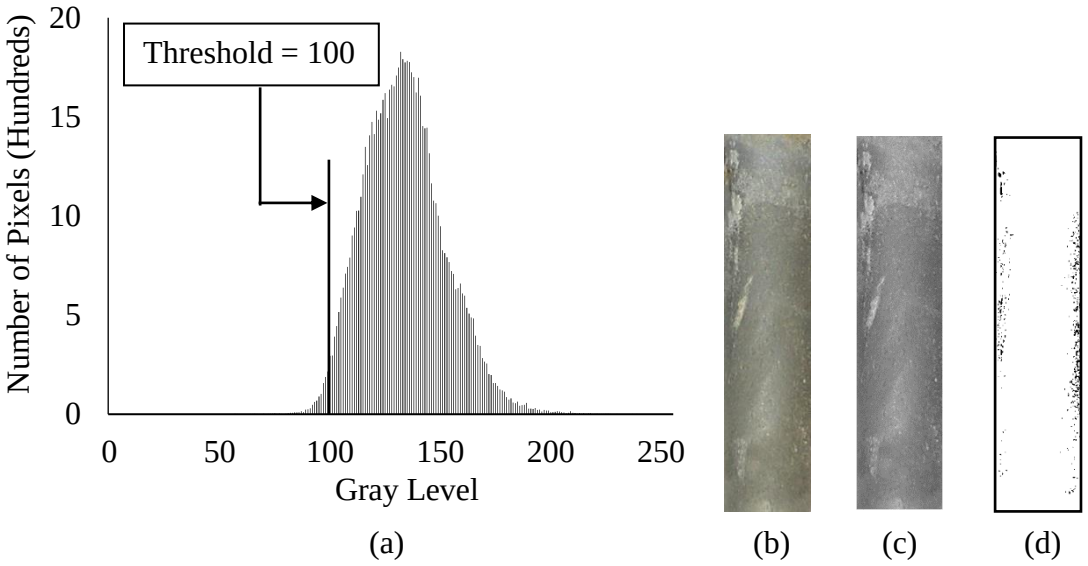

Figure D-11: Image analysis results of steel bar in MMA-treated HCP specimen 2 of Group 1 (O-MMA). (a) Histogram of grayscale image of control bar. (b) Raw image of control bar. (c) Grayscale image of control bar. (d) Binary image of control bar (exclude the black boundary).

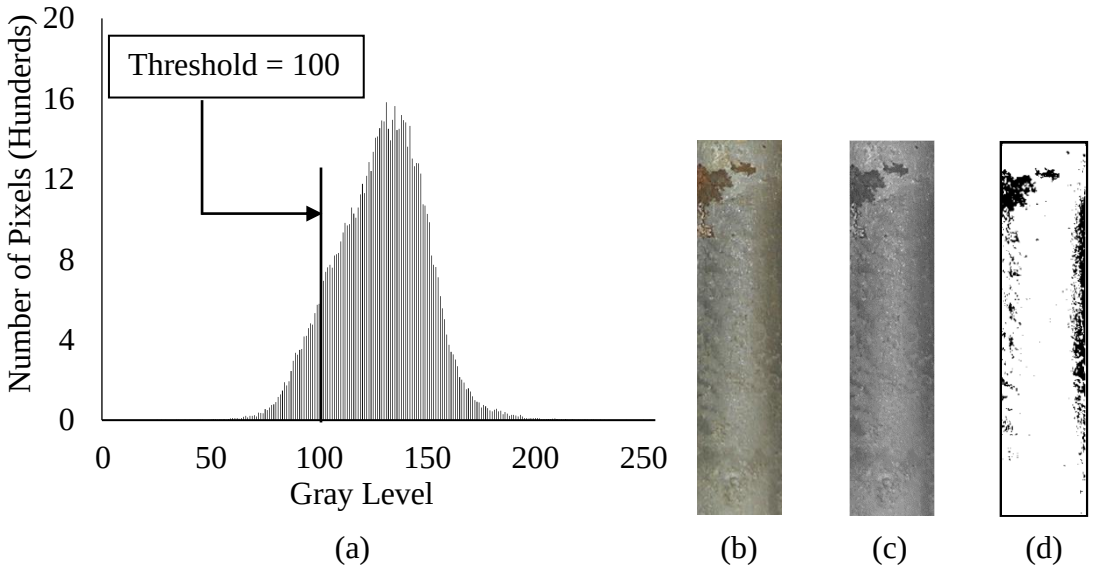

Figure D-13: Image analysis results of steel bar in MMA-treated HCP specimen 3 of Group 1 (O-MMA). (a) Histogram of grayscale image of control bar. (b) Raw image of control bar. (c) Grayscale image of control bar. (d) Binary image of control bar (exclude the black boundary).

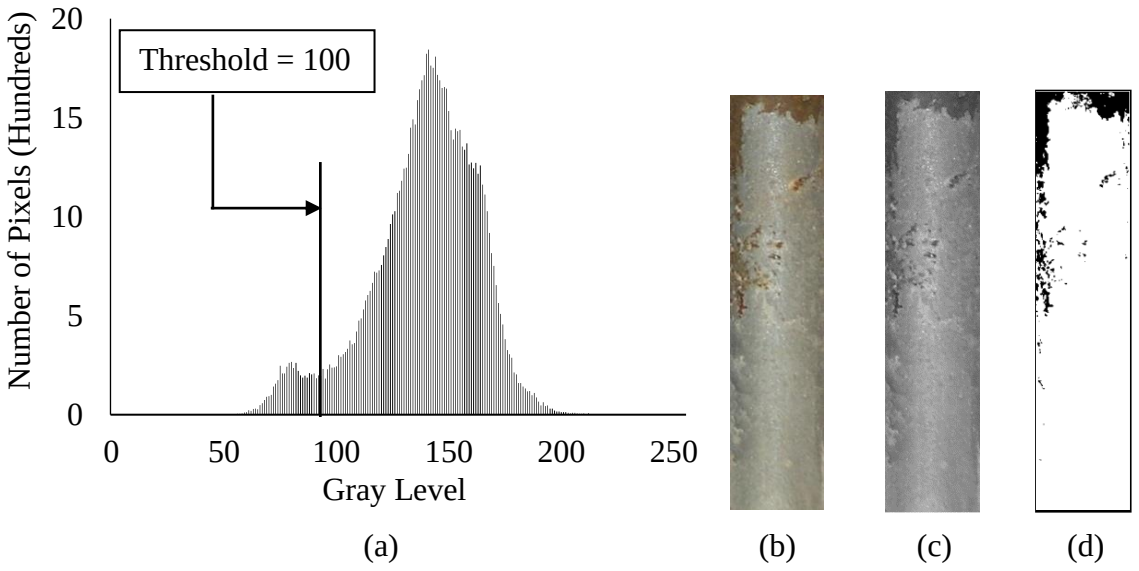

Figure D-15: Image analysis results of steel bar in MMA-treated HCP specimen 4 of Group 1 (O-MMA). (a) Histogram of grayscale image of control bar. (b) Raw image of control bar. (c) Grayscale image of control bar. (d) Binary image of control bar (exclude the black boundary).

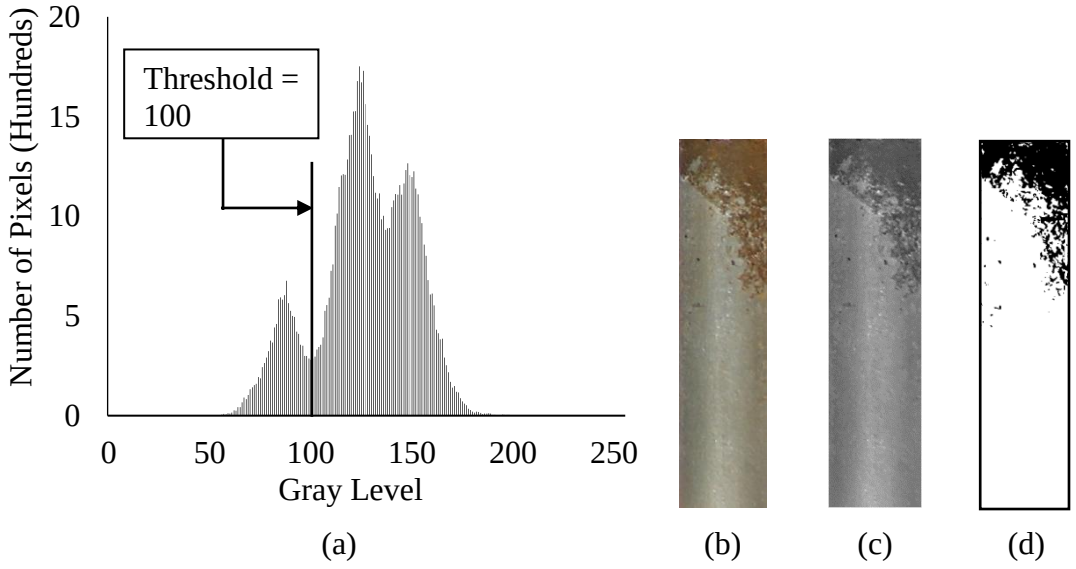

Figure D-17: Image analysis results of steel bar in MMA-treated HCP specimen 5 of Group 1 (O-MMA). (a) Histogram of grayscale image of control bar. (b) Raw image of control bar. (c) Grayscale image of control bar. (d) Binary image of control bar (exclude the black boundary).

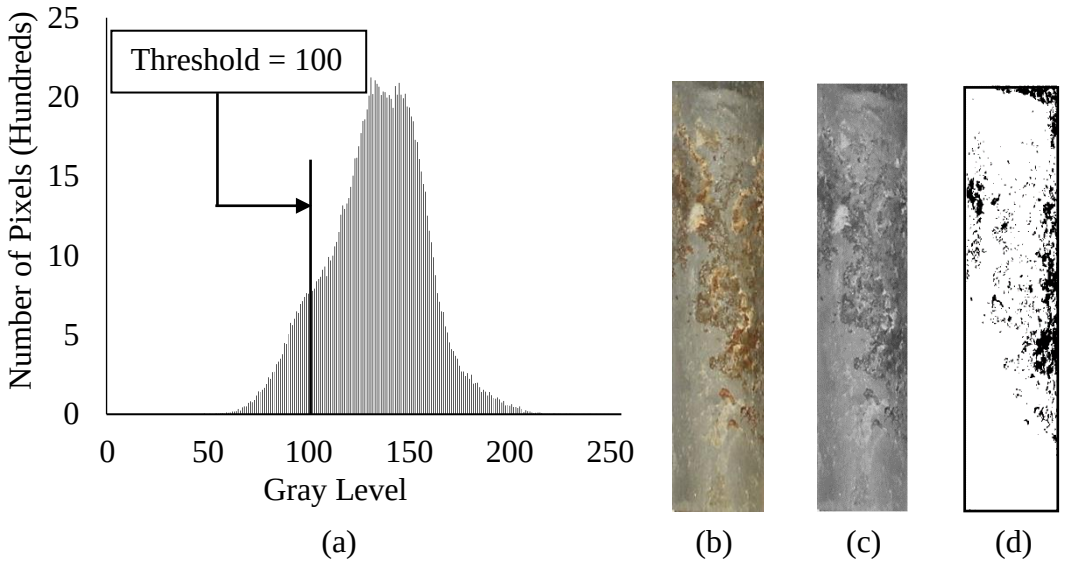

Figure D-19: Image analysis results of steel bar in MMA-treated HCP specimen 1 of Group 2 (LCLV). (a) Histogram of grayscale image of control bar. (b) Raw image of control bar. (c) Grayscale image of control bar. (d) Binary image of control bar (exclude the black boundary).

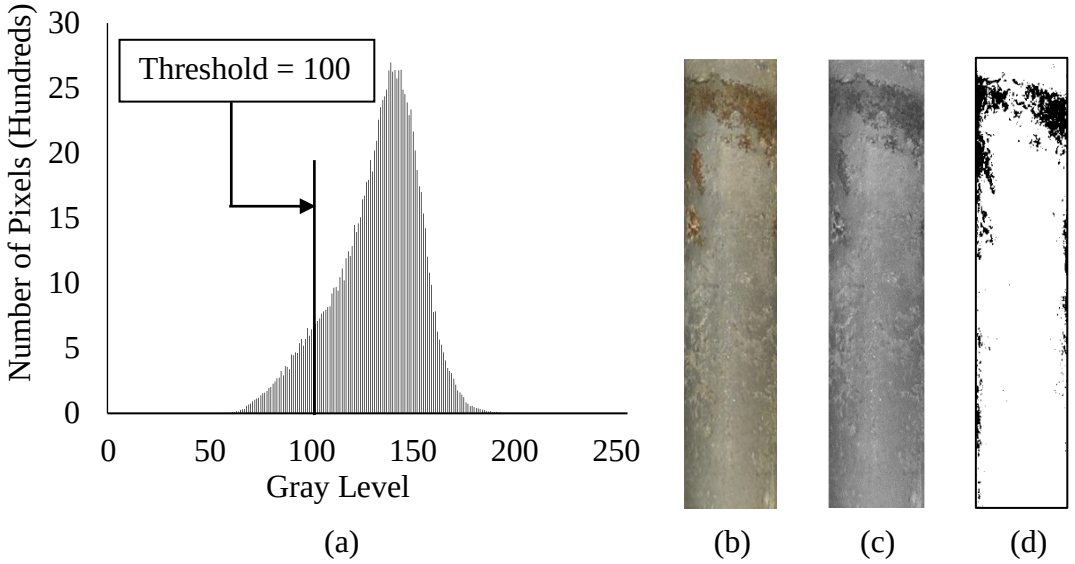

Figure D-21: Image analysis results of steel bar in MMA-treated HCP specimen 2 of Group 2 (LCLV). (a) Histogram of grayscale image of control bar. (b) Raw image of control bar. (c) Grayscale image of control bar. (d) Binary image of control bar (exclude the black boundary).

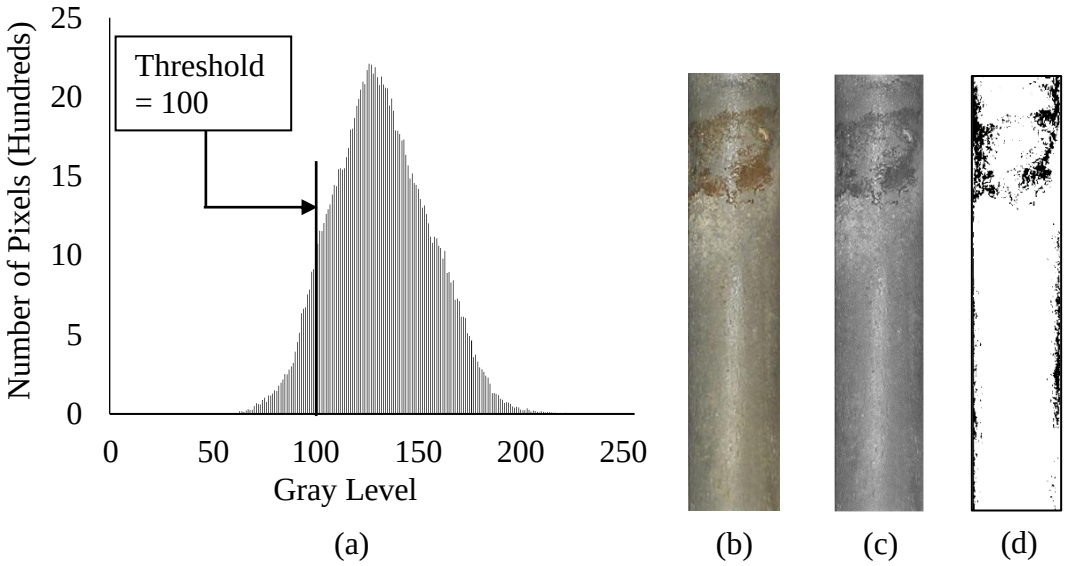

Figure D-23: Image analysis results of steel bar in MMA-treated HCP specimen 3 of Group 2 (LCLV). (a) Histogram of grayscale image of control bar. (b) Raw image of control bar. (c) Grayscale image of control bar. (d) Binary image of control bar (exclude the black boundary).

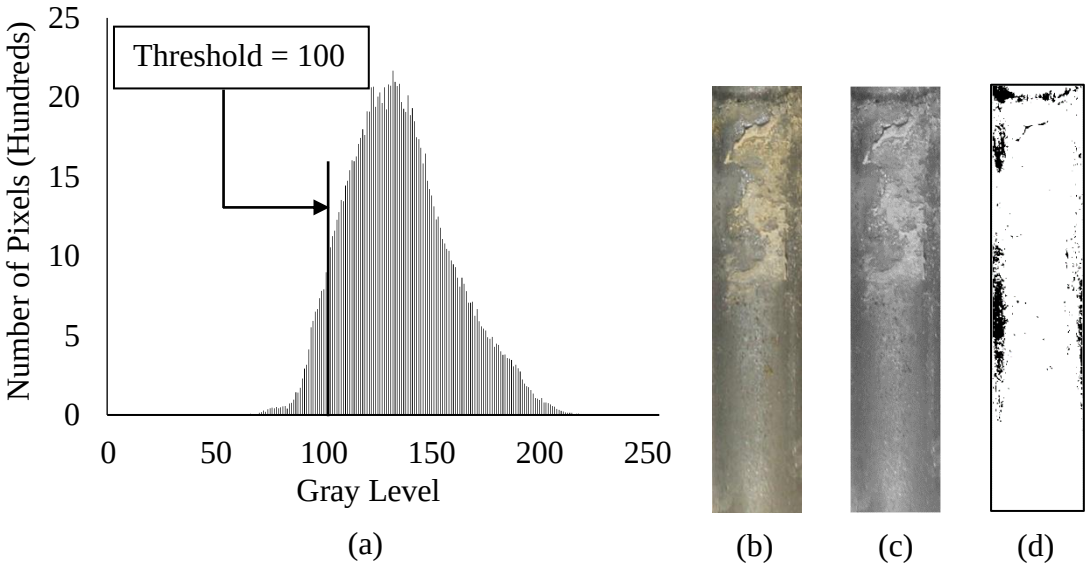

Figure D-25: Image analysis results of steel bar in MMA-treated HCP specimen 4 of Group 2 (LCLV). (a) Histogram of grayscale image of control bar. (b) Raw image of control bar. (c) Grayscale image of control bar. (d) Binary image of control bar (Exclude the black boundary).

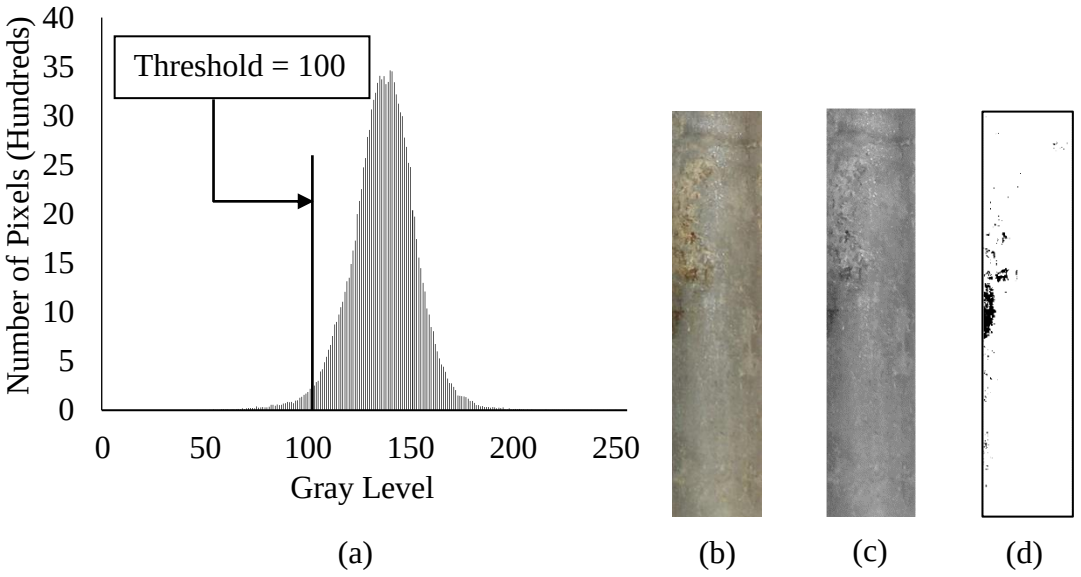

Figure D-27: Image analysis results of steel bar in MMA-treated HCP specimen 5 of Group 2 (LCLV). (a) Histogram of grayscale image of control bar. (b) Raw image of control bar. (c) Grayscale image of control bar. (d) Binary image of control bar (exclude the black boundary).

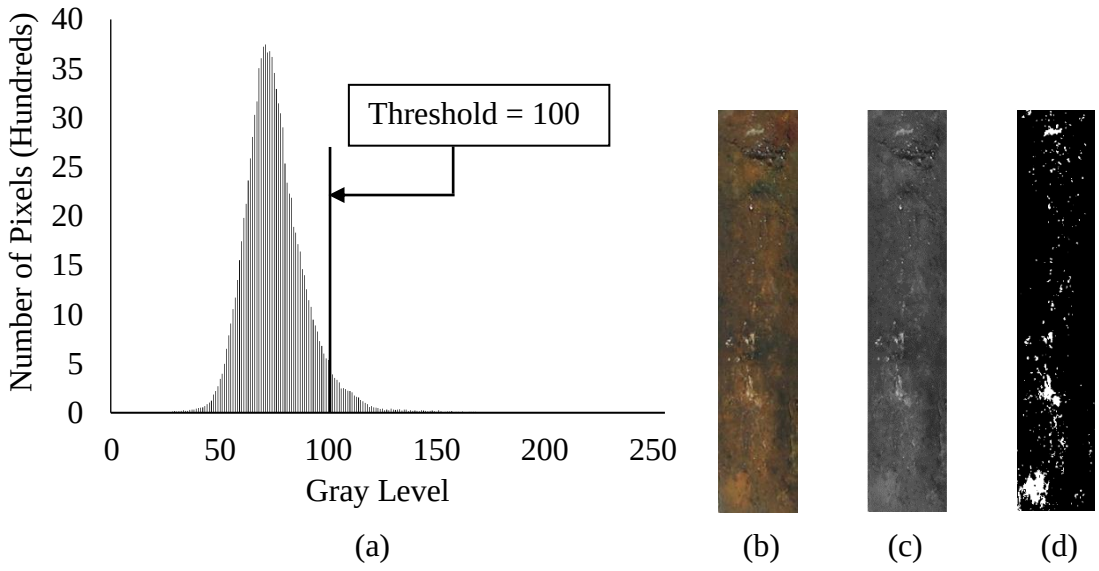

Figure D-29: Image analysis results of steel bar in MMA-treated HCP specimen 1 of Group 3 (LCHV). (a) Histogram of grayscale image of control bar. (b) Raw image of control bar. (c) Grayscale image of control bar. (d) Binary image of control bar.

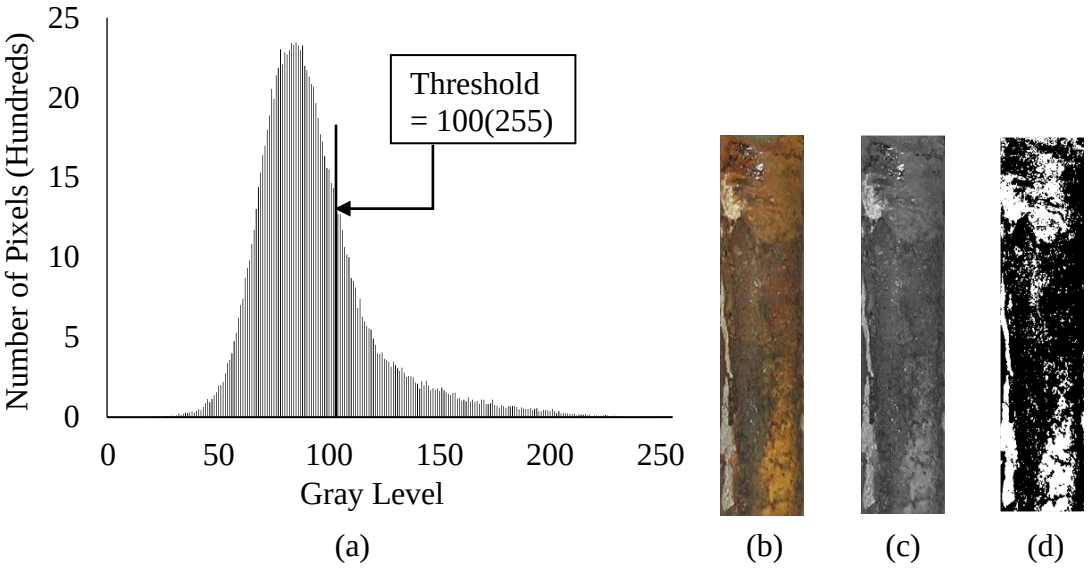

Figure D-31: Image analysis results of steel bar in MMA-treated HCP specimen 2 of Group 3 (LCHV). (a) Histogram of grayscale image of control bar. (b) Raw image of control bar. (c) Grayscale image of control bar. (d) Binary image of control bar.

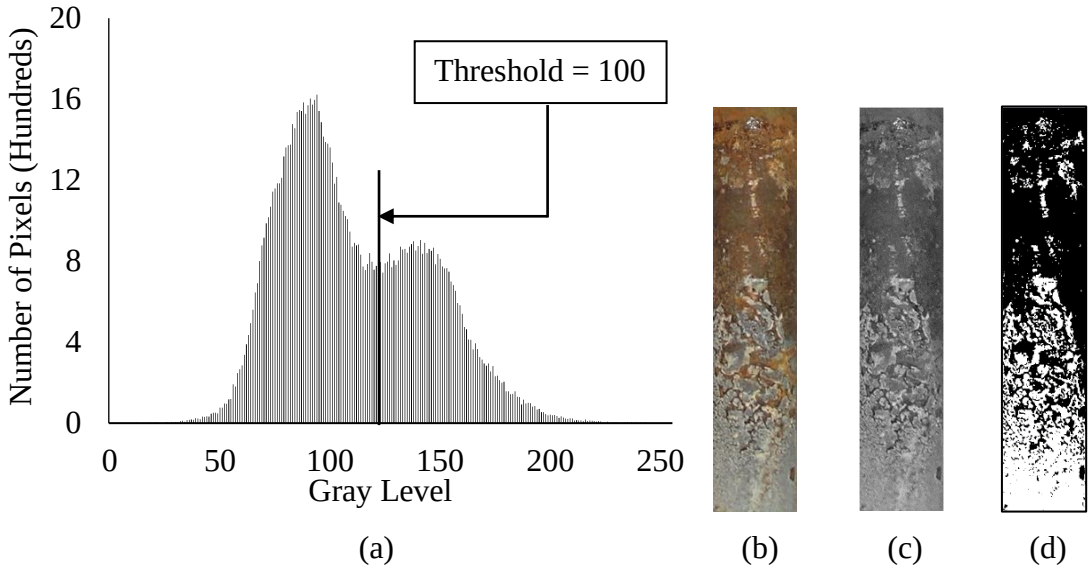

Figure D-33: Image analysis results of steel bar in MMA-treated HCP specimen 3 of Group 3 (LCHV). (a) Histogram of grayscale image of control bar. (b) Raw image of control bar. (c) Grayscale image of control bar. (d) Binary image of control bar (exclude the black boundary).

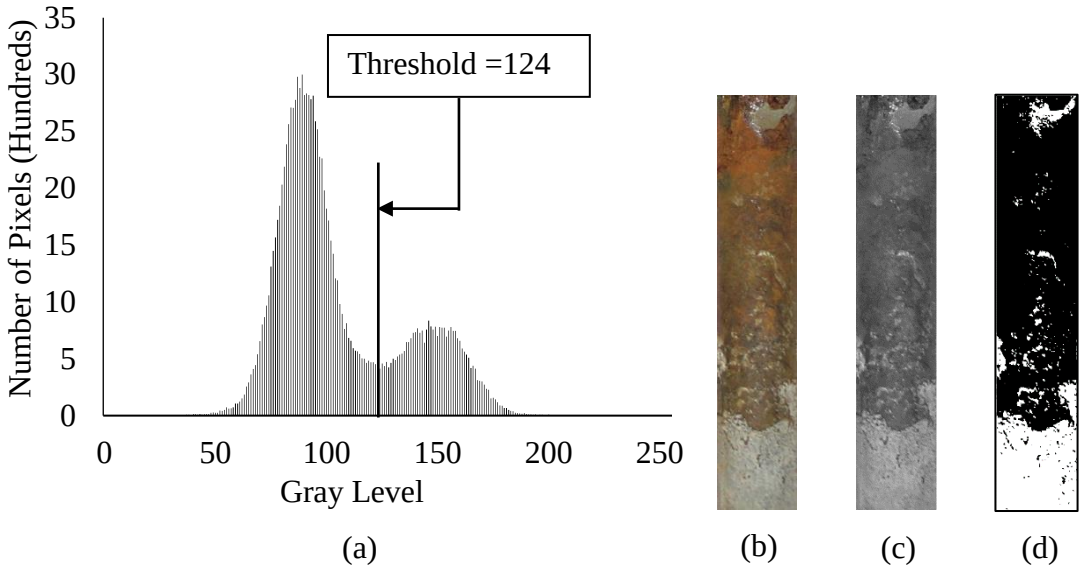

Figure D-35: Image analysis results of steel bar in MMA-treated HCP specimen 5 of Group 3 (LCHV). (a) Histogram of grayscale image of control bar. (b) Raw image of control bar. (c) Grayscale image of control bar. (d) Binary image of control bar (exclude the black boundary).

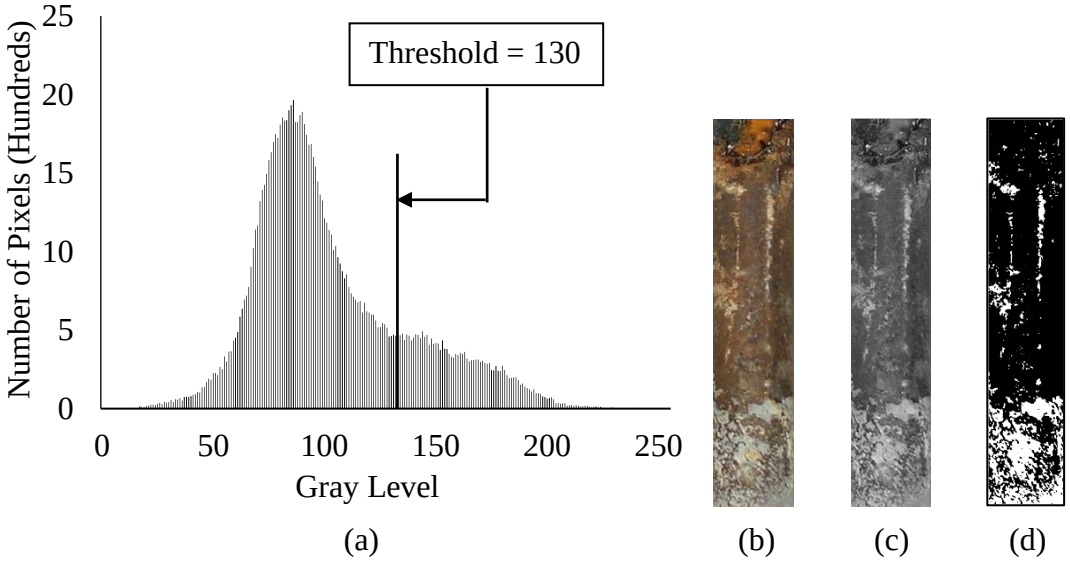

Figure D-37: Image analysis results of steel bar in MMA-treated HCP specimen 4 of Group 3 (LCHV). (a) Histogram of grayscale image of control bar. (b) Raw image of control bar. (c) Grayscale image of control bar. (d) Binary image of control bar (exclude the black boundary).

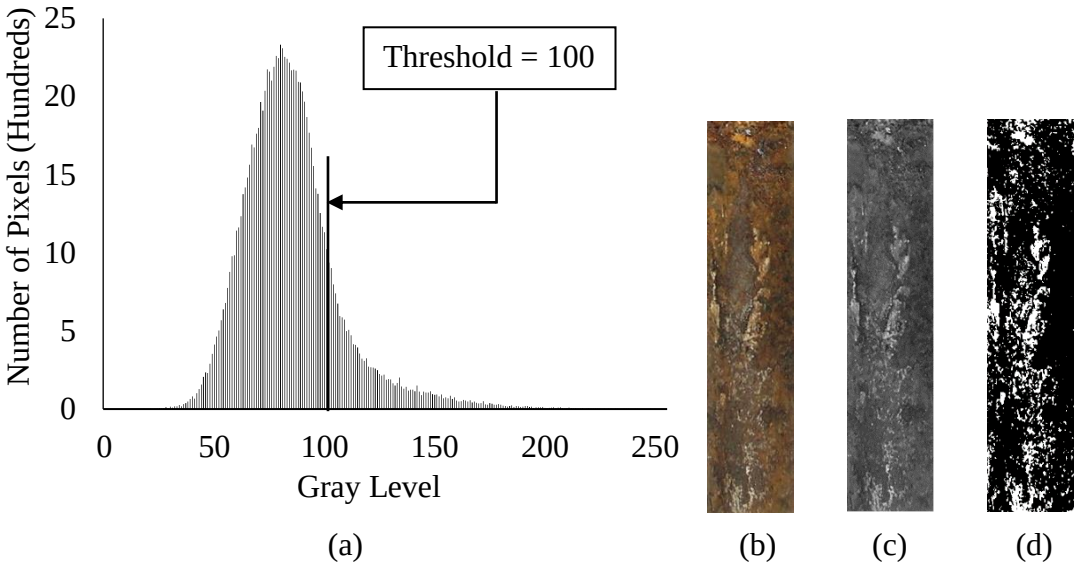

Figure D-39: Image analysis results of steel bar in MMA-treated HCP specimen 1 of Group 3 (LCHV). (a) Histogram of grayscale image of control bar. (b) Raw image of control bar. (c) Grayscale image of control bar. (d) Binary image of control bar.

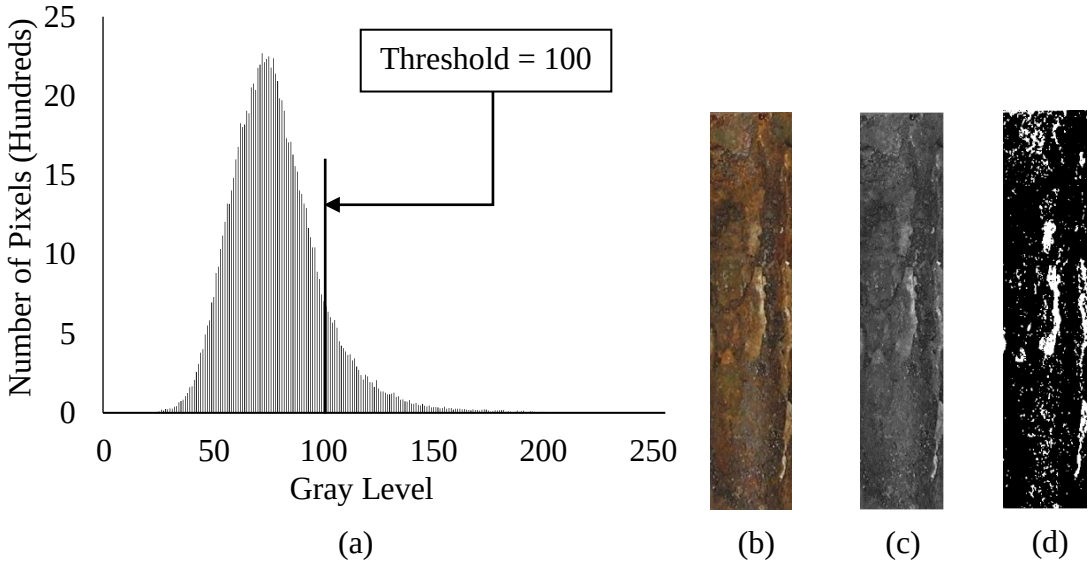

Figure D-41: Image analysis results of steel bar in MMA-treated HCP specimen 2 of Group 4 (HCHV). (a) Histogram of grayscale image of control bar. (b) Raw image of control bar. (c) Grayscale image of control bar. (d) Binary image of control bar.

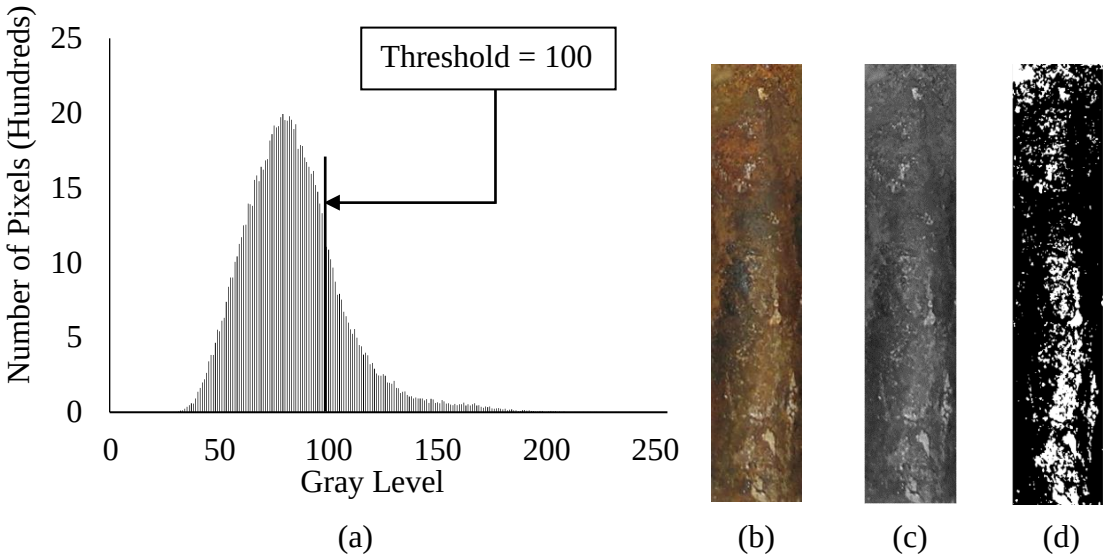

Figure D-43: Image analysis results of steel bar in MMA-treated HCP specimen 3 of Group 4 (HCHV). (a) Histogram of grayscale image of control bar. (b) Raw image of control bar. (c) Grayscale image of control bar. (d) Binary image of control bar.

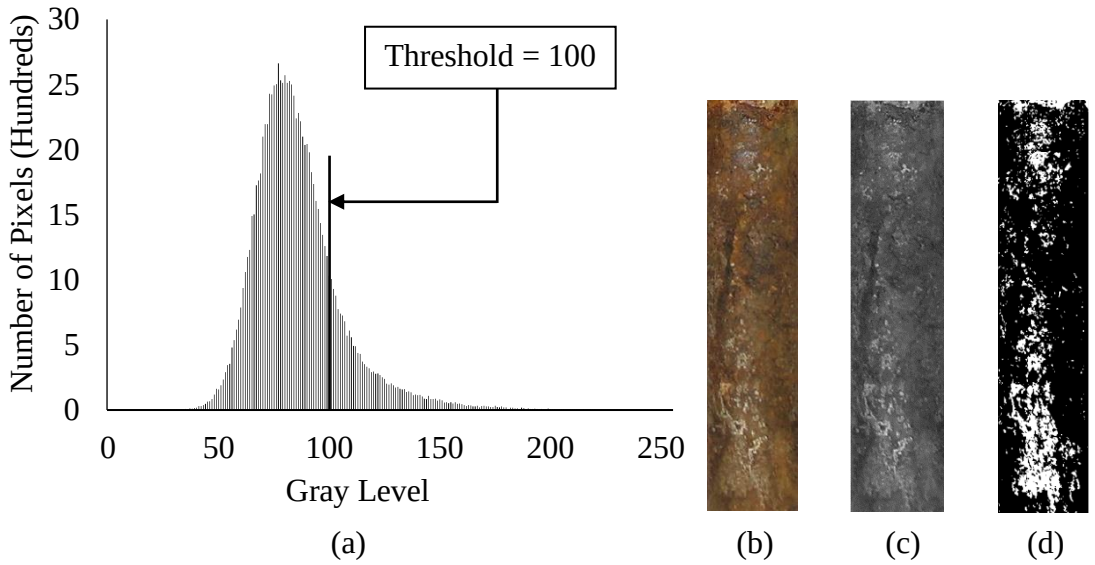

Figure D-45: Image analysis results of steel bar in MMA-treated HCP specimen 4 of Group 4 (HCHV). (a) Histogram of grayscale image of control bar. (b) Raw image of control bar. (c) Grayscale image of control bar. (d) Binary image of control bar.

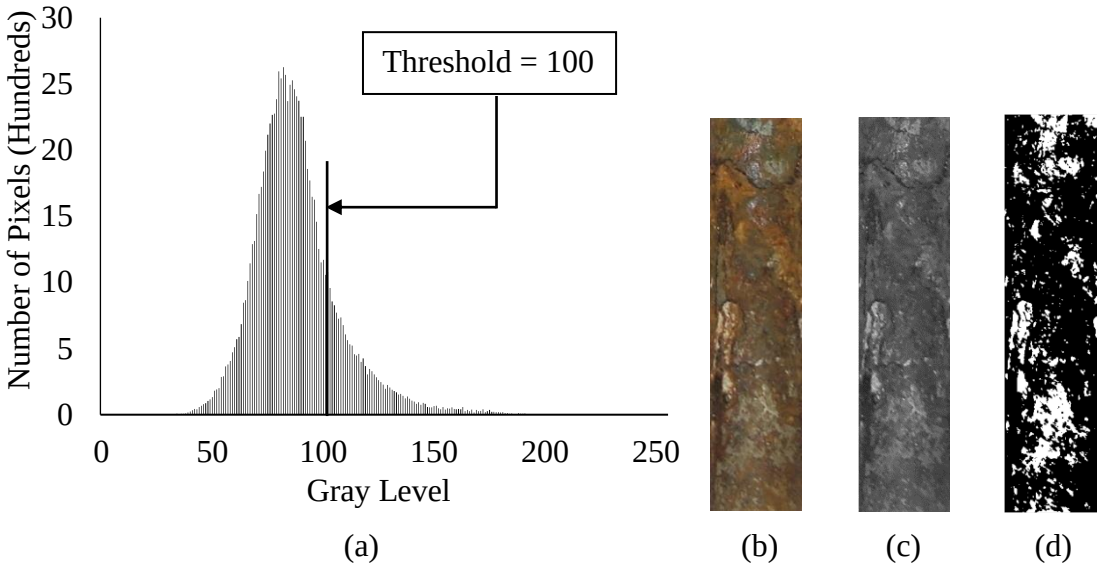

Figure D-47: Image analysis results of steel Bar in MMA-treated HCP specimen 5 of Group 4 (HCHV). (a) Histogram of grayscale image of control bar. (b) Raw image of control bar. (c) Grayscale image of control bar. (d) Binary image of control bar.

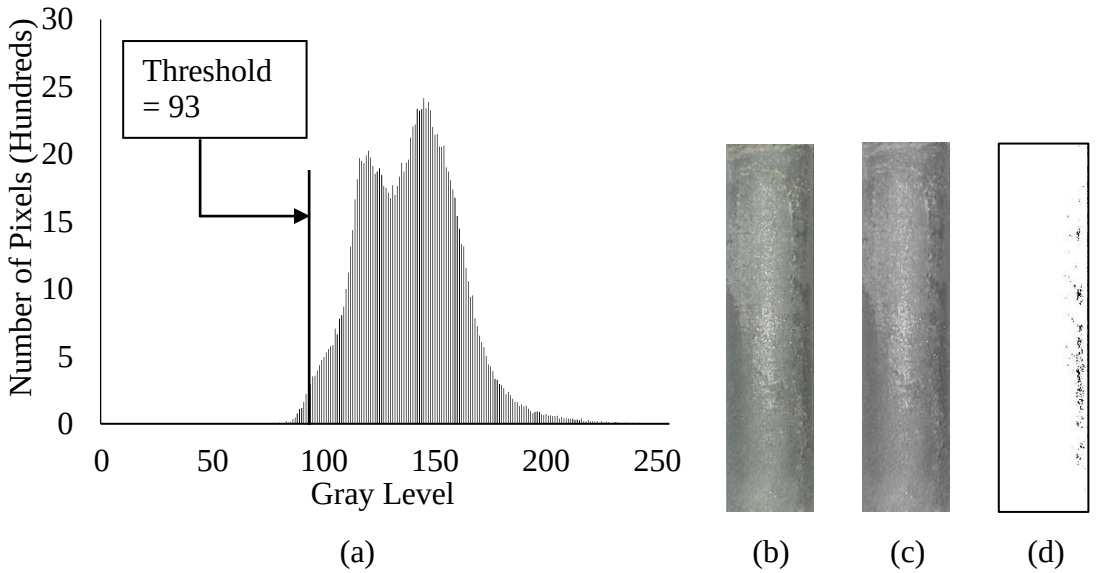

Figure D-49: Image analysis results of steel bar in control HCP specimen 1 of Group 5 (O-Control). (a) Histogram of grayscale image of control bar. (b) Raw image of control bar. (c) Grayscale image of control bar. (d) Binary image of control bar (exclude the black boundary).

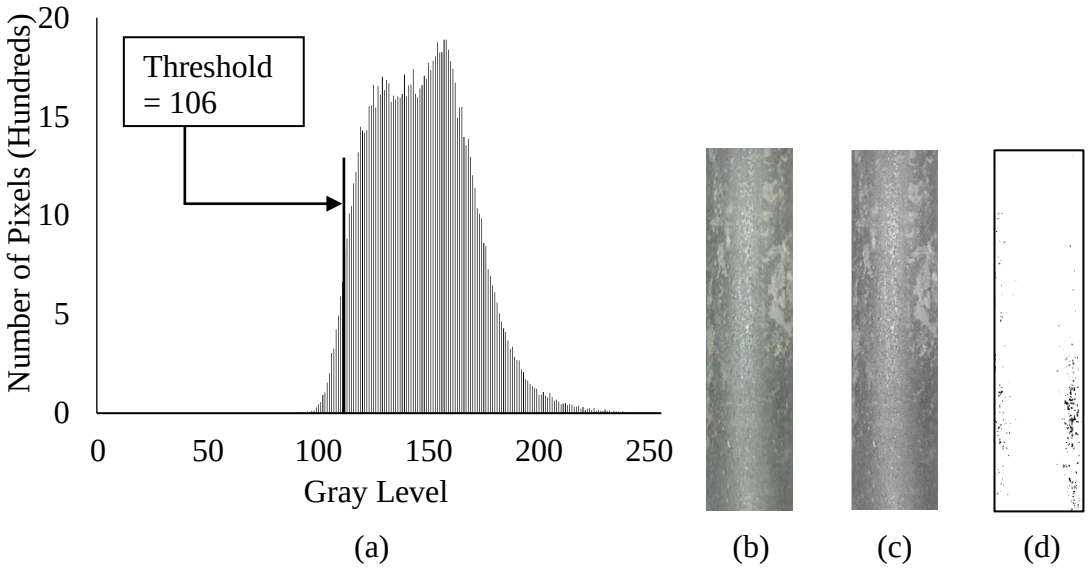

Figure D-51: Image analysis results of steel bar in control HCP specimen 2 of Group 5 (O-Control). (a) Histogram of grayscale image of control bar. (b) Raw image of control Bar. (c) Grayscale image of control bar. (d) Binary image of control bar (exclude the black boundary).

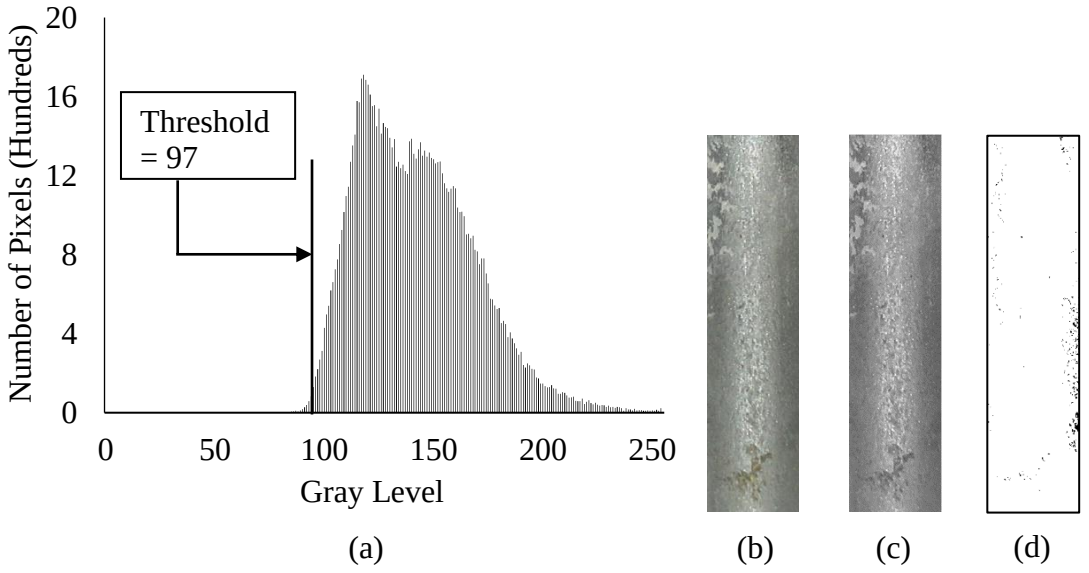

Figure D-53: Image analysis results of steel bar in control HCP specimen 3 of Group 5 (O-Control). (a) Histogram of grayscale image of control bar. (b) Raw image of control Bar. (c) Grayscale image of control bar. (d) Binary image of control bar (exclude the black boundary).

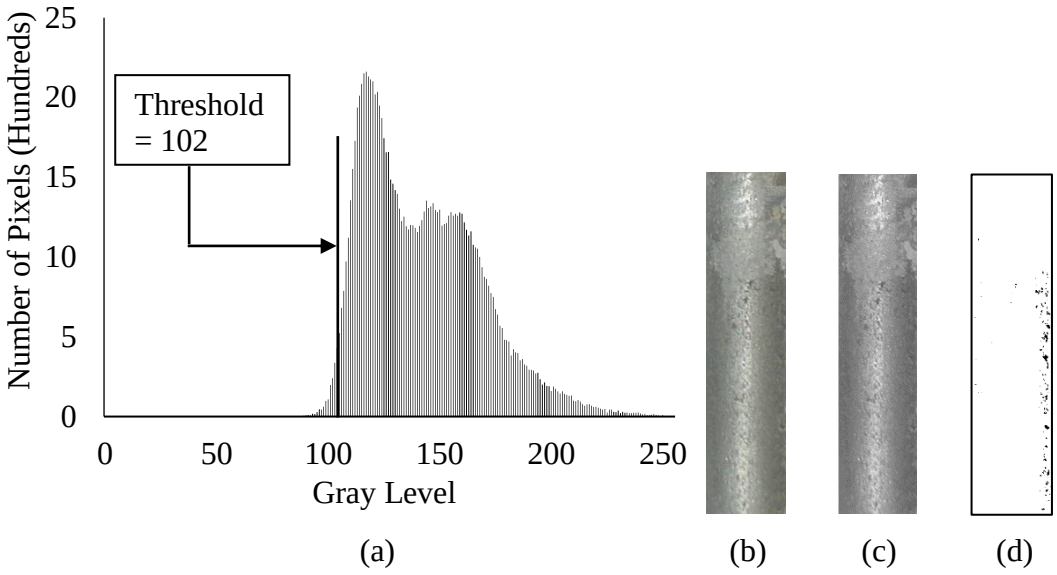

Figure D-55: Image analysis results of steel bar in control HCP specimen 4 of Group 5 (O-Control). (a) Histogram of grayscale image of control bar. (b) Raw image of control bar. (c) Grayscale image of control bar. (d) Binary image of control bar (exclude the black boundary).

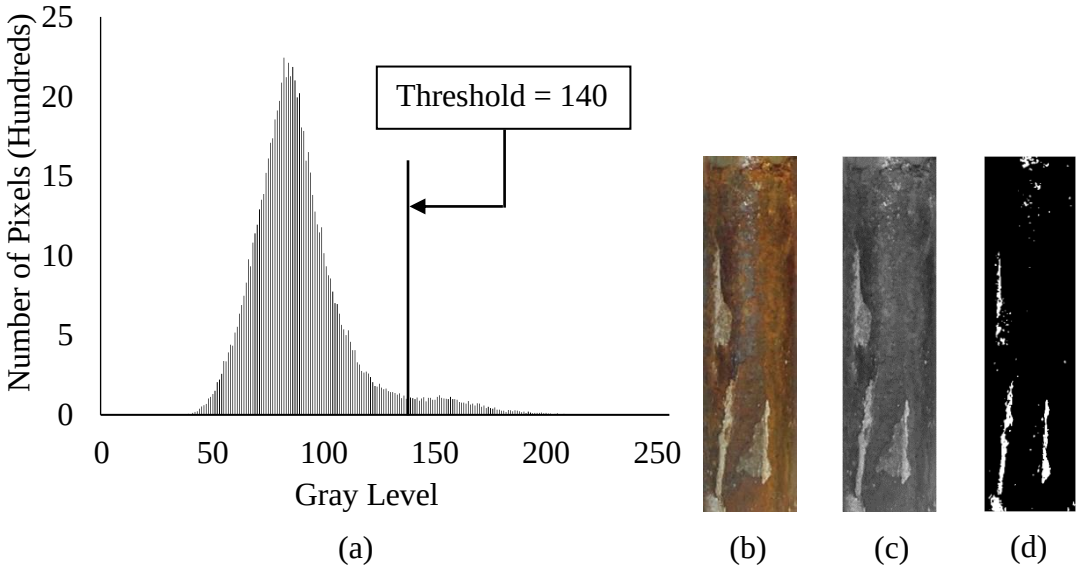

Figure D-57: Image analysis results of steel bar in MMA-treated HCP specimen 1 of Group 6 (Y-MMA). (a) Histogram of grayscale image of the steel bar. (b) Raw image of control bar. (c) Grayscale image of control bar. (d) Binary image of control bar.

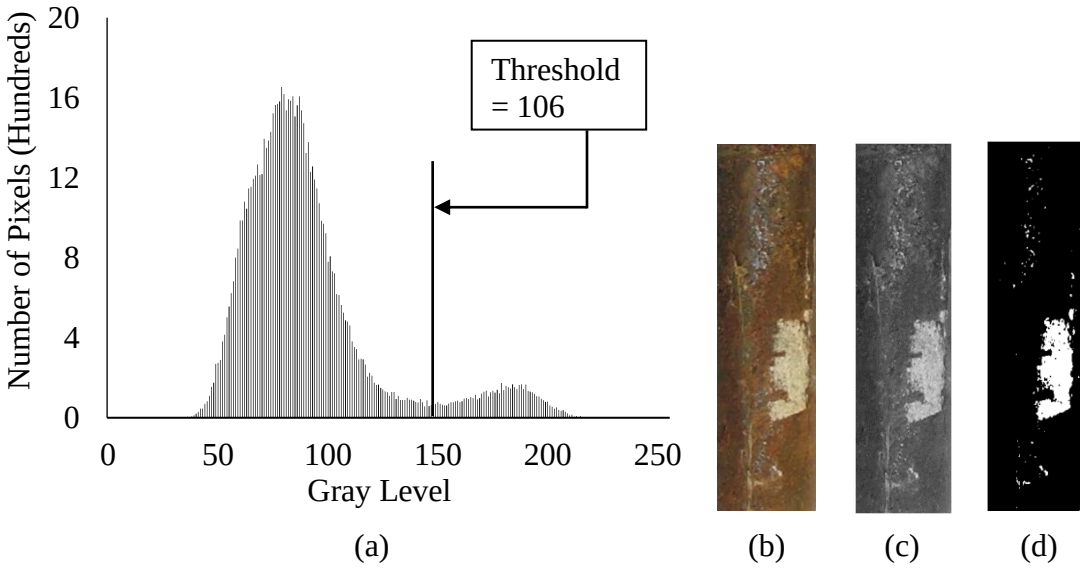

Figure D-59: Image analysis results of steel bar in MMA-treated HCP specimen 2 of Group 6 (Y-MMA). (a) Histogram of grayscale image of the steel bar. (b) Raw image of control bar. (c) Grayscale image of control bar. (d) Binary image of control bar.

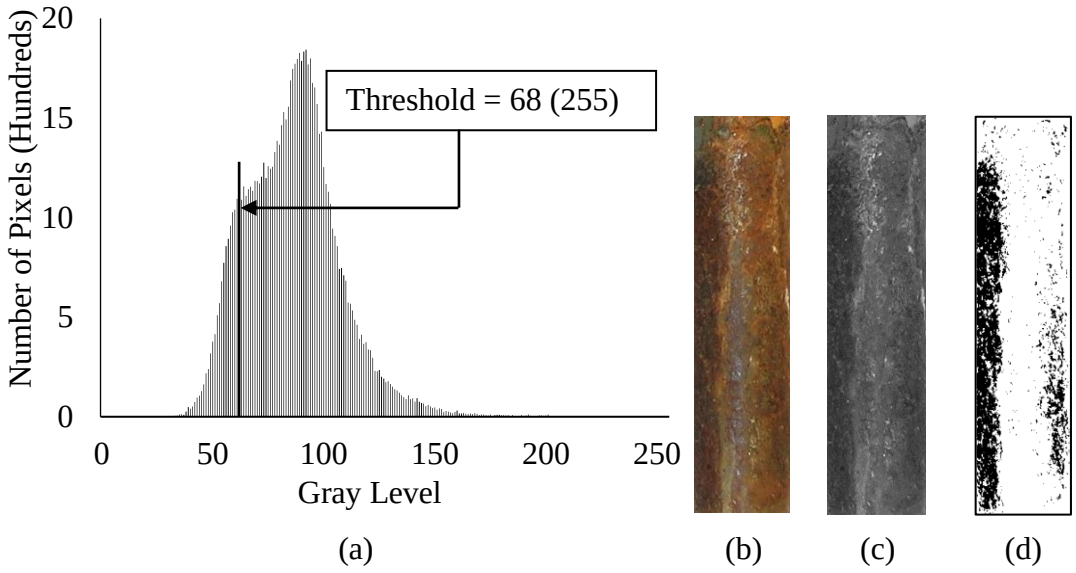

Figure D-61: Image analysis results of steel bar in MMA-treated HCP specimen 3 of Group (Y-MMA). (a) Histogram of grayscale image of the steel bar. (b) Raw image of control bar. (c) Grayscale image of control bar. (d) Binary image of control bar (exclude the black boundary).

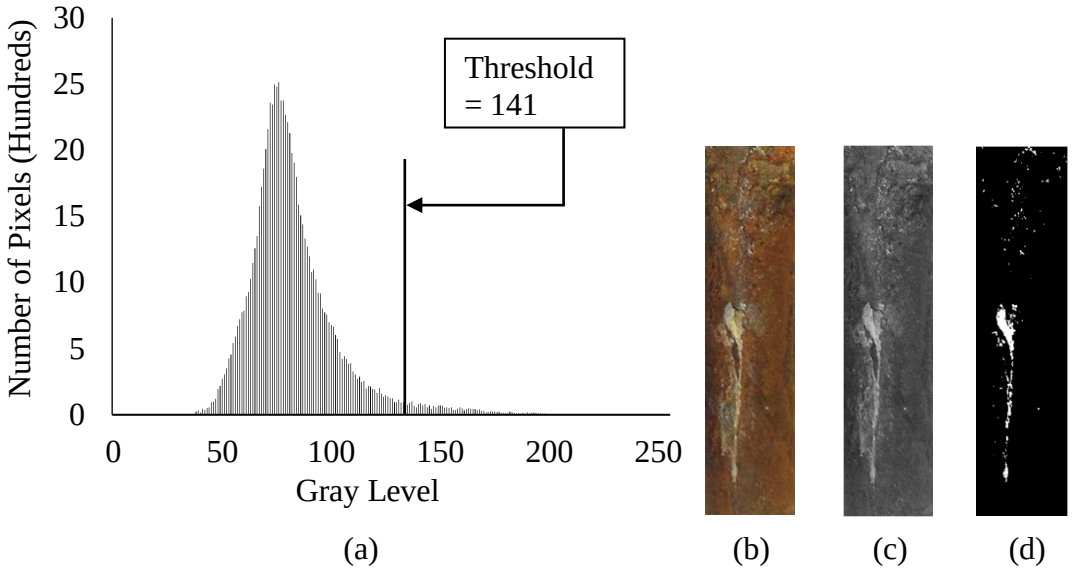

Figure D-63: Image analysis results of steel bar in MMA-treated HCP specimen 4 of Group 6 (Y-MMA). (a) Histogram of grayscale image of the steel bar. (b) Raw image of control bar. (c) Grayscale image of control bar. (d) Binary image of control bar

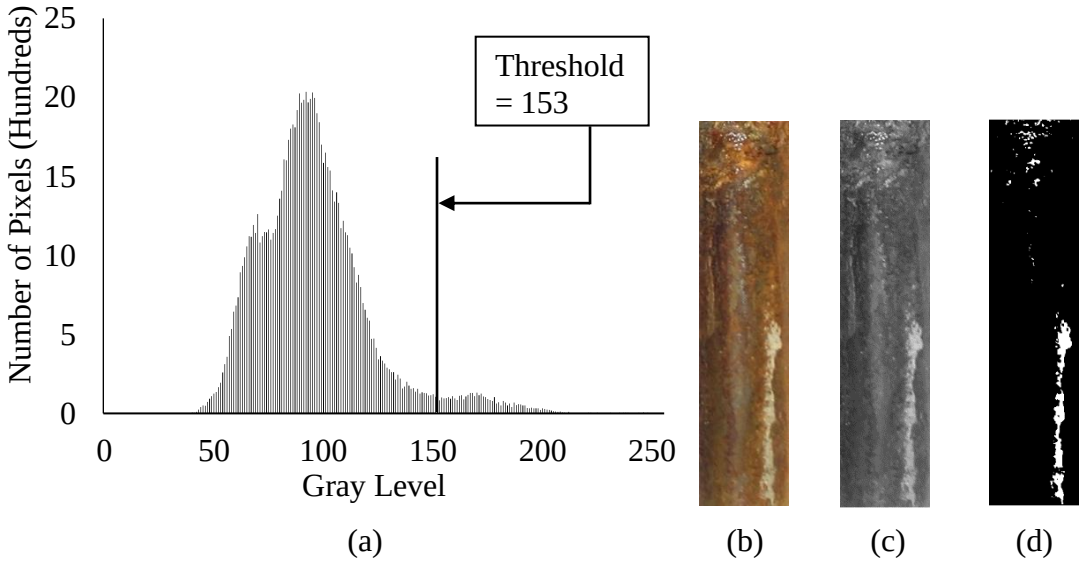

Figure D-65: Image analysis results of steel bar in MMA-treated HCP specimen 5 of Group 6 (Y-MMA). (a) Histogram of grayscale image of the steel bar. (b) Raw image of control bar. (c) Grayscale image of control bar. (d) Binary image of control bar.

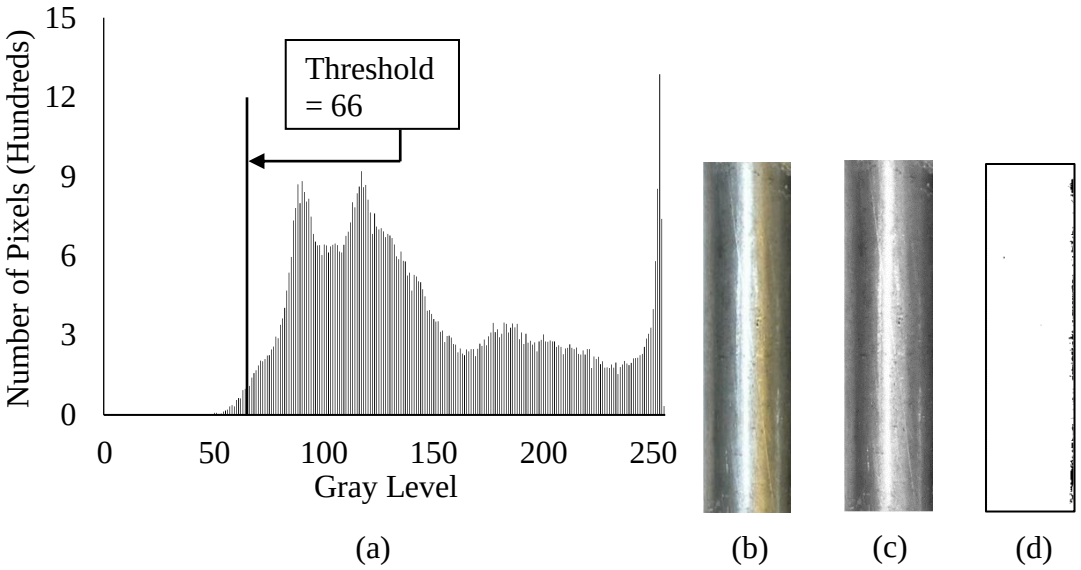

Figure D-67: Image analysis results of steel bar in MMA-treated HCP specimen 1 of Group 7 (Y-Control). (a) Histogram of grayscale image of the steel bar. (b) Raw image of control bar. (c) Grayscale image of control bar. (d) Binary image of control bar (exclude the black boundary).

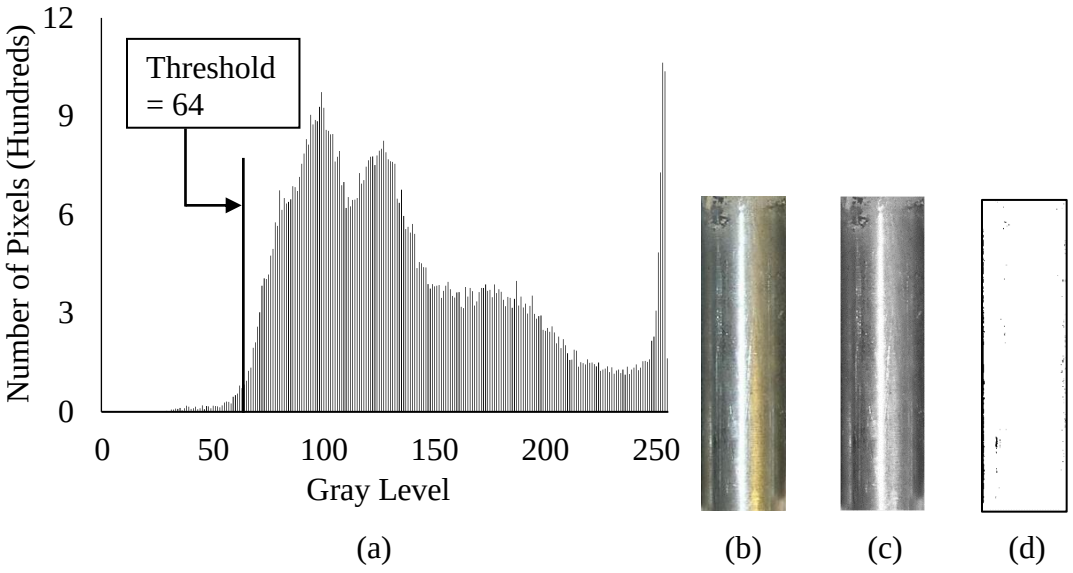

Figure D-69: Image analysis results of steel bar in MMA-treated HCP specimen 2 of Group 7 (Y-Control). (a) Histogram of grayscale image of the steel bar. (b) Raw image of control bar. (c) Grayscale image of control bar. (d) Binary image of control bar (exclude the black boundary).

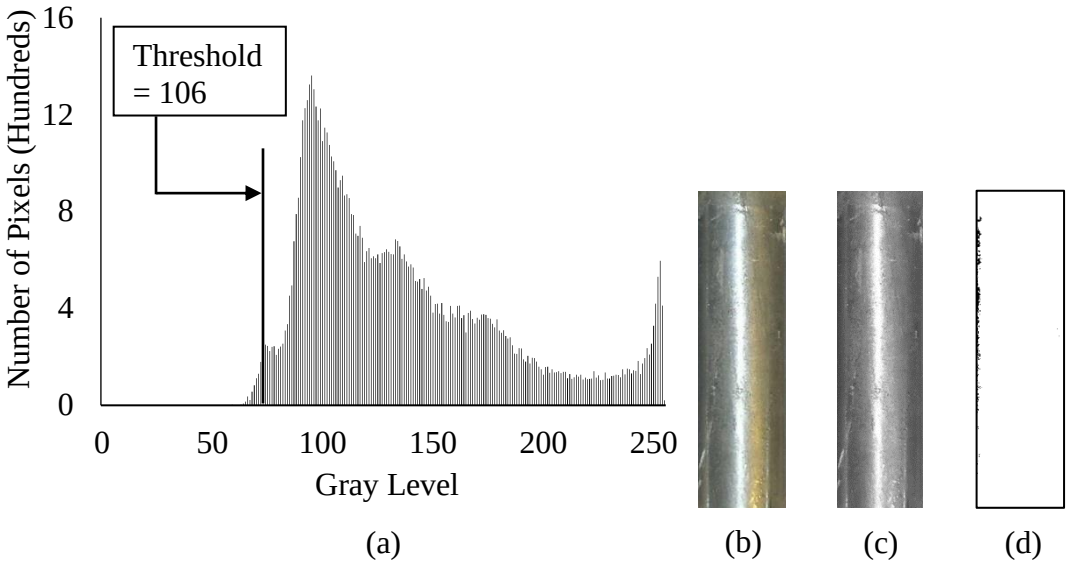

Figure D-71: Image analysis results of steel bar in MMA-treated HCP specimen 3 of Group 7 (Y-Control). (a) Histogram of grayscale image of the steel bar. (b) Raw image of control bar. (c) Grayscale image of control bar. (d) Binary image of control bar (exclude the black boundary).

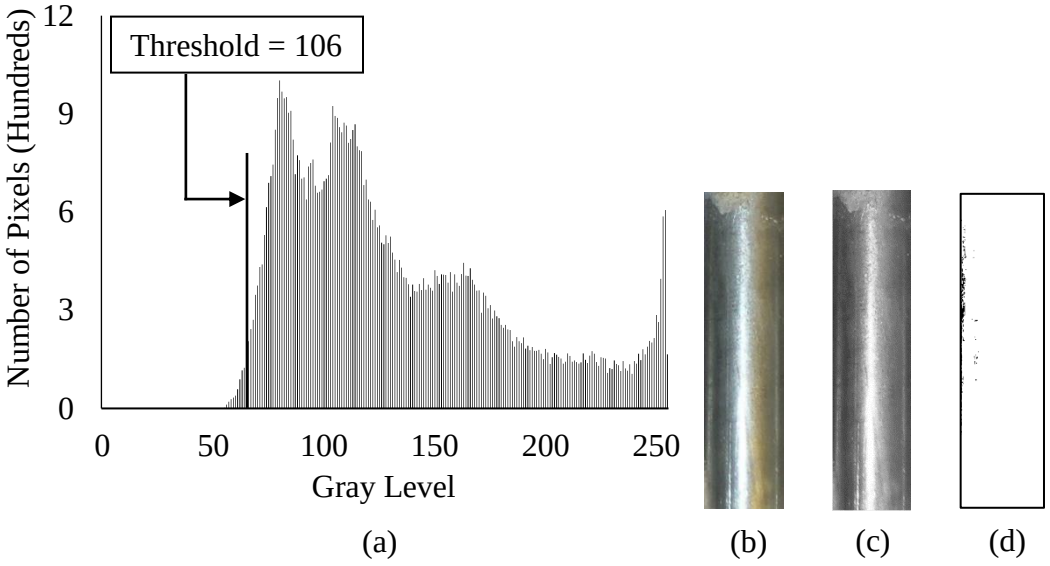

Figure D-73: Image analysis results of steel bar in MMA-treated HCP specimen 4 of Group 7 (Y-Control). (a) Histogram of grayscale image of the steel bar. (b) Raw image of control bar. (c) Grayscale image of control bar. (d) Binary image of control bar (exclude the black boundary).

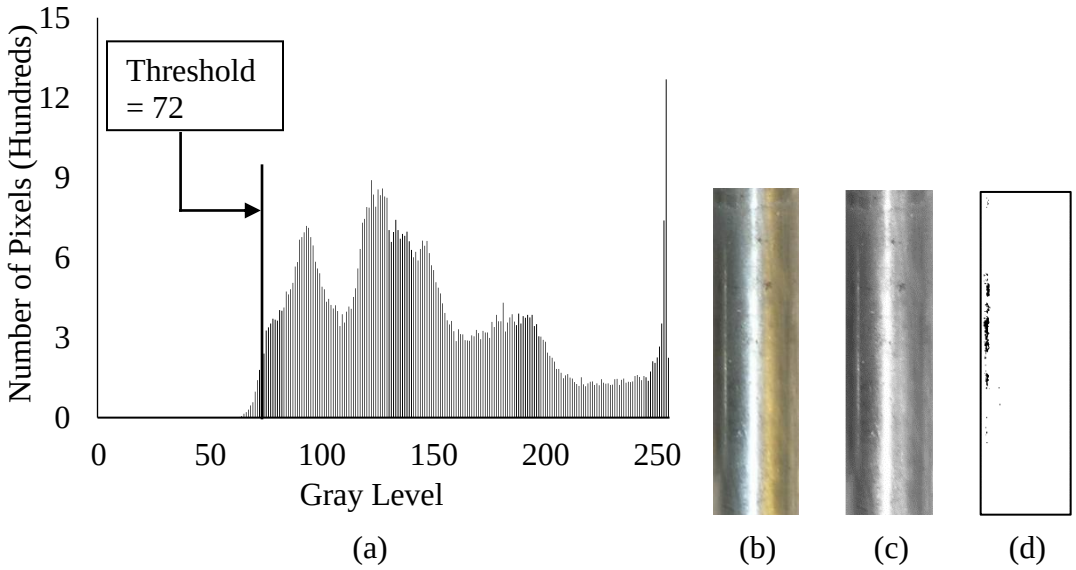

Figure D-75: Image analysis results of steel bar in MMA-treated HCP specimen 5 of Group 7 (Y-Control). (a) Histogram of grayscale image of the steel bar. (b) Raw image of control bar. (c) Grayscale image of control bar. (d) Binary image of control bar (exclude the black boundary).

Table D-1: Corroded area analysis results of steel bars in MMA-treated HCP specimens after MMA treatments. (Unit: %)

Group No.	Sample 1	Sample 2	Sample 3	Sample 4	Sample 5	Average	STDEV*	Error Bar
1	17	2	10	8	15	10	0.062	0.045
2	10	9	9	6	2	7	0.034	0.025
3	95	99	63	79	74	82	0.148	0.109
4	82	88	81	82	80	83	0.029	0.021
5	1	1	1	1		1	-	-
6	96	92	99	98	96	95	0.023	0.017
7	1	1	1	1%	1	1	-	-

* STDEV is the standard deviation.
Underlined values were regarded as the completely corroded steel bars.

Table D-2: Porosities of MMA-treated and control HCP specimens after MMA treatments. (Unit: %)

	3-month Batch					1-week Batch	
Sample No.	Group 1	Group 2	Group 3	Group 4	Group 5	Group 6	Group 7
1	24.4	24	24.2	20.6	21.2	25.4	23.4
2	27	24.6	22.1	23.3	25	23.8	23.4
3	24.7	20.2	25.1	25	22.9	24	21.6
4	25.7	25.6	23.4	25.2	20.7	25.7	23.4
5	24.2	21.2	22	21.1	0	22.7	22.6
Average	25.2	23.1	23.4	23.0	22.5	24.3	22.9
STDEV*	1.16	2.31	1.34	2.14	10.18	1.23	0.79
Error Bar	0.85	1.70	0.99	1.57	8.37	0.91	0.58

* STDEV is the standard deviation.

APPENDIX E

POTENTIODYNAMIC POLARIZATION TEST AND

UNCERTAINTY ANALYSIS

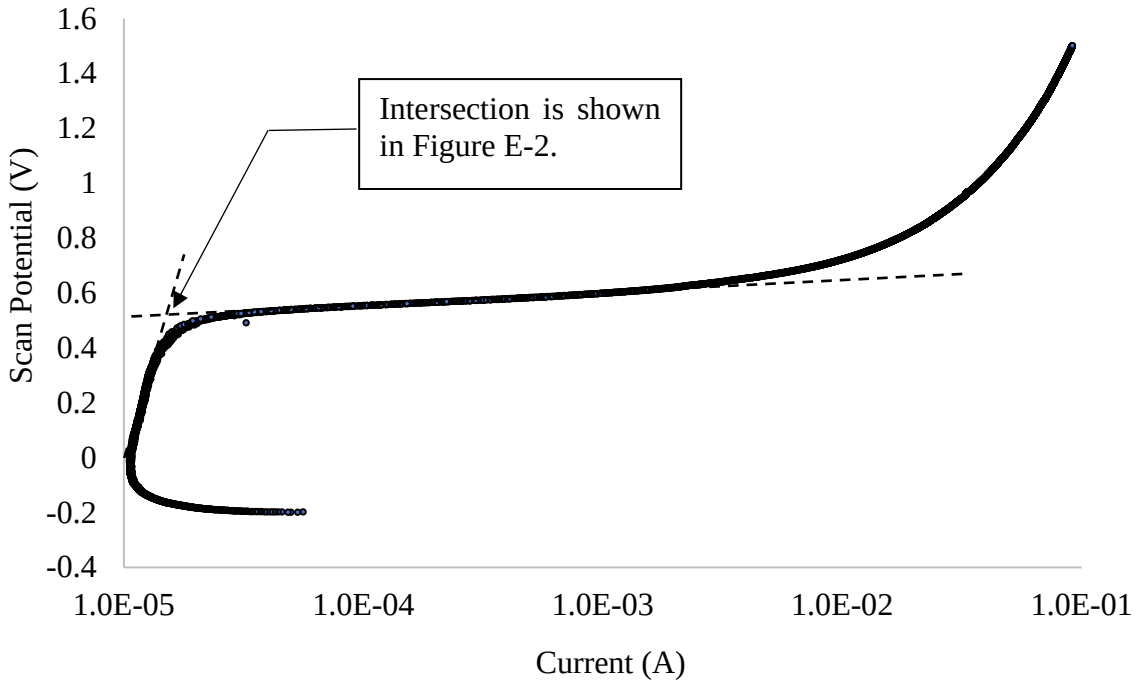

Figure E-1: Potentiodynamic polarization current of 1018 steel bar was scanned in simulated pore fluid. Scanning potential ranged from -0.2 V to +1.5 V. Absolute current was monitored during scanning. The 0.1 A current corresponds to a current density of 64.4 A/m^2. (Trial 1)

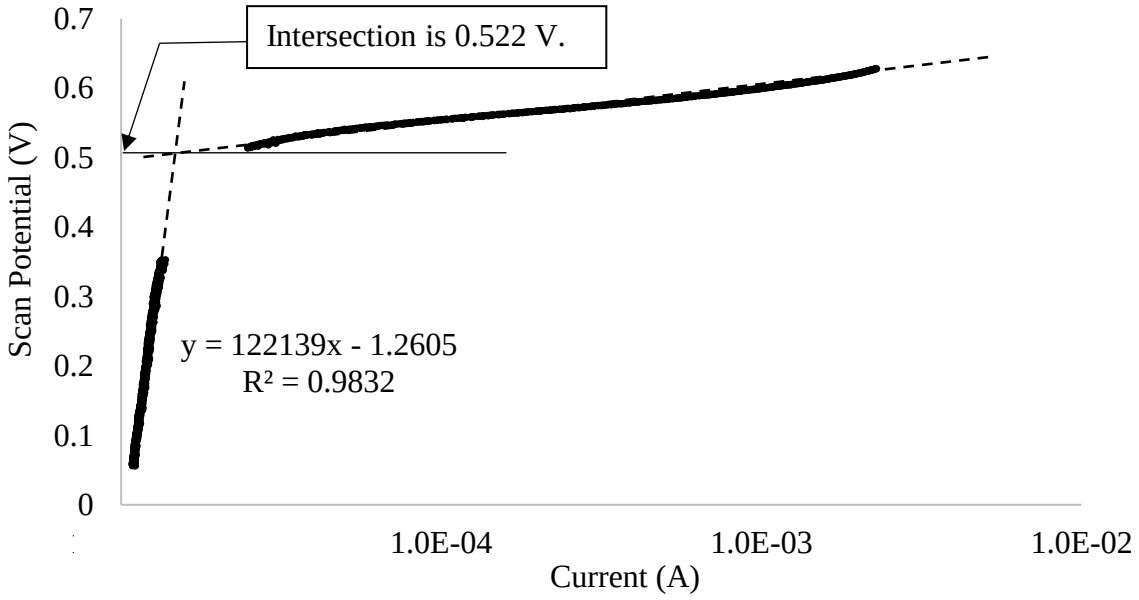

Figure E-2: Two sections of curve were selected from Figure E-1 to calculate the critical point at which the current began increasing significantly in the transpassive region. The intersection of these two dash lines is the critical point. (Trial 1)

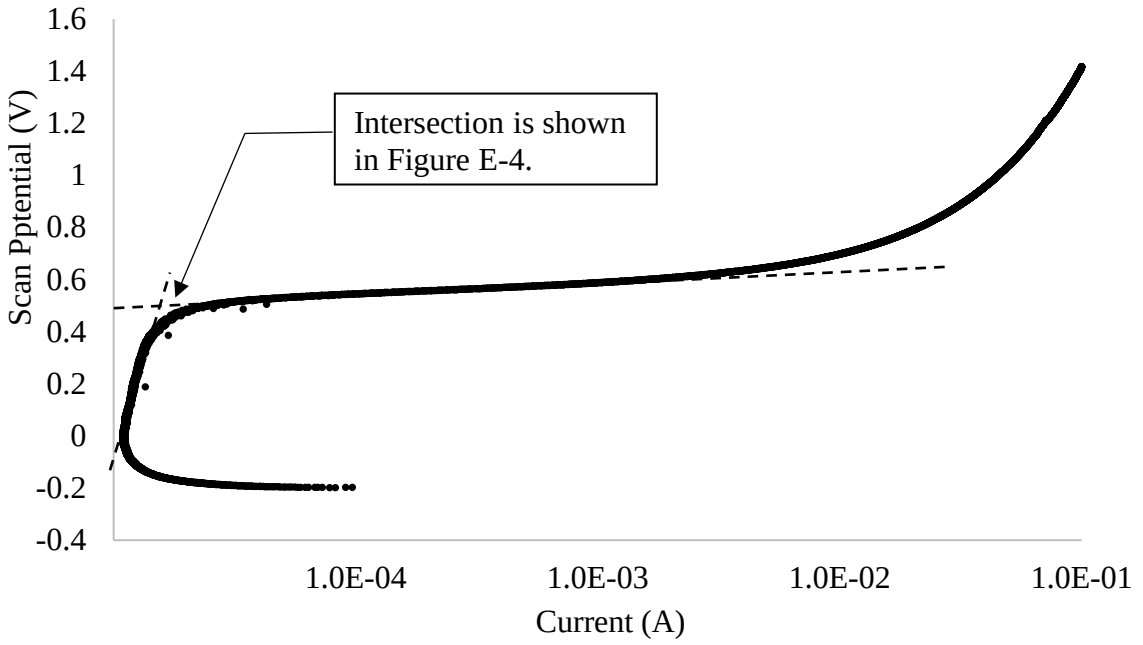

Figure E-3: Potentiodynamic polarization current of 1018 steel bar was scanned in simulated pore fluid. Scanning potential ranged from -0.2 V to +1.5 V. Absolute current was monitored during scanning. The 0.1 A current corresponds to a current density of 64.4 A/m^2. (Trial 2)

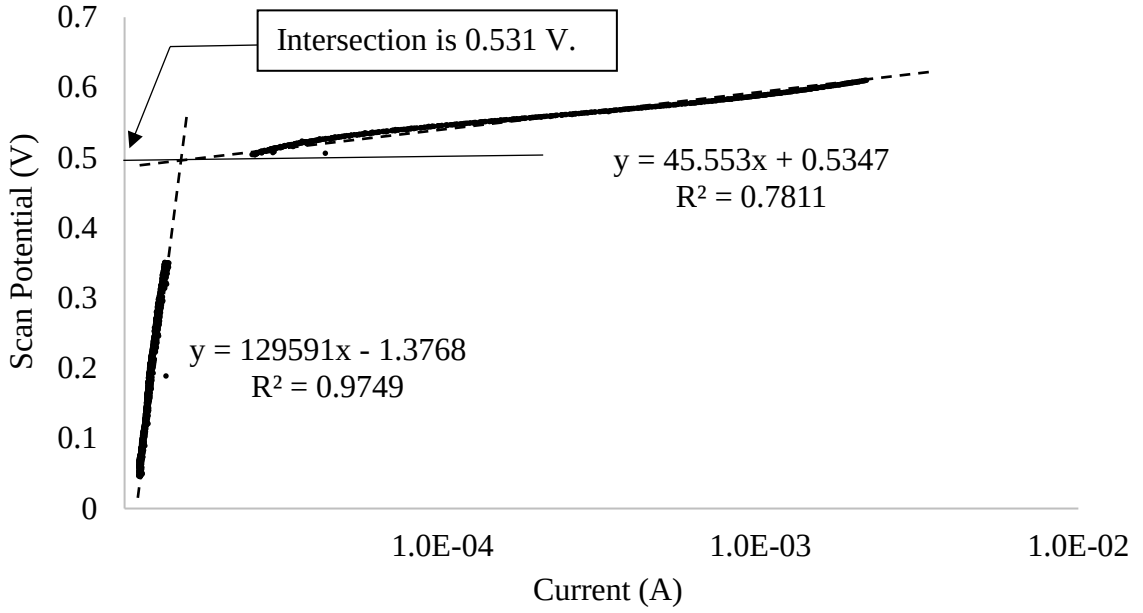

Figure E-4: Two sections of curve were selected from Figure E-3 to calculate the critical point at which the current began increasing significantly in the transpassive region. The intersection of these two dash lines is the critical point. (Trial 2)

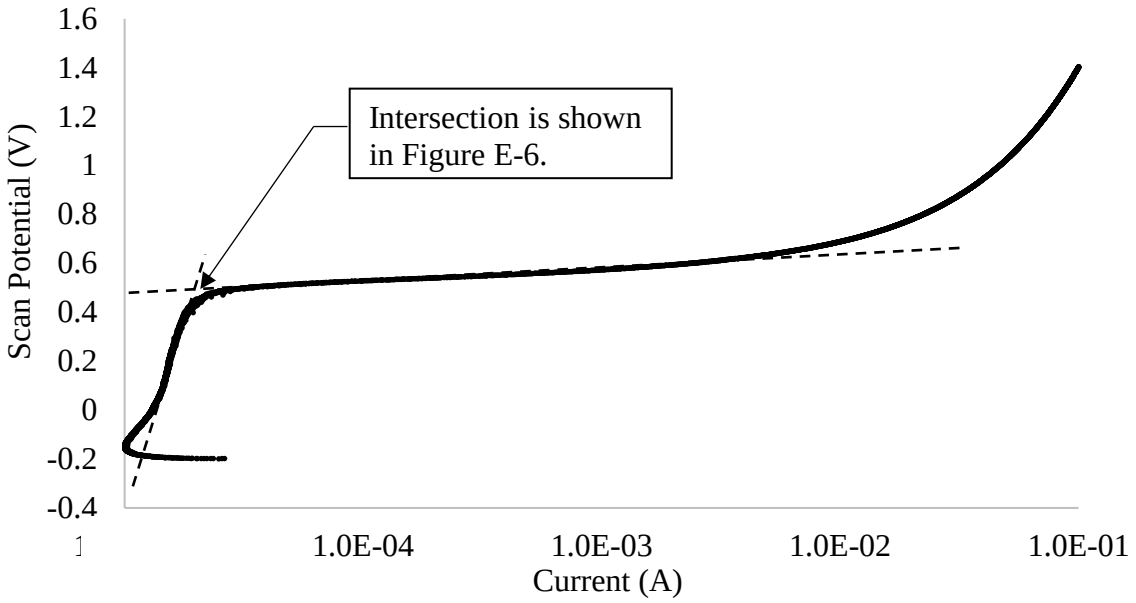

Figure E-5: Potentiodynamic polarization current of 1018 steel bar was scanned in simulated pore fluid. Scanning potential ranged from -0.2 V to +1.5 V. Absolute current was monitored during scanning. The 0.1 A current corresponds to a current density of 64.4 A/m^2. (Trial 3)

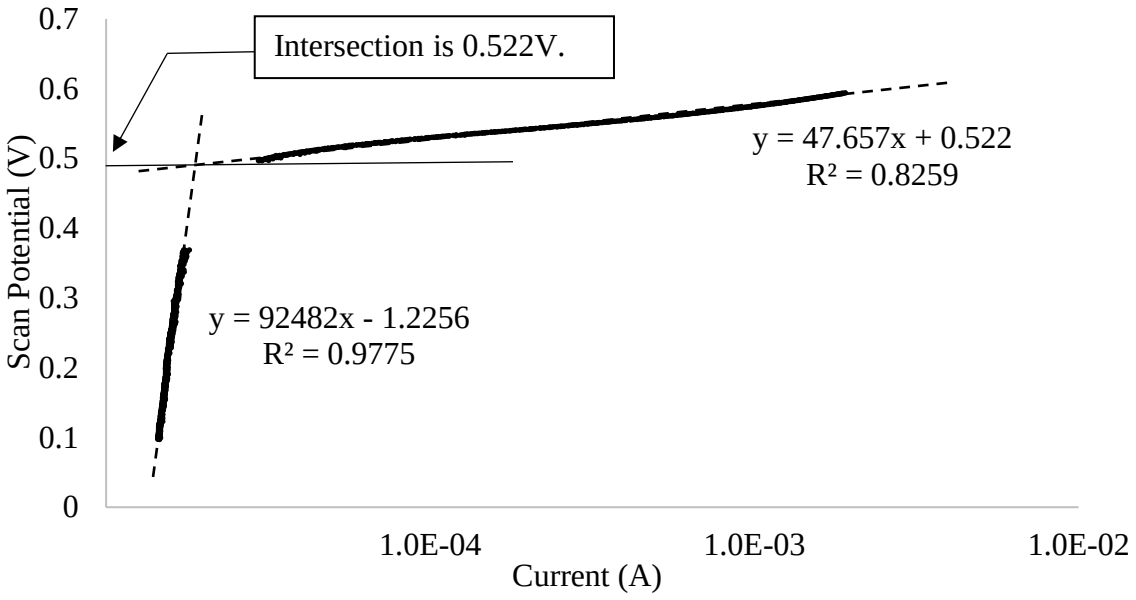

Figure E-6: Two sections of curve were selected from Figure E-5 to calculate the critical point at which the current began increasing significantly in the transpassive region. The intersection of these two dash lines is the critical point. (Trial 3)

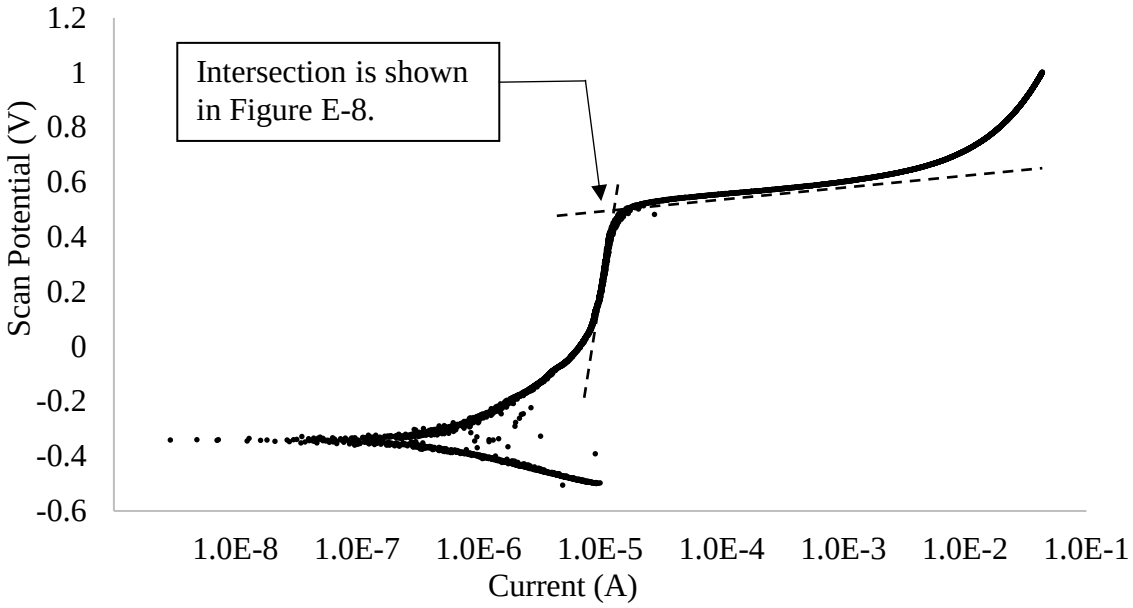

Figure E-7: Potentiodynamic polarization current of 1018 steel bar was scanned in simulated pore fluid. Scanning potential ranged from -0.2 V to +1.0 V. Absolute current was monitored during scanning. The 0.1 A current corresponds to a current density of 64.4 A/m^2. (Trial 4)

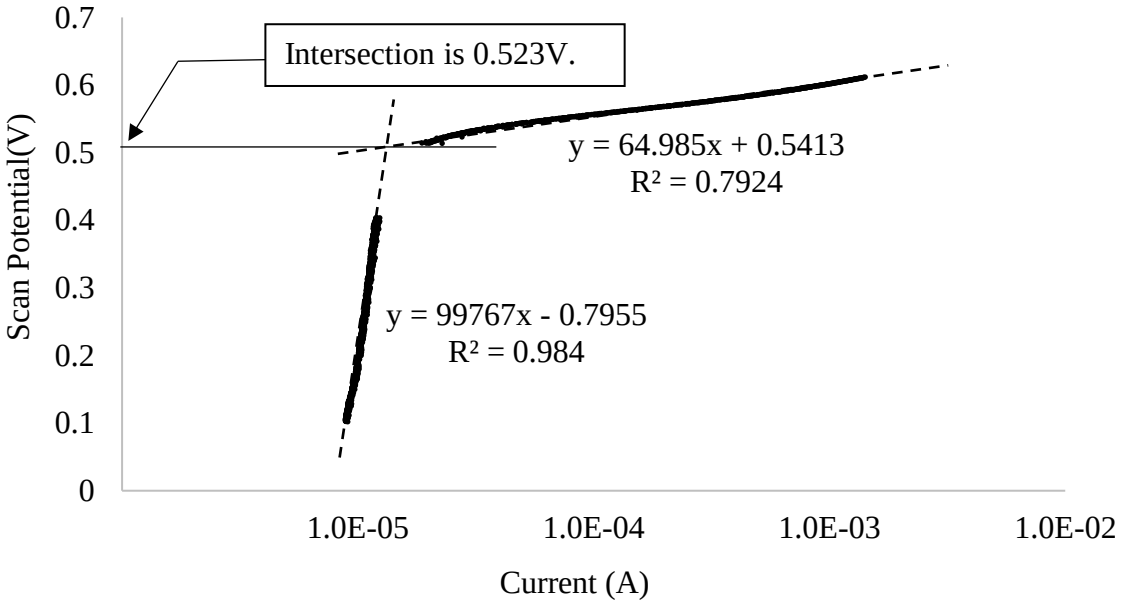

Figure E-8: Two sections of curve were selected from Figure E-7 to calculate the critical point at which the current began increasing significantly in the transpassive region. The intersection of these two dash lines is the critical point. (Trial 4)

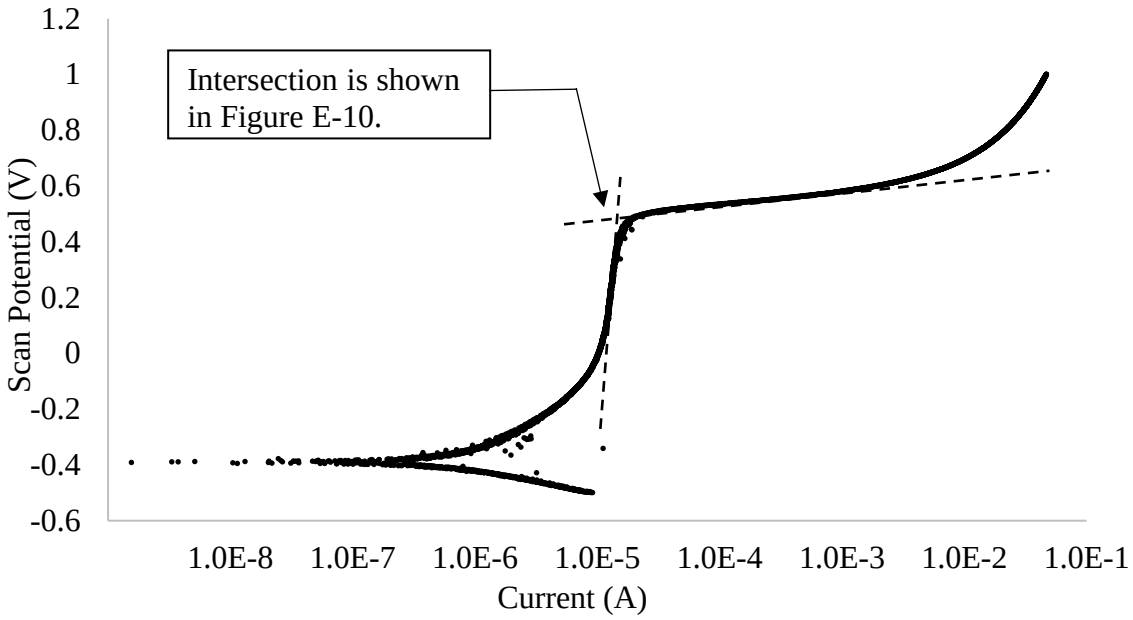

Figure E-9: Potentiodynamic polarization current of 1018 steel bar was scanned in simulated pore fluid. Scanning potential ranged from -0.2 V to +1.0 V. Absolute current was monitored during scanning. The 0.1 A current corresponds to a current density of 64.4 A/m^2. (Trial 5)

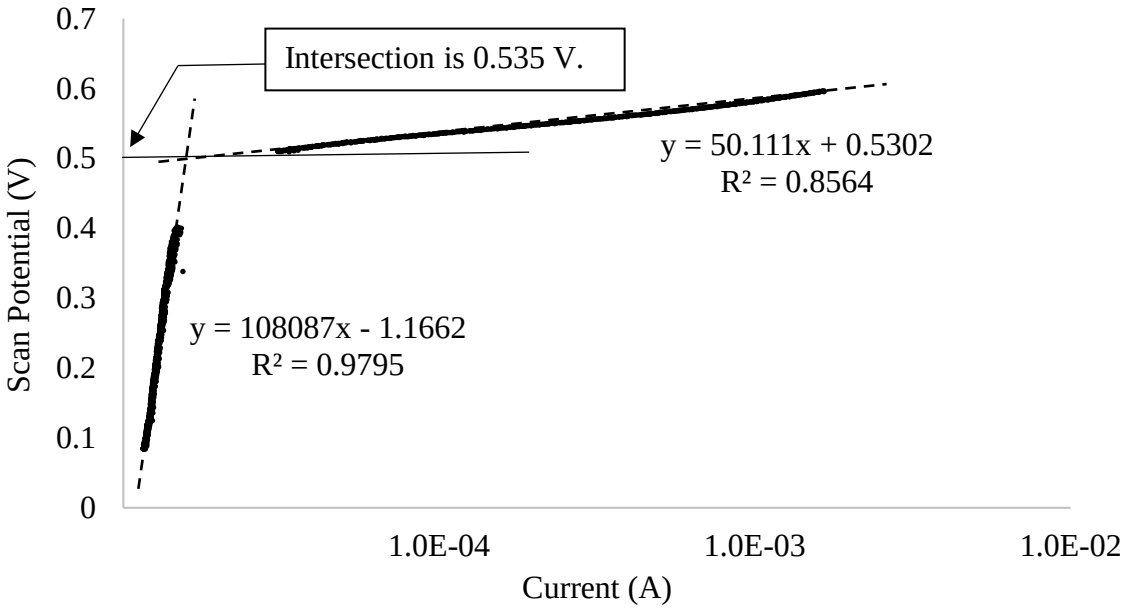

Figure E-10: Two sections of curve were selected from Figure E-9 to calculate the critical point at which the current began increasing significantly in the transpassive region. The intersection of these two dash lines is the critical point. (Trial 5)

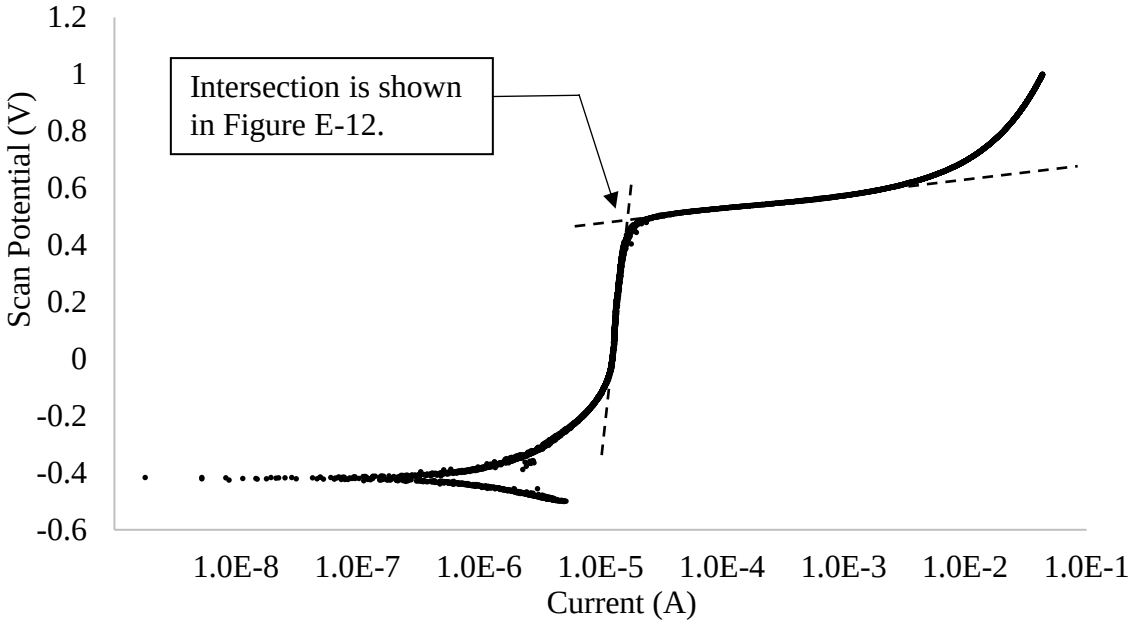

Figure E-11: Potentiodynamic polarization current of 1018 steel bar was scanned in simulated pore fluid. Scanning potential ranged from -0.2 V to +1.0 V. Absolute current was monitored during scanning. The 0.1 A current corresponds to a current density of 64.4 A/m^2. (Trial 6)

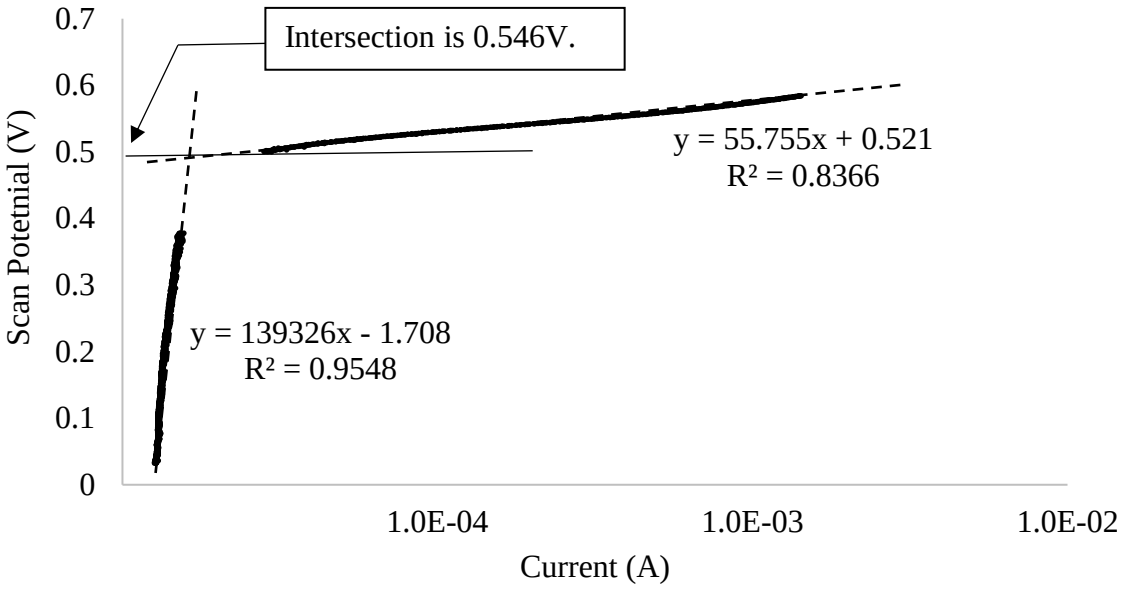

Figure E-12: Two sections of curve were selected from Figure E-11 to calculate the critical point at which the current began increasing significantly in the transpassive region. The intersection of these two dash lines is the critical point. (Trial 6)

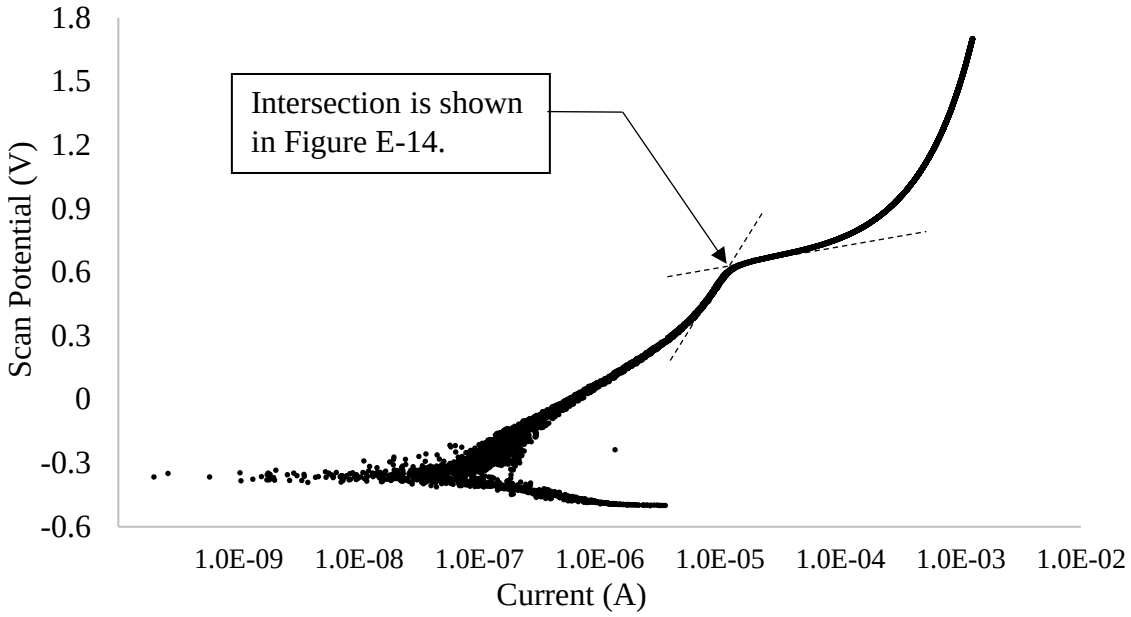

Figure E-13: Potentiodynamic polarization current of 1018 steel embedded within HCP specimen was scanned in lime water. Scanning potential ranged from -0.5V to +1.7V. Absolute current was monitored during scanning. The 0.01A current corresponds to a current density of 0.705 A/m^2 (HCP specimen surface).

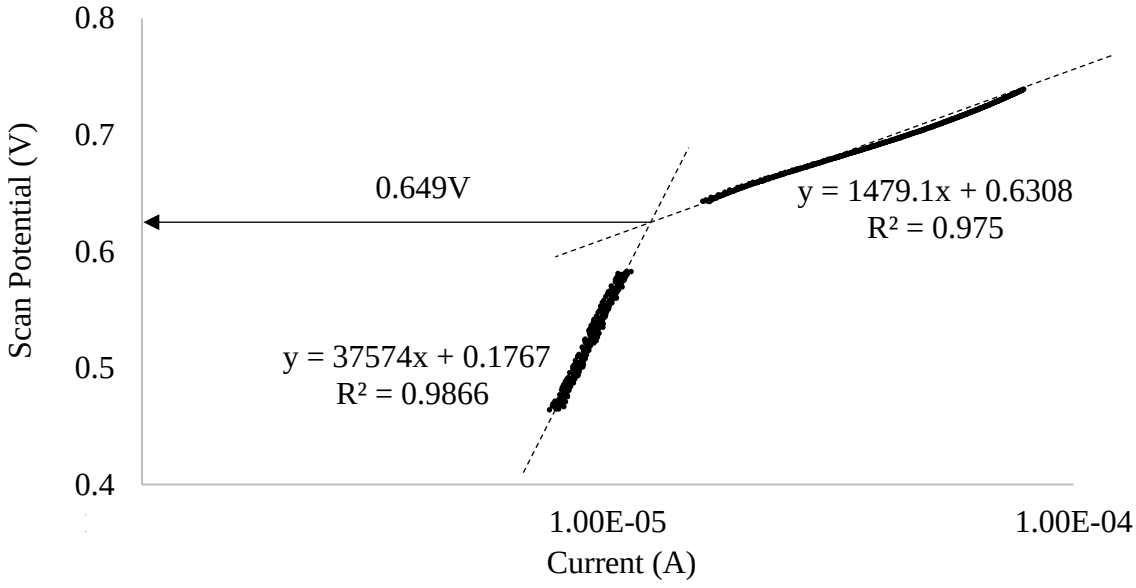

Figure E-14: Two sections of curve were selected from Figure E-13 to calculate the critical point at which the current began increasing significantly in the transpassive region. The intersection of these two dash lines is the critical point. (Trial 7)

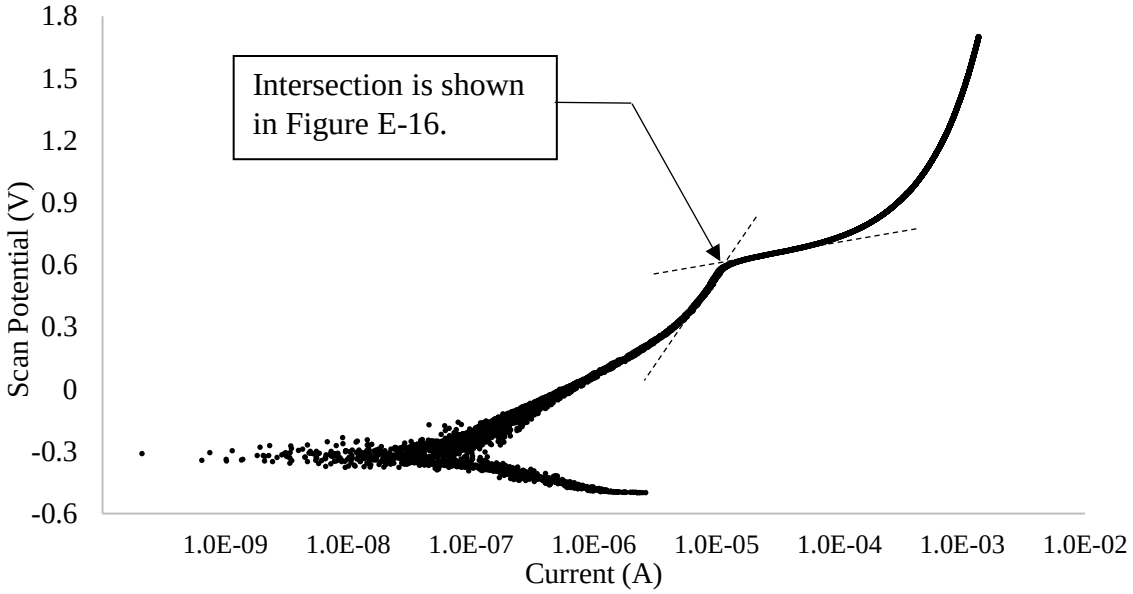

Figure E-15: Potentiodynamic polarization current of 1018 steel embedded within HCP specimen was scanned in lime water. Scanning potential ranged from -0.5V to +1.7V. Absolute current was monitored during scanning. The 0.01A current corresponds to a current density of 0.705 A/m^2 (HCP specimen surface).

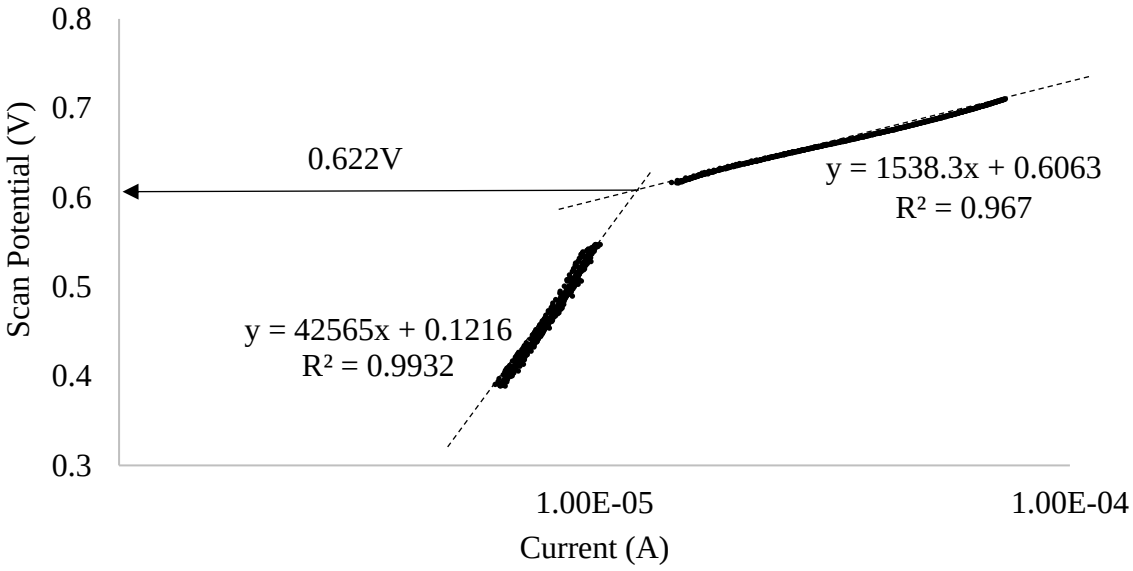

Figure E-16: Two sections of curve were selected from Figure E-15 to calculate the critical point at which the current began increasing significantly in the transpassive region. The intersection of these two dash lines is the critical point. (Trial 8)

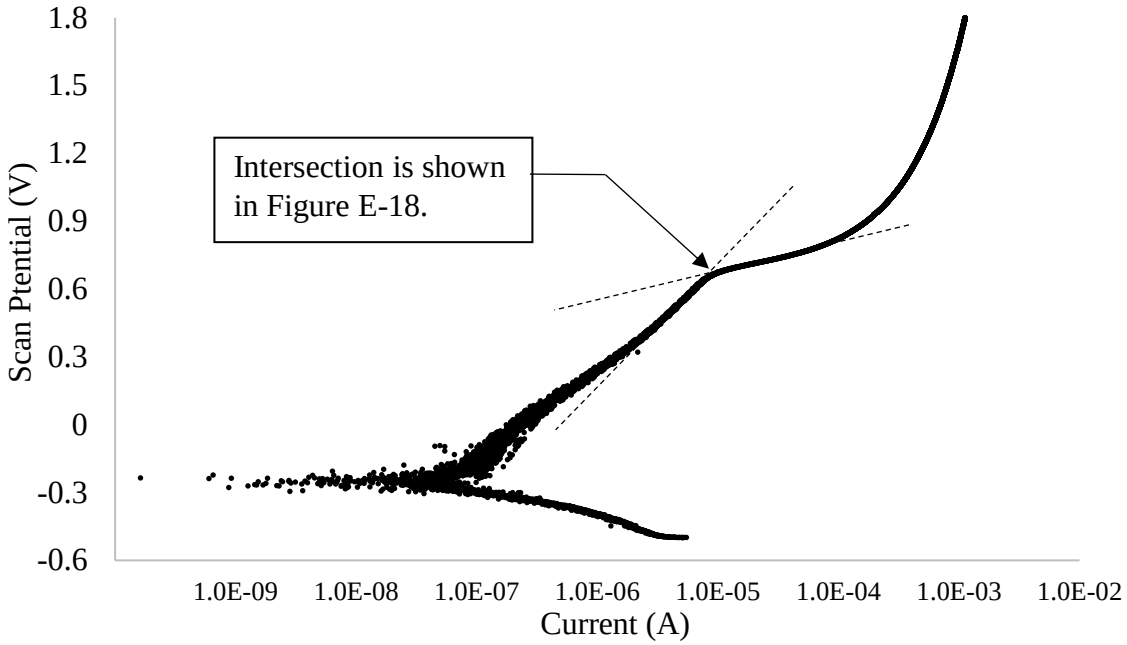

Figure E-17: Potentiodynamic polarization current of 1018 steel embedded within HCP specimen was scanned in lime water. Scanning potential ranged from -0.5V to +1.7V. Absolute current was monitored during scanning. The 0.01A current corresponds to a current density of 0.705 A/m^2 (HCP specimen surface).

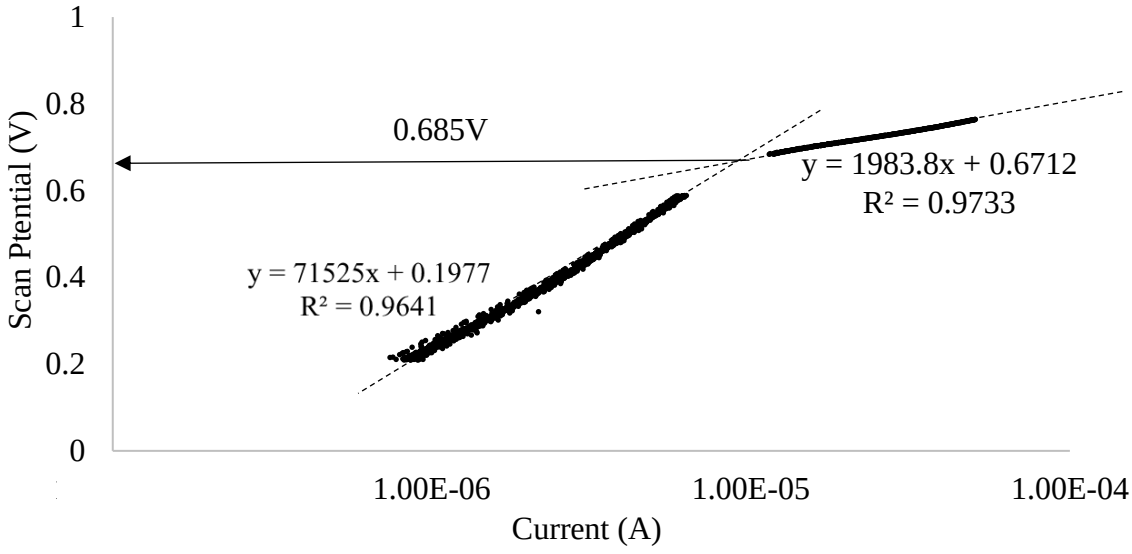

Figure E-18: Two sections of curve were selected from Figure E-17 to calculate the critical point at which the current began increasing significantly in the transpassive region. The intersection of these two dash lines is the critical point. (Trial 9)

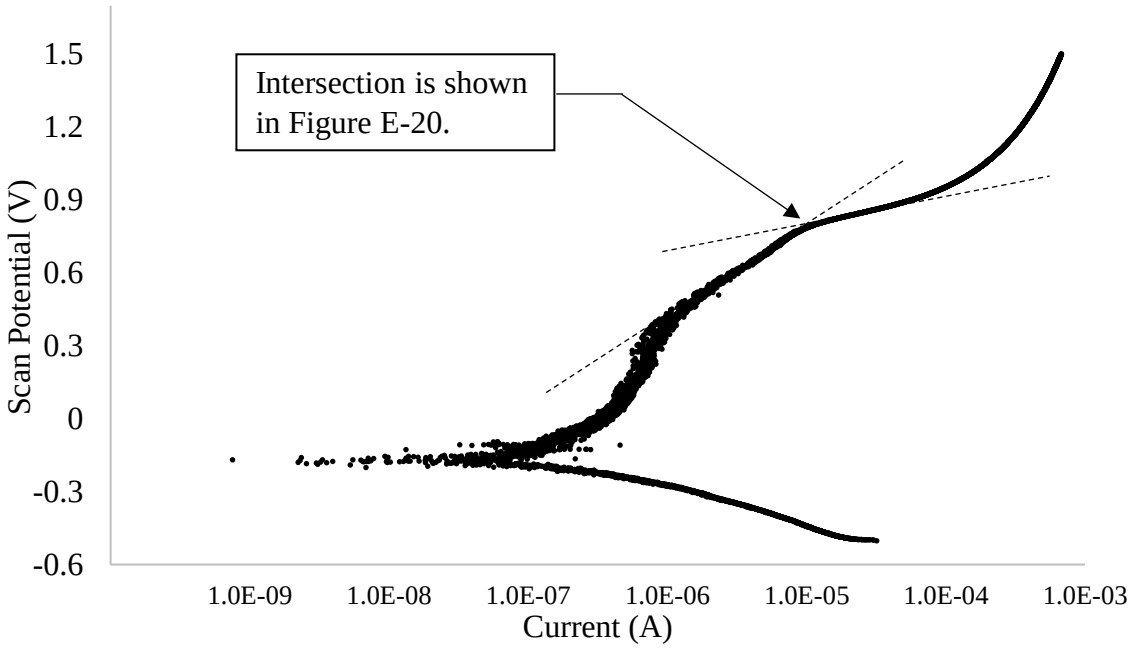

Figure E-19: Potentiodynamic polarization current of 1018 steel embedded within HCP specimen was scanned in lime water. Scanning potential ranged from -0.5V to +1.5V. Absolute current was monitored during scanning. The 0.01A current corresponds to a current density of 0.705 A/m^2 (HCP specimen surface).

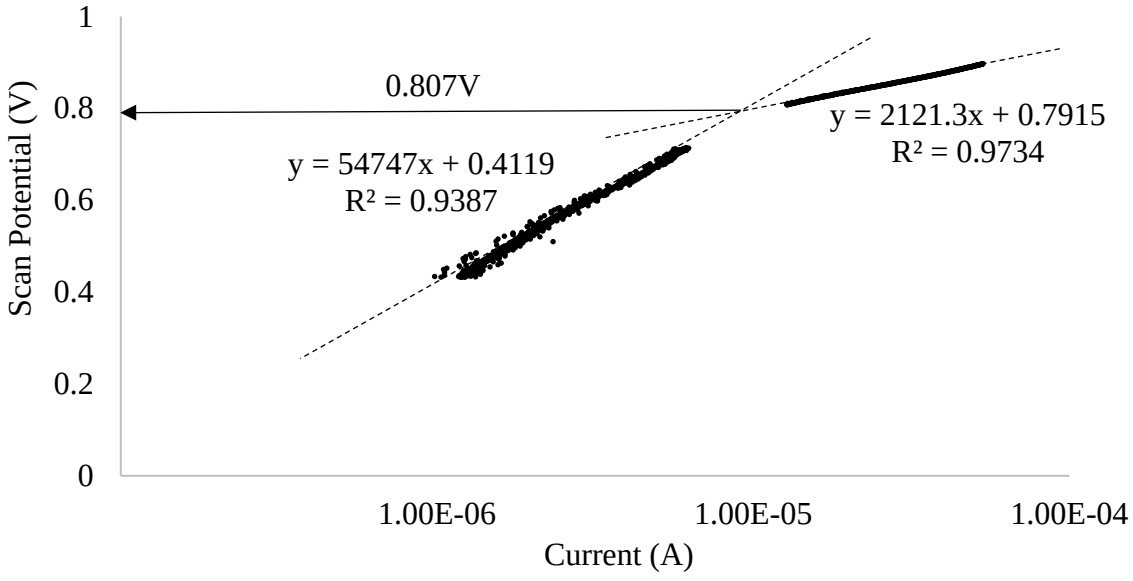

Figure E-20: Two sections of curve were selected from Figure E-19 to calculate the critical point at which the current began increasing significantly in the transpassive region. The intersection of these two dash lines is the critical point. (Trial 10)

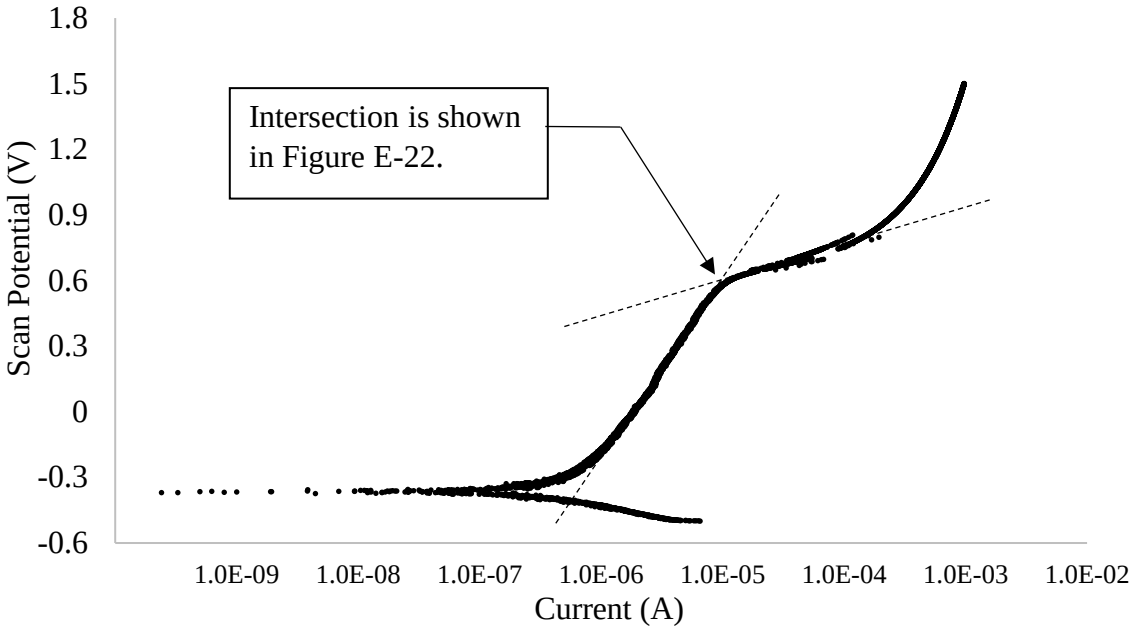

Figure E-21: Potentiodynamic polarization current of 1018 steel embedded within HCP specimen was scanned in lime water. Scanning potential ranged from -0.5V to +1.5V. Absolute current was monitored during scanning. The 0.01A current corresponds to a current density of 0.705 A/m^2 (HCP specimen surface).

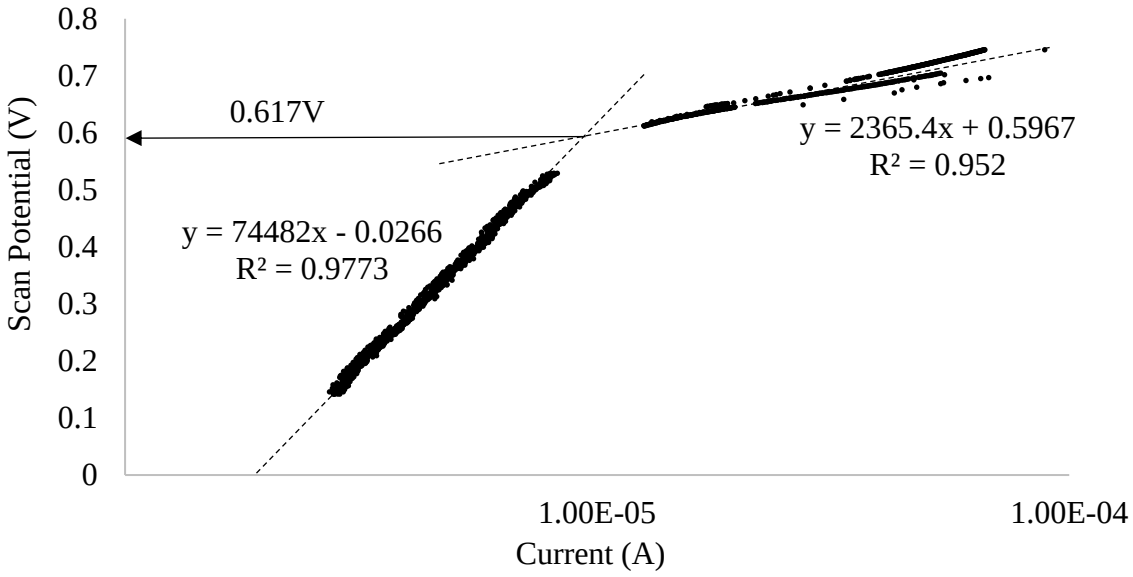

Figure E-22: Two sections of curve were selected from Figure E-21 to calculate the critical point at which the current began increasing significantly in the transpassive region. The intersection of these two dash lines is the critical point. (Trial 11).

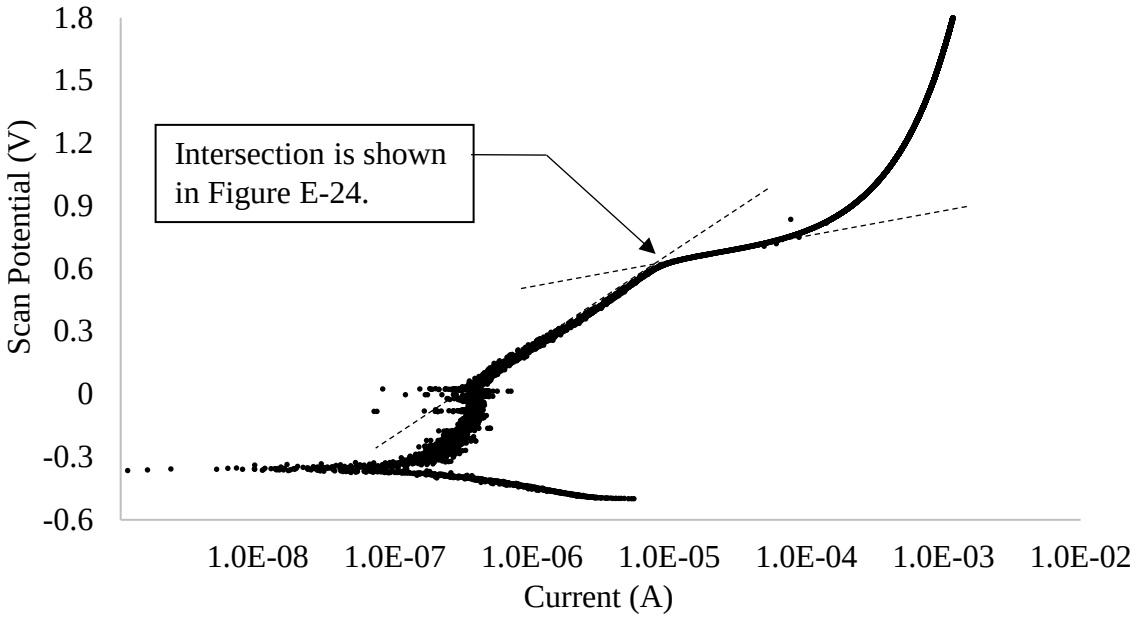

Figure E-23: Potentiodynamic polarization current of 1018 steel embedded within HCP specimen was scanned in lime water. Scanning potential ranged from -0.5V to +1.5V. Absolute current was monitored during scanning. The 0.01A current corresponds to a current density of 0.705 A/m^2 (HCP specimen surface).

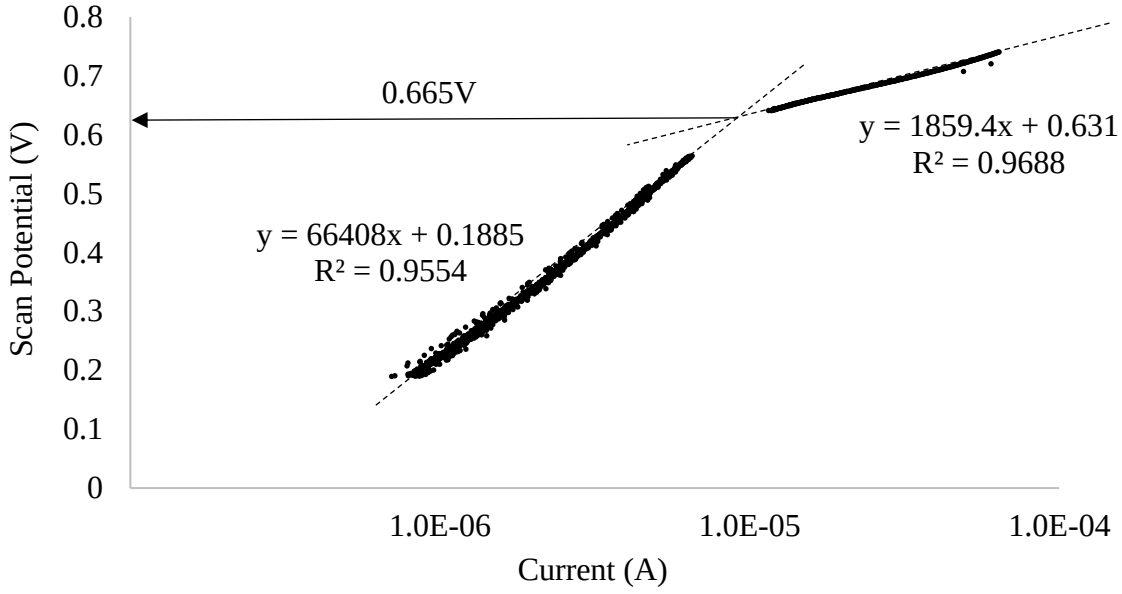

Figure E-24: Two sections of curve were selected from Figure E-23 to calculate the critical point at which the current began increasing significantly in the transpassive region. The intersection of these two dash lines is the critical point. (Trial 12)

Table E-1: Power supply (PS) drifts during MMA treatments and reference electrode (RE) uncertainties during potentiodynamic polarization tests (drift unit: Volts).

Trial No.	PS Drift	Trial No.	PS Drift	Trial No.	PS Drift	Trial No.	RE Uncertainty
1	12	11	37	21	25	1	8
2	0	12	-32	22	11	2	30
3	8	13	38	23	-17	3	15
4	-2	14	-5	24	38	4	20
5	44	15	10	25	7	5	30
6	-16	16	4	26	48	6	30
7	3	17	15	27	16	7	6
8	-4	18	3	28	-3	8	28
9	-1	19	24			9	12
10	-1	20	36			10	5
Average	10.6						18.4
STDEV*	19.7						10.5
Error Bar	6.1						5.5

* STDEV is the standard deviation.

APPENDIX F

MMA TREATEMENT WITH SMALL CORROSION POTENTIAL

Methyl Methacrylate (MMA) Dosage Calculation for MMA Treatments with Small Corrosion Potentials:

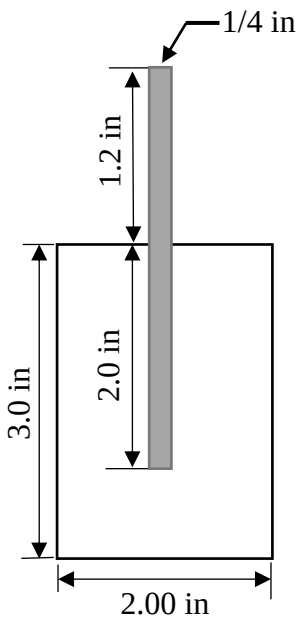

Volume of HCP Specimen:

$$V_{HCP} = \pi\left(\frac{D}{2}\right)^2 \cdot Height = \pi\left(\frac{2}{2}\right)^2 \cdot 3 = 9.425\ in^3$$

$$\approx 154\ cm^3$$

Assuming the porosity of HCP specimen was 23%, the volume of the pores in an HCP specimen was:

$$V_{pore} = V_{HCP} \cdot 23\% = 154 \cdot 0.23 = 35.4\ cm^3$$

The density [154] of Poly(methyl methacrylate) was:

$$\rho_{PMMA} = 1.20\ g/cm^3$$

The required MMA monomer to fill the pores of HCP specimen:

$$m_{MMA} = \rho_{PMMA} \cdot V_{pore} = 1.20 \times 35.4 = 42.5\ g$$

Each group (described in Table 3-7) contained five HCP specimens. The required MMA monomer to fill the pores of six HCP specimens:

$$m_{Total} = 6 \cdot m_{MMA} = 6 \times 42.5 = 255.0\ \text{g}$$

The volume of the solution applied in the MMA treatment was 3641 cm^3. The concentration of MMA monomer was 0.15 mol/L. The capacity of dissolved MMA monomer in the solution was:

$$m_{MMA\ in\ Container} = 0.15\frac{mol}{L} \times 3.641\ L \times 100.12\frac{g}{mol} = 54.7\ g$$

It was assumed that all the MMA monomer in the container would polymerize and evaporate in two days. A new MMA dosage ($m_{MMA\ in\ Container}$) was added every

two days in the solution during MMA treatment to maintain the concentration of MMA monomer. The MMA treatment time was calculated:

$$Dosage\ times = \frac{m_{MMA,dosage}}{m_{MMA\ in\ Container}} = \frac{255g}{54.7g} = 4.66\ \approx 5$$

$$Treatment\ time = Dosage\ times \times 2\ days = 10\ days$$

Table F-1: Indirect tensile strength of MMA-treated and control HCP specimens. (Unit: psi)

	Trial 1		Trial 2		Trial 3		Trial 4	
Specimen No.	Control	Treated	Control	Treated	Control	Treated	Control	Treated
1	668	627	429	220	341	292	327	300
2	1040	1190	415	233	352	87	430	201
3	1328	1200	527	310	389	281	329	292
4	1260	1417	350	186	338	362	351	222
5	998	1301	445	221	393	291	410	213
6	1006	1417	348	237	348	Crack	376	261
Average	1050	1192	419	234	360	262	370	248
STDEV*	233	294	67	41	24	103	43	42
Error Bar	157	198	45	28	16	76	29	28

* STDEV is the standard deviation.

Table F-2: Porosities of MMA-treated and control HCP specimens in Trials 1-4. (Unit: %)

	Trial 1		Trial 2		Trial 3		Trial 4	
Specimen No.	Control	Treated	Control	Treated	Control	Treated	Control	Treated
1	24.8	25.5	24.4	24.2	24.7	25.7	25.1	25.4
2	26.5	24.9	24.0	24.5	24.9	24.8	24.4	26.0
3	25.6	25.6	23.7	23.7	24.6	24.9	24.7	27.3
4	23.9	26.5	23.6	24.7	24.8	24.5	24.7	25.4
5	25.8	24.9	24.4	24.2	24.9	24.2	25.9	25.8
6	24.7	25.6	23.7	24.3	24.4	0.0	25.2	26.3
Average	25.2	25.5	24.0	24.3	24.7	24.8	25.0	26.0
STDEV*	0.9	0.6	0.4	0.3	0.2	0.6	0.5	0.7
Error Bar	0.6	0.4	0.2	0.2	0.1	0.4	0.4	0.5

* STDEV is the standard deviation.

APPENDIX G

REPRODUCIBILITY CHECK ON STRENGTH BENEFIT OF MMA TREATMENT

Methyl Methacrylate (MMA) Dosage Calculation for Checking Strength Benefits of HCP Specimens after MMA Treatments:

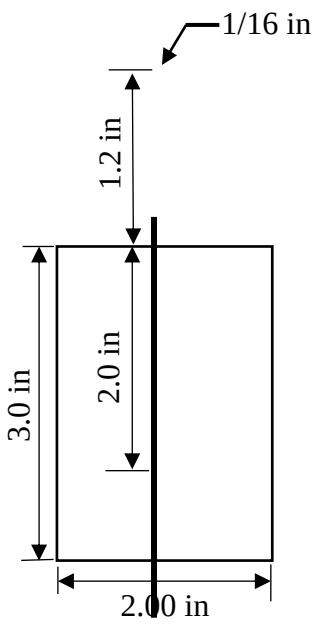

Volume of HCP Specimen:

$$V_{HCP} = \pi\left(\frac{D}{2}\right)^2 \cdot Height = \pi\left(\frac{2}{2}\right)^2 \cdot 3 = 9.425\ in^3$$

$$\approx 154\ cm^3$$

Assuming the porosity of HCP specimen was 23%, the volume of the pores in an HCP specimen was:

$$V_{pore} = V_{HCP} \cdot 23\% = 154 \cdot 0.23 = 35.4\ cm^3$$

The density [154] of Poly(methyl methacrylate) was:

$$\rho_{PMMA} = 1.20\ g/cm^3$$

The required MMA monomer to fill the pores of HCP specimen:

$$m_{MMA} = \rho_{PMMA} \cdot V_{pore} = 1.20 \times 35.4 = 42.5\ g$$

The volume of the solution applied in the MMA treatment was 400 cm^3. The concentration of MMA monomer was 0.1 mol/L. The capacity of dissolved MMA monomer in the solution was:

$$m_{MMA\ in\ Container} = 0.1\frac{mol}{L} \times 0.4\ L \times 100.12\frac{g}{mol} = 4.0\ g$$

It was assumed that all the MMA monomer in the container would polymerize and evaporate in one day. A new MMA dosage ($m_{MMA\ in\ Container}$) was added daily in the solution during MMA treatment to maintain the concentration of MMA monomer. The MMA treatment time was calculated:

$$Dosage\ times = \frac{m_{MMA,dosage}}{m_{MMA\ in\ Container}} = \frac{42.5g}{4.0g} = 10.6 \approx 10 \text{ times (for just one specimen)}$$

$$Treatment\ time = Dosage\ times \times 1\ days = 10\ days$$

Table G-1: Electric currents monitored daily during MMA treatments in Trial NSR (no solution replacement). (units: mA)

Time	Specimen 1	Specimen 2	Specimen 3	Specimen 4	Specimen 5	Specimen 6
1	14.20	14.20	14.20	14.24	14.27	14.20
2	15.16	13.58	15.30	14.83	13.95	11.68
3	14.10	11.46	13.15	13.30	13.05	10.77
4	12.64	9.30	10.96	11.80	11.37	9.15
5	12.15	8.48	9.70	9.59	15.34	8.22
6	10.90	8.09	9.41	9.95	8.04	8.60
7	10.15	7.68	9.20	9.75	9.62	8.04
8	9.41	7.48	9.65	9.50	9.95	8.01
9	8.99	8.66	9.97	11.63	11.78	9.61
10	8.85	8.74	10.55	11.76	10.54	9.41

Table G-2: Average currents and average current densities (HCP specimen surface) of MMA-treated HCP specimens in Trial NSR. Each value represents the average of six trials from Table G-1.

Time	Average Current (mA)	STDEV*	Error Bar (Current)	Average Current Density (A/m^2)	Error Bar (Current Density)
1	14.22	0.03	0.02	1.002	1.42E-03
2	14.08	1.36	0.91	0.992	6.44E-02
3	12.64	1.26	0.84	0.891	5.94E-02
4	10.87	1.39	0.93	0.766	6.58E-02
5	10.58	2.72	1.82	0.746	1.28E-01
6	9.17	1.13	0.76	0.646	5.37E-02
7	9.07	0.99	0.67	0.639	4.70E-02
8	9.00	1.00	0.67	0.634	4.75E-02
9	10.11	1.32	0.89	0.712	6.25E-02
10	9.98	1.18	0.79	0.703	5.58E-02

* STDEV is the standard deviation.

Table G-3: Electric currents monitored daily during MMA treatments in Trial DSR (daily solution replacement). (units: mA)

Time	Specimen 1	Specimen 2	Specimen 3	Specimen 4	Specimen 5	Specimen 6
1	14.20	14.24	14.20	14.20	14.20	14.20
2	8.65	14.20	9.63	6.72	5.81	6.00
3	6.57	10.86	7.93	6.70	5.71	4.20
4	6.40	10.00	6.97	5.85	5.36	4.44
5	7.60	11.36	7.62	5.96	5.31	5.04
6	4.45	5.00	3.20	2.78	2.46	2.50
7	2.96	5.20	3.32	4.15	2.26	1.85
8	2.53	8.53	2.41	2.39	1.50	8.29
9	3.60	4.60	2.17	2.25	1.63	1.33
10	2.50	5.33	2.97	2.20	1.92	1.85

Table G-4: Average currents and average current densities (HCP specimen surface) of MMA-treated HCP specimens in Trial DSR. Each value represents the average of six trials from Table G-3.

Time	Average Current (mA)	STDEV*	Error Bar (Current)	Average Current Density (A/m^2)	Error Bar (Current Density)
1	14.21	0.02	0.01	1.001	7.73E-04
2	8.50	3.18	2.13	0.599	1.50E-01
3	7.00	2.26	1.52	0.493	1.07E-01
4	6.50	1.92	1.29	0.458	9.09E-02
5	7.15	2.34	1.57	0.504	1.11E-01
6	3.40	1.08	0.72	0.239	5.09E-02
7	3.29	1.24	0.83	0.232	5.85E-02
8	4.28	3.22	2.17	0.301	1.53E-01
9	2.60	1.25	0.84	0.183	5.93E-02
10	2.80	1.31	0.88	0.197	6.19E-02

* STDEV is the standard deviation.

Table G-5: Indirect tensile strengths of MMA-Treated and control HCP specimens from trials NSR and DSR. (unit: psi)

	(Trial NSR)		(Trial DSR)	
	No Soln Replacement		Daily Soln Replacement	
Specimen No.	**Control**	**Treated**	**Control**	**Treated**
1	494	428	551	365
2	503	268	470	430
3	560	343	538	384
4	499	295	505	522
5	502	396	485	508
6	315	315	644	527
Average	479	341	532	456
Standard Deviation	83.8	60.9	62.9	72.5
Error Bar Limit	56.3	40.9	42.1	48.7

Table G-6: Porosities of MMA-Treated and control HCP specimens from trials NSR and DSR. (unit: %)

	(Trial NSR)		(Trial DSR)	
	No Soln Replacement		Daily Soln Replacement	
Specimen No.	**Control**	**Treated**	**Control**	**Treated**
1	24.1	26.7	26.2	28.9
2	24.4	27.8	25.1	26.8
3	25	27.1	25.1	25.2
4	25.3	28	25.5	26.3
5	26.6	25.7	24.4	25.1
6	25.1	24.9	25.2	24.9
Average	25.1	26.7	25.3	26.2
Standard Deviation	0.9	1.2	0.6	1.5
Error Bar Limit	0.6	0.8	0.4	1.0

Table G-7: pH of solutions monitored daily during MMA treatments. D1-D3 represents the solutions from Trial DSR. N1-N3 represents the solutions from Trial NSR.

Time	Specimen D1	Specimen D2	Specimen D3	Specimen N1	Specimen N2	Specimen N3
1	11.08	10.7	10.68	10.99	10.86	10.78
2	10.48	10.49	10.43	10.92	11.34	11.03
3	10.56	10.41	10.47	11.06	11.18	10.95
4	10.44	10.56	10.66	11.19	11.24	11.5
5	10.01	10.27	10.05	10.95	11.14	10.41
6	9.94	10.39	10.13	10.76	10.75	10.46
7	9.88	9.96	9.9	9.77	10.58	10.45
8	9.91	10.11	9.7	10.17	10.38	10.35
9	9.8	9.82	9.76	9.67	10.15	9.88
10	9.97	9.91	9.72	9.71	9.95	9.87

Table G-8: Average pH of the solutions from trials DSR and NSR (calculated from Table G-7). Each value represents the average of three trials.

Time	Trial DSR	STDEV	Error bar Limit	Trial NSR	STDEV	Error bar Limit
1	10.82	0.23	0.21	10.88	0.11	0.10
2	10.47	0.03	0.03	11.1	0.22	0.21
3	10.48	0.08	0.07	11.06	0.12	0.11
4	10.55	0.11	0.10	11.31	0.17	0.16
5	10.11	0.14	0.13	10.83	0.38	0.36
6	10.15	0.23	0.21	10.66	0.17	0.16
7	9.91	0.04	0.04	10.27	0.44	0.41
8	9.91	0.21	0.19	10.30	0.11	0.11
9	9.79	0.03	0.03	9.90	0.24	0.23
10	9.87	0.13	0.12	9.84	0.12	0.12

* STDEV is the standard deviation.

APPENDIX H

MMA TREATEMENT WITH POTASSIUM PERSULFATE

INITIATOR

Methyl Methacrylate (MMA) Dosage Calculation for MMA Treatments with Potassium Persulfate as Initiator:

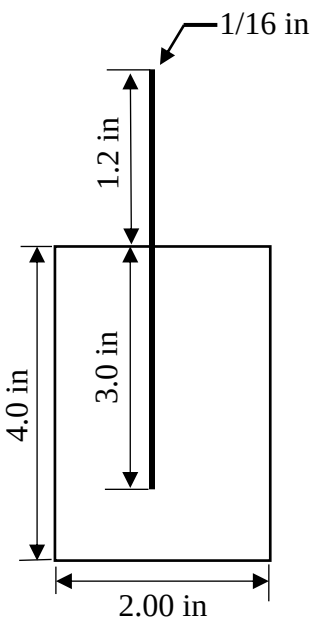

Volume of HCP Specimen:

$$V_{HCP} = \pi\left(\frac{D}{2}\right)^2 \cdot Height = \pi\left(\frac{2}{2}\right)^2 \cdot 4 = 12.566\ in^3$$

$$\approx 206\ cm^3$$

Assuming the porosity of HCP specimen was 23%, the volume of the pores in an HCP specimen was:

$$V_{pore} = V_{HCP} \cdot 23\% = 206 \cdot 0.23 = 47.4\ cm^3$$

The density [154] of Poly(methyl methacrylate) was:

$$\rho_{PMMA} = 1.20\ g/cm^3$$

The required MMA monomer to fill the pores of HCP specimen:

$$m_{MMA} = \rho_{PMMA} \cdot V_{pore} = 1.20 \times 47.4 = 56.9\ g$$

The volume of the solution applied in the MMA treatment was 570 cm^3. The concentration of MMA monomer was 0.1 mol/L. The capacity of dissolved MMA monomer in the solution was: $m_{MMA\ in\ Container} = 0.1\frac{mol}{L} \times 0.57\ L \times 100.12\frac{g}{mol} = 5.7\ g$

It was assumed that the MMA particles were spherical. The packing factor was 0.5 [155]. The actual required MMA monomer to fill the pores of HCP specimen was

$$m_{MMA,Packing} = 0.5 \cdot m_{MMA} = 0.5 \times 56.9 = 28.5\ g$$

It was assumed that all the MMA monomer in the container would polymerize and evaporate in two days. The treatment solution was replaced every two days. The MMA treatment time was calculated:

$$Dosage\ times = \frac{m_{MMA,Packing}}{m_{MMA\ in\ Container}} = \frac{28.5g}{5.7g} = 5 \text{ times}$$

$$Treatment\ time = Dosage\ times \times 2\ days = 10\ days$$

Potassium Persulfate Molecular Penetration Time into HCP Specimen for MMA Treatments Using Potassium Persulfate as Initiator:

In order to transport the persulfate ions into the HCP specimens, the transportation system was designed and shown in Figure H-1. Figure H-1 shows that the penetration path P is divided into two parts. One part is the distance ($d_c = 2.54$ cm) from the HCP specimen surface to the center of the specimen. The other part is the distance ($d_w =$ 2.71 cm) from the beaker wall to the HCP specimen surface. The external electrode was attached to the beaker wall. The mobility (μ) of persulfate ions was approximately equal to that of the sulfate ions ($\mu_{sulfate} \approx 10 \times 10^{-8}\ m^2/(s \cdot V)$). The mobility was calculated based on the Einstein relation Equation [156] [157]. The applied voltage was 6.0 V. Based on the particle penetration relation Eq. 2-35, the penetration time of persulfate ions from the beaker wall to the center of HCP specimen was:

$$t = t_w + t_c = \frac{d_w P}{\mu U} + \frac{6 d_c P}{\mu U}$$

$$= \frac{2.71 \times 10^{-2} \times 5.25 \times 10^{-2}}{10 \times 10^{-8} \times 6.0} + \frac{6 \times 2.54 \times 10^{-2} \times 5.25 \times 10^{-2}}{10 \times 10^{-8} \times 6.0}$$

$$= 2371s + 13335s = 15706 = 4.37\ h \approx 4\ h$$

t_w is the penetration time of ions from the beaker wall to the surface of the HCP specimen.

t_c is the penetration time of ions from the surface of the HCP specimen to the center of the HCP specimen. Other symbols were described in the previous illustrations.

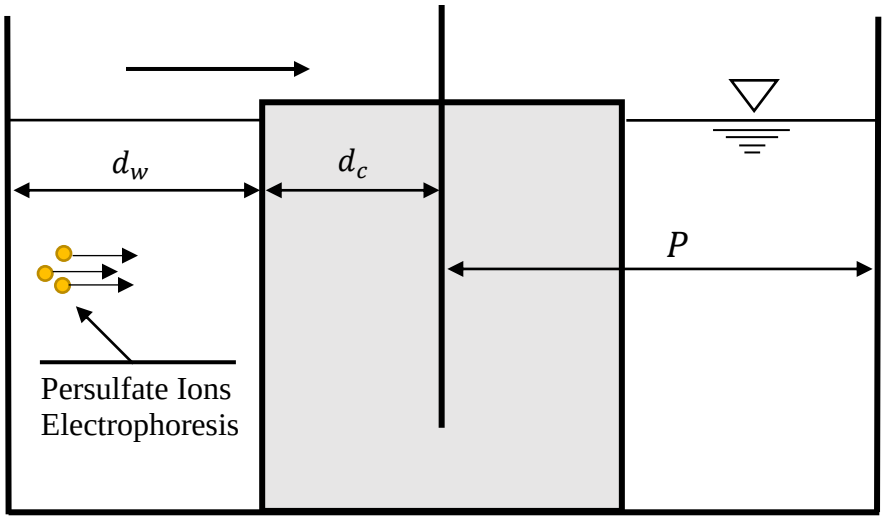

Figure H-1: Persulfate ions electrical conduction model under electric field (E). P = 5.25 cm. d_w = 2.71 cm. d_c = 2.54 cm.

Table H-1: Expected masses of PMMA in persulfate and MMA-treated HCP specimens after 48-hour segments in L-Trial 1. (unit: g)

	Specimen No.								
Segment No.	1	2	3	4	5	6	Average	STDEV*	Error Bar
1	0.36	0.42	0.40	0.43	0.39	-	0.40	0.03	0.02
2	0.40	0.18	0.39	0.59	0.39	0.32	0.38	0.13	0.09
3	0.27	0.26	0.27	0.25	0.26	0.22	0.26	0.02	0.01
4	0.22	0.17	0.17	0.17	0.25	0.20	0.20	0.03	0.02
5	0.21	0.20	0.21	0.16	0.19	0.18	0.19	0.02	0.01

* STDEV is the standard deviation.
The mass of PMMA in Specimen 6 after Segment 1 was missing.

Table H-2: Expected masses of PMMA in persulfate and MMA-treated HCP specimens after 48-hour segments in L-Trial 2. (units: g)

	Specimen No.								
Segment No.	1	2	3	4	5	6	Average	STDEV*	Error Bar
1	0.51	0.46	0.41	0.44	0.49	0.42	0.46	0.04	0.03
2	0.38	0.35	0.29	0.39	0.40	0.37	0.36	0.04	0.03
3	0.22	0.20	0.17	0.25	0.21	0.23	0.21	0.03	0.02
4		0.34	0.36	0.31	0.22	0.21	0.29	0.07	0.05
5	0.19	0.20	0.18	0.17	0.20	0.18	0.19	0.01	0.01

* STDEV is the standard deviation.
The mass of PMMA in Specimen 1 after Segment 4 was missing.

Table H-3: Expected masses of PMMA in persulfate and MMA-treated HCP specimens after 48-hour segments in S-Trial 3. (units: g)

	Specimen No.								
Segment No.	1	2	3	4	5	6	Average	STDEV*	Error Bar
1	0.56	0.52	0.57	0.51	0.56	0.50	0.54	0.03	0.02
2	0.40	0.40	0.47	0.40	0.42	0.40	0.41	0.03	0.02
3	0.33	0.31	0.35	0.33	0.31	0.26	0.32	0.03	0.02
4	0.27	0.29	0.31	0.27	0.29	0.28	0.28	0.02	0.01
5	0.25	0.22	0.24	0.26	0.23	0.22	0.24	0.02	0.01

* STDEV is the standard deviation.

Table H-4: Expected masses of PMMA in persulfate and MMA-treated HCP specimens after 48-hour segments in LC-Trial 4. (units: g)

Segment No.	Specimen No.						Average	STDEV*	Error Bar
	1	2	3	4	5	6			
1	0.06	0.08	0.05	0.08	0.11	0.08	0.08	0.02	0.01
2	0.08	0.11	0.05	0.08	0.09	0.10	0.08	0.02	0.01
3	0.02	0.04	0.03	0.02	0.03	0.04	0.03	0.01	0.01
4	0.03	0.05	0.05	0.05	0.06	0.05	0.05	0.01	0.01
5	0.04	0.06	0.05	0.07	0.04	0.04	0.05	0.01	0.01

* STDEV is the standard deviation.

Table H-5: Indirect tensile strengths of persulfate-MMA-treated and control HCP specimens in trials 1-4. (unit: psi)

Specimen No.	**Long Treated Time**		**Long Treated Time**		**Short Treated Time**		**Low [S] Version of Trial 3**	
	L-Trial 1		L-Trial 2		S-Trial 3		LC-Trial 4	
	Control	Treated	Control	Treated	Control	Treated	Control	Treated
1	511	191	3090	1856	352	343	576	437
2	534	202	3421	2218	516	490	534	483
3	536	412	4147	3183	358	363	436	543
4	377	343	2279	1674	329	424	472	512
5	390	377	3272	1894	420	585	475	504
6	497	212	4080	2155	291	341	302	498
Average	474	289	3382	2163	378	424	466	496
STDEV*	71.8	98.7	691.2	538.3	79.8	97.4	94.3	35.2
Error Limit	48.2	66.3	464.2	361.5	53.6	65.4	63.3	23.7

* STDEV is the standard deviation.

Table H-6: Porosities of persulfate-MMA-treated and control HCP specimens in trials 1-4. (unit: %)

	Long Treated Time		**Long Treated Time**		**Short Treated Time**		**Low [S] Version of Trial 3**	
Specimen No.	L-Trial 1		L-Trial 2		S-Trial 3		LC-Trial 4	
	Control	Treated	Control	Treated	Control	Treated	Control	Treated
1	28.6	29.6	25.2	25.5	25.0	25.5	24.5	25.0
2	27.5	28.8	24.4	24.3	25.4	25.3	24.9	25.1
3	30.6	27.5	24.2	24.0	25.5	25.1	24.0	24.3
4	28.1	26.0	24.2	24.5	25.1	25.1	24.4	24.5
5	28.5	28.2	25.4	24.4	24.9	24.9	24.8	24.1
6	27.9	26.4	24.0	23.8	24.4	25.2	23.9	24.2
Average	28.5	27.8	24.6	24.4	25.1	25.2	24.4	24.5
STDEV*	1.1	1.4	0.6	0.6	0.4	0.2	0.4	0.4
Error Limit	0.7	0.9	0.4	0.4	0.3	0.1	0.3	0.3

* STDEV is the standard deviation.

Table H-7: Detected counts of elemental sulfur of control HCP specimens via EDXRF in L-Trial 1. (unit: count)

	Specimen No.					
Trial	1	2	3	4	5	6
1	20456	20200	20479	20192	20052	19890
2	20415	20193	19475	20181	19660	20522
3	20423	20434	19868	20297	20064	20429
4	20666	19844	20136	20220	20421	20478
5	20536	20027	19954	20450	20768	19680
Average Count	20214					
Standard Deviation	314					
Error Bar Limit	94					

Table H-8: Detected counts of elemental sulfur of MMA-treated HCP specimens via EDXRF in L-Trial 1. (unit: count)

	Specimen No.					
Trial	1	2	3	4	5	6
1	21249	20638	20052	20496	21269	20878
2	21359	20884	20432	20565	20766	20413
3	21411	20004	20962	19930	19779	21196
4	22060	20635	20719	20637	20342	20640
5	21566	20740	20764	20548	21188	20471
Average Count	20753					
Standard Deviation	508					
Error Bar Limit	152					

Table H-9: Detected counts of elemental sulfur of control HCP specimens via EDXRF in S-Trial 3. (unit: count)

	Specimen No.					
Trial	1	2	3	4	5	6
1	18641	18665	18321	18520	19465	18532
2	18988	19445	18732	18465	18856	18435
3	19228	19626	19299	18526	18648	18456
4	18583	18822	19005	18351	19184	18219
5	19220	18964	19056	18216	19327	19231
Average Count		18834				
Standard Deviation		403				
Error Bar Limit		121				

Table H-10: Detected counts of elemental sulfur of MMA-treated HCP specimens via EDXRF in S-Trial 3. (unit: count)

	Specimen No.					
Trial	1	2	3	4	5	6
1	18929	19635	19227	19394	19208	18979
2	18855	18675	18223	19836	18708	19061
3	19134	19382	18810	19635	19475	18632
4	18911	19167	18715	19185	19316	18160
5	18789	19323	18765	19328	19173	19383
Average Count		19067				
Standard Deviation		391				
Error Bar Limit		117				

Table H-11: Detected counts of elemental sulfur of control HCP specimens via EDXRF in LC-Trial 4. (unit: count)

	Specimen No.					
Trial	1	2	3	4	5	6
1	18860	19016	19217	18861	19329	18470
2	18568	18889	18787	18682	18705	19359
3	18272	18547	18609	18597	18713	18917
4	18827	19299	19863	19114	18995	19101
5	18994	19597	19065	19078	18391	19160
Average Count	18929					
Standard Deviation	356					
Error Bar Limit	107					

Table H-12: Detected counts of elemental sulfur of MMA-treated HCP specimens via EDXRF in LC-Trial 4. (unit: count)

	Specimen No.					
Trial	1	2	3	4	5	6
1	19298	20804	20950	20608	20175	20574
2	19764	21015	20621	19424	20427	19808
3	19955	20467	19883	19479	21150	20867
4	19772	20366	19893	19335	21184	20496
5	19834	20635	20589	20029	21333	20023
Average Count	20292					
Standard Deviation	577					
Error Bar Limit	173					

REFERENCES

[1] AZoM, "Polymethylmethacrylate - Acrylic - PMMA General Purpose," AZO Materials, 4 9 2001. [Online]. Available: https://www.azom.com/article.aspx?ArticleID=788.

[2] G. H. Koch, M. Brongers and N. G. Thompson, "Corrosion Costs and Preventive Strategies in the United States," U.S. Department of Transportation, Mclean, 2002.

[3] S. Mindess, J. Young and D. Darwin, *Concrete*, Upper Saddle River: Pearson Education, 2003.

[4] Z. Ahmad, *Principles of Corrosion Engineering and Corrosion Control*, 1st ed., Burlington: Elsevier, 2006.

[5] Portland Cement Association, "How Cement is Made," Portland Cement Association, [Online]. Available: https://www.cement.org/cement-concrete-applications/how-cement-is-made#.

[6] N. Winter, "Cement History," Nicholas Winter, [Online]. Available: https://www.understanding-cement.com/history.html.

[7] C150M-18, "Standard Specification for Portland Cement," *ASTM International*, vol. 04, no. 01.

[8] Portland Cement Association, "Cement Types," Portland Cement Association, [Online]. Available: https://www.cement.org/cement-concrete-applications/concrete-materials/cement-types.

[9] J. Thomas and H. Jennings, "3.6 Mineral and oxide composition of portland cement," The Science of Concrete, [Online]. Available: http://iti.northwestern.edu/cement/monograph/monograph3_6.html.

[10] P. K. Mehata and P. J. M. Monteiro, *Concrete: Microstructure, Properties, and Materials*, New York: McGraw-Hill, 2006.

[11] Q. Ding, J. Yang, D. Hou and G. Zhang, "Insight on the mechanism of sulfate

attacking on the cement paste with granulated blast furnace slag: An experimental and molecular dynamics study," *Construction and Building Materials,* vol. 169, pp. 601-611, 2018.

[12] M. Merlini, G. Artioli, T. Cerulli, F. Cella and A. Bravo, "Tricalcium aluminate hydration in additivated systems. A crystallographic study by SR-XRPD," *Cement and Concrete Research,* vol. 38, no. 4, pp. 477-486, 2008.

[13] K. Liu, L. Mo, M. Deng and J. Tand, "Deterioration mechanism of Portland cement paste subjected to sodium sulfate attack," *Advances in Cement Research,* vol. 27, no. 8, pp. 477-486, 2015.

[14] X. Wang, Z. Pan, X. Shen and W. Liu, "Stability and decomposition mechanism of ettringite in presence of ammonium sulfate solution," *Construction and Building Materials,* vol. 124, pp. 786-793, 2016.

[15] B. Dilnesa, B. Lothenbach and G. Renaudin, "Stability of Monosulfate in the Presence of Iron," *Journal of the American Ceramic Society,* vol. 95, no. 10, pp. 3305-3316, 2012.

[16] M. Syarif, V. Sampebulu and M. W. Tjaronge, "Characteristic of compressive and tensile strength using the organic cement compare with portland cement," *Case Studies in Construction Materials,* vol. 9, 2018.

[17] Z. Li, B. Han, X. Yu, S. Dong, L. Zhang, X. Dong and J. Qu, "Effect of nano-titanium dioxide on mechanical and electrical properties and microstructure of reactive powder concrete," *Materials Research Express* , vol. 4, 2017.

[18] E. J. Garboczi and D. P. Bentz, "Computer simulation of the diffusivity of cement-based materials," *Journal of Materials Science,* vol. 27, no. 8, pp. 2083-2092, 1992.

[19] H. Cardenas, "Investigation of Reactive Electrokinetic Processes for Permeability Reduction in Hardened Cement Paste", Ph.D Dissertation, Champaign: University of Illinois at Urbana-Champaign, 2002.

[20] S. Diamond and M. E. Leeman, "Pore Size Distributions in Hardened Cement Paste by SEM Image Analysis," *MRS Proceedings,* vol. 370, 2011.

[21] Particle Technology Labs, "Mercury Intrusion Porosimetry Testing," PTL, [Online]. Available: https://www.particletechlabs.com/analytical-testing/gas-adsorption-porosimetry-analyses/mercury-intrusion-porosimetry.

[22] T. C. Powers, "Structure and Physical Properties of Hardened Portland Cement

Paste," *Journal of the American Ceramic Society,* vol. 41, pp. 1-6, 1958.

[23] F. Goran, Porosity and specific surface of Portland cement paste: an analysis of experimental work performed by Åke Grudemo during the years 1973-1979, Lund: Lund University, 2006.

[24] P. Yimprasert, D. W. Fowler and D. R. Paul, *Durability, Strength, and Method of Application of Polymer-Impregnated Concrete for Slabs,* Research Report Number 114-4, Center for Highway Research, University of Texas, Austin, 1976, Available: https://library.ctr.utexas.edu/digitized/texasarchive/phase1/114-4-chr.pdf.

[25] K. Fukuzawa, T. Numao, S. Iwamatsu, K. Nomaguchi and H. Tashiro, "Compressive Strength of Polymer Impregnated Mortars Using High Molecular Weight Methacrylate Monomers," *Journal of the Society of Materials Science, Japan,* vol. 42, no. 476, pp. 581-587, 1993.

[26] W. F. Chen, H. C. Mehta and L. W. Lu, *Polymer impregnated concrete (pic) for building construction,* Fritz Laboratory Reports, Lehigh Univerisity, Bethlehem, PA, 1974, Available: http://preserve.lehigh.edu/engr-civil-environmental-fritz-lab-reports/2081.

[27] C. E. Porter and F. D. Blum, "Thermal Characterization of PMMA Thin Films Using Modulated Differential Scanning Calorimetry," *Macromolecules,* vol. 33, no. 19, pp. 7016-7020, 2000.

[28] S. Chinchon-Paya, A. Aguado, H. W. Nugteren and J. S. Chinchon, "External sulfate attack in dam concretes with thaumasite formation," *Materiales de Construcción,* vol. 65, no. 317, 2015.

[29] Z. Liu, W. Hu, L. Hou and D. Deng, "Effect of carbonation on physical sulfate attack on concrete by Na2SO4," *Construction and Building Materials,* vol. 193, pp. 211-220, 2018.

[30] M. M. Rahman and M. T. Bassuoni, "Thaumasite sulfate attack on concrete: Mechanisms, influential factors and mitigation," *Construction and Building Materials,* vol. 73, pp. 652-662, 2014.

[31] B. Tian and M. D. Cohen, "Does gypsum formation during sulfate attack on concrete lead to expansion?," *Cement and Concrete Research,* vol. 30, no. 1, pp. 117-123, 2000.

[32] F. Bellmann and J. Bensted, "On the formation of thaumasite CaSiO3 · CaSO4 · CaCO3 · 15H2O: Part II," *Advances in Cement Research,* vol. 18, no. 3, pp. 129-

134, 2006.

[33] K. Liu, D. Sun, A. Wang, G. Zhang and J. Tang, "Long-Term Performance of Blended Cement Paste Containing Fly Ash against Sodium Sulfate Attack," *Journal of Materials in Civil Engineering,* vol. 30, no. 12, pp. 1-10, 2018.

[34] J. Haufe and A. Vollpracht, "Tensile strength of concrete exposed to sulfate attack," *Cement and Concrete Research,* vol. 116, pp. 81-88, 2019.

[35] M. Santhanam, M. D. Cohen and J. Olek, "Effects of gypsum formation on the performace of cement mortars during external sulfate attack," *Cement and Concrete Research,* vol. 33, no. 3, pp. 325-32, 2003.

[36] P. J. M. Monteiro and K. E. Kurtis, "Time to failure for concrete exposed to severe sulfate attack," *Cement and Concrete Research,* vol. 33, no. 7, pp. 987-993, 2003.

[37] J. Skalny, J. Marchand and I. Odler, *Sulfate Attack on Concrete*, London: Taylor and Francis Publications, 2001.

[38] D. Wang, X. Zhou, Y. Meng and Z. Chen, "Durability of concrete containing fly ash and silica fume against combined freezing-thawing and sulfate attack," *Construction and Building Materials,* vol. 147, pp. 398-406, 2017.

[39] X. Yan, L. Jiang, M. Guo, Y. Chen, Z. Song and R. Bian, "Evaluation of sulfate resistance of slag contained concrete under steam curing," *Construction and Building Materials,* vol. 195, pp. 231-237, 2019.

[40] M. Khan and O. Kayali, "Effect of NaOH activation on ettringite in concrete containing ground granulated blast furnace slag," in *Third International Conference on Sustainable Construction Materials and Technologies*, Kyoto, Japan, 2013.

[41] K. Kupawade-Patil, "Mitigation of Chloride and Sulfate Based Corrosion in Reinforced Concrete via Electrokinetic Nanoparticle Treatment", Ph.D Dissertation, Ruston: Louisiana Tech University, 2010.

[42] H. Cardenas and L. Struble, "Electrokinetic Nanoparticle Treatment of Hardened Cement Paste for Reduction of Permeability," *ASCE Journal of Materials in Civil Engineering,* vol. 18, no. 4, pp. 554-560, 2006.

[43] T. Iseley, *Guide to Water and Wastewater Asset Management,* M. Najafi and J. Rush, Eds., UIM/Benjamin Media, Inc., 2018.

[44] E. Q. Zhang, Z. Abbas and L. Tang, "Predicting degradation of the anode–concrete interface for impressed current cathodic protection in concrete," *Construction and Building Materials,* vol. 185, pp. 57-68, 2018.

[45] K. Wilson, M. Jawed and V. Ngala, "The selection and use of cathodic protection systems for the repair of reinforced concrete structures," *Construction and Building Materials,* vol. 39, pp. 19-25, 2013.

[46] H. Lin, Y. Li and Y. Li, "A study on the deterioration of interfacial bonding properties of chloride-contaminated reinforced concrete after electrochemical chloride extraction treatment," *Construction and Building Materials,* vol. 197, pp. 228-240, 2019.

[47] L. Souza, M. Medeiros, E. Pereira and A. Capraro, "Electrochemical chloride extraction: Efficiency and impact on concrete containing 1% of NaCl," *Construction and Building Materials,* vol. 145, pp. 435-444, 2017.

[48] J. Xia, Q.-f. Liu, J.-h. Mao, Z.-h. Qian, S.-j. Jin, j.-y. Hu and W.-l. Jin, "Effect of environmental temperature on efficiency of electrochemical chloride removal from concrete," *Construction and Building Materials,* vol. 193, pp. 189-195, 2018.

[49] A. Canon, P. Garces, M. A. Climent, J. Carmona and E. Zornoza, "Feasibility of electrochemical chloride extraction from structural reinforced concrete using a sprayed conductive graphite powder–cement paste as anode," *Corrosion Science,* vol. 77, pp. 123-134, 2013.

[50] M. Siegwart, J. F. Lyness, B. J. McFarland and G. Doyle, "The effect of electrochemical chloride extraction on pre-stressed concrete," *Construction and Building Materials,* vol. 19, no. 8, pp. 585-594, 2005.

[51] M. Kutz, *Handbook of Environmental Degradation of Materials,* Norwich: William Andrew, 2013.

[52] M. Balonis, G. Sant and O. B. Lsgor, "Mitigating steel corrosion in reinforced concrete using functional coatings, corrosion inhibitors, and atomistic simulations," *Cement and Concrete Composites,* 2018.

[53] C. L. Page, "Durability of Concrete and Cement Composites," in *Corrosion and protection of reinforcing steel in concrete*, Sawston, Woodhead Publishing, 2007, pp. 136-186.

[54] P. A. Wedding, C. Andrade, C. Alonso and J. A. Gonzalez, "Some Laboratory Experiments on the Inhibitor Effect of Sodium Nitrite on Reinforcement

Corrosion," *Cement Concrete and Aggregates,* vol. 8, no. 2, 1986.

[55] J. Gaidis and A. Rosenberg, "The Inhibition of Chloride-Induced Corrosion in Reinforced Concrete by Calcium Nitrite," *Cement, Concrete and Aggregates,* vol. 9, pp. 30-33, 1987.

[56] ConcreteNetwork, "Epoxies Vs. Polyurethanes," ConcreteNetwork, [Online]. Available: https://www.concretenetwork.com/concrete/crack_injection/epoxies_vs_polyurethanes.html.

[57] S. Lin, D. Meng, H. Choi, S. Shams and H. Azari, "Laboratory assessment of nine methods for nondestructive evaluation of concrete bridge decks with overlays," *Construction and Building Materials,* vol. 188, pp. 966-982, 2018.

[58] A. C877-16, "Standard Specification for External Sealing Bands for Concrete Pipe, Manholes, and Precast Box Sections," *ASTM International,* 2016.

[59] LANZO Lining Services Inc., "Engineering Design Guide for Rehabilitation with Cured-in-place Pipe," 2010. [Online]. Available: http://lanzo.net/pdf/lanzo-lining-guide-2410.pdf.

[60] A. N. Nayeem, "In Situ Electrokinetic Polymer Formation to Prevent Reinforcement Corrosion in Concrete", M.S. Thesis, Ruston: Louisiana Tech University, 2012.

[61] National Center for Biotechnology Information, "Methyl Methacrylate," PubChem Compound Database, [Online]. Available: https://pubchem.ncbi.nlm.nih.gov/compound/methyl_methacrylate#section=Top.

[62] G. Odian, *Principles of Polymerization,* 4th, Ed., New Jersey: John Wiley & Sons, Inc., 2004, pp. 307-308.

[63] W.-F. Su, "Radical Chain Polymerization," in *Principles of Polymer Design and Synthesis,* Berlin, Springer, 2013, pp. 137-183.

[64] T. O. Kazuko Hayashi, "Effect of structure of vinyl esters on radical polymerization," *Macromolecular Chemistry and Physics,* vol. 127, no. 1, pp. 54-65, September 1969.

[65] D. R. Hensley, S. D. Goodrich, A. Y. Huckstep, H. J. Harwood and P. L. Rinadi, "2D-Inadequate NMR evidence for the termination mechanism of styrene Free-Radical Polymerization," *Macromolecules,* vol. 28, no. 5, pp. 1586-1591, February 1995.

[66] D. W. Ovenall and R. E. Uschold, "Detection of branching on poly(vinyl fluoride) by NMR and the effect of synthesis conditions on polymer structure," *Macromolecules,* vol. 24, no. 11, pp. 3235-3237, 1991.

[67] R. E. Cais and J. M. Kometani, "New isomers of poly(vinyl fluoride) with controlled regiosequence microstructure," *Polymer,* vol. 29, no. 1, pp. 168-172, 1988.

[68] J. Guiot, B. Ameduri and B. Boutevin, "Radical Homopolymerization of Vinylidene Fluoride Initiated by tert-Butyl Peroxypivalate. Investigation of the Microstructure by 19F and 1H NMR Spectroscopies and Mechanisms," *Macromolecules,* vol. 35, no. 23, pp. 8694-8707, 2002.

[69] R. E. Cais and J. M. Kometani, "Synthesis of pure head-to-tail poly(trifluoroethylenes) and their characterization by 470-MHz fluorine-19 NMR," *Macromolecules,* vol. 17, no. 10, pp. 1932-1939, 1984.

[70] O. Vogl, M. F. Qin and A. Zilkha, "Head to head polymers," *Progress in Polymer Science,* vol. 24, no. 10, pp. 1481-1525, 1999.

[71] Y. Nakamura and S. Yamago, "Termination Mechanism in the Radical Polymerization of Methyl Methacrylate and Styrene Determined by the Reaction of Structurally Well-Defined Polymer End Radicals," *Macromolecules,* vol. 48, no. 18, pp. 6450-6456, 2015.

[72] A. Korbar and T. Malavasic, "Influence of different initiators on methyl methacrylate polymerization, studied by differential scanning calorimetry," *Journal of thermal analysis,* vol. 44, no. 6, pp. 1357-1365, 1995.

[73] Sigma-Aldrich, "Applications: Free Radical Initiators," [Online]. Available: https://www.sigmaaldrich.com/content/dam/sigma-aldrich/docs/Aldrich/General_Information/thermal_initiators.pdf?utm_source=redirect&utm_medium=promotional&utm_campaign=insite_thermal_initiators.

[74] Santa Cruz Biotechnology, "Potassium persulfate Material Safety Data Sheet," 21 04 2010. [Online]. Available: http://datasheets.scbt.com/sc-203362.pdf.

[75] C. H. Bamford, "9 - Redox Initiators," *Comprehensive Polymer Science and Supplements,* vol. 3, pp. 123-139, 1989.

[76] T. Kochthongrasamee and P. Prasassarakich, "Effects of redox initiator on graft copolymerization of methyl methacrylate onto natural rubber," *Journal of Applied Polymer,* vol. 101, no. 4, pp. 2587-2601, 2006.

[77] S. Hernández, J. K. Papp and D. Bhattacharyya, "Iron-Based Redox Polymerization of Acrylic Acid for Direct Synthesis of Hydrogel/Membranes, and Metal Nanoparticles for Water Treatment," *Industrial & Engineering Chemistry research,* vol. 53, no. 3, pp. 1130-1142, 2013.

[78] R. b. Li, J. Kong, H. Liu, P. Chen, G. Liu, F. Li and W. Lv, "A sulfate radical based ferrous–peroxydisulfate," *RSC Advances,* vol. 7, pp. 22802-22809, 2017.

[79] D. Zhao, X. Liao, X. Yan, S. G. Huling, T. Chai and H. Tao, "Effect and mechanism of persulfate activated by different methods for PAHs removal in soil," *Journal of Hazardous Materials,* Vols. 254-255, pp. 228-235, 2013.

[80] C. Liang and H.-W. Su, "Identification of Sulfate and Hydroxyl Radicals in Thermally Activated Persulfate," *Industrial & Engineering Chemistry Research,* vol. 48, no. 11, pp. 5558-5562, 2009.

[81] M. D. Fernandez and G. M. Guzman, "Aqueous polymerization of methyl methacrylate initiated by Ce(IV)-disaccharide redox systems. effects of acid concentration and additives," *European Polymer Journal,* vol. 25, no. 11, pp. 1165-1168, 1989.

[82] X. Ni, J. Ye and C. Dong, "Kinetics studies of methyl methacrylate photopolymerization initiated by titanium dioxide semiconductor nanoparticles," *Journal of Photochemistry and Photobiology A: Chemistry,* vol. 181, no. 1, pp. 19-27, 2006.

[83] T. Corrales, C. Peinado, F. Catalina, M. G. Neumann, N. S. Allen, A. M. Rufs and M. V. Encinas, "Photopolymerization of methyl methacrylate initiated by thioxanthone derivatives: photoinitiation mechanism," *Polymer,* vol. 41, no. 26, pp. 9103-9109, 2000.

[84] J. P. Fouassier, *Photoinitiation, Photopolymerization, and Photocuring: Fundamentals and Applications*, Cincinnati: Hanser/Gardner, 1995.

[85] S. P. Pappas, "Photopolymerization," in *Encyclopedia of Polymer science and Engineering*, vol. 11, New York, Wiley-Interscience, 1988, pp. 186-212.

[86] S. Baccaro, C. Casieri, A. Cemmi, M. Chiarini, V. D'Aiuto and M. Tortora, "Characterization of γ-radiation induced polymerization in ethyl methacrylate and methyl acrylate monomers solutions," *Radiation Physics and Chemistry,* vol. 141, pp. 131-137, 2017.

[87] G. J. Price, P. F. Smith and P. J. West, "Ultrasonically initiated polymerization of methyl methacrylate," *Ultrasonics,* vol. 29, no. 2, pp. 166-170, 1991.

[88] G. Zhang, J. Qiu, L. Shao, M. Liu, M. Zhang and Y. Wu, "Ultrasonic weld properties of heterogeneous polymers: Polylactide and poly (methyl methacrylate)," *Journal of Materials Processing Technology,* vol. 211, no. 8, pp. 1358-1363, 2011.

[89] C. Liu, N. Cui, S. Osbeck and H. Liang, "Air plasma processing of poly(methyl methacrylate) micro-beads: Surface characterisations," *Applied Surface Science,* vol. 259, pp. 840-846, 2012.

[90] G. Pistoia, A. Ricci and M. A. Voso, "Electroinitiated Polymerization of Methyl Methacrylate in Aqueous Sulfuric Acid," *Journal of Applied Polymer Science,* vol. 20, pp. 2441-2450, 1976.

[91] G. Pistoia, O. Bagnarelli and M. Maiocco, "Evaluation of factors affecting the radical electropolymerization of methyl metharylate in the presence of HNO3," *Journal of Applied Electrochemistry,* vol. 9, no. 3, pp. 343-349, 1979.

[92] J. R. Maccallum and D. H. Mackeron, "Electropolymerisation of methyl methacrylate on carbon fibre surface," *European Polymer Journal,* vol. 18, pp. 717-724, 1982.

[93] M. P. Yashoda, B. S. Sherigara and G. Venkateswaran, "Electroinitiated polymerisation of methyl methacrylate mediated by titanium(3)-hydroxylamine redos system: a kinetic study," *Polymer,* vol. 41, pp. 7381-7389, 2000.

[94] A. Aurizi, V. Filippeschi and G. Pistoia, "Anodic polymerization of methyl methacrylate in CH3OH-H2SO4 solutions," *Journal of Applied Electrochemistry,* vol. 7, pp. 139-145, 1977.

[95] A. S. Sarac, S. Ozkara, B. Ustamehmetoglu and E. Sezer, "Controlled Electroinduced Polymerization of Methyl Methacrylate in the Presence of Catalytic Amount of Cerium(4)," *Journal of Macromolecular Science,* vol. 40, no. 2, pp. 193-207, 2003.

[96] A. S. Sarac and F. C. Cebeci, "Electroinduced Dispersive Polymerization of Methyl Methacrylate in Aqueous Media," *International Journal of Polymeric Materials,* vol. 53, pp. 762-776, 2004.

[97] T. Hao, *Electrorheological Fluids: The Non-aqueous Suspensions,* Amsterdam, Netherlands: Elsevier, 2005.

[98] M. Albeck, M. Konigsbuch and J. Relis, "Electroinitiated Polymerization of Vinylic Monomers in Polar Systems. 1. Contribution of the Electrolysis of Methanol to Free-Radical Polymerization," *Journal of Polymer Science,* vol. 9,

no. 5, pp. 1375-1386, 1971.

[99] P. Cheah, C. N. Bhikha, J. H. O'Haver and A. E. Smith, "Effect of Oxygen and Initiator Solubility on Admicellar Polymerization of Styrene on Silica Surfaces," *International Journal of Polymer Science,* vol. 2017, no. Article ID 6308603, p. 7, 2017.

[100] S. L. Cram, G. M. Spinks, G. G. Wallace and H. R. Brown, "Mechanism of electropolymerization of methyl methacrylate and glycidyl acrylate on stainless steel," *Electrochimica Acta,* vol. 47, pp. 1935-1948, 2002.

[101] S. Nakahama, K. Hashimoto and N. Yamazaki, "Anode-Initiated Polymerization of Olefins and Tetrahydrofuran," *Polymer Journal*, vol. 4, no. 4, pp. 437-445, 1973.

[102] E. D. Giglio, S. Cometa, L. Sabbatini, P. G. Zambonin and G. Spoto, "Electrosynthesis and analytical characterization of PMMA coatings on titanium substrates as barriers against ion release," *Analytical and Bioanalytical Chemistry*, pp. 626-633, 2005.

[103] Polysciences, Inc., "Methyl Methacrylate Casting & Embedding Kit for making hard, clear castings," [Online]. Available: http://www.polysciences.com/default/catalog-products/life-sciences/histology-microscopy/plastic-embedding-media-kits/additional-embedding-kits-reagents/methyl-methacrylate-embedding-and-casting-kit/.

[104] S. Zhu, Y. Tian, A. E. Hamielec and D. R. Eaton, "Radical trapping and termination in free-radical polymerization of MMA," *Macromolecules* , vol. 23, no. 4, 1990.

[105] D. C. Harris, *Exploring Chemical Analysis*, New York: W. H. Freeman and Company, 2013.

[106] A. Wheeler and A. Ganji, *Introduction to Engineering Experimentation*, New Jersey: Prentice-Hall Inc., 1996.

[107] R. M. Silverstein, G. C. Bassler and T. C. Morrill, *Spectrometric Identification of Organic Compounds*, New York: John Wiley & Sons, 1991.

[108] C. Schaller, "IR11. Appendix: IR Table of Organic Compounds," Chemistry LibreTexts, 14 12 2013. [Online]. Available: https://chem.libretexts.org/Bookshelves/Physical_and_Theoretical_Chemistry_Textbook_Maps/Supplemental_Modules_(Physical_and_Theoretical_Chemistry)/Spectroscopy/Vibrational_Spectroscopy/Infrared_Spectroscopy/Interpreting_Infr

ared_Spectra/IR11._Appendix%3A_.

[109] R. J. Fritsch and I. Krause, "Electrophoresis," in *Encyclopedia of Food Sciences and Nutrition*, Cambridge, Academic Press, 2003, pp. 2055-2062.

[110] H. Cardenas and L. J. Struble, "Modeling Electrokinetic Nanoparticle Penetration for Permeability Reduction of Hardened Cement Paste," *Journal of Materials in Civil Engineering,* vol. 20, no. 11, 2008.

[111] NACE International, "Economic Impact," NACE International, 2016. [Online]. Available: http://impact.nace.org/economic-impact.aspx.

[112] H. Luo, H. Su, G. Ying, C. Dong and X. Li, "Effect of cold deformation on the electrochemical behaviour of 304L stainless steel in contaminated sulfuric acid environment," *Applied Surface Science,* vol. 425, pp. 628-638, 2017.

[113] H. Luo, H. Su, C. Dong, K. Xiao and X. Li, "Electrochemical and passivation behavior investigation of ferritic stainless steel in alkaline environment," *Construction and Building Materials,* vol. 96, pp. 502-507, 2015.

[114] S. A. Saadi, Y. Yi, P. Cho, C. Jang and P. Beeley, "Passivity breakdown of 316L stainless steel during potentiodynamicpolarization in NaCl solution," *Corrosion Science,* vol. 111, pp. 720-727, 2016.

[115] Biologic Science Instruments, "Ohmic Drop I- Effect on measurements," [Online]. Available: https://www.bio-logic.net/wp-content/uploads/Application-note-27.pdf.

[116] AMETEK, "Basics of Corrosion Measurements," [Online]. Available: https://www.ameteksi.com/-/media/ameteksi/download_links/documentations/library/princetonappliedresearch/application_note_corr-1.pdf?la=en.

[117] J. M. Deus, B. Diaz, L. Freire and X. R. Novoa, "The electrochemical behaviour of steel rebars in concrete: an Electrochemical Impedance Spectroscopy study of the effect of temperature," *Electrochimica Acta,* vol. 131, pp. 106-115, 2014.

[118] J. Yao, D. D. Macdonald and C. Dong, "Passive film on 2205 duplex stainless steel studied by photo-electrochemistry and ARXPS methods," *Corrosion Science,* vol. 146, pp. 221-232, 2019.

[119] B. Li, Y. Huan and W. Zhang, "Passivation and Corrosion Behavior of P355 Carbon Steel in Simulated Concrete Pore Solution at pH 12.5 to 14," *International Journal of Electrochemical Science,* vol. 12, pp. 10402-10420,

2017.

[120] ASTM C 876, "Standard Test Method for Half-Cell Potentials of Uncoated Reinforcing Steel in Concrete," *American Society of Testing and Materials,* 1999.

[121] Tinker and Rasor, "Portable Copper-Copper / Sulfate Reference Electrodes," January 2010. [Online]. Available: http://tinker-rasor.com/wp-content/uploads/2014/06/COPPER-SULFATE_HALF_CELLS.pdf.

[122] National Center for Biotechnology Information, "Calcium Hydroxide (Ca(OH)2)," PubChem Compound Database, [Online]. Available: https://pubchem.ncbi.nlm.nih.gov/compound/14777.

[123] A. C. 305, "Standard Practice for Mechanical Mixing of Hydraulic Cement Pastes and Mortars of Plastic Consistency," *Annual Book of ASTM Standards,* vol. 04, no. 01, 2006.

[124] A. C496/C496M-17, "Standard Test Method for Splitting Tensile Strength of Cylindrical Concrete Specimens," *ASTM International,* vol. 04, no. 02, 2017.

[125] A. C39/C39M-18, "Standard Test Method for Compressive Strength of Cylindrical Concrete Specimens," *American Society of Testing and Materials,* vol. 04, no. 02.

[126] A. C617/C617M-15, "Standard Practice for Capping Cylindrical Concrete Specimens," *ASTM International,* vol. 4, no. 2, 2015.

[127] B. A. Horri, M. Choolaei, A. Chaudhry and H. Qaalib, "A highly efficient hydrogen generation electrolysis system using alkaline zinc hydroxide solution," *International Journal of Hydrogen energy,* vol. 44, pp. 72-81, 2019.

[128] International Telecommunication Union, "Studio encoding parameters of digital television for standard 4:3 and wide-screen 16:9 aspect ratios," 03 2011. [Online]. Available: https://www.itu.int/dms_pubrec/itu-r/rec/bt/R-REC-BT.601-7-201103-I!!PDF-E.pdf.

[129] N. A. Surplice, "The electrical conductivity of calcium and strontium oxides," *British Journal of Applied Physics,* vol. 17, no. 2, p. 175, 1966.

[130] ASM Handbook Program, *ASM Handbook: Properties and Selection: Irons, Steels, and High-Performance Alloys*, 10th ed., vol. 1, Metals Park, Ohio: ASM International, 1990.

[131] B. Elsener and A. Rossi, "Passivation of Steel and Stainless Steel in Alkaline Media Simulating Concrete," *Encyclopedia of Interfacial Chemistry,* pp. 365-

375, 2018.

[132] B. Beverskog and I. Puigdomenech, "Revised Pourbaix Diagrams for Iron at 25-300 °C," *Corrosion Science,* vol. 38, no. 12, pp. 2121-2135, 1996.

[133] S. Sharifi-Asl, F. Mao, P. Lu, B. Kursten and D. D. Macdonald, "Exploration of the effect of chloride ion concentration and temperature on pitting corrosion of carbon steel in saturated Ca(OH)2 solution," *Corrosion Science,* vol. 98, pp. 708-715, 2015.

[134] B. Li and W. Zhang, "Electrochemical Deposition of Ni-Co/SiC Nanocomposite Coatings for Marine Environment," *International Journal of Electrochemical Science,* vol. 12, p. 7017, 2017.

[135] M. F. Arenas and R. G. Reddy, "CORROSION OF STEEL IN IONIC LIQUIDS," *Journal of Mining and Metallurgy,* vol. 39, pp. 81-91, 2003.

[136] Kurt J Lesker Company, "SDS - Iron Oxide (Fe2O3) Pieces," 1 5 2012. [Online]. Available: https://www.lesker.com/msds/pdfs/cd72f997d54d3bc42d09a34d6bdca56ebf2ea7fd3a31f08843ec5bd413.pdf.

[137] C. Lian, Y. Zhuge and S. Beecham, "The relationship between porosity and strength for porous concrete," *Construction and Building Materials,* pp. 4294-4298, 2011.

[138] O. F. Olaj, "Electrolytically Initiated Vinyl Polymerization," *Macromolecular Symposia,* vol. 8, no. 1, pp. 235-254, 1987.

[139] B. L. Schmick and A. Pollington, Concrete Repair Manual, vol. 1, Des Plaines: International Concrete Repair Insitute.

[140] S. Bewick, R. Parsons, T. Forsyhe, S. Robinson and J. Dupon, "6.20: Periodic Trends: Electronegativity," Chemistry LibreTexts, 28 06 2016. [Online]. Available: https://chem.libretexts.org/Bookshelves/Introductory_Chemistry/Book%3A_Introductory_Chemistry_(CK-12)/06%3A_The_Periodic_Table/6.20%3A_Periodic_Trends%3A_Electronegativity.

[141] R. Ouellette and J. D. Rawn, *Principles of Organic Chemistry,* Amsterdam: Elsevier, 2015.

[142] M. Blaber, "Dipole Moments," Chemistry LibreTexts, 16 1 2018. [Online]. Available:

https://chem.libretexts.org/Bookshelves/Physical_and_Theoretical_Chemistry_Textbook_Maps/Supplemental_Modules_(Physical_and_Theoretical_Chemistry)/Physical_Properties_of_Matter/Atomic_and_Molecular_Properties/Dipole_Moments.

[143] R. D. Nelson, D. R. Lide and A. A. Maryott, "Selected Values of Electric Dipole Moments for Molecules in the Gas Phase," U.S. National Bureau of Standards, Washigton, D.C. , 1967.

[144] M. Shima, M. Sato, M. Atsumi and K. Hatada, "Dipole Moments of Isotactic and Syndiotactic Poly(methyl methacrylate) and Their Temperature Dependence," *Polymer Journal,* vol. 26, pp. 579-585, 1994.

[145] N. J. Tro, *Chemistry: A Molecular Approach*, Upper Saddle River: Pearson Education, 2008.

[146] L. Hunt, "Hydrolysis of Esters," University of Calgary, [Online]. Available: http://www.chem.ucalgary.ca/courses/351/Carey5th/Ch20/ch20-3-3-1.html.

[147] F. C. Baines and J. C. Bevington, "A tracer study of the hydrolysis of methyl methacrylate and methyl acrylate units in homopolymers and copolymers," *Polymer Chemistry,* vol. 6, no. 9, pp. 2433-2440, 1968.

[148] M. B. Blanco, M. A. Teruel, I. Bejan, I. Barnes and P. Wiesen, "Methyl Methacrylate In The Atmosphere: Oh- And Cl-Initiated Oxidation In The Gas Phase," *Simulation and Assessment of Chemical Processes in a Multiphase Environment,* pp. 485-494, 2008.

[149] National Center for Biotechnology Information, "Sodium methacrylate," PubChem Database, [Online]. Available: https://pubchem.ncbi.nlm.nih.gov/compound/3255932.

[150] S. Polowinski, "Copolymerization of methacrylic acid with methyl methacrylate on a polyethylene glycol matrix," *European Polymer Journal,* vol. 19, no. 8, p. 679–681, 1983.

[151] S. Fleischmann and V. Percec, "Copolymerization of methacrylic acid with methyl methacrylate by SET-LRP," *Journal of Polymer Science,* vol. 48, no. 21, pp. 4884-4888, 2010.

[152] Sigma-Aldrich, "Safety Data Sheet of Sodium Methacrylate," 10 11 2018. [Online]. Available: https://www.sigmaaldrich.com/catalog/product/aldrich/408212?lang=en&region=US.

[153] L. M. Gan, K. C. Lee, C. H. Chew and S. C. Ng, "Effects of Surfactant Concentration on Polymerization of Mehtyl Methacrylate and Styrene in Emulsions and Microemulsions," *Langmuir,* vol. 11, pp. 449-454, 1995.

[154] Sigma-Aldrich, "Poly(methyl methacrylate)," Sigma-Aldrich, [Online]. Available: https://www.sigmaaldrich.com/catalog/substance/polymethylmethacrylate12345901114711?lang=en&region=US&attrlist=Physical%20Form|Density.

[155] B. Harbick, L. Suh and J. Fong, "Closest Packed Structures," Chemistry LibreTexts, 19 06 2017. [Online]. Available: https://chem.libretexts.org/Bookshelves/Physical_and_Theoretical_Chemistry_Textbook_Maps/Supplemental_Modules_(Physical_and_Theoretical_Chemistry)/Physical_Properties_of_Matter/States_of_Matter/Properties_of_Solids/Crystal_Lattice/Closest_Pack_Structures.

[156] Z. Suo, "Motions of Microscopic Surfaces in Materials," *Advances in Applied Mechanics,* vol. 33, pp. 193-294, 1997.

[157] N. Iversen and B. B. Jorgensen, "Diffusion coefficients of sulfate and methane in marine sediments: Influence of porosity," *Geochimica et Cosmochimica Acta,* vol. 57, no. 3, pp. 571-578, 1993.